SOLID STATE SUPERCAPACITORS BASED ON REDUCED GRAPHENE OXIDE/RUTHENIUM OXIDE COMPOSITE THIN FILMS

A THESIS SUBMITTED TO

D. Y. PATIL EDUCATION SOCIETY (DEEMED TO BE UNIVERSITY), KOLHAPUR

FOR THE DEGREE OF

DOCTOR OF PHILOSOPHY

IN

PHYSICS

UNDER THE FACULTY OF
INTERDISCIPLINARY STUDIES

BY

Mr. AJINKYA GOVINDRAO BAGDE
M. Sc.

UNDER THE SUPERVISION OF

Prof. CHANDRAKANT. D. LOKHANDE
M. Sc., Ph. D.

DEAN & RESEARCH DIRECTOR,
CENTRE FOR INTERDISCIPLINARY RESEARCH,
D. Y. PATIL EDUCATION SOCIETY (DEEMED TO BE UNIVERSITY), KOLHAPUR
416 006, MAHARASHTRA, (INDIA)

2025

DECLARATION

I am **Ajinkya Govindrao Bagde**, hereby declare that the thesis entitled ***"SOLID STATE SUPERCAPACITORS BASED ON REDUCED GRAPHENE OXIDE/RUTHENIUM OXIDE COMPOSITE THIN FILMS"*** submitted for the degree of **Doctor of Philosophy (Ph.D.)** in the **Physics**, Faculty of Interdisciplinary Studies, under the guidance of **Prof. C. D. Lokhande, Centre for Interdisciplinary Research (CIR), D. Y. Patil Education Society (Deemed to be University), Kolhapur** is completed and written by me, has not before made the basis for the award of any other higher education institute in India or any other country. To the best of my knowledge and belief the thesis contains no material previously published or written by another person except where due reference is made. Further, I declare that I have not violated any of the provisions under the copyright and piracy/cyber/IPR Act amended from time to time.

Research Student

Place: Kolhapur

Date: 16/01/2025

Mr. Ajinkya Govindrao Bagde

CERTIFICATE OF GUIDE

This is to certify that the thesis entitled ***"SOLID STATE SUPERCAPACITORS BASED ON REDUCED GRAPHENE OXIDE/RUTHENIUM OXIDE COMPOSITE THIN FILMS"*** which is being submitted herewith for the award of the Degree of **Doctor of Philosophy (Ph.D.)** in **Physics, Faculty of Interdisciplinary Studies, under the guidance of Prof. C. D. Lokhande, Center for Interdisciplinary Research (CIR), D. Y. Patil Education Society (Deemed to be University), Kolhapur**, is the result of the original research work completed by **Mr. Ajinkya Govindrao Bagde** under my supervision and guidance and to the best of my knowledge and belief the work embodied in this thesis has not formed earlier the basis for the award of any degree or similar title of this or any other university or examining body.

Research Guide

Place: Kolhapur

Date: 16/01/2025

Prof. C. D. Lokhande
Dean and Research Director
Centre for Interdisciplinary Research,
D. Y. Patil Education Society,
(Deemed to be University),
Kolhapur - 416 006

PROF. C. D. LOKHANDE
Dean
Centre For Interdisciplinary Studies
D. Y. Patil Education Society
(Institution Deemed to be University)
869, 'E', Kasaba Bawada
KOLHAPUR- 416006

ACKNOWLEDGEMENT

This was a beautiful journey, a journey of expanding the boundaries of knowledge, a journey of finding your strengths and weaknesses, a journey of becoming mentally and emotionally strong. It became more beautiful and interesting because of the people I met along the way. I would like to take this opportunity to acknowledge those fascinating people.

I would like to express my first profound thanks and respect towards my cherished guide ***Prof. Chandrakant D. Lokhande*** *(Dean and Research Director, Centre for Interdisciplinary Research, D. Y. Patil Education Society, Kolhapur) for his keen awareness, valuable guidance, encouragement, and support. I am always amazed by his enthusiasm for science and how effectively he has shaped the young minds of two generations. I am very thankful to him for choosing me as his PhD student and I feel very fortunate to be part of CDL group.*

I would like to express my sincere thanks to President ***Dr. Sanjay D. Patil Saheb****, Vice President* ***Mr. Satej D. Patil Saheb****, Vice-Chancellor* ***Prof. R. K. Mudgal,*** *and Registrar* ***Dr. V. V. Bhosale*** *for the inspiration and support. I am thankful to faculty of CIR* ***Dr. R. S. Patil, Dr. J. L. Gunjakar****,* ***Dr. U. M. Patil****,* ***Dr. Vishwajeet Khot, Dr. Sharad Patil, Dr. Mayakannan and Dr. Pravin Pawar*** *who helped me to analyze the results with all their empathy and cooperative mind. I also thank* ***Dr. A. C. Lokhande****,* ***Dr. V. C. Lokhande****,* ***and Dr. D. B. Malavekar*** *for providing me important sample characterization data.*

In addition, I acknowledge the funding support from ***Chhatrapati Shahu Maharaj Research Training and Human Development Institute (SARTHI) Pune, Government of Maharashtra, India,*** *for funding support* ***(sanction number CSMNRF: 2022/2022-23/2341)****.*

I would like to express sincere thanks to my seniors ***Dr. Prity Bagwade, Dr. Shivaji Ubale, Dr. Sachin Pujari, Dr. Yogesh Chitare, Vikas Magdum, Dr. Shirin Kulkrani, Sambhaji Khot, Shraddha Bhosale, Sambhaji Kumbhar, Rushiraj Bhosale Ranjit Nikam, Ketaki Kadam and Manohar Lad*** *for insightful guidance, scientific discussions and valuable suggestions on the present work.*

I would like to acknowledge my colleagues at Centre for Interdisciplinary Research, ***Divya Pawar, Jyoti Thorat, Dilip Patil, Sagar Patil, Shraddha Pawar, Tamseen Nejakar, Najiya Mulla, Nadiya Patel, Sohel Shaikh, Shweta Talekar, Prashant Sawant, Kuldip Belekar, Sumita Patil, Sujata Patil, Suraj Sankapal, Dhanashree More, Suhasini Yadav, and Ganesh Jadhav*** *for their wonderful collaboration. I want to thank them for their support and valuable suggestions during research work.*

I am thankful to the non-teaching staff of CIR ***Mr. Nirmal, Mr. Shirake, Mrs. Namrata, Mr. Ramdas, Mr. Omkar, Mr. Shubham, and Mrs. Sarita*** *for their co-operation.*

My heartfelt appreciation goes out to my father ***Dr. Govindrao****, my mother* ***Mrs. Shobha****, my sister* ***Dr. Sharwari****, my wife* ***Mrs. Priyanka,*** *my two lovely daughters* ***Jija and Tara****, and all my family members who despite their hard times and sufferings, continuously supported and encouraged me to complete my research.*

~Ajinkya

Place: Kolhapur

LIST OF PATENTS, PUBLICATIONS AND CONFERENCES ATTAINED

Patents: (Granted 01, Published 06)

1. Method of synthesizing reduced graphene oxide/polyaniline coating for energy storage application thereof, Prof. C. D. Lokhande, Miss. D. C. Pawar, **Mr. A. G. Bagde**, Mr. S. R. Sankapal, Grant number: **542485**.

2. Porous reduced graphene oxide/ruthenium oxide coating for energy storage application, Prof. C. D. Lokhande, **Mr. A. G. Bagde**, Miss. D. C. Pawar, Mrs. J. P. Thorat, Dr. A. C. Lokhande, Application no: 202321038525.

3. A Method of synthesizing reduced graphene oxide-Nickel Cobalt oxide (rGo-NiCO2O4) composite coating on solid surface for energy storage application, Prof. C. D. Lokhande, Mrs. J. P. Thorat, **Mr. A. G. Bagde**, Miss. D. C. Pawar, Mr. S. D. Khot, Dr. V. C. Lokhande, Application no: 202321047985.

4. A chemical method of reduced graphene oxide/polypyrrole coating for energy storage, Prof. C. D. Lokhande, Miss. D. C. Pawar, Dr. V. C. Lokhande, Mrs. J. P. Thorat, **Mr. A. G. Bagde**, Application no: 202421002872.

5. Synthesizing method of copper vanadate oxide coating for energy storage application, Prof. C. D. Lokhande, Mr. S. R. Sankapal, **Mr. A. G. Bagde**, Miss. D. C. Pawar, Mrs. J. P. Thorat, Dr. V. C. Lokhande, Application no: 202421017358.

6. A method of multiwalled carbon nanotubes/copper vanadate oxide coating for energy storage application, prof. C. D. Lokhande, Mr. S. R. Sankapal, Prof. B. R. Sankapal, **Mr. A. G. Bagde**, Application no. 202421038823

7. Method of synthesizing reduced graphene oxide/dysprosium sulfide composite coating for energy storage application thereof, Prof. C. D. Lokhande, Mr. S. D. Khot, **Mr. A. G. Bagde**, Miss. D. C. Pawar, Mr. S. B. Shaikh, Dr. V. C. Lokhande, Application no: 202421063773.

Papers and Review Article Published in International Journals: (06)

1. **A. G. Bagde**, D. B. Malavekar, A. C. Lokhande, S. D. Khot, C. D. Lokhande*, Flexible asymmetric supercapacitor based on reduced graphene oxide (rGO)/ruthenium oxide (RuO_2)

composite electrodes, J. Alloys Compd., 19, 2024, 173591, https://doi.org/10.1016/j.jallcom.2024.173591. **(IF- 5.8)**

2. **A. G. Bagde**, D. B. Malavekar, D. C. Pawar, S. D. Khot, C. D. Lokhande, Pseudocapacitive performance of amorphous ruthenium oxide deposited by successive ionic layer adsorption and reaction (SILAR): Effect of thickness, J. Phys. Chem. Solids, 179, (2023), 111386-111397, https://doi.org/10.1016/j.jpcs.2023.111386 **(IF- 4.3)**.

3. D. C. Pawar, **A. G. Bagde**, J. P. Thorat, C. D. Lokhande, Synthesis of reduced graphene oxide (rGO)/polyaniline (PANI) composite electrode for energy storage: Aqueous asymmetric supercapacitor, Eur. Polym. J., 218, (2024), 113366-113378, https://doi.org/10.1016/j.eurpolymj.2024.113366 **(I.F.- 5.8)**.

4. D. C. Pawar, D. B. Malavekar, S. D. Khot, **A. G. Bagde**, C. D. Lokhande, Performance of chemically synthesized polyaniline film-based asymmetric supercapacitor: Effect of reaction bath temperature, Mater. Sci. Eng. B., 292, (2023), 116432-116448, https://doi.org/10.1016/j.mseb.2023.116432 **(I.F.- 3.9)**.

5. S. R. Sankapal, T. B. Deshmukh, **A. G. Bagde**, K. Patil, B. R. Sankapal, C. D. Lokhande*, Sequential Growth Controlled Copper Vanadate Nanopebbles Embedded Thin Films: Electrode for Asymmetric Supercapacitive Device, J. Phys. Chem. Solids, 195, (2024), 112286-112298, https://doi.org/10.1016/j.jpcs.2024.112286 **(I.F.-4.3).**

6. D. Malavekar, D. Pawar, **A. Bagde**, S. Khot, S. Sankapal, S. Bachankar, S. Patil, C. Lokhande, J. Kim, Advancements in 2D Carbon Composite Materials: A Comprehensive Review on Synthesis, Characterization, and Supercapacitive Charge Storage, J. Chem. Eng., 501, (2024), 157533-157576, https://doi.org/10.1016/j.cej.2024.157533 **(I.F. - 13.3)**.

Papers/Poster Presented at National/International Conferences: (05)

1. Presented poster in international conference on **''Advanced Material Synthesis, Characterizations, and Applications''** (AMSCA-2022), 18th to 20th October 2022, Department of Physics, Savitribai Phule University, Pune.
2. Best Paper Award for presented paper in Three-day International Conference on **"Nano Composite for Aerospace Applications"**, 2th to 4th February 2023, Department of Basic Science and Electronics and Communication Engineering, Cambridge Institute of Technology, Bengaluru.
3. Oral presentation at an International Conference on **"Advanced Materials Synthesis, Characterization and Applications (AMSCA- 2023)** Organized by Department of Physics (SPPU), Pune. 21 to 24 November 2023.

4. Presented Paper at One Day International Conference **on "Recent Trends in Fabrication of Nanomaterials and Their Applications (ICRTFNA-2023)"**, 15th March 2023, Rajarshri Chhatrapati Shahu College, Kolhapur.

5. Presented oral in Three days International Conference on **"Nanotechnology Addressing the Convergence of Materials Science, Biotechnology and Medical Science (IC-NACMBM-2024)"**, 12th to 14th February 2024, organized by CIR, D.Y. Patil Education Society, Kolhapur.

Conference/Seminar/Workshop Participation: (07)

1. Workshop and Hands-On Training on **"Bio-Atomic Force Microscopy"** 04-05 January 2022, SAIF (CFC), Shivaji University, Kolhapur.
2. National Conference on **"Emerging Trends in Chemistry"**- 10th February 2022, SMM Akluj.
3. Workshop on **''Intellectual Property Rights''** under National IPR Awareness Mission, 12th August 2022, D. P. Bhosale College, Koregaon.
4. International Conference on **"Emerging Trends in Material Science"**- 9th & 10th November 2022, D. P. Bhosale College, Koregaon.
5. National seminar on **"Emerging Nano Materials for Renewable Energy"**, 26th December 2022, Sanjay Ghodawat University, Kolhapur.
6. One Day National Conference on "**Physical, Chemical and Biological Strategies, Tools and Ideas for Promising Future"**, 10th March 2023, K. N. Bhise Arts, Commerce and Vinayakrao Patil Science College, Vidyanagar, Bhosare (Kurduwadi), Solapur.
7. One Day National Conference on "**EMERGING TRENDS IN BASIC SCIENCE (NCETBS-2023)",** 20th March 2023, Madhavrao Patil Arts, Commerce and Science college, Palam.

CONTENTS

LIST OF FIGURES

LIST OF TABLES AND CHARTS

LIST OF ABBREVIATIONS

AC	Activated carbon	**LIBs**	Lithium-ion batteries
Ag/AgCl	Silver/Silver chloride	**LBL**	Layer-by-layer
APS	Ammonium persulfate	**LEDs**	Light emitting diodes
AR	Analytical grade	**MWCNT**	Multi-walled carbon nanotube
ASC	Asymmetric supercapacitor	**P**	Adsorptive pressure
BET	Brunauer-Emmett-Teller	**PANI**	Polyaniline
BJH	Barrett-Joyner-Halenda	**Ppy**	Polypyrrole
CC	Carbon cloth	**Pt**	Platinum plate
CBD	Chemical bath deposition	**PT**	Polythiophene
CE	Counter electrode	**PVA**	Polyvinyl alcohol
CNT	Carbon nanotubes	**PVP**	Polyvinyl pyrrolidone
CPs	Conducting polymers	**Q**	Constant phase element
C_s	Specific capacitance	R_{ct}	Charge transfer resistance
CV	Cyclic voltammetry	**RE**	Reference electrode
CVD	Chemical vapour deposition	**RF**	Radio frequency
DDW	Double distilled water	**rGO**	Reduced graphene oxide
ΔV	Potential window	R_s	Equivalent series resistance
EDLC	Electric double-layer capacitor	S_E	Specific energy
EDTA	Ethylenediamine tetra acetic acid	S_P	Specific power
EIS	Electrochemical impedance spectroscopy	**SSC**	Symmetric supercapacitor
FT-IR	Fourier transform infrared spectroscopy	**SS**	Stainless steel
GCD	Galvanostatic charge-discharge	**SWCNT**	Single-walled carbon nanotube
GNR	Graphene nanoribbon	t_d	Discharge time
H_2SO_4	Sulphuric acid	**TEA**	Triethylammonium
HCl	Hydrochloric acid	W	Warburg
HRGO	Highly reduced graphene oxide	**WE**	Working electrode
IUPAC	International Union of Pure and Applied Chemistry	WO_3	Tungsten oxide
KCl	Potassium chloride	**XPS**	X-ray photoelectron spectroscopy
KOH	Potassium hydroxide	**XRD**	X-ray diffraction

CHAPTER-I

GENERAL INTRODUCTION AND LITERATURE SURVEY

CHAPTER-I

GENERAL INTRODUCTION AND LITERATURE SURVEY

1.1 General introduction:

1.1.1 Energy storage system and importance of supercapacitors:

Energy consumption is increasing with the global population and economy improving. This globalisation impacts present energy sources and infrastructure. Developing renewable and environmentally friendly energy sources, such as solar, wind, hydroelectric, and nuclear power, is essential for achieving future energy demands while decreasing environmental effects **[1]**. Renewable energy sources may address such a problem quickly and freely, giving them a tremendous potential for development. However, these unpredictable energies are challenged by factors like climate effects and unbalanced distribution **[2, 3]**. Electrical energy storage devices are essential for many kinds of real-world uses. Energy storage technologies have become crucial in renewable energy generation **[4, 5]**. Moreover, energy storage technologies that are economical, lightweight, adaptable, and reliable are necessary to meet the energy demands of the coming decades. Technology is becoming more efficient, durable, and environmentally friendly **[6]**. Energy storage devices (ESD) are crucial for meeting the energy demands of various applications while reducing our reliance on fossil fuels and mitigating environmental impact **[7-9]**. Researchers are actively improving ESD technologies to enhance performance, safety, and affordability, ultimately driving innovation across these diverse sectors. To address this challenge, ESD technologies such as batteries, capacitors, supercapacitors, flywheels, and fuel cells, are utilized **[10-13]**.

Supercapacitors, also known as ultracapacitors or electrochemical capacitors, are energy storage devices that have gained significant attention and found applications in various fields due to their unique characteristics. Unlike traditional batteries, supercapacitors store energy through the electrostatic separation of charges rather than chemical reactions **[14]**. After a million cycles, the most stable carbon-based supercapacitor maintained more than 80% of its initial capacitance, with a power density of 8500 W kg^{-1}. Its energy density, nonetheless, is still less than 7.4 Wh kg^{-1} **[15]**. An aqueous or non-aqueous electrolyte and a substance like a porous membrane separate the positive and negative electrodes of a supercapacitor. Supercapacitors work as electrical double-layer capacitors (EDLCs) by adsorbing ions from the electrolyte onto the electrode surface. Supercapacitors are frequently employed in hybrid automobiles, communications equipment (infrared remote, cell

phones, walkie-talkies, satellites, etc.), memory backup systems, pacemakers, and portable electronic gadgets, among other things **[16-18]**.

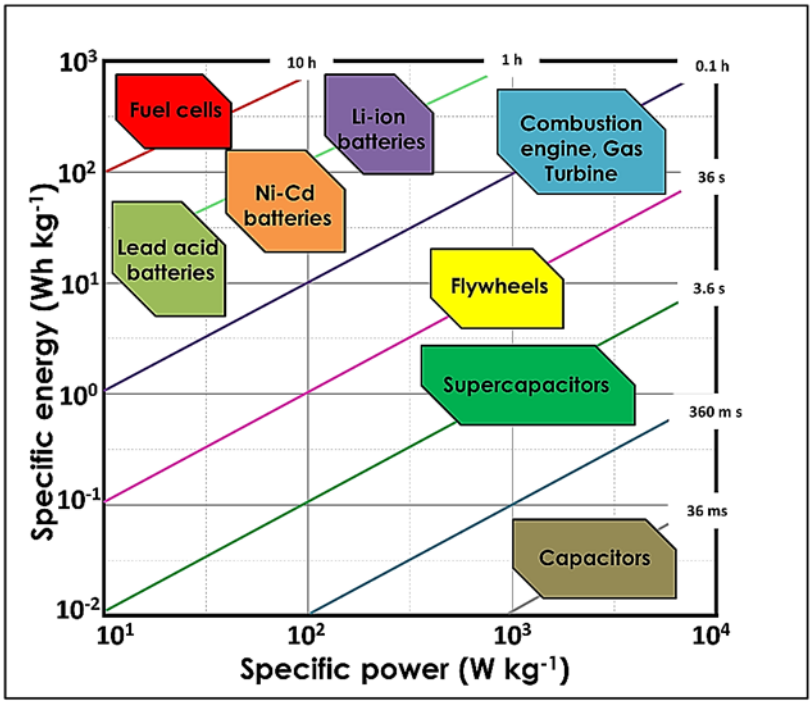

Figure 1.1: Ragone plot compares the energy and power density of several energy storage systems.

Figure 1.1 depicts the Ragone plot, which contrasts the energy and power density of several energy storage technologies, including batteries, fuel cells, supercapacitors, and traditional capacitors. A supercapacitor, by comparison, exists between a regular capacitor and batteries. Compared to capacitors and supercapacitors, batteries have a very high energy density **[19, 20]**. Traditional capacitors offer high power density but have limited energy density. SCs play a significant role in the Ragone plot, filling the gap between batteries, fuel cells, and ordinary capacitors. Conversely, supercapacitors offer more power than a battery and store more energy than a standard capacitor. Furthermore, supercapacitors offer more extended cycle stability than batteries, higher capacitance, and lower internal resistance than regular capacitors **[21]**.

1.1.2 Recent research and advancements in supercapacitors:

Supercapacitors have attracted a lot of interest as a promising energy storage technology that could be extremely important to global energy systems in the future. Supercapacitors stand out from other energy storage technologies like batteries due to

their great capacity. This is one of its key selling points. Because of their high energy density, supercapacitors can rapidly store and release huge amounts of energy, making them ideal for applications requiring high power output or rapid charge and discharge cycles **[22]**. Due to this property, supercapacitors are especially desirable for application in the automotive, renewable energy integration, grid stabilisation, and portable electronics sectors. Consumer electronic devices such as cell phones, sensors, wearable, and other portable gadgets often have diverse power requirements due to variations in their functionalities and usage patterns. Traditional batteries, which rely on chemical reactions to store and release energy, may struggle to meet these devices' instantaneous and variable power demands. Researchers are constantly pursuing improvements in materials science, electrode design, and manufacturing processes to increase the energy density of supercapacitors. Hybrid systems that combine supercapacitors with batteries or other energy storage technologies are being investigated to take advantage of the advantages of both kinds of devices. These hybrid systems may combine the superior energy density of batteries with the high power capabilities of supercapacitors. As a result, experts are investigating at new electrode materials with improved conductivity, a larger surface area, and improved electrochemical performance **[23-25]**. This involves analysing conductive polymers, transition metal oxides, and carbon-based materials like graphene, carbon nanotubes, and activated carbon. Nanostructure and surface modification methods are also being explored to enhance the interaction between electrode materials and the electrolyte, improving ion transport and capacitance. Novel fabrication techniques are being developed to enhance the supercapacitor manufacturing process and facilitate expandable production. This covers techniques for fine control over electrode structure and thickness, like template-assisted synthesis, atomic layer deposition, and inkjet printing. Researchers are also determining materials and production techniques to increase the environmental sustainability of supercapacitors. This involves utilising carbon materials derived from biomass, recycling electrode materials, and reducing the fabrication process on hazardous or harmful chemicals **[26]**.

Commercial supercapacitors have made major use of carbon-based materials in the last few decades because of their high surface area, good electrical conductivity, stability, and affordability. Flexible solid-state devices (SSD) are also used in implantable medical devices. Furthermore, solid-state

supercapacitor devices that are small and lightweight can be used in portable electronic devices **[27]**.

1.1.3 Fundamental concept of supercapacitors:

In an electrochemical capacitor, often called an electric double-layer capacitor (EDLC) or supercapacitor, the charge storage mechanism involves the formation of an electric double layer at the interface between the electrode and the electrolyte. When a voltage is applied, ions from the electrolyte migrate to the surface of the electrode, forming layers of positive and negative charges. This separation of charges creates an electric field across the interface, storing energy electrostatically. The EDLC is made very close to the surface of the electrode, typically within a few Angstroms, and the distance between the layers depends on the specific electrolyte used **[16, 28]**. In the conventional capacitor, the charge storage mechanism is purely electrostatic, as seen in **Figure 1.2**. After applying a potential between the conducting plates separated by a dielectric material, the plates accumulate opposite charges (positive and negative) due to the electric field established by the applied voltage. This accumulation of charges creates an electric field within the dielectric, which stores energy in the form of electrostatic potential energy. A conventional capacitor's capacitance is the ratio of the charge stored on one plate to the voltage applied across the plates **[29]**.

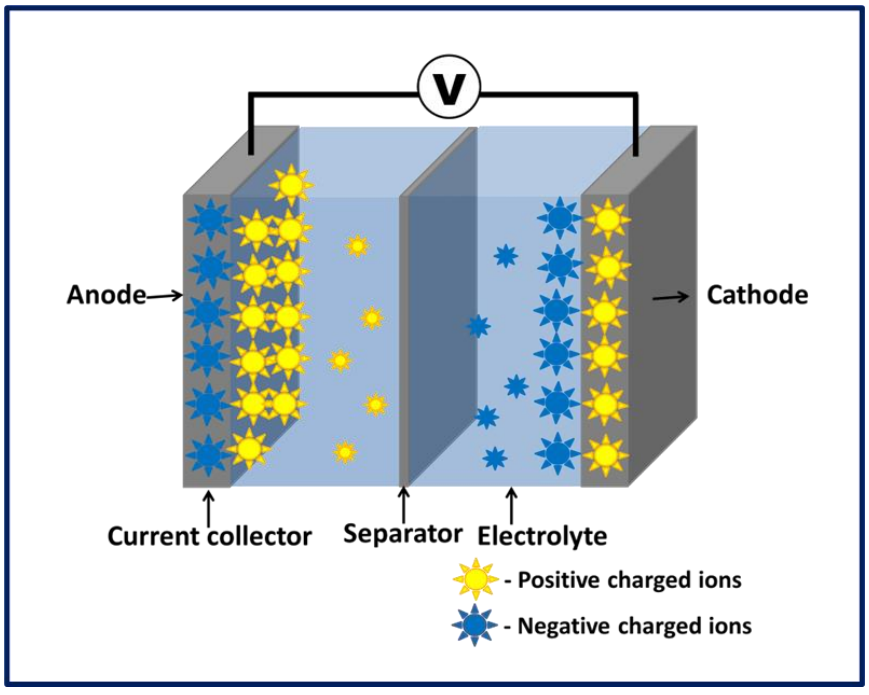

Figure 1.2: The schematic representation of conventional electrochemical capacitor.

The EC capacitance C is estimated by using the following equation,

$$C = \varepsilon_r \frac{A}{d} \quad \textbf{(1.1)}$$

The surface area of the active material is denoted by 'A', the double layer thickness by 'd', and the relative permittivity by 'ε_r'. This is the formula used to determine energy density (S_E),

$$S_E = \frac{CV^2}{2} \quad \textbf{(1.2)}$$

where, *C* is capacitance, and *V* is the voltage range of EC.

'S_E' specific energy density and '*V*' electrochemical capacitor voltage window, respectively. Specific power density is the energy released concerning time. Generally, the resistance across the supercapacitor components (e.g. substrate, electrode material, separator and electrolyte) is required for evaluating power density, known as the ESR. It is calculated from the voltage drop during the discharge, which gives the maximum voltage. The maximum power density is calculated by following relation;

$$S_P = V^2 \frac{1}{ESR} \quad \textbf{(1.3)}$$

here, S_P and '*V*' are the power density and cell voltage.

Eq. (1.1) can be used to compute capacitance, which quantifies a capacitor's ability to store energy. Another important factor is S_P, which is the amount of energy provided per unit of time. When assessing energy density in supercapacitors, physical resistance from the substrate, electrode material, and electrolyte must be taken into account. Supercapacitors (electrochemical capacitors) use electrodes with a thicker electric double layer (d) and larger surface area (A), which results in higher capacitance and S_E (Eq. (1.2)) as well as higher S_P (Eq. (1.3)), despite operating on similar principles to conventional capacitors. Eq. (1.4) can be used to further determine power density.

1.2 Taxonomy of supercapacitors:

EDLCs, pseudocapacitors (faradaic capacitors), and hybrid capacitors are the three primary categories of supercapacitors. The classification of supercapacitors mostly depends on the material and charge storage technique implemented. The ability of this kind of supercapacitor to store charge depends on its distinct charge storage mechanism. Redox, electrostatic, and the combination of the two processes

are all included in that sequence. In the redox process, oxidation and reduction between the electrode surface and the applied electrolyte cause energy transfer. Charges are physically stored across the electrode surface in the electrostatic process, which does not involve chemical processes. Using an electrostatic mechanism, EDLCs charge storage mechanism is a composite of carbon-based materials. The charge storage mechanism in a faradic capacitor via a redox process occurs in bulk material or near the surface **[30, 31]**. Faradic capacitors are often constructed from metal oxides, conducting polymers, and metal sulphides **[32-34]**. Hybrid capacitors are metal oxides, hydroxides, and sulphides combined with carbon-based materials **[35, 36]**. Each type of supercapacitor is detailed in **chart 1.1**.

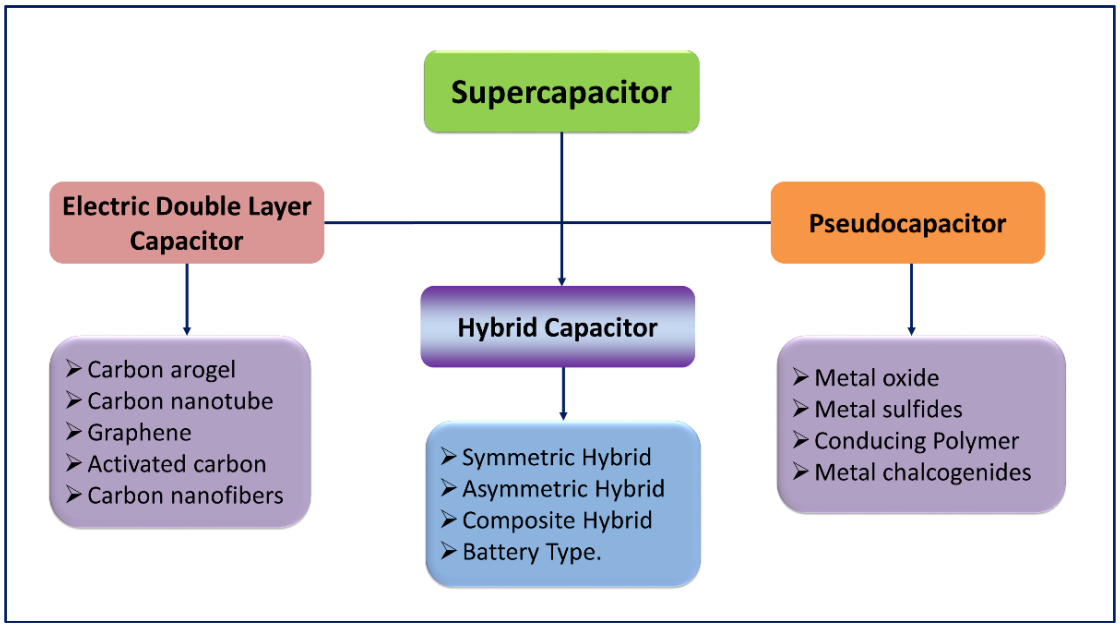

Chart 1.1: Classification of supercapacitors with different types and subtypes.

1.2.1 Electrochemical double-layer capacitor (EDLC):

EDLC typically consist of two carbon-based electrodes separated by a separator and immersed in an electrolyte solution. The carbon electrodes provide a high surface area for charge accumulation. Unlike traditional capacitors, which store charge by forming a dielectric layer between conductive plates (Faradic process), EDLC stores charge electrostatically. Charge storage occurs at the interface between the carbon electrodes and the electrolyte solution, forming what is known as the electric double layer. This double layer comprises a layer of ions from the electrolyte and a layer of opposite charges on the electrode surface. During the charging process,

electrons flow from the negative electrode (anode) through the external circuit to the positive electrode (cathode). Simultaneously, ions in the electrolyte migrate toward oppositely charged electrodes anions move toward the anode, while cations move toward the cathode **[37]**. **Figure 1.3 (A)** shows the charge storage mechanism of EDLC.

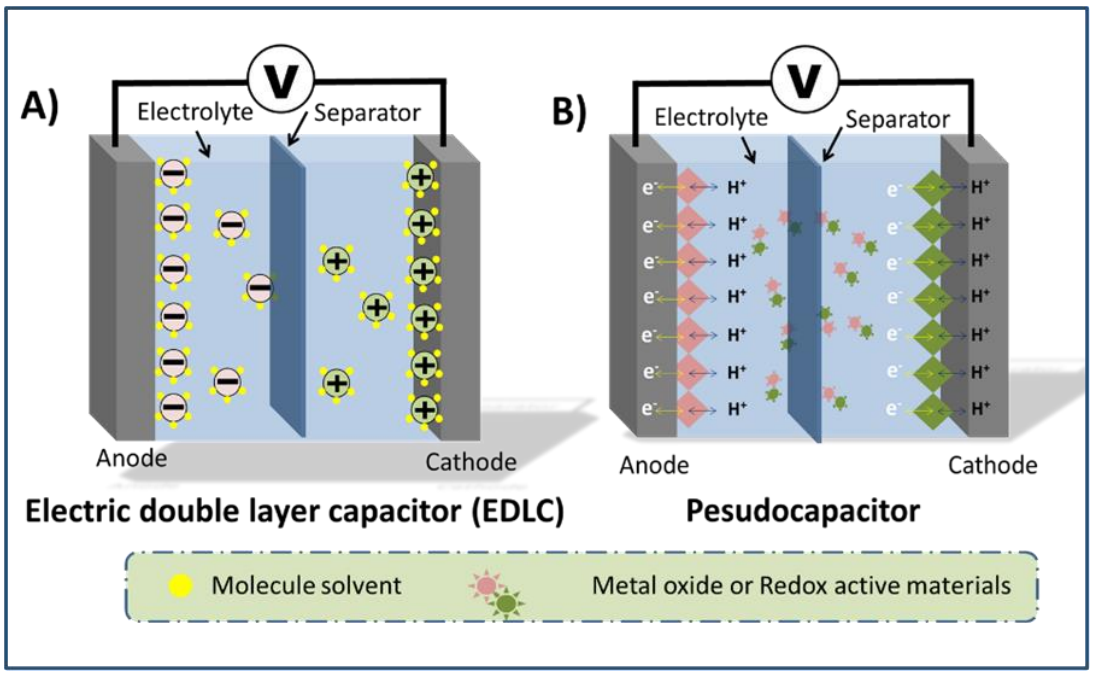

Figure 1.3: Energy storage mechanism schematics for the (A) EDLC and (B) pseudocapacitor.

EDLCs are capable of rapid charge and discharge cycles due to the electrostatic nature of their charge storage. They are often used in applications requiring high S_P and frequent cycling, such as hybrid vehicles, renewable energy systems, and portable electronics **[38]**. Compared to other energy storage technologies like batteries, EDLCs offer advantages such as high S_P, long cycle life, and fast charging/discharging rates. Their unique charge storage mechanism makes them suitable for various applications where rapid energy storage and release are essential. The absence of charge transfer processes allows the EDLCs to offer outstanding stability and high S_P. Carbon-based materials are included in EDLCs, such as graphene, carbon aerogels, carbon nanotubes, activated carbon, mesoporous carbon, etc **[27]**.

1.2.2 Pseudocapacitor:

A pseudocapacitor is an electrochemical capacitor that operates through faradaic and non-faradaic charge storage mechanisms. Unlike EDLC, which predominantly stores charges electrostatically at the interface between the electrode and electrolyte, pseudocapacitors involve reversible Faradaic redox reactions at the electrode surface. For the purpose of to accomplish a pseudocapacitor, the charge storage mechanism requires chemical reactions, insertion and de-insertion, and electrosorption processes **[39-42]**. Usually, metal oxide, conducting polymer, sulphides, metal-doped carbon and phosphates are utilised as pseudocapacitors. Due to their higher energy density and C_s, pseudocapacitive materials are attracting research. **Figure 1.3 B** is a schematic representation of the charge storage mechanism of a pseudocapacitor.

Three categories of pseudocapacitors are distinguished: Intrinsic, Intercalation, and Extrinsic.

1.2.2.1 Intrinsic pseudocapacitors:

Intrinsic pseudocapacitors store energy through reversible faradaic redox reactions at the electrode surface. During charging, ions from the electrolyte undergo oxidation or reduction reactions at the electrode, forming a double charge layer. This highly reversible process allows for efficient energy storage and release **[43, 44]**. Intrinsic pseudocapacitors typically exhibit higher specific capacitance values than EDLC due to the additional contribution from faradaic redox reactions. They offer intermediate S_E between traditional capacitors and batteries, making them suitable for applications requiring high S_P and long cycle lifetimes. Examples of materials commonly used in intrinsic pseudocapacitors include transition metal oxides/hydroxides (e.g. ruthenium oxide (RuO_2), manganese dioxide (MnO_2) etc.), conducting polymers (e.g. polyaniline, polypyrrole), and layered transition metal dichalcogenides (r.g. molybdenum disulfide, tungsten disulfide). Quasi-rectangular curves resembling those of EDLCs, indicating that the charge storage mechanism in MnO_2 initially appeared more capacitive **[45, 46]**.

1.2.2.2 Intercaltion pseudocapacitors:

Intercalation pseudocapacitors represent a class of pseudocapacitors where the charge storage mechanism involves reversible intercalation of ions or molecules into

the crystal lattice of the electrode material. Unlike traditional capacitors, where charge storage occurs through physical adsorption or electrostatic attraction of ions at the electrode-electrolyte interface, intercalation pseudocapacitors involve a more complex process of ion insertion and extraction within the bulk structure of the electrode material.

Augustyn et al. **[47]** define intercalation pseudocapacitors as those that maintain the structural integrity of the electrode material during the charge and discharge processes. Their ability to avoid structural phase transformations through electrochemical reactions is a significant advantage contributing to their superior cycling stability, high power performance, and safety compared to other energy storage technologies. This property underscores the potential of intercalation pseudocapacitors for various practical applications in energy storage and conversion systems.

In intercalation pseudocapacitors, ions are incorporated through a solid solution mechanism without undergoing a phase change, leading to heightened energy retention even during rapid charge-discharge cycles.

1.2.2.3 Extrinsic pseudocapacitors:

When the particle size is lowered to within the nanoscale range, materials that in their bulk form show battery-like charge-discharge curves with peaks and prominent redox peaks in cyclic voltammetry can instead exhibit pseudocapacitive properties. This occurrence, termed "extrinsic pseudocapacitors," was first described by Augustyn et al. **[47]**. Notably, the electrochemical properties undergo significant changes, enabling these materials to exhibit a pseudocapacitive response similar to certain battery-type materials. Transitioning to nanoscale dimensions (below 10 nm) allows battery-type materials to overcome their profile change limitations by reducing ion diffusion lengths. Such extrinsic pseudocapacitive materials include nanosized cobalt and nickel hydroxides **[48, 49]**.

1.2.2.4 Hybrid capacitors:

A hybrid supercapacitor, also known as a super battery, combines the features of both traditional supercapacitors and batteries. This hybrid device typically consists of two electrodes: one with a high specific surface area of EDLC and another with

pseudocapacitive or battery-like behaviour. Researchers are exploring developing novel electrode materials for supercapacitors, like composite electrodes. This material aims to achieve high specific capacitance (C_s), cyclic stability, S_E, S_P, and other desirable properties. Combining various materials and leveraging the advantages of forming composites is an effective approach **[50]**. It allows for optimizing each component and enhancing their performance in supercapacitors. Conducting polymers or metal oxides are combined with carbon-based materials to create the hybrid electrode, offering the advantage of a single electrode that integrates chemical and physical charge storage systems.

1.3 Electrode materials for supercapacitors:

1.3.1 Carbon materials:

Carbon materials are essential in supercapacitors (SCs) because of their unique blend of physical and chemical characteristics. These include excellent conductivity, a large active surface area (3,000 m^2/g), strong durability against corrosion, excellent heat and chemical resistance, a distinct pattern of pores, and connectivity with other materials **[51]**. Furthermore, carbon materials can be easily processed within composite materials, enhancing their application flexibility and overall performance in supercapacitors. The capacitance of supercapacitors primarily depends on the surface area that is accessible to electrolyte ions. Carbon-based materials, including graphene and reduced graphene oxide, are extensively researched as electrode materials because of their appealing physical and chemical properties. These properties make them highly effective for use in supercapacitor applications. Porous carbons with tailored hierarchical structures encompassing micro, meso, and macro pores show considerable potential as electrode materials for supercapacitors. Activated carbon (AC), carbon Black, graphite, carbon nanotubes (CNTs), graphene, diamond, fullerenes, carbon fiber, and carbon foam each of these carbon materials has unique properties that make them suitable for specific applications **[52, 53]**.

1.3.2 Metal oxides:

Metal oxides are emerging as a superior class of electrode materials for supercapacitors due to their robust cycling stability and higher S_E compared to other materials like conducting polymers and carbon-based options. The enhanced S_E is

primarily attributed to the rapid and reversible electrochemical reactions at the electrode/electrolyte interface. Transition metal oxides such as NiO **[54]**, Fe_2O_3 **[55]**, CO_3O_4 **[56]**, MnO_2 **[57]**, and RuO_2 **[58]** have been thoroughly explored for supercapcitor applications. RuO_2 has been extensively researched due to its exponential electrical conductivity and broader 1.2 V window. However, the use of RuO_2 is limited by its environmental toxicity and rarity **[59]**. In recent developments, transition metal oxide composition has garnered significant interest due to its superior supercapacitive properties compared to singular metal oxides **[60]**.

1.3.3 Conducting polymer:

Conducting polymers are increasingly popular as electrode materials in supercapacitors due to their ability to enhance performance. These materials are noted for their relatively higher C_s because the charge storage mechanism involves the surface and the bulk of the material through redox reactions. Additionally, conducting polymers offer higher porosity, superior electrical conductivity, and a wider potential window than carbon-based materials **[61]**. This combination of features makes them highly effective for use in advanced supercapacitor designs. Interestingly, during the charging process, polymers absorb electrolytic ions onto their surface and release them during discharging. However, a significant challenge arises from the reduction of the polymer during electrochemical reactions, which can lead to the breakdown of the nanostructure and a subsequent decrease in C_s **[62, 63]**. Doping is the process by which conducting polymers undergo oxidation as well as reduction processes which result in positive or negative charge. Studies involving conducting polymer electrodes with ionic liquid electrolytes have demonstrated improved electrochemical performance, highlighting their potential to enhance supercapacitor functionality **[64, 65]**. The benefits of polymer gel electrolytes include mechanical flexibility, interfacial stability, a suitable potential window (3.0 V), and higher ionic conductivity (on par with SSEs). Polymer gel electrolytes were previously prepared using polyacrylate (PAA), poly (ethylene oxide) (PEO), poly (vinyl alcohol) (PVA), polyacrylonitrile (PAN), poly (vinylidene fluoride) (PVdF), poly (vinylidene fluoride-hexafluoropropylene) (PVdF-HFP), and poly (methyl methacrylate) (PMMA) as host polymers. EC, PC, and ethyl methyl carbonate (EMC) are often used organic solvents; nonetheless, organic solvents are typically costly, poisonous, and combustible. Thus, it makes perfect sense to use aqueous solvents in place of organic ones.

1.4 Reason for choosing the topic.

1.4.1 Purpose of Ruthenium oxide:

RuO_2 is a metal oxide, used as a component of nanocomposite material in supercapacitor applications **[66, 67]**. Recently, transition metal RuO_2 is widely used in many fields such as solar cell **[68, 69]**, sensor **[70]**, energy storage devices **[71-73]** and bioelectronics **[74-76]** due to their unique physical and chemical properties. RuO_2 has excellent electrical characteristics, very low resistivity, electrocatalytic activity and thermal stability **[77]**. RuO_2 enables fast faradic redox reactions. Rutile form of RuO_2 includes oxygen in electron transport processes **[78]**. The high price of ruthenium is a major disadvantage that prevents it from being used widely in commercial activity, considering its benefits. To preserve high performance while reducing expenditures, current research focuses on how to use less RuO_2 or combine it with other materials.

1.4.2 Purpose of reduced graphene oxide:

The reduced graphene oxide (rGO) is characterized by layer structure with oxygen functional group. It is highly conductive, high theoretical specific surface area (>1,000 m^2 g^{-1}), and excellent mechanical strength (tensile strength 1 Gpa and Young's modulus 1 Tpa). The rGO offers a robust scaffold for the polymer matrix, favorable lightweight excellent conductivity and electrochemical stability **[79]**. In this topic composite material is chosen of RuO_2 and rGO. 2-D graphene based supercapacitor form mesopores that are accessible to and wettable by ionic electrolytes at voltage up to 4 V.

Use of rGO control pore structure in electrode, enhance effective surface area and lower equivalent series resistance (R_s). Thus, rGO offers high surface area and stability while RuO_2 offer distinct redox activity and higher reduction potential provide large potential window due to their multiple oxidations states and effectively improves specific capacitance (C_s), S_E and S_P of composite thin films. Hence, the problem of poor stability and specific power of RuO_2 materials can be solved employing rGO and it is backbone material of pseudocapacitive RuO_2.

1.4.3 Purpose of deposition method selection:

To be applicable for supercapacitors, thin films should have electrochemical active sites with required nanopores. Hence, our aim is to deposit thin films with large specific surface areas with porous morphology. Composite thin films of rGO/RuO_2 will be deposited on a stainless steel (SS) substrate using SILAR and CBD methods. Firstly, the SS substrate will coated with rGO using the dip-dry method, and this prepared substrate will used for SILAR method. The following procedure will be adopted to deposit thin films using SILAR method. The growth of thin film by SILAR method involves four main steps:

Step 1 Cleaned substrate will be immersed in reaction beaker containing a cationic ruthenium chloride ($RuCl_3$) precursor solution. This process will lead to positive ions being adsorbed on the surface of the SS substrate.

Step 2 In this step, the substrate will be rinsed with double-distilled water (DDW) to remove excess positive ions loosely bound to the SS substrate.

Step 3 The substrate will then be immersed in the sodium hydroxide (NaOH) anionic precursor solution. The negative ions will react with previously adsorbed positive ions on the active centre of the substrate to form a thin film.

Step 4 The substrate will be rinsed in DDW to remove loosely bounded and unreacted ions.

These four steps will complete one SILAR immersion cycle of thin film deposition. Hence, several repeated immersion cycles result in the required rGO/RuO_2 composite thin film of desired thickness. The uniqueness of this SILAR method lies in the easy control of the parameters. This allows one to properly control the thickness necessary for various device applications. Also, composite thin films of rGO/RuO_2 will be deposited on the SS substrate using CBD method. The appropriate amount of precursors will be weighted accurately and dissolved in DDW to get the desired solution concentration. The pH of the solution bath will be adjusted by using complexing agent. The well-cleaned SS substrates will be dipped in the solution bath. The reaction process occurred in the solution bath based on two reaction mechanisms; (i) ion-by-ion or heterogeneous reaction, and (ii) cluster-by-cluster also called homogeneous reaction, the precursor material deposits in thin film form. After optimization of preparative parameters of thin films. Above mentioned chemical synthesis method of thin films can offer required supercapacitive properties.

1.5 Literature survey on ruthenium oxide, reduced graphene oxide/ruthenium oxide for supercapacitor application.

1.5.1 Literature survey on ruthenium oxide (RuO_2):

RuO_2 has been extensively researched for its application in supercapacitors due to its high specific capacitance, excellent electrical conductivity, and stability. Here are some significant findings from recent research: **Table 1.1** shows the capacitance values with a potential window of pristine RuO_2 material and using different chemical preparation methods, with electrolytes used in supercapacitors. Deshmukh et al. **[80]** prepared RuO_2-nH_2O thin film by SILAR method and it exhibited electrochemical C_s of 162 F g^{-1} in 0.5 M H_2SO_4 electrolyte. Patake and Lokhande **[81]** reported C_s of 50 F g^{-1} for RuO_2 thin film using CBD method. Patil et al. **[82]** synthesized RuO_2 thin film via CBD method with exhibited electrochemical C_s of 73 F g^{-1} in 0.5 M H_2SO_4 electrolyte. Deshmukh et al. **[83]** reported maximum electrochemical C_s of 192 F g^{-1} in 0.5 M H_2SO_4 electrolyte for RuO_2-nH_2O electrode through CBD method. Dubal et al. **[84]** prepared RuO_2 thin film using CBD method and obtained C_s of 234 F g^{-1} in 1 M H_2SO_4 electrolyte. Patake et al. **[85]** reported maximum C_s of 1190 F g^{-1} in 1 M H_2SO_4 electrolyte for deposited RuO_2 thin film by electrodeposition method. Hong and Yim. **[86]** synthesized RuO_2 thin film via electrodeposition method and exhibited electrochemical C_s of 35 F g^{-1} in 1 M KCl electrolyte with capacity retention of 78% after 5,000 cycles. Yu et al. **[87]** prepared RuO_2 thin film via hydrothermal method and exhibited C_s of 400 F g^{-1} in 1 M H_2SO_4 electrolyte. Joshi and Sutrave. **[88]** Reported C_s of 489 F g^{-1} for RuO_2 thin film via spin coated method. Jeon et al. **[89]** synthesized RuO_2 thin film by CBD method and exhibited electrochemical C_s of 188 F g^{-1} in 6 M KOH electrolyte with capacitive retention of 83% after 3,000 cycles. Thakur et al. **[90]** prepared RuO_2 thin film using SILAR method with exhibited C_s of 1321.67 F g^{-1} in 0.2 M Na_2SO_4 electrolyte. Mevada et al. **[91]** synthesized RuO_2 thin film via spin coating method and exhibited electrochemical C_s of 676 F g^{-1} in 1 M Na_2SO_4 electrolyte with capacity retention of 91.6% after 5,000 cycles. Shankar et al. **[92]** prepared RuO_2 thin film by precipitation method and exhibited C_s of 476 F g^{-1} in 1 M Na_2SO_4 electrolyte. Asbani et al. **[93]** synthesized RuO_2 thin film using electrodeposition synthesis method and exhibited electrochemical arial C_s of 4.5 F cm^{-2} in 0.5 M H_2SO_4 electrolyte with capacity

retention of 90% after 10,000 cycles. Thangappan et al. **[94]** prepared RuO_2 thin film by hydrothermal method and exhibited C_s of 226 F g^{-1} in 1 M Na_2SO_4 electrolyte.

Conclusions:

The above literature survey presents a detailed overview of recent research on various ruthenium oxide materials. It outlines the synthesis methods employed and the electrolytes used across these studies. It shows that the highest recorded capacitance value is 1321.67 F g^{-1}. This impressive result was obtained by utilizing a RuO_2 electrode in a 0.2 M Na_2SO_4 electrolyte through the SILAR (Successive Ionic Layer Adsorption and Reaction) method **[90]**. These findings highlight the notable progress in the field and underscore the potential of ruthenium oxide for supercapacitor applications.

Table 1.1: Ruthenium oxide (RuO_2) thin films for supercapacitor application.

Sr. No.	Material	Deposition methods	Substrate	Electrolyte	Specific capacitance ($F\ g^{-1}$)	Retention stability(%) (cycles)	Potential window (V)	Ref.
1	RuO_2-nH_2O	SILAR	SS	0.5 M H_2SO_4	162	80 (2,000)	0 to 1.0 (V/SCE)	**[80]**
2	RuO_2	CBD	ITO Glass	0.5 M H_2SO_4	50	-	-0.1 to 0.7 (V/SCE)	**[81]**
3	RuO_2	CBD	SS	0.5 M H_2SO_4	73	-	0 to 1.0 (V/SCE)	**[82]**
4	RuO_2-nH_2O	CBD	SS	0.5 M H_2SO_4	192	-	0 to 1.0 (V/SCE)	**[83]**
5	RuO_2	CBD	SS	1 M H_2SO_4	234	-	-0.2 to 0.8 (V/SCE)	**[84]**
6	RuO_2	Electrodeposition	SS	0.5 M H_2SO_4	1190	-	-0.1 to 0.6 (V/SCE)	**[85]**
7	RuO_2	Electrodeposition	ITO Glass	1 M KCl	35 mF/cm^2	78 (5,000)	0.3 to 0.8 (V/Ag/AgCl)	**[86]**
8	RuO_2	Hydrothermal	SS	1 M H_2SO_4	400	85 (6,000)	0 to 1.0 (V/SCE)	**[87]**
9	RuO_2	Sol-gel	SS	1 M KOH	489	83 (1,000)	0.5 to 0.6 (V/SCE)	**[88]**
10	RuO_2	Precipitation	CF	6 M KOH	188	93 (3,000)	-0.2 to 0.8	**[89]**
11	RuO_2	SILAR	SS	0.2 M Na_2SO_4	1321.67	96 (5,000)	-1.75 to 1.25 (V/Ag/AgCl)	**[90]**
12	RuO_2	Spin coating	SS	1M Na_2SO_4	676	91.6 (5,000)	0 to 1.0	**[91]**
13	RuO_2	Precipitation	SS	1M Na_2SO_4	476	-	0 to 0.75 (V/Ag/AgCl)	**[92]**
14	RuO_2	Electrodeposition	-	0.5 M H_2SO_4	4.5 Fcm^{-2}	90 (10,000)	0 to 1.0 (V/Ag/AgCl)	**[93]**
15	RuO_2	Hydrothermal	-	1M Na_2SO_4	228	-	0 to 1.0 (V/Ag/AgCl)	**[94]**

1.5.2 Literature survey on reduced graphene oxide (rGO)/ruthenium oxide (RuO_2):

Table 1.2 illustrates the capacitance values within the specified potential window for pristine rGO composite RuO_2 materials, highlighting the differences observed using various chemical preparation methods. The table captures key parameters of optimising RuO_2-based supercapacitors for enhanced energy storage applications. Amir et al. **[95]** prepared HRGO-RuO_2 thin film by electrodeposition method and exhibited electrochemical C_s of 418.5 F g^{-1} in PVA-H_2SO_4 electrolyte. Amir et al. **[96]** prepared rGO-RuO_2 film using sol-gel method and revealed maximum electrochemical C_s of 500 F g^{-1} in 1 M H_2SO_4 electrolyte. Ates and Yildirim **[97]** synthesized rGO/RuO_2/PANI thin film via polymerization method and showed C_s of 723.09 F g^{-1} in 1 M H_2SO_4 electrolyte. Hsieh et al. **[98]** deposited hydrous RuO_2/MWCNTs/Ti electrode by electrodeposition method and reported C_s of 1652 F g^{-1} at scan rate of 5 mV s^{-1}. Karimi et al. **[99]** GO/MWCNT/RuO_2 prepared by aerogel method and exhibit C_s 518 F g^{-1} with 94.38% capacitive retention over 5,000 cycles. Wang et al. **[100]** prepared rGO/RuO_2 film by ultrasonication method and exhibited electrochemical C_s of 2.34 mF/cm^2 in PVA-H_2SO_4 electrolyte. Shankar et al. **[92]** prepared rGO/RuO_2 thin film using precipitation method and exhibited C_s of 679 F g^{-1} in 1 M Na_2SO_4 electrolyte with 96% capacitive retention over 5,000 cycles. Chang Hu et al. **[101]** synthesized rGO/RuO_2 film via dip coating method and showed C_s of 1200 F g^{-1} in 0.5 M H_2SO_4 electrolyte. Ates et al. **[102]** rGO/RuO_2/PVK prepared by aerogel method and exhibit C_s 518 F g-1 with 94.38% capacitive retention over 1,000 CV cycles. Korkmaz et al. **[103]** rGO/RuO_2 prepared by aerogel method and exhibit C_s 328 F g-1 with 82% capacitive retention over 5,000 cycles. Zhao et al. **[104]** prepared RuO_2 thin film by hydrothermal method and exhibited C_s of 1126 F g^{-1} in 1 M H_2SO_4 electrolyte with 89% capacitive retention over 10,000 GCD cycles. Upadhyay et al. **[105]** prepared rGO/RuO_2 thin film using polymerization technique and exhibited C_s of 1.5 F cm^{-2} in 1 M H_2SO_4 electrolyte 85% capacitive retention over 1,000 cycles. Wang et al. **[106]** the synthesis of Ru nanoclusters in aqueous phase under the control of pH value and subsequent loading on carbon-based substrates. Then the Ru nanoclusters are converted into ultrafine RuO_2 particles on the same supports by a thermal treatment in air with exhibited electrochemical C_s of 1099 F g^{-1} in 1 M H_2SO_4 electrolyte with capacity retention of 98% after 2,000 cycles.

Conlusions:

This literature review offers a comprehensive overview of recent studies on composites of rGOwith RuO_2 materials. It delves into various synthesis methods and investigates the diverse electrolytes used in these investigations. Notably, the most remarkable C_s value documented is 1625 F g^{-1}. This outstanding achievement was attained using a RuO_2/MWCNT (multi-walled carbon nanotube) composite electrode in a 1 M H_2SO_4 aqueous electrolyte **[98]**. These outcomes underscore the substantial potential of RuO_2/rGO composites in enhancing the performance of supercapacitors.

Table 1.2: Reduced graphene oxide/ruthenium oxide (rGO/RuO_2) thin films for supercapacitor applications.

Sr. No.	Material	Deposition Methods	Substrate	Electrolyte	Specific Capacitance ($F\ g^{-1}$)	Retention Stability(%) (Cycles)	Potential Window (V)	Ref.
1	HRGO-RuO_2	Electrodeposition	SS	PVA-H_2SO_4	418.5	85 (10,000)	0 to 1.0 (V/Ag/AgCl)	**[95]**
2	RGO-RuO_2	sol-gel	SS	1M H_2SO_4	500	86 (2,000)	0 to 1.0 (V/Ag/AgCl)	**[96]**
3	rGO/RuO_2/PANI	Polymerization	SS	1 M H_2SO_4	723	85 (5,000)	0 to 0.8 (V/Ag/AgCl)	**[97]**
4	RuO_2/MWCNT	Electrodeposition	SS	1 M H_2SO_4	1652	-	0 to 1.0 (V/SCE)	**[98]**
5	GO/ MWCNT /RuO_2	Arogel	-	3M H_2SO_4	518	94.38 (5,000)	-0.1 to 1.0	**[99]**
6	rGO/RuO_2	Ultrasonication	-	1 M H_2SO_4	2.34 mF cm^{-2}	90 (4,000)	0 to 1.0	**[100]**
7	rGO/RuO_2	Precipitation	SS	1 M Na_2SO_4	679	96 (5,000)	0 to 0.75	**[92]**
8	rGO/RuO_2	Dip coating	Ti	0.5M H_2SO_4	1200	65	0 to 1.0 (V/Ag/AgCl)	**[101]**
9	rGO/RuO_2/PVK	Microwave assisted	-	1 M H_2SO_4	1688	87 (1,000)	0 to 0.8	**[102]**
10	rGO/RuO_2	Aerogel	-	3 M H_2SO_4	328	82 (5,000)	0 to 1.0	**[103]**
11	RuO_2/rGO	Hydrothermal	SS	1 M H_2SO_4	1126	89 (10,000)	0 to 1.0(V/SCE)	**[104]**
12	rGO/RuO_2	Polymerization	-	1 M H_2SO_4	1.5 F cm^{-2}	80 (1,000)	0 to 0.8	**[105]**
13	RuO_2/rGO	Ultrafine	-	1 M H_2SO_4	1099	98 (2,000)	0 to 1.2	**[106]**

1.5.3 Literature survey on ruthenium oxide (RuO_2) composite-based symmetric and asymmetric supercapacitor devices.

Table 1.3 presents a detailed comparison of ruthenium oxide (RuO_2) composite-based symmetric and asymmetric supercapacitor devices. The table includes key performance metrics such as specific capacitance, energy density, power density, and cycling stability. By showcasing these devices side by side, the table is a valuable resource for understanding the practical applications and optimization strategies for RuO_2 composite-based supercapacitors in energy storage technologies. Chen et al. **[107]** reported C_s of 138 F g^{-1} in PVA-H_3PO_4 electrolyte for RuO_2/SWCNT through Ink jet printing method. Thakur et al. **[90]** prepared RuO_2/Ppy via SILAR method and exhibited C_s of 71 F g^{-1} in 1 M H_2SO_4 electrolyte with specific energy and power 286.18 Wh g^{-1} and 36.36 Wg^{-1} respectively. Shankar et al. **[92]** prepared rGO/RuO_2//RuO_2 device via precipitation method. They exhibited C_s of 155 F g^{-1} in Na_2SO_4 electrolyte and achieved power density of 5.026 kW kg^{-1} for a total energy density of 26.53 Wh kg^{-1}. Maveda and Mukhopadhyay **[108]** prepared a symmetric device via the chemical activation method and exhibited C_s of 796 F g^{-1} in PVA-Na_2SO_4 electrolyte achieved with power density of 3.5 kW/kg for a total energy density of 156 Wh/kg. Xia et al. **[109]** prepared RuO_2 electrode using CBD method and prepared aqueous symmetric device with C_s of 52.66 F g^{-1} in 1 M H_2SO_4 electrolyte. Muniraj et al. **[110]** synthesized PHQ/hRO/E-FGS thin film via electrodeposition method and exhibited C_s of 378 mF g^{-1} in PVA-H_2SO_4 electrolyte with capacitive retention of 91% after 10,000 cycles. Guduru et al. **[111]** prepared RuO_2//activated carbon thin film and prepared asymmetric aqueous supercapacitor device and showed C_s of 238 F g^{-1} in 1 M $Ni(NO)_3$ electrolyte with capacity retention of 94% after 1,000 cycles. Yu et al. **[87]** prepared RuO_2-TiO_2//activated carbon thin film via hydrothermal method and showed C_s of 70 F g^{-1} in 1 M H_2SO_4 electrolyte with capacity retention of 84 % after 6,000 cycles. Ahuja et al. **[112]** synthesized RuO_2//GNR electrode via micro-emulsion method and exhibited C_s of 156 F g^{-1} in 0.5 M Na_2SO_4 electrolyte with capacitive retention of 91% after 7,000 cycles.

Conclusions:

This survey provides an overview of recent research on symmetric and asymmetric devices incorporating various ruthenium oxide materials. It covers a

variety of fabrication and synthesis methods, along with the utilization of different aqueous and gel electrolytes. Remarkably, the symmetric device exhibited the highest specific capacitance value of 796 F g^{-1}. This result was accomplished using PVA-Na_2SO_4 aqueous electrolytes, resulting in an energy density of 150 Wh kg^{-1} and a power density of 3.5 kW kg^{-1} **[110]**. These findings highlight the progress made in developing high-performance supercapacitors utilizing ruthenium oxide materials.

Table 1.3: Ruthenium oxide (RuO_2) composite-based symmetric and asymmetric supercapacitor devices.

Sr. No.	Device configuration	Deposition Methods	Substrate	Electrolyte	Specific capa. ($F\ g^{-1}$)	Energy density ($Wh\ Kg^{-1}$)	Power density ($W\ Kg^{-1}$)	Retention stability (%) (cycles)	Potential window (V)	Ref.
Symmetric devices										
1	Ru:338	CBD	SS	PVA-H_2SO_4	234	-	-	-	-0.2 to 0.8	**[60]**
2	RuO_2/SWCNT	Inkjet printing	-	PVA-H_3PO_4	138	-	-	-	0 to 1.0	**[107]**
3	RuO_2/Ppy	SILAR	SS	1 M H_2SO_4	71	286	36.6	-	-2 to 1.0	**[90]**
4	RuO_2/rGO	Precipitation	SS	1 M Na_2SO_4	155	26.53	5.2 kW Kg^{-1}	88 (2,000)	0 to 1.2	**[92]**
5	RuO_2-NPs// CACC	-	SS	PVA-Na_2SO_4	796	156	3.5 kW Kg^{-1}	91 (5,000)	0 to 2.0	**[108]**
6	RuO_2/RuO_2	Hydrothermal	SS	1 M Na_2SO_4	52.66	18.77	500	92 (2,000)	0 to 1.5	**[109]**
Asymmetric devices										
7	PHQ/hRO/E-FGS	Electrodeposition	Graphite	PVA-H_2SO_4	378 mF cm^{-2}	8.4 Wh cm^{-2}	1.99 mW cm^{-2}	91 (10,000)	0 to 0.8	**[110]**
8	RuO_2//AC	-	SS	1 M $Ni(NO_3)_2$	248	-		93.3 (1,000)	-1.0 to 1.0	**[111]**
9	RuO_2//AC	Hydrothermal	-	1 M H_2SO_4	70	25	160	84.7 (6,000)	0 to 1.6	**[87]**
10	RuO_2//GNR	Micro emulsion	graphite plates	0.5 M Na_2SO_4	156	60	14	91 (7,000)	0 to 2.0	**[112]**

1.6 Objectives:

Title: Solid state supercapacitors based on reduced graphene oxide/ruthenium oxide composite thin films.

Objectives:

1. To prepare graphene oxide by modified Hummer's method and reduced graphene oxide (rGO)/ruthenium oxide composite thin films on solid substrate using SILAR and CBD methods.
2. To characterize reduced graphene oxide (rGO)/ruthenium oxide composite electrodes using different physico-chemical techniques.
3. To study supercapacitive properties of reduced graphene oxide (rGO)/ruthenium oxide composite electrodes using cyclic voltammetry study (CV), galvanostatic charge-discharge (GCD) electrochemical impedance spectroscopy (EIS) studies and to form asymmetric device with supercapacitive performance evaluation.

1.7 Orientation and work plan of thesis:

The ongoing energy crisis of the 21st century, fueled by the rapid expansion of the global economy, dwindling fossil fuel reserves, and escalating pollution, has underscored the need for clean, renewable, and efficient energy solutions. Supercapacitors are increasingly seen as a viable alternative to traditional batteries due to their potential to transform energy storage. These devices have numerous advantages, such as exceptional stability, high power density, and quick charge-discharge cycles. To maximize the practical applications of supercapacitors, it is critical to improve their energy and power density while maintaining their other qualities. The effectiveness of supercapacitors typically depends on their large surface area and the rapid, reversible redox reactions of the active materials used. Thus, innovating and refining electrode materials is crucial in advancing supercapacitor technology.

Research indicates that various materials, such as metal oxides/sulfides, carbon-based substances, conducting polymers, and their composites, have been explored as potential electrode materials in supercapacitor production. Recent studies have predominantly concentrated on applying mixtures of metal oxides or carbon composites to improve supercapacitive properties, focusing on both energy and power

density. rGO composites combined with metal oxides are relatively underexplored yet promising materials in supercapacitor development. To achieve supercapacitors with high performance, crafting advanced electrode materials that support high capacitance and improved energy density without sacrificing power density is crucial. The primary goal of developing rGO/RuO_2 composite thin films is to elevate supercapacitive performance. The comparative study of SILAR (Successive Ionic Layer Adsorption and Reaction) and CBD (Chemical Bath Deposition) methods for various reasons. The deposition of thin film quality, such as uniformity, and adhesion to the substrate, can vary significant impact between SILAR and CBD. Comparing the SILAR and CBD methods provides valuable insights due to their efficiency performance, adjustable parameters, cost-effectiveness, environmental impact, and potential for innovative advancements.

Research work will be divided into three phases and is expected to be carried out in three years.

PHASE (I)

In this phase,

1) Chemical synthesis of graphene oxide by using modified Hummer's method, and 2) Chemical synthesis of thin films will be carried out using SILAR and CBD deposition methods for comparative study. By these methods, rGO/RuO_2 composite thin films will be synthesized with different morphologies. The preparative parameters to monitor for deposition of thin films will be:

SILAR method	**CBD method**
1) Concentration of the reactants	1) Concentration of the reactants,
2) Adsorption and reaction time,	2) Time of deposition,
3) Rinsing time,	3) Temperature of chemical bath,
4) Temperature,	4) Complexing agent,
5) Complexing agent, and	5) Nature of the substrate, and
6) pH of the solution.	6) pH of the solution.

PHASE (II)

Different characterizations will be carried out in this phase for structural and morphological analysis of rGO/RuO_2 composite thin films. The structural phase of material will be determined using X-ray diffraction (XRD), while chemical bonds within the material will be analyzed through Fourier transform infrared spectroscopy (FT-IR). The surface morphology of the thin films will be assessed using Field emission scanning electron microscopy (FE-SEM), and their elemental composition will be identified by Energy dispersive x-ray spectroscopy (EDS). Further analysis of chemical composition of materials and oxidation states will be conducted using X-ray photoelectron spectroscopy (XPS). The contact angle (CA) will be also study for nature of material. The electrochemical characteristics of the films will evaluated through techniques such as cyclic voltammetry (CV), galvanostatic charge-discharge (GCD), and electrochemical impedance spectroscopy (EIS). A three-electrode cell configuration will be utilized in the electrochemical studies, employing the thin films as the working electrode, platinum or graphite plates as counter electrodes, and a saturated calomel electrode (SCE) as the reference electrode. Moreover, the performance of these films will be quantified in terms of their potential window, specific capacitance (C_s), specific energy, specific power, and cyclic lifespan.

PHASE (III)

The primary objective of this research will be to develop asymmetric solid-state supercapacitor devices (ASC), utilizing rGO/RuO_2 composite thin films as the active cathode material and WO_3 as the anode, packed and sealed with PVA-H_2SO_4 gel electrolyte. The effectiveness of the electrode materials and the functionality of the electrolytes will be assessed by constructing solid-state devices (SSD). The performance of these asymmetric devices (ASDs) will be analyzed in terms of capacitance, energy density (ED), power density (PD), and cyclic stability. The study concludes with an evaluation of the performance metrics specific to devices based on rGO/RuO_2 composites. Research work will be published in international journals based on (rGO/RuO_2) composites. Thesis writing will be covered in last six months of phase III.

References:

[1] B. Dunn, H. Kamath, J. Tarascon, Sci. 334, (2011), 928–935.

[2] H. Wang, and L. Pilon, J. Phys. Chem. C, 115, (2011), 16711-16719.

[3] G. Zhou, L. Xu, G. Hu, L. Mai, Y. Cui, Chem. Rev., 119, (2019), 11042-11109.

[4] J. Tarascon, and M. Armand, Nature, 414, (2001), 171-179

[5] M. Dupont, A. Hollenkamp, S. Donne, J. Electrochem. Soc., 161, (2014), 648-656.

[6] H. Omanda, T. Brousse, C. Marhi, D. Schleich, J. Electrochem. Soc., 151, (2004), 922-929.

[7] D. Dubal, N. Chodankar, D. Kim, P. Gomez-Romero, Chem. Soc. Rev., 47, (2018), 2065-2129.

[8] S. Maiti, A. Pramanik, S. Chattopadhyay, G. De, S. Mahanty, J. Colloid Interf. Sci., 464, (2016), 73-82.

[9] H. Jung, H. Wang, T. Hu, J. Power Sources, 267, (2014), 566-575.

[10] C. Zhou, Y. Zhang, Y. Li, J. Liu, Nano Lett., 13, (2013), 2078-2085.

[11] T. Pandolfo, V. Ruiz, S. Sivakkumar, J. Nerkar, J. Power Sources, (2013), 69-109.

[12] S. Zhang, N. Pan, Adv. Energy Mater., 5, (2015), 1401401-1401420.

[13] W. Raza, F. Ali, N. Raza, Y. Luo, K. Kim, J. Yang, S. Kumar, A. Mehmood, E. Kwon, Nano Energy, 52, (2018), 441-473.

[14] F. Beguin, V. Presser, A. Balducci, E. Frackowiak, Adv. Mater., (2014), 26, 2219-2251.

[15] A. Burke, J. Power Sources, 91, (2000), 37-50.

[16] B. E. Conway, "Electrochemical supercapacitors: scientific fundamentals and technological applications", Kluwer–Plenum, New York (1999), 1-697.

[17] P. Simon and Y. Gogotsi, Nat. Mater., 7, (2008), 845–854.

[18] J. Xu, D. Zhang, Electrochim. Acta, 224, (2017), 105-112.

[19] D. Xu, C. Mu, J. Xiang, F. Wen, C. Su, C. Hao, W. Hu, Y. Tang, Z. Liu, Electrochim. Acta, 220, (2016), 322-330.

[20] M. Kiamahalleh, S. Zein, G. Najafpour, S. Sata, S. Buniran, Nano, 7, (2012), 1-27.

[21] M. Hashemi, M. Rahmanifar, M. Kady, A. Noori, M. Mousavi, R. Kaner, Nano Energy, 44, (2018), 489-498.

[22] M. Ho, P. Khiew, D. Isa, T. Tan, W. Chiu, C. Chia, Nano, 9, (2014), 1430002-1430027.

[23] S. Kim, S. Kim, K. Jung, J. Kim, J. Jang, Nano Energy, 24, (2016), 17-24.

[24] A. Castaings, W. Lhomme, R. Trigui, A. Bouscayrol, Appl. Energy, 163, (2016), 190-200.

[25] L. Zhang, X. Zhao, Chem. Soc. Rev., 38, (2009), 2520-2531.

[26] C. Lokhande, D. Dubal, O. Joo, Curr. Appl. Phys., 11, (2011), 255-270.

[27] H. Pang, X. Li, Q. Zhao, H. Xue, W. Lai, Z. Hu, W. Huang, Nano Energy, 35, (2017), 138-145.

[28] L. Miao, H. Duan, M. Liu, W. Lu, D. Zhu, T. Chen, L. Li, L. Gan, Chem. Eng., 317, (2017), 651-659.

[29] G. Wang, H. Wang, X. Lu, Y. Ling, M. Yu, T. Zhai, Y. Tong, Y. Li, Adv. Mater., 26, (2014), 2676-2682.

[30] Y. Wang, Y. Song, Y. Xia, Chem. Soc. Rev., 45, (2016), 5925-5950.

[31] B. Zhang, W. Li, J. Sun, G. He, R. Zou, J. Hu, Z. Chen, Mater. Lett., 114, (2014), 40-48.

[32] W. Li, G. He, J. Shao, Q. Liu, K. Xu, J. Hu, I. Parkin, Electrochim. Acta., 186, (2015), 1-6.

[33] A. Xie, F. Tao, C. Jiang, W. Sun, Y. Li, L. Hu, X. Du, S. Luo, C. Yao, J. Electroanal. Chem., 789, (2017), 29-46.

[34] A. Patil, A. Lokhande, N. Chodankar, V. Kumbhar, C. Lokhande, Mater. Des., 97, (2016), 407- 416.

[35] Y. Li, X. Wang, Q. Yang, M. Javed, Q. Liu, W. Xu, C. Hu, D. Wei, Electrochim. Acta., 234, (2017), 63-70.

[36] M. Hosseini and E. Shahryari, J. Colloid Interface Sci., 496, (2017), 371-381.

[37] G. Ma, G. Srikesh, A. Mohan, V. Arivazhagan, Appl. Surf. Sci., 403, (2017), 578-583.

[38] K. Jost, G. Diona, Y. Gogotsi, J. Mater. Chem. A, 2, (2014), 10776-10786.

[39] F. Shi, L. Li, X. Wang, C. Gu, J. Tu, RSC Adv., 4, (2014), 41910-41921.

[40] R. Pujari, A. Lokhande, A. Yadav, J. Kim, C. Lokhande, Mater. Des, 108, (2016), 510-517.

[41] Z. Wen, W. She, Y. Li, R. Che, J. Mater. Chem. A, 2, (2014), 20729-20738.

[42] L. Xing, K. Huang, L. Fang, Dalton Trans., 45, (2016), 17439-17446.

[43] J. Xu, T. Xiao, X. Tang, P. Xiang, L. Jiang, D. Wu, J. Li, S. Wang, J. Alloys Compd., 706, (2017), 351-357.

[44] W. Chen, R. Rakhi, H. Alshareef, Nanoscale, 5, (2013), 4134-4138.

[45] N. Chodankar, H. Pham, A. Nanjundan, J. Fernando, K. Jayaramulu, D. Golberg, Y. Han, D. Dubal, Small, 16, (2020), 2002806-2002841.

[46] S. Devaraj, N. Munichandraiah, J. Phys. Chem. C, 112, (2008), 4406-4417.

[47] V. Augustyn, P. Simon, B. Dunn, Energy Environ. Sci., 7 (5), (2014), 1597-1614.

[48] S. Pawar, B. Pawar, J. Kim, O. Joo, C. Lokhande, Curr. Appl. Phys., 11, (2011), 117-161.

[49] J. Cook, T. Lin, H. Kim, A. Siordia, B. Dunn, S. Tolbert, ACS Nano, 13, (2019), 1223-1231.

[50] K. Kumar, S. Archana, R. Namitha, B. Prasanna, S. Sharma, M. Raghu Mater. Res. Bull., 107, (2018), 347–354.

[51] H. Li, M. Yu, F. Wang, P. Liu, Y. Liang, J. Xiao, C. Wang, Y. Tong, G. Yang, Nat. Commun., 4, (2013), 1-7.

[52] D. Cericol, R. Kotz, Electrochim. Acta, 72, (2012), 1-17.

[53] X. Lu, M. Yu, G. Wang, Y. Tong, Y. Li, Energy Environ. Sci., 7 (5), (2014), 2160-2181.

[54] L. Zhang, D. Shi, T. Liu, M. Jaroniec, J. Yu, Mater. Today, 25, (2019), 35-65.

[55] P. Kulal, D. Dubal, C. Lokhande, V. Fulari, J. Alloys Compd., 509, (2011), 2567-2571.

[56] Y. Jiang, L. Chen, H. Zhang, Q. Zhang, W. Chen, J. Zhu, D. Song, Chem. Eng. J., 292, (2016), 1-12.

[57] W. Wei, X. Cui, W. Chen, D. Ivey, Chem. Soc. Rev., 40, (2011), 1697-1721.

[58] S. Makino, T. Ban, W. Sugimoto, J. Electrochem. Soc., 162, (2015), A5001-A5006.

[59] D. Dubal, P. Romero, B. Sankapal, R. Holze, Nano Energy, 11, (2015), 377-399.

[60] Y. Zhang, L. Li, H. Su, W. Huang, X. Dong, J. Mater. Chem. A, 3, (2015), 43-59.

[61] C. Xu, Z. Li, C. Yang, P. Zou, B. Xie, Z. Lin, Z. Zhang, B. Li, F. Kang, C. Wong, Adv. Mater., 28, (2016), 4105-4110.

[62] M. Zhang, Q. Zhou, J. Chen, X. Yu, L. Huang, Y. Li, C. Li, G. Shi, Energy Environ. Sci., 9, (2016), 2005-2010.

[63] Z. Zhang, J. Deng, X. Li, Z. Yang, S. He, X. Chen, G. Guan, J. Ren, H. Peng, Adv. Mater., 27, (2015), 356-362.

[64] Y. Li, G. Ren, Z. Zhang, C. Teng, Y. Wu, X. Lu, Y. Zhu, L. Jiang, J. Mater. Chem. A, 4, (2016), 17324-17323.

[65] G. Cai, P. Darmawan, M. Cui, J. Wang, J. Chen, S. Magdassi, P. Lee, Adv. Energy Mater., 6, (2016), 1501882-1501894.

[66] T. Gujar, V. Shinde, C. Lokhande, W. Kim, K. Jung, O. Joo, Electrochem Commun., 9, (2007), 504–510.

[67] A. Ananth, S. Dharaneedharan, M. Gandhi, M. Heo, Y. Mok, Chem. Eng. J., 223, (2013), 729-736.

[68] K. Naoi, S. Ishimoto, N. Ogihara, Y. Nakagawa, S. Hatta, J. Electrochem Soc., 156, (2009), 52–59.

[69] C. Su, Y. Xu, W. Zhang, J. Zhao, X. Tang, C. Tsai, L. Li, Chem. Mater., 21, (2009), 5674-5680.

[70] K. Krishnamoorthy, P. Pazhamalai, S. Kim, Electrochim. Acta, 227, (2017), 85-94.

[71] H. Jung, Y. Jeong, J. Park, Y. Sun, B. Scrosati, Y. Lee, ACS Nano., 7, (2013), 3532-3539.

[72] H. Li, R. Wang, R. Cao, Microporous Mesoporous Mater., 111, (2008), 32-38.

[73] L. Li, Z. Wu, S .Yuan, X. Zhang, Energy Environ Sci., 7 (5), (2014), 2101–2122.

[74] S. Gunes, H. Neugebauer, N. Sariciftci, Chem Rev., 107, (2007), 1324–1338.

[75] G. Yang, K. Kampstra, M. Abidian, Adv Mater., 26, (2014), 495-4960.

[76] K. Huang, C. Lin, A. S, T. Huang, J. Lin, F. Tseng, C. Hsieh, J. Power Sources, 417, (2019), 108-116.

[77] G. Borah and P. Sharma, Indian J. Chem., 50, (2011), 41–45.

[78] Y. Chueh, Adv. Mater. 19, (2007), 143–149.

[79] S. Lee, B. Kim, S. Chen, Y. Shao-Horn, P. Hammond, J. Am. Chem. Soc., 131, (2009), 671–679.

[80] P. Deshmukh, S. Pusawale, A. Jagadale, C. Lokhande, J. Mater. Sci., 47, (2012), 1546–1553.

[81] V. Patake and C. Lokhande, Appl. Surf. Sci., 254, (2008), 2820–2824.

[82] U. Patil, S. Kulkarni, V. Jamadade, C. Lokhande, J. Alloys Compd., 509, (2011), 1677–1682.

[83] P. Deshmukh, S. Pusawale, R. Bulakhe, C. Lokhande, Bull. Mater. Sci., 36, (2013), 1171–1176.

[84] D. Dubal, G. Gund, R. Holze, H. Jadhav, C. Lokhande, C. Park, Electrochim. Acta, 103, (2013), 103–109.

[85] V. Patake, C. Lokhande, O. Joo, Appl. Surf. Sci., 255, (2009), 4192–4196.

[86] D. Hong and S. Yim, Langmuir, 14, (2018), 4249–4254.

[87] F. Yu, L. Pang, H. Wang, Rare Met., 40, (2021), 440–447.

[88] P. Joshi and D. Sutrave, Thin Film Tech., 97, (2016), 42049-42052.

[89] S. Jeon, J. Jeong, H. Yoo, H. Yu, B. Kim, M. Kim, ACS Appl. Nano Mater. 4, (2020), 3847–3858.

[90] A. Thakur, H. Pathan, B. Lokhande, ES energy environ., 18, (2022), 75-89.

[91] C. Mevada, M. Mukhopadhyay, J Energy Storage, 30, (2020), 101453-101466.

[92] V. Shankar, P. Kumar, D. Govindarajan, P. Nethaji, G. Balji, Sustain. Energy Technol. Assess., 53, (2022), 102444-102453.

[93] B. Asbani, G. Buvat, J. Freixas, M. Huve, D. Troadec, P. Roussel, T. Brousse, C. Lethien, Energy Storage Mater., 42, (2021), 259-267.

[94] R. Thangappan, M. Arivanandhan, R. Kumar, R. Jayavel, J. Phys. Chem. Solids, 121, (2018), 339-349.

[95] F. Amir, V. Pham, D. Mullinax, J. Dickerson, Carbon, 107, (2016), 338-343.

[96] F. Amir, V. Pham, J. Dickerson, RSC Adv., 5, (2015), 67638-67645.

[97] M. Ates and M. Yildirim, Polym. Bull., 77, (2020), 2285–2307.

[98] T. Hsieh, C. Chuang, W. Chen, J. Huang, W. Chen, C. Shu, Carbon, 50, (2012), 1740–1747.

[99] F. Karimi, S. Korkmaz, C. Karaman, O. Karaman, I. Kariper, Fuel, 328, (2022), 125398-125403.

[100] L.Wang, Y. Ding, J. Li, Y. Guan, L. Yang, H. Fang, X. Lv, J. Yuan, JEAC, 919, (2022), 116501-116509.

[101] C. Hu, C. Wang, K. Chang, M. Chen, Nanotechnology, 26, (2015), 274004-274015.

[102] M. Ates, Y. Yildirim, O. Kuzgun, H. Ozkan, J. Alloys Compd., 787, (2019), 851-864.

[103] S. Korkmaz, I. Kariper, O. Karaman, C. Karaman, Ceram. Int., 15, (2021), 34514-34520.

[104] J. Zhao, J. Zhang, H. Yin, Y. Zhao, G. Xu, J. Yuan, X. Mo, J. Tang, F. Wang, Nanomater., 12, (2022), 1210-1220.

[105] J. Upadhyay, T. Das, B. Borah, K. Paul, K. Acharya, Solid State Commun., 334, (2021), 114382-114386.

[106] P. Wang, H. Liu, Y. Xu, Y. Chen, J. Yang, Q. Tan, Electrochim. Acta, 194, (2016), 211-218.

[107] P. Chen, H. Chen, J. Qiu, C. Zhou, Nano Res., 3, (2010), 594–603.

[108] C. Mevada, M. Mukhopadhyay, Mater. Chem. Phys., 245, (2020), 122784-122798.

[109] H. Xia, Y. Meng, G. Yuan, C. Cui, L. Luc, ESL, 15 (4), (2012), A60-A63.

[110] V. Muniraj, P. Dwivedi, P. Tamhane, S. Szunerits, R. Boukherroub, M. Shelke, ACS Appl. Mater. Interfaces, 11, (2019), 18349−18360.

[111] R. Guduru, J. Icaza, S. Pudi, J. Energy Storage, 34, (2021), 102170-102183.

[112] P. Ahuja, S. Ujjain, R. Kanojia, Appl. Surf. Sci., 427, (2018), 102-111.

CHAPTER-II

THEORETICAL BACKGROUND OF DEPOSITION METHODS AND CHARACTERIZATIONS

CHAPTER-II

THEORETICAL BACKGROUND OF DEPOSITION METHODS AND CHARACTERIZATIONS

2.1 Overview:

This chapter provides an overview of thin films and covers the theoretical framework of chemical deposition methods. It investigates the specifics of the successive ionic layer adsorption and reaction (SILAR) and chemical bath deposition (CBD) methods. The chapter also covers surface morphology, wettability, and structural property analysis techniques using thin film characterization techniques. Furthermore, it describes the electrochemical performance and important supercapacitor parameters.

2.2 Overview of thin films:

The distinctive electrical purposes optics, and magnetized characteristics of thin film technology have attracted a lot of attention lately and have applications in a variety of sectors **[1,2]**. The specific characteristics of film materials, easily controlled by changing preparative parameters, form the basis for using this technology. When considering thin films, it's important to note that the bulk and thin film properties of the materials differ significantly. A thin film is defined as a material with a thickness in the fractional range (less than one micrometer to nanometer) or a surface that is infinitely long in two directions and has dimensions that are limited along a third direction. It is bounded by two parallel planes. A thin film is any liquid or solid system with at most two-dimensional structures or patterns. Typically, thin films consist of material layers with thicknesses ranging from a few micrometers. The process of depositing these thin films onto substrates is known as thin film deposition. As shown in **Chart 2.1**, there are several ways to categorize this process. The two main ways to create nanomaterial in thin-film form are chemical and physical processes. In the top-down approach, bulk materials are initially utilized after which they are broken up into smaller pieces by mechanical or other energy sources. Conversely, the bottom-up strategy creates materials by producing precursor particles through chemical processes from molecular or atomic species. In contemporary technologies, diverse types of thin films are indispensable for numerous applications, driven by both scientific curiosity and technical potential. The performance of these thin films in specific applications is influenced by properties such as shape, agglomeration, size, and particle composition, as well as factors like crystallinity, surface morphology, porosity, and thickness, which play a critical role.

A variety of traditional chemical and innovative preparation routes, both in bulk and thin film forms, enable materials to attain nanocrystalline structures. When materials are in thin film form as opposed to their bulk counterparts, their physio-chemical characteristics can change significantly. A greater surface area, improved diffusivity, increased electrical conductivity, and decreased thermal conductivity are just a few benefits of nanocrystalline thin film materials **[3, 4]**.

Thin film characteristics are usually closely connected to the deposition approach used. Sputtering and vacuum techniques are the two main categories of physical procedures. These methods include depositing materials after they have been transformed into a gaseous state by impact or evaporation processes. Chemical techniques can be divided into two major branches. A variety of techniques are included in the gas-phase branch, including metal organo-chemical vapor deposition (MOCVD), photo CVD, plasma-enhanced CVD, laser CVD, and conventional CVD. The liquid-phase segment includes techniques like spray pyrolysis, sol-gel process, liquid phase epitaxy, electrodeposition, hydrothermal, reflux, CBD, and SILAR. However, there are disadvantages to physical and gas-phase chemical deposition techniques, including the need for costly equipment and maintenance, high operating temperatures as pressures, waste products, and high expenditures. Conversely, solution-phase chemical methods are simpler, more economical, and suitable for a wide range of material deposition **[5, 6]**. As a result, chemical methods are widely employed for the preparation of nanostructured materials in thin film form for diverse applications **[7]**.

The structural and elemental properties are studied using different characterization techniques like X-ray diffraction (XRD), energy dispersive X-ray analysis (EDAX), Fourier transform infrared (FT-IR) spectroscopy, scanning electron microscopy (SEM), and contact angle measurement. The electrochemical properties of RuO_2, rGO/RuO_2, and WO_3 are investigated in terms of varying mass loadings (film thickness). Changes in mass loading can significantly influence parameters such as specific capacitance, charge transfer resistance, and cycling stability. For instance, increasing the film thickness may enhance the active material content but could also hinder ion diffusion or increase internal resistance. By optimizing the mass loading, an optimal balance between high electrochemical performance and structural stability can be achieved, ultimately improving the efficiency and effectiveness of these materials in supercapacitor applications.

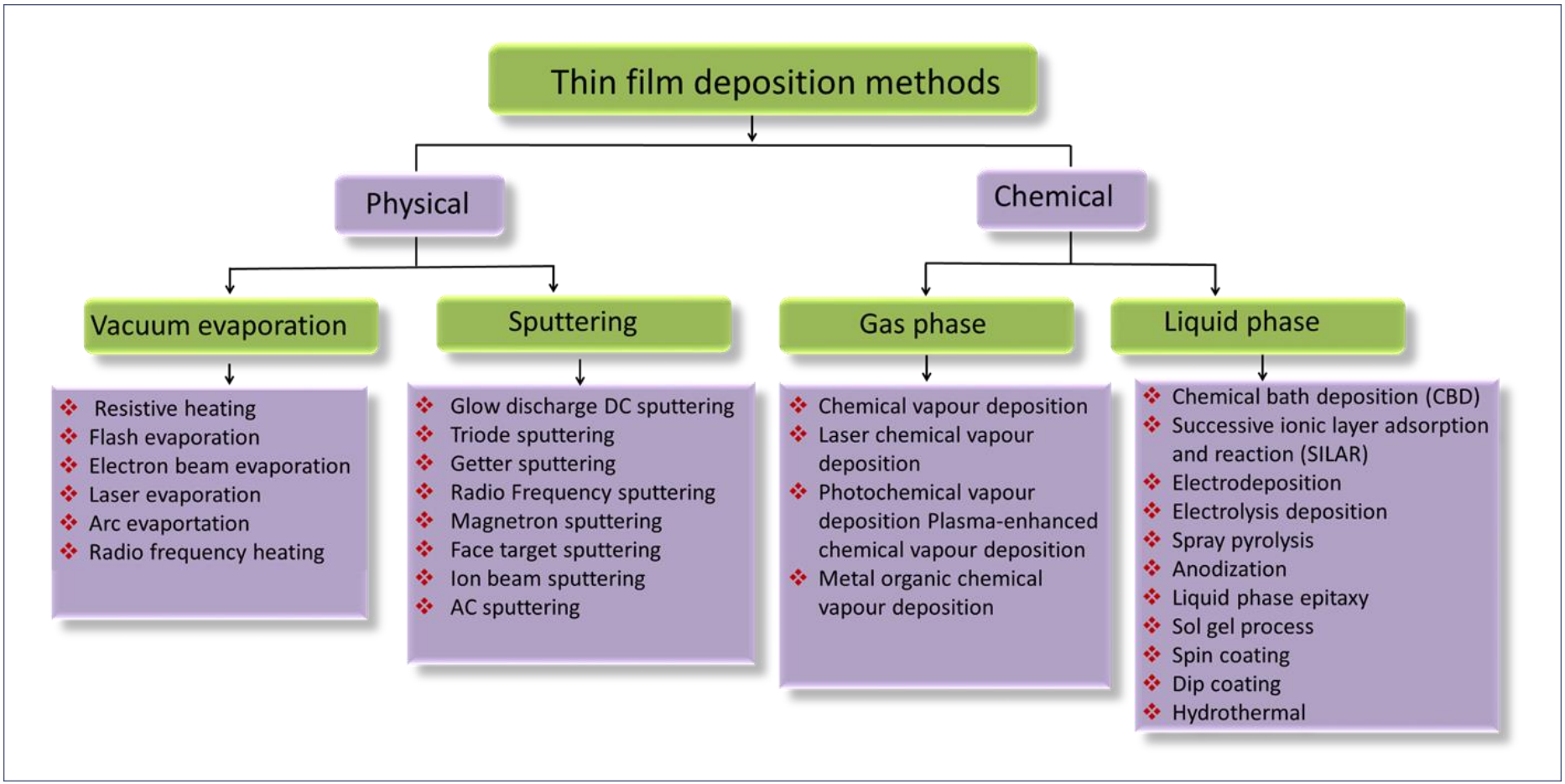

C**hart 2.1** General classification of thin film deposition methods.

2.3 Basics of Successive Ionic Layer Adsorption and Reaction (SILAR) method:

Deposition thin films of numerous materials are simple as well as affordable with the SILAR method. It offers excellent control over deposition parameters, making it advantageous. Mechanism of SILAR method was first reported by Ristov et al. **[8]** and Nicolau et al. **[9]** referred name as SILAR for the method. This technique, a modified version of the CBD method, is effective for depositing different chemical compounds and composite films. In order to assure uniform solid-phase development, the SILAR technique depends on successive reactions taking place at the substrate surface, followed by washing. With this method, adsorbed cations (pK_a^+) and anions (aA_p^-) react heterogeneously at the interface between solid and solution via thin films of covalent compounds that are insoluble in water, specifically KpAa. The following relation can be used to characterize the responsewith $ap = bq = b'q'$

$$(pK_{aq}^{a+} + qX_{aq}^{b-}) + (b'Y_{aq}\, q'^{+} + aA^{p-}) \rightarrow KpAa_s \downarrow + qX_{aq}^{b-} + b'Y_{aq}^{\,q'+} \qquad (2.1)$$

where, X is an ion in cationic precursors with a negative charge ($X = SO_4^{2-}$, Cl^-, NO_3^-, etc), q is the number of X in cationic precursors, b is the numerical value of charges on X, K is the number of cations(Zn^{2+}, Fe^{2+}, Co^{2+}, Fe^{3+}, Cu^{2+}, Ni^{2+}, etc), and p is the number of cations. In an anionic solution, b' is the number of Y ions, q' is the numerical value of the charge on Y, and Y is linked to a chalcogen ion. A is the number of anions, while A is the chalcogen ion. The above response can be expressed as follows when a complexing agent is present:

$$p[(KC)^{a+}]_{aq} + qX_{aq}^{b-} + b'Y^{q'+}{}_{aq} + aA^{p-} \rightarrow Kp'Aa'_s \downarrow + C + qX^{b-}{}_{aq} + b'Y^{q'+}{}_{aq} \qquad (2.2)$$

where, complexing agent is C. The SILAR process typically involves adsorption, reaction, and rinsing steps in a specific order.

a) Adsorption:

During the initial stage of SILAR reaction, the process begins with the placement of cations in a beaker. When immersed in the beaker, a substrate attracts and retains the cations on its surface. A Helmholtz double layer forms as a result of this interaction, with negatively charged ions accumulating on the outer side and positively charged ions on the inner side. A weak van der waals force holds each of these layers together **[10]**.

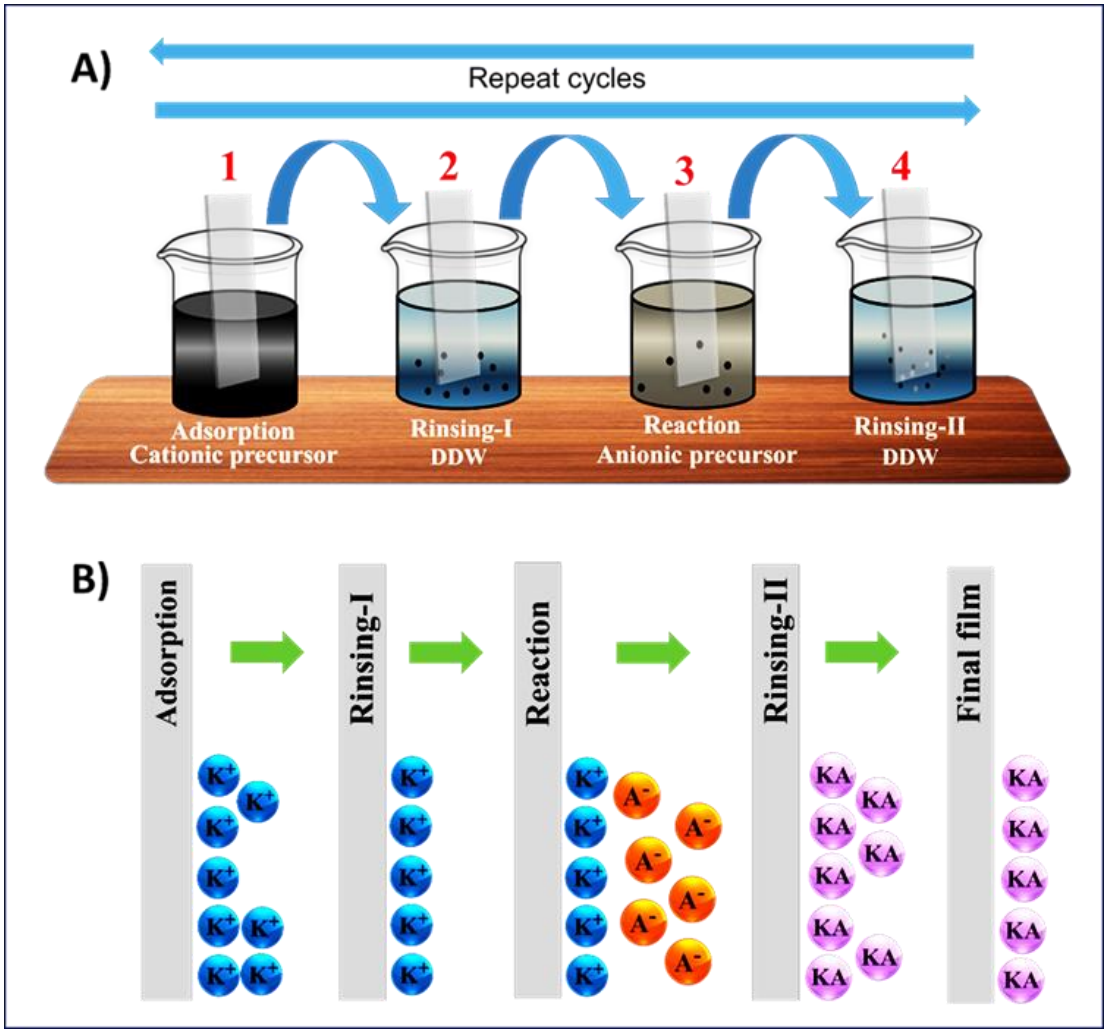

Figure 2.1: A) Schematic representation of SILAR method, and B) detailed ionic adsorption on film by SILAR method.

b) Rinsing-I:

The rinsing step is the second phase in the deposition process. It involves removing loosely bound ions from the substrate by immersing it in a rinsing solution. This step is crucial because it significantly affects the morphology, particle size, and degree of agglomeration of the deposited film. Double-distilled water is used for rinsing to ensure the highest purity and avoid introducing additional contaminants. The rinsing process ensures that only the desired ions remain on the substrate, which helps achieve a more uniform and well-ordered thin film. While it is possible to skip this step for convenience, doing so may lead to suboptimal results, including irregular film morphology and increased particle agglomeration. Therefore, careful rinsing is recommended to enhance the overall quality and consistency of the thin film **[11]**.

c) Reaction:

Anions from the anionic precursor solution take part in the reaction in this third stage. At the contact, a solid material with the chemical composition K^+A^- forms as a result of the high reactivity between cations and anions. In this step, adsorbed cations (K^+) and anions (A^-) from the solution undergo an irreversible chemical reaction.

d) Rinsing-II:

In the final stage of the deposition process, any unreacted substances on the substrate surface are eliminated by dipping the substrate into a rinsing solution. This step also helps to get rid of any excess substances on the substrate's surface. Rinsing is usually done with double distilled water (DDW). The substrate in the solution can be rotated using specific mechanically operated SILAR systems.

Figure 2.2: Photograph of SILAR used to deposit thin film electrodes **[12]**.

Additionally, there are three distinct ways to apply SILAR deposition method:

1) Operate by hand: In this method, the substrate is immersed in each beaker by hand, making it a labour-intensive and time-consuming process.

2) Operate by computer function programme: Here, a computer program controls the vertical and translational movements of the arm to which the substrates are attached.

3) Microprocessor-oriented function: In this approach, substrates are fixed to a horizontal robotic arm that moves vertically and transnationally. This method has gained popularity among researchers for its ease of operation and suitability for synthesizing binary, ternary chalcogenides, and composite materials.

Figure 2.2 depicts a microprocessor-based SILAR machine from Holmarc Opto-Mechatronics PVT. LTD., which is commonly used for depositing thin-film electrodes due to its efficient operation and user-friendly settings.

2.3.1 Benefits of the SILAR method:

a) The SILAR method is binder-free, environmentally friendly, straightforward, and convenient for depositing large-area thin films.
b) This method can be performed at low or room temperatures.
c) The deposition rate is easily adjustable.
d) It is compatible with any substrate.
e) There is no need for vacuum conditions or high-quality targets at any stage, and
f) Modifying the deposition parameters can easily control the film thickness.

2.3.2 Effect of Preparative Parameters:

Ion concentration, reaction and adsorption timings, rinse period, temperature, and the presence of complexing agents are some of the factors that influence the growth kinetics in the SILAR method:

a) Concentration:

In practically all chemical deposition approaches, the rate at which films develop is significantly influenced by the concentration of precursor solutions. The concentration of these solutions affects both adsorption and reaction rates. A thicker film results from an increase in the efficiency of adsorption when the concentration of cations beyond a particular threshold. Conversely, increasing the concentration of the anionic precursor speeds up the reaction rate, resulting in larger particle growth.

However, a higher reaction rate can cause the film to become nonadherent and exhibit non-uniform thickness. Furthermore, optimum film thickness and the formation of undissolved contaminants can result from high precursor concentrations **[13]**. Therefore, it's crucial to experimentally determine the optimal concentration of both precursors to achieve the desired film quality.

b) pH:

The pH of solutions is crucial in chemical deposition processes. Extreme pH values can impact the substrate surface condition, the solubility of the desired compounds, impurities, and even the substrate itself. At specific pH levels, the reaction rate can increase, while at other pH levels, a metal-chalcogenide ionic product might be less soluble than the metal-chalcogenide solubility product, preventing film formation. The pH of the cationic solution can be adjusted using a complexing agent.

c) Temperature:

The temperature of the bath influences film thickness. Higher temperatures enhance the dissociation of compounds, resulting in increased deposition rates and thicker films. Conversely, lower temperatures slow down film formation.

d) Complexing agent:

A complexing agent is a substance that can form a complex compound with another material in solution. Common complexing agents used in chemical deposition methods include ammonia (NH_3), ethylenediamine tetra acetic acid (EDTA), triethylammonium (TEA), polyvinyl alcohol (PVA), and polyvinyl pyrrolidone (PVP). These agents bind to simple metal ions, creating complex ions. As the reaction progresses, metal ions are gradually released to react with other ions. This process helps maintain a consistent concentration of metal ions during the chemical reaction. In the SILAR method, the slow release of metal ions results in a slower film growth rate, allowing the use of complexing agents to control the growth kinetics of the film.

e) Adsorption, reaction and rinsing time:

The balance between adsorption and reaction times is crucial. Longer adsorption times relative to reaction times lead to thicker films, while equal times result in uniform, well-adhered films **[14]**.

f) Deposition cycles:

Each cycle of deposition in the SILAR method adds a few layers of material to the substrate, leading to an increase in film thickness with a higher number of cycles. However, an excessive number of cycles can result in the formation of particle clusters. Once a critical number of cycles is reached, the accumulated stress and thickness can cause the thin film to lose its adhesion to the substrate and begin peeling off. This phenomenon occurs because the mechanical stability of the film diminishes as the thickness increases and the clusters grow, leading to detachment from the substrate. To achieve optimal film quality and adhesion, it is important to determine the appropriate number of deposition cycles.

2.4 Chemical bath deposition (CBD):

The simple and affordable method for synthesizing large-area thin films is CBD. For thin film deposition from the liquid phase, techniques such spray pyrolysis, electrophoresis, electrodeposition, dip coating, anodization, and CBD are used. This procedure is accessible and inexpensive because it does not require complex equipment like vacuum systems. It needs a glass beaker, a heated plate, and a stirrer to start the deposition. The main ingredients are affordable and easily accessible **[15]**. This process does not require the substrates to be electrically conductive in order to cover several substrates in a single run. **Figure 2.3** provides a schematic illustration of CBD method.

Any insoluble surface can be successfully coated with free access to a solution using CBD method. This method of low-temperature thin-film deposition avoids metallic substrates from corrosion. Whenever the solution develops the coating on the substrate, it produces material deposits which are consistent and free of holes. As opposed to using atoms as the basic building blocks, the use of ions enables accurate stoichiometric production. Grain structure and orientation are improved by the easy controllability of preparation conditions. Particle growth and nucleation are the two essential phases in thin film deposition. The precipitate affects particle size, and when

the required molecules and ions combine with the solution, the stable solid phase, or nucleus, forms. Precipitate development involves nucleation **[5]**. Clusters of particles and molecules rapidly develop and increase in solution through nucleation, developing a uniform film thickness. A number of factors, such as bath temperature, stirring rate, pH, and solution concentration, affect the thin film deposition conditions. Ion-by-ion deposition or the adsorption of colloidal particles on the substrate are the two methods through which films grow. The CBD method is employed to deposit various binary compounds like MnO_2, PbO, CuO, Bi_2S_3, CdSe, PbSe, CdS, MoS_2, Ag_2S_3, ZnS, PbS, RuO_2, and CuS, as well as ternary compounds such as CdPbSe, CdSSe, $CuInSe_2$, $ZnCo_2O_4$, and Cu_2SnS_3.

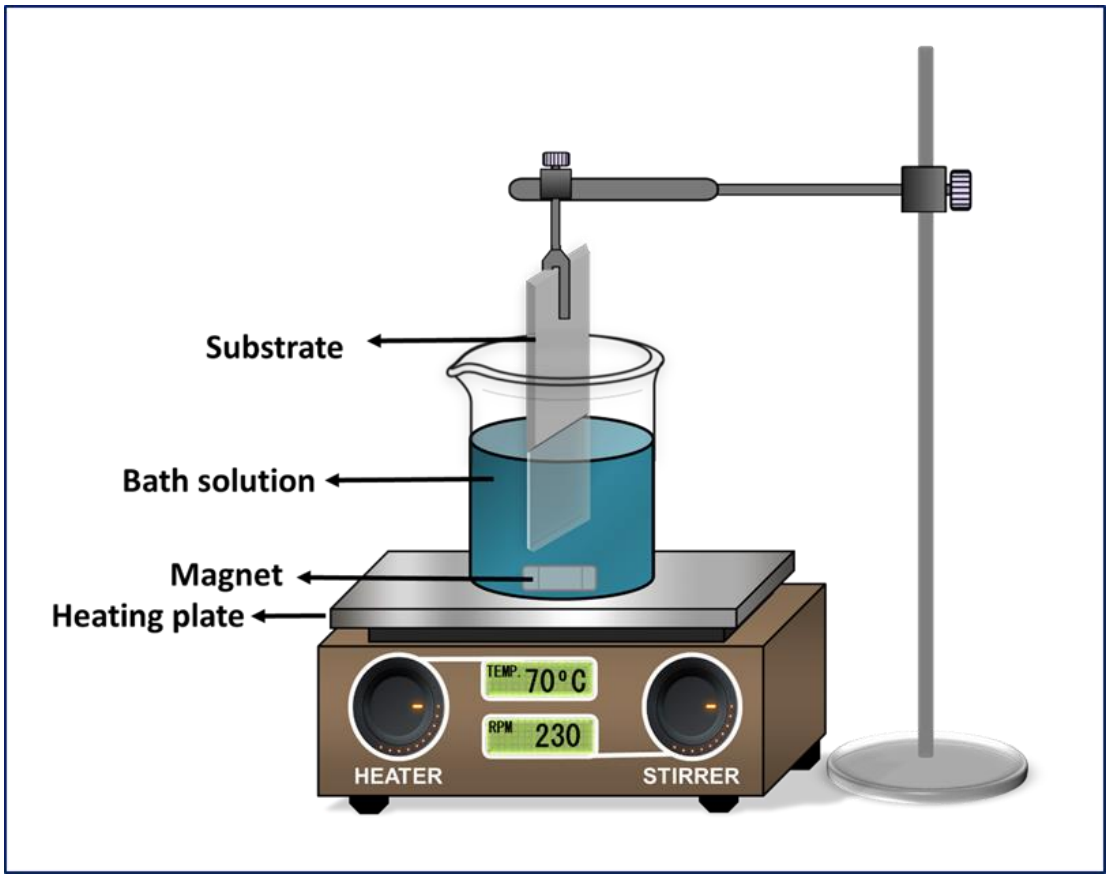

Figure 2.3: Schematic diagram of chemical bath deposition (CBD) method.

2.4.1 Deposition mechanisms of CBD method:

There are four distinct thin film deposition mechanisms for the CBD method, and these mechanisms vary depending on the particular approach and reaction parameters **[16]**.

a) Formation of ion-by-ion:

The ion-by-ion method, which entails successive ionic reactions, is thought to be very effective. The following is an explanation of the general response mechanism:

$$M^{n+} + X^{m-} \rightarrow M_m X_n \quad (2.3)$$

When the ionic product $[M^{n-}]$ $[X^{m+}]$ exceeds the solubility product Ksp of M_mX_n, a thin film of the compound MmXn forms. As a result, a solid phase of the chemical forms. It might take a greater ionic product for supersaturating to happen. Except in situations where there are minor variations in the solution, no solid phase is generated if the ionic product does not surpass the Ksp. In these conditions, small solid nuclei separate before developing into stable

b) Cluster (hydroxide) mechanism:

In order to stop metal hydroxide from forming, CBD methods preceding conditions are essential. Even so, metal hydroxide and hydrated oxide will inevitably develop under conventional CBD conditions. The CBD process seems to start with the formation of a metal hydroxide $[M(OH)_n]$ precipitate. Instead of remaining in most of the solution, this metal hydroxide is absorbed onto the substrate and forms as a colloid rather as a precipitate. In this process, the X^{m+} ion reacts with the $M(OH)_n$ to form the metal chalcogenides (M_mX_n).

$$M^{n+} + n(OH)^- \rightarrow M(OH)_n \quad (2.4)$$

Which follows,

$$X^{n+} + M(OH)_n \rightarrow M_m N_x \quad (2.5)$$

c) Ion-by-ion complex dissociation development:

Mn^+ thiourea compound ions are created in this method when thiourea complexes free metal cations (Mn^+). This process works especially well in acidic solutions because the breakdown of thioacetamide usually happens at intermediate pH values, usually in mildly acidic environments (pH > 2). Compared to transitional sulfide production, it is proposed that this process proceeds through the creation of a thioacetamide molecule.

d) Complex-decomposition cluster mechanism:

In the complex-decomposition cluster mechanism, solid-phase particles are formed as an alternative to direct reaction with free anions. This involves the formation of an intermediate compound with the anion from the reagent. The decomposition of thiourea to sulfide species may be catalyzed by the solid surface, however the complex itself may not always be catalyzed.

2.4.2 Preparative Parameters of the CBD Method:

The CBD method involves several preparative parameters that influence the formation of thin films. These parameters are detailed below:

a) Substrate:

The substrate on which the thin film is deposited plays a crucial role. There are two primary states for this deposition: the first involves substrates optimized for the deposition of metal ion (M^+) and anion (X^-) compounds, ensuring proper bonding and stability. The second state involves using a single crystalline substrate, which provides the ideal conditions for the material deposition. This allows the thin film of the MX complex to form, with its lattice structure aligning with that of the substrate material, ensuring better structural integrity and coherence.

b) Effect of Anion Concentration:

The concentration of anions in the solution significantly affects the thickness of the MX compound film. As the anion concentration increases, the deposition rate of the MX compound also increases, leading to a thicker film. However, if the anion concentration is too high, it can result in rapid and homogeneous precipitation in the solution, which can reduce the overall film thickness due to excessive particle formation in the bulk solution rather than on the substrate surface.

c) pH of the Solution:

The pH level of the solution is another critical factor. At lower pH values, the supersaturation of M and X ions is increased, which promotes a higher reaction rate and results in thicker film formation at lower temperatures. Conversely, as the pH increases, the supersaturation decreases, leading to fewer free M and X ions available to form the MX compound, and thus, thin film formation is hindered. At higher

temperatures, increasing the pH enhances the supersaturation rate, which subsequently increases the reaction rate and promotes film growth.

d) Concentration of Complexing Agent:

The role of a complexing agent in this process is to supply ligands to the metal ion (M), thereby keeping the solution unsaturated. Increasing the concentration of the complexing agent reduces the absorption of free metal ions. As a result, the growth rate of the film thickness decreases, although the final thickness of the film ultimately increases.

e) Temperature:

The dissociation rates of the metal ion (M^{+}) and the anion ($X^{-)}$ increase with rising temperature in the solution bath. Therefore, at higher temperatures, the dissociation rate of M and X ions is higher, leading to greater film thickness. This effect is dependent on the supersaturation of the solution.

2.4.3 Benefits of CBD method:

a) The method offers significant flexibility in substrate selection and substantially reduces manufacturing costs. It allows for low-temperature processing and capable large area deposition.
b) Safety and environmental impact.
c) The method ensures a high rate of reproducibility, which is crucial for consistent quality, and
d) It generates minimal wastage, making it efficient and environmentally friendly.

2.5 Physicochemical characterization techniques:

The physicochemical properties of a material are closely related to its performance. Thus, describing materials with a variety of methods and closely reviewing the outcomes are crucial research processes. This procedure supports discovering and improving the materials desirable properties as well as choosing the best material for a particular use. In this work, a number of material characterization methods were used to analyze the thin film electrodes as deposited.

2.5.1 X-ray diffraction (XRD):

X-ray diffraction (XRD) is a fundamental quick method in materials science that verifies the identity of a material by comparing its diffraction patterns to databases which have been built. The XRD offers useful information on the unit cells dimensions in along with material confirmation. It is also used to investigate chemical composition, measure crystallite size, and evaluate lattice strain. In addition, phase diagram construction and the assessment of crystallographic ordering degree depend on XRD. This technique is highly versatile and fast, making it an essential tool for thorough material characterization. It provides valuable information about structural properties and helps create and improve new materials **[17]**.

Basic Principle:

Monochromatic X-rays are diffracted by parallel lattice planes separated by an interplanar distance *d*, when they impact a crystalline sample at an incidence angle θ. By measuring the intensity of these diffracted X-rays as a function of the scattering angle, a diffraction pattern is produced. According to Bragg's law, constructive interference of the diffracted X-rays occurs when the path difference is an integer multiple of the X-ray wavelength. At such conditions, peaks obtained in diffraction patterns are known as Bragg peaks. A monochromatic X-ray source, a specimen holder, and an X-ray detector are the three main parts of an X-ray diffractometer. The cathode, monochromator, and target material are all located inside a vacuum-sealed glass or ceramic container, which is the X-ray generator, also referred to as a cathode ray tube. To release electrons, the cathode, which is usually composed of a tungsten filament, is heated. After that, a voltage is applied to accelerate these electrons in the direction of the target material, which might be copper (Cu), iron (Fe), molybdenum (Mo), or chromium (Cr). Electrons from outer shells transition to fill the inner vacancies when the accelerated electrons have enough energy to remove electrons from the target material's inner shell. This transition releases the unique radiation of the target material. When copper is used as the target material, for example, Kα and Kβ lines are emitted. To generate monochromatic X-rays, the released radiation is filtered. CuKα = 1.5418 Å is the wavelength for copper radiation. After that, these monochromatic X-rays are collimated and focused on the object that has to be characterized. Peaks in X-ray intensity are recorded when Bragg's condition is

satisfied as the specimen and the detector spin. After converting these signals into count rates, the detector records the information and transfers it to a computer for additional examination. There are three ways to find out a samples crystal structure: the Laue method, the rotating crystal method, and the powder method **[18]**.

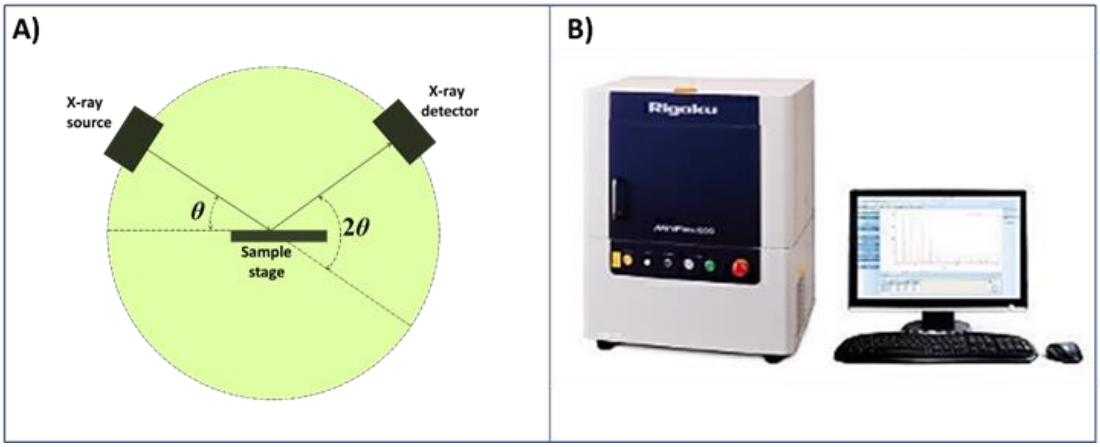

Figure 2.4: A) Schematic of X-ray instrument **[19]**, and B) photograph of RIGAKU MiniFlex600 diffractometer **[20]**.

The powder approach is frequently used to facilitate the crystal structure investigation of a material easier. A continuous spectrum of X-rays with a fixed angle of incidence is used in the Laue method, one of the first techniques used for identifying crystal structure. This technique is appropriate for detecting dynamic processes inside the crystal structure because it yields diffraction conclusions more quickly than those obtained with monochromatic X-rays. This method is called the centered crystal method when the wavelength varies but the angle of incidence remains fixed. The sample in this procedure rotates at a fixed angular velocity and is exposed to a monochromatic hard X-ray beam. On the other hand, the angle of incidence varies while the wavelength remains constant with the powder approach. The D2 Phaser X-ray diffractometer is depicted in **Figure 2.4 A**. **Figure 2.4 B** shows a photograph of RIGAKU MiniFlex600 diffractometer. Calculating crystal dimensions with the Scherrer equation is an essential use of XRD in nanocrystal studies **[21]**.

$$D = \frac{0.9\lambda}{\beta cos\theta} \qquad (2.6)$$

where, β is full width at half maximum (FWHM) of the diffraction peak, and θ is the peak position in radians.

2.5.2 Fourier transform infrared spectroscopy (FT-IR):

FT-IR spectroscopy is a powerful tool for identifying interatomic forces and the atomic arrangement within a crystal lattice. This technique can analyze a wide range of materials in various forms, including thin films, bulk materials, pastes, fibers, liquids, solids, and powders. FT-IR spectroscopy provides valuable information about the molecular structure and chemical bonding of both organic and inorganic materials. It is particularly useful for identifying unknown substances within a specimen. A material that interacts in an electromagnetic field has two energy levels (E1 and E2), with the energy level difference being equal to 'h' times the incident radiation frequency (v), as shown in the following formula:

$$\Delta E = hv \qquad (2.7)$$

When the change in energy (ΔE) is positive, it indicates that the molecule absorbs energy. Conversely, when ΔE is negative, the molecule emits energy in the form of radiation, resulting in an emission spectrum. A unique spectrum for the molecule is obtained when the energy difference between two levels corresponds to the frequency of the incident radiation, as described by the eq. 2.7.

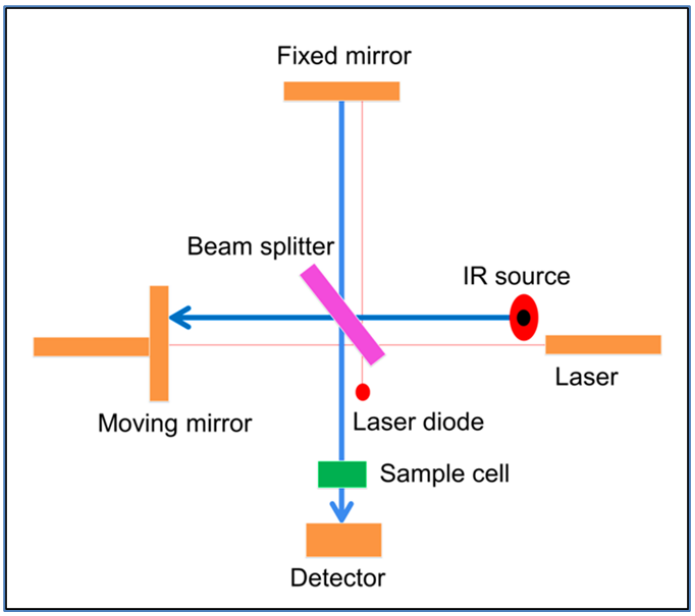

Figure 2.5: Basic ray diagram of FT-IR spectrometer.

A small section of the spectrum (close to visible) can be examined using FT-IR analysis; this area includes the UV, visible, and IR regions (10^{-6}-10^{-3}cm). The

absorption in an atom indicates the way the orbital electrons in molecules change between the various permitted levels, thus the atoms inside the molecule rotate or vibrate, and how the equation may be used to describe all of the energy contributions **[22, 23]**.

$$E_{total} = E_{elect} + E_{vib} + E_{rot} + E_{trans} \quad (2.8)$$

where, E_{total}, E_{elect}, E_{vib}, E_{rot}, and E_{trans} represent the electronic energy, vibrational energy, rotational energy, and translational energy, respectively. **Figure 2.5** illustrates the basic schematic diagram of an FT-IR spectrometer. Due to the quantized nature of energy levels, only certain transitions are possible for electronic, rotational, and vibrational energies. The translational energy, being relatively small, is often negligible in this context. FT-IR spectroscopy is especially valuable because it can serve as a molecular fingerprint, uniquely identifying materials based on their infrared spectra. This method complements X-ray techniques in material characterization by providing detailed insights into the molecular and chemical structure. The infrared spectrum, characterized by its distinct peaks, reveals information about molecular vibrations, bond strengths, and functional groups within the material. By combining FT-IR spectroscopy with X-ray diffraction, researchers can achieve a comprehensive understanding of both the structural and molecular characteristics of a material, enhancing the accuracy and depth of material analysis.

2.5.3 Raman spectroscopy:

Raman spectroscopy is an incredibly flexible method for fast, straightforward, and non-destructive examination of materials, both organic and inorganic **[24]**. This method provides important information about the characteristics and composition of the material through examining the way light interacts with it. Several molecular modes, such as rotational, vibrational, and other low-frequency modes, are measured using Raman spectroscopy **[25]**. Different vibrational states of the molecule are identified by distinct energy differences **(Figure 2.6)**. An electron in the sample absorbs energy from the photon and transitions to a higher energy state when it interacts with monochromatic light. The electron then depletes its energy and returns to its initial state. Through Rayleigh scattering, the electron releases a photon with the same frequency if the energy lost is equal to the energy of the incident photon.

Sometimes, when electrons lose energy from the virtual state, they can transition to a different vibrational level instead of returning to their original state. This causes the emitted photon to have a different energy than the absorbed incident photon, resulting in a frequency shift known as Raman scattering. The Stokes and anti-Stokes lines in Raman scattering are classified according to the ultimate vibrational state. When the emitted radiation has less energy than the incident radiation, Stokes lines appear. On the other hand, when the energy of the radiation emitted exceeds that of the incident radiation, anti-Stokes lines are produced. Anti-Stokes lines have a negative Raman shift ($\Delta\upsilon$), while Stokes lines have a positive one, providing a unique molecular fingerprint characteristic of the material being analyzed. The relative intensities of Stokes and anti-Stokes lines can provide insights into the thermal population distribution of vibrational states, since anti-Stokes lines are weaker due to fewer molecules naturally being in an excited state at lower temperatures. This behavior is governed by the principles of Boltzmann distribution. By examining the Raman spectra, researchers can identify specific molecular vibrational and rotational levels, allowing for the qualitative analysis of the sample and the identification of different molecules. **[26]**.

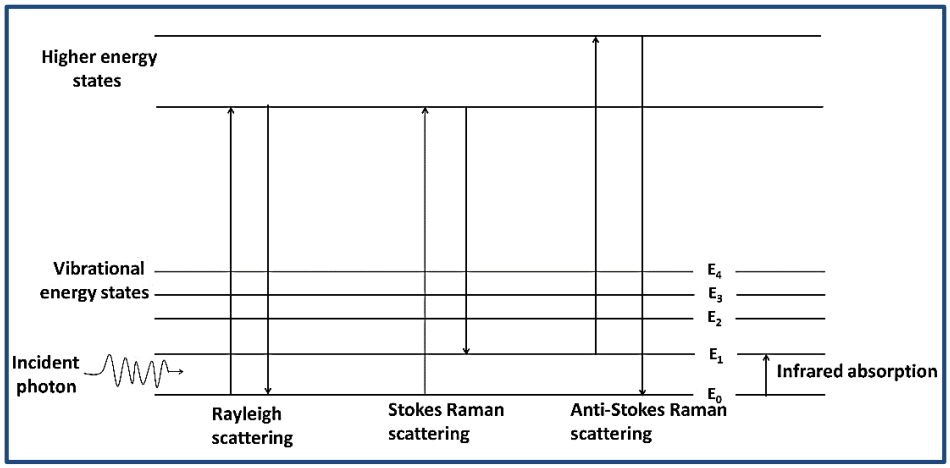

Figure 2.6: Energy level diagram showing the states involved in Raman spectrum.

Working of instruments:

Three main parts create to a Raman spectrometer: a detector, a sampling device, and an excitation source. The fundamental block diagram of a Raman spectrometer is shown in **Figure 2.7**. A monochromatic excitation source, usually a laser with a very narrow and constant bandwidth, can be used in this technique. A tiny

form factor, low power consumption, narrow line width, consistent power output, and stable wavelength output are among the qualities that the laser source must have. Shifting the laser wavelength into the near-infrared range is essential for examining organic compounds since it reduces fluorescence while maintaining charge-coupled device (CCD) spectral detection limitations.

Due to their availability and ability to significantly reduce fluorescence without compromising spectral range or resolution, 785 nm diode lasers have become increasingly popular. For highly colored or strongly fluorescent samples, a 1064 nm laser is a preferable option. In the case of inorganic molecules, a 532 nm laser is ideal as it provides enhanced sensitivity. The second component is the sample interface, which typically employs a fiber optic probe. This flexible sampling interface allows the probe to be used with solid samples and immersed in liquid slurries, making it suitable for both laboratory processes and various environmental conditions. The versatility of fiber optics ensures that the probe can be easily adapted to different sampling requirements. The fiber optic probe can also be connected to microscopes and cuvette holders, enhancing its versatility. The third component of a Raman spectrometer is the spectrometer itself, such as low noise, a small form factor, low power consumption, and high resolution to effectively detect very weak Raman scattering signals **[27]**. Additionally, the choice of detector depends on the type of excitation laser used. Typically, CCD is employed as the detector in Raman spectroscopy. For detecting weak Raman signals at low concentrations, a back-thinned CCD may be necessary to further enhance the sensitivity of the spectrometer.

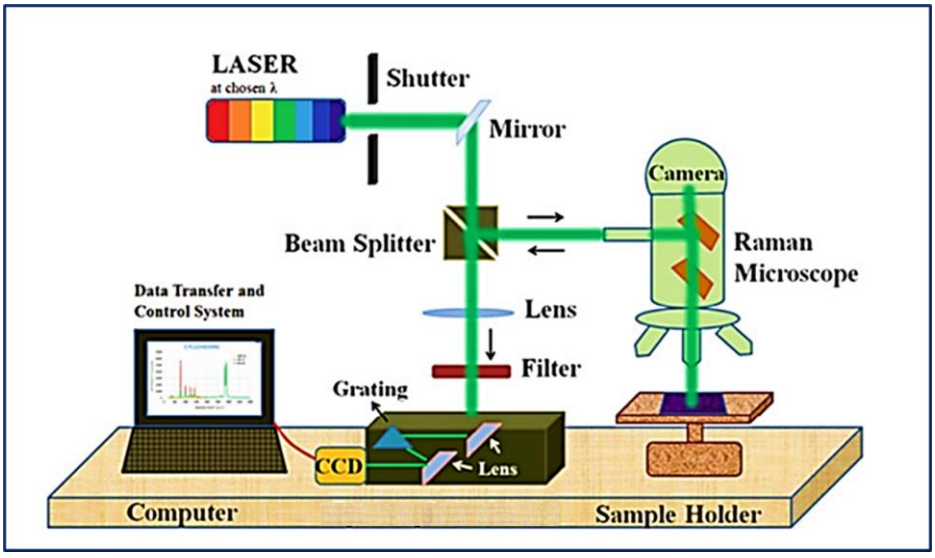

Figure 2.7: The basic block diagram of Raman spectrometer **[28]**.

2.5.4 X-Ray photoelectron spectroscopy (XPS):

X-ray Photoelectron Spectroscopy (XPS), also known as Electron Spectroscopy for Chemical Analysis (ESCA), is a highly utilized surface analysis technique. It is applicable to a wide variety of materials and offers valuable quantitative and chemical state information from the material's surface. Monochromatic X-rays are used as the photon source in the XPS technique, which is based on the photoelectric effect. During an XPS analysis, when the X-ray beam strikes the surface of a thin film, it induces the emission of electrons from the top surface layer of the material. These emitted electrons are referred to as photoelectrons **[30]**. When determining the elemental arrangement, stoichiometry, quantities, and molecular configuration of an element present in a thin film material, a photoelectron is needed. The binding energy of the photoelectron is determined by the following formula:

$$E_{binding} = E_{photon} - E_{Kinetics} + \varphi \quad (2.9)$$

Where,

$E_{binding}$ = Binding energy of atomic orbital

E_{photon} = Photon energy

$E_{Kinetics}$ = Ejected photoelectrons of kinetic energy, and

φ = Spectrometer work function

During the emission of photoelectrons in XPS, there is also a probability of Auger electron emission. Electrons of varying energy levels are released due to the different energy levels in different atoms. Since electrons undergo significantly more interactions with matter compared to photons, their path length is considerably shorter. Peaks in the XPS spectrum represent the background signal and indicate the presence of escaped electrons due to absorption in the material.

The main data modes obtained from XPS include the energy, spatial, and depth distribution of specific electrons. Elemental mapping and determining the chemical state of an element are achieved through depth distribution, while spatial distribution provides information about the probability of electron emission. Additionally, energy distribution offers insights into the electronic structure and binding energies, which are essential for identifying the chemical environment and oxidation states of the elements present in a sample.

2.5.5 Energy dispersive X-ray spectroscopy (EDS):

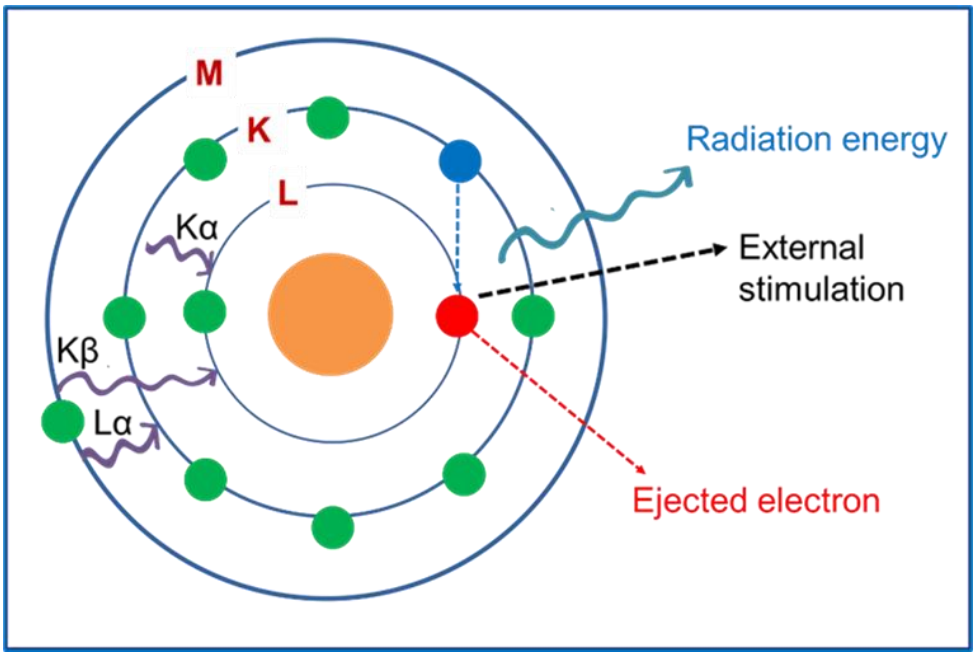

Figure 2.8: Principle of Energy-dispersive X-ray spectroscopy.

One of the most effective methods for doing elemental analysis on a sample is Energy Dispersive X-ray Spectroscopy (EDS), also referred to as EDX or EDAX. The ability of high-energy electromagnetic radiation (X-rays) to release core electrons those not in the outermost shell from an atom is the fundamental working principle of EDS. Moseley's Law defines a relationship between the atomic number of an atom and the frequency of light it emits. EDS is typically combined with FE-SEM, which cannot function without it.

High-energy X-ray beams are used in this investigation to aim at the specimen with the goal to generate background (a range) or distinctive X-ray emissions. An atom in the sample has electrons in its ground state at discrete energy levels as it is at rest. A vacancy or hole is formed when an electron from an inner shell is excited with an incident beam and is ejected **(Figure 2.8)**. This vacancy can then be filled by an electron from a higher energy shell, releasing an X-ray as a result of the energy differential between the higher and lower energy shells. Energy-dispersive X-ray analysis allows for the quantitative measurement of both the energy and the number of emitted X-rays. The energy of these X-rays is characteristic of the difference between the two shells and the atomic structure of the emitting element, making this technique suitable for elemental analysis. For example, when K-shell electrons are

excited, they emit characteristic X-rays known as “K Lines.” Similarly, X-rays emitted from the L and M shells are referred to as “L Lines” and “M Lines,” respectively. Heavier elements, having higher characteristic X-ray energies, require incident electrons of higher energies to be effectively analyzed.

2.5.6 Contact angle measurement:

A surfaces wettability, or the degree to which a liquid can spread over or attach to it, is measured by the contact angle. Its definition is the angle that forms at the point where a solid surface and a droplet of liquid contact. Higher wettability and strong liquid adhesion to the surface are indicated by a smaller contact angle, whereas lower wettability and weak adhesion are indicated by a higher contact angle. Since it reveals light on surface energy and the interactions between solids and liquids, this parameter is essential in many applications, such as coating processes, material science, and surface-related investigations. Rame-Hart contact angle measuring tool is shown in **Figure 2.9 A**. Contact angle measurement of an unidentified sample is shown in **Figure 2.9 B.**

The angle that results from forming a tangent to a liquid while measuring the angle from within the liquid is known as the contact angle. Via the use of this device, the material's hydrophobicity or hydrophilicity and surface can be verified throughout a number of applications.The angle (θ) between a liquid and a solid surface is important. If the angle is greater than 90°, it confirms the hydrophobic nature of the surface, meaning it's less wettable. When the angle exceeds 170°, it indicates that the surface is superhydrophobic. These surfaces are useful in manufacturing self-cleaning materials **[29]**. On the other hand, a contact angle of less than 90° indicates a hydrophilic surface, signifying good interaction with the liquid. A contact angle of less than 5° indicates a superhydrophilic and highly wettable surface, which is required for applications like supercapacitors, where ions from a liquid electrolyte need to intercalate in the material. The contact angle (θ) is calculated by Young’s relation **[30, 31]**.

$$\gamma_{s,v} = \gamma_{s,i} + \gamma_{i,v}\, cos\theta \qquad (2.10)$$

where, ‘$\gamma_{s,v}$’ is solid-vapour, ‘$\gamma_{s,i}$’ is solid-liquid, and ‘$\gamma_{i,v}$’ is liquid-vapour interfacial energies. The Rame-Hart goniometer (modal 260) is used in this investigation to record contact angle images of thin film electrodes.

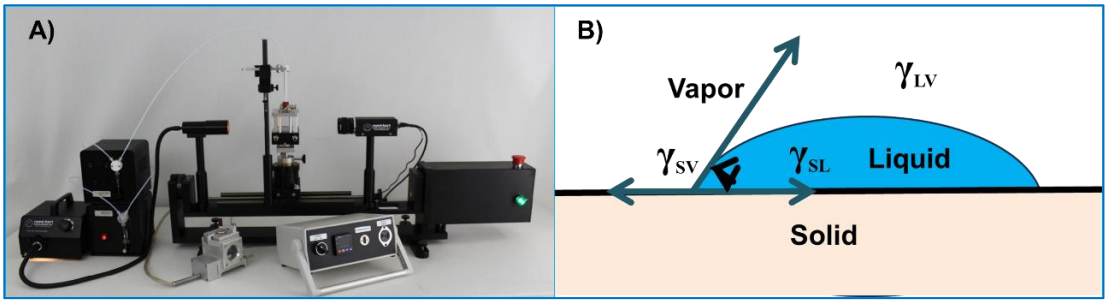

Figure 2.9: A) Rame-Hart NRL contact angle meter photo **[32]** and B) contact angle of a liquid drop contacting a solid object.

2.5.7 Field emission-scanning electron microscopy (FE-SEM):

The investigation of thin film structure through the application of an electron beam to the examining sample and gathering of slow-motion additional electrons released by the specimen. These secondary electrons are then gathered, amplified, and displayed on a computer monitor. The SEM is primarily used to examine the external structure of a variety of targets, including samples like metals, rocks, and ceramics, which can also be observed under a light microscope. As a type of electron microscope, the SEM creates images of high-energy electrons are used to examine the surface of a specimen in specific patterns. The interaction of the electron beams with the atoms in the sample generates signals that provide detailed information about the sample's composition, surface topography, and electrical conductivity properties. The SEM produces various signals, such as backscattered electrons (BSE), secondary electrons, characteristic X-rays, transmitted electrons, and light emissions from the specimens, each requiring specific detectors for their detection. These signals result from the interaction of electrons with the surface atoms of the sample. The most commonly used detection mode is secondary electrons. SEM is capable of producing extremely high-resolution images of the specimen's surface, revealing details as small as 1 to 5 nm. These SEM micrographs have a large depth of field, which is advantageous for identifying the surface structure of the specimen.

The schematic diagram of FE-SEM shows in **Figure 2.10**. The magnification range of a light microscope can vary extensively, from approximately 25X to 250,000X. Backscattered electrons (BSE) are electron beams that are transmitted from the specimen through elastic scattering. BSE is commonly used in investigative SEM, often in conjunction with spectra generated from characteristic X-rays. The intensity

of the BSE signal is strongly correlated with the atomic number (Z) of the sample, allowing BSE images to provide detailed information about the distribution of various elements within the specimen. This capability makes BSE imaging particularly useful for visualizing colloidal gold immune-labels. Characteristic X-rays are emitted when the electron beam ejects an inner shell electron from the specimen, causing a higher energy electron to fill the vacancy and release energy. These characteristic X-rays are utilized to determine the composition and quantify the abundance of elements within the specimen **[33]**.

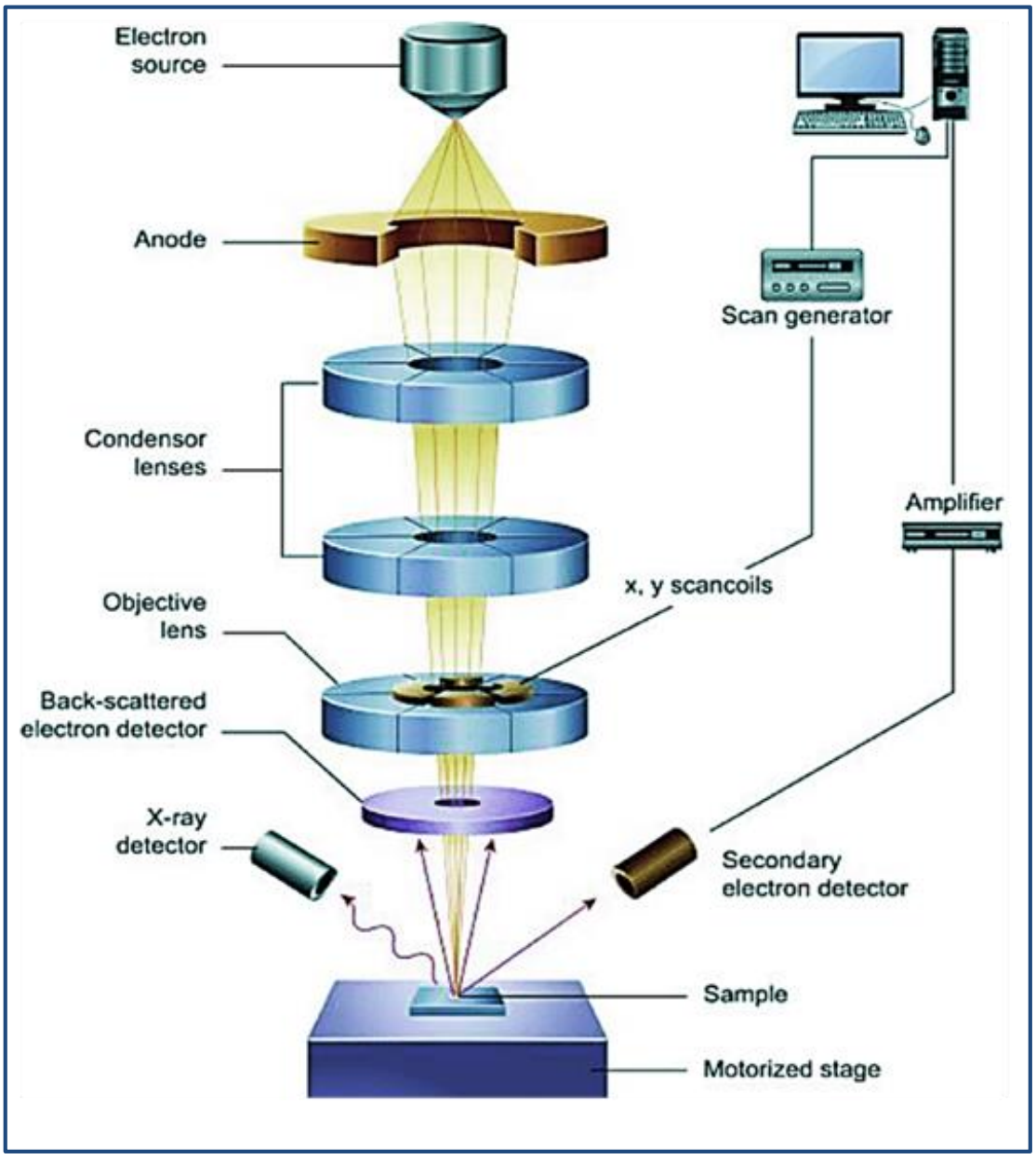

Figure 2.10: Schematic of FE-SEM **[34].**

2.5.8 Transmission Electron Microscopy (TEM):

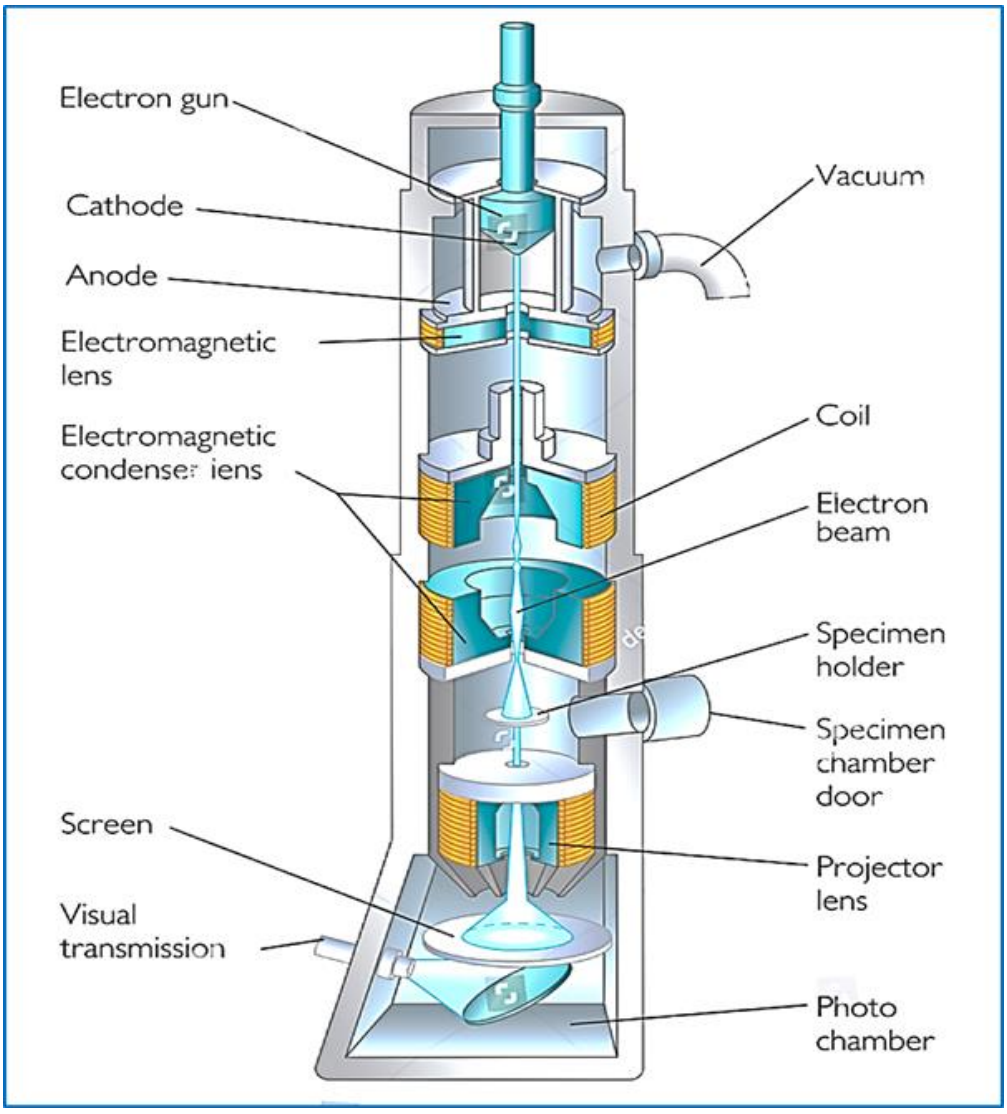

Figure 2.11: Schematic of TEM **[35]**.

Transmission Electron Microscopy (TEM) is a technique where a beam of electrons interacts with and passes through a specimen. An electron source emits the beam, which is then focused to create a magnified image using a series of magnetic lenses. TEM operates on similar principles to Scanning Electron Microscopy (SEM), but in TEM, the sample must be thin enough for the electron beam to penetrate it. The produced image is magnified and focused onto a fluorescent screen, and it can also be printed on photographic film. Advanced TEM machines can capture images using a charge-coupled device (CCD) **[36]**. Because the wavelength of the electron source is shorter than that of light, TEM images can achieve high resolution**. Figure 2.11** shows a schematic diagram of TEM. It consists of four main parts as follows:

1. Electron Source: The anode and cathode are essential. A beam of electrons is accelerated toward the sample specimen by the anode's positive potential. A tungsten filament heated electromagnetically to release electrons serves as the cathode, which has a negative potential.

2. Electromagnetic Lenses: The aperture and magnetic lens are combined in this component. A specific magnetic field can be generated by the magnetic lens that functions similarly to an optical lens, focusing the electrons. The aperture, a thin disc with a diameter ranging from 2 to 100 μm, removes unnecessary electrons from hitting the sample. The electromagnetic system ensures a well-determined narrow electron energy beam hits the target sample under analysis.

3. Sample Holder: The electrons radiated by the electron source pass through the sample without interacting with it, depending on the sample thickness. Thinner regions of the sample appear lighter, while thicker regions appear darker.

4. Imaging System: This system consists of additional electromagnetic lenses and a display. The scattered electrons from the sample, all with equal energy, are refocused by the electromagnetic lenses after transmission through the specimen, creating an enlarged image on the projector display.

2.6 Electrochemical characterization Techniques:

Supercapacitor performance was evaluated using several electrochemical properties. These techniques are frequently used in supercapacitor evaluation and in investigating batteries, sensors, and fuel cells. They offer crucial novel perspectives of corrosion rates, electrode surface porosity, reaction kinetics, and interfacial capacitance. Such thorough studies are essential for enhancing the performance and design of electrochemical energy storage systems.

2.6.1 Cyclic voltammetry (CV):

Analyzing electrochemical reactions is often done with the use of cyclic voltammetry (CV). The redox potential of active materials, adsorption processes, heterogeneous electron transport mechanisms, and redox reactions are all covered in detail. A working electrode and a counter electrode are used in this potentiostatic approach to measure the current flowing between them. It is possible to see these electrochemical processes by calculating the resulting CV curve, represented as

current vs applied potential. **Figure 2.12** illustrates the electrode potential changes steadily and consistently during time in CV studies. The electrolyte concentration, electrode materials, and scan rate influence the peak height and width for the particular process **[37, 38]**. To clarify the processes occurring on the electrode surfaces, CV is utilized in this research.

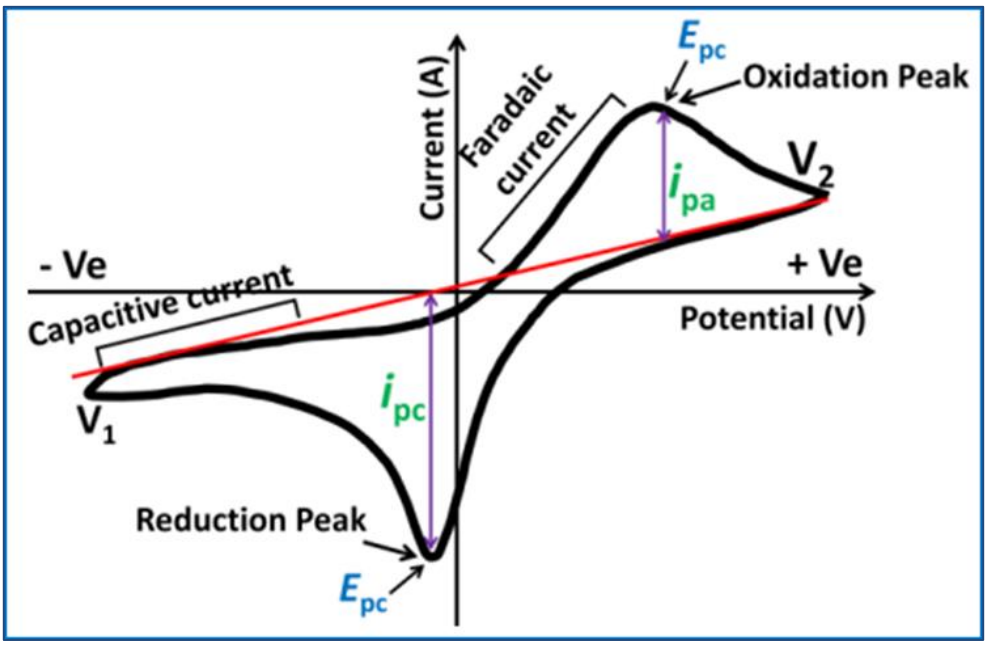

Figure 2.12: The reversible single electrode transfer reactions (CV curve) **[39]**.

Reversible or non-redox reactions can occur on the electrode surface. The applied potential in a reversible process could affect the electrode surface's physical structure. The adsorption of species to produce an electrical double layer is involved in this kind of reaction, sometimes referred to as a non-faradaic reaction. The peak potentials for anodic and cathodic reactions in redox reactions are represented by E_{pa} and E_{pc}, respectively, whereas the peak currents are denoted by I_{pa} and I_{pc}. The scan rates impacted the voltammograms widths, peak potentials, and amplitudes. Examining the functions of adsorption, diffusion, and chemical reaction mechanisms is a beneficial application of this technique **[39, 40]**. This is the most common method for determining a specific capacitance (C_s) of CV. The formula below is used to determine C_s,

$$C_s = \frac{1}{mv(V_i - V_f)} \int_{V_i}^{V_f} i(V)dv \qquad (2.11)$$

Where, $\int_{V_1}^{V_2} I(V)dV$ is the area enclosed in a CV curve, m (g) is deposited mass of material on both electrodes.

2.6.2 Galvanostatic charging-discharging (GCD):

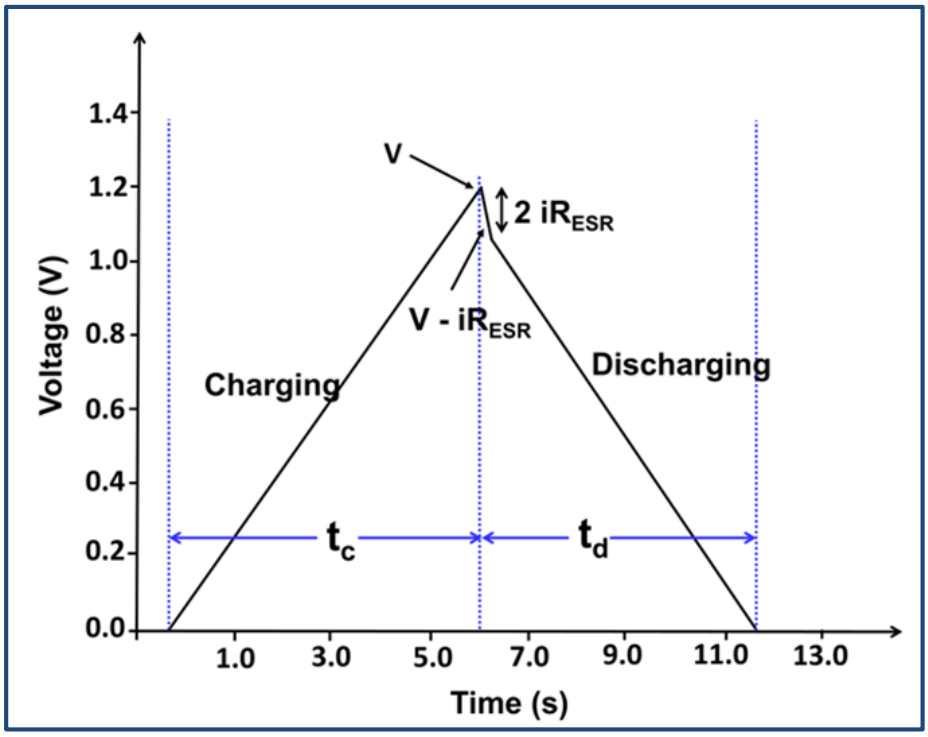

Figure 2.13: Schematic diagram of charge-discharge curve.

The steady current is applied to the working electrode, charging it to a higher potential V_2. The electrode is then discharged in the opposite direction until it reaches a lower potential V_1 with the same current scale. The GCD plots, which applied potential against time, is essential for analyzing the charging and discharging processes. With the use of GCD curves, it is possible to determine the specific capacitance, specific energy, specific power, cycling stability, and coulombic efficiency of the materials **[41]**. **Figure 2.13** illustrates a schematic of the charge-discharge curve.

The GCD technique is necessary to evaluate the electrode material average capacitance, energy density, and power density. The shape of the GCD curve also provides information on the properties of the electrode material **[42]**. The electrode material C_s is determined by applying the following formula:

$$C_s = \frac{i \times t}{m \times \Delta V} \quad (2.12)$$

Where, ΔV, i, m, and t are referred to as voltage of potential in Volt, discharge current in Ampere, mass in gram and discharge time in seconds, respectively.

The S_E and S_P of rGO/RuO_2 electrodes are calculated using following equations,

$$S_E = \frac{0.5 \times C_S \times \Delta V^2}{3.6} \quad (2.13)$$

$$S_P = \frac{S_E \times 3600}{t} \quad (2.14)$$

where, ΔV is the potential window in (Volt).

2.6.3 Electrochemical impedance spectroscopy (EIS):

The process for applying a low-amplitude sinusoidal signal throughout a broad frequency range and measuring the current and temperature responses is the Electrochemical Impedance Spectroscopy (EIS) approach. It is standard procedure to measure electrochemical impedance using an analogous circuit **[43, 44]** and the resulting graph **(Figure 2.14)**. Ohmic resistance may be visually represented using EIS thanks to its plot structure, which is a noteworthy benefit. The EIS graph reveals a straight line in the low-frequency region, which corresponds to the Warburg resistance **[45]**, and a half semicircle in the high-frequency region, representing the parallel combination of capacitance and resistance. The following important electrochemical terms are highlighted in EIS spectroscopy,

1. Electrolyte resistance:

The series resistance is an essential factor in the electrochemical impedance, which is mainly influenced by the electrolyte resistance. The series resistance between the reference and counter electrodes in a three-electrode cell arrangement is compensated for. It is imperative to consider the series resistance between the working and reference electrodes when modelling electrochemical cells. Many variables, including temperature, areal geometry, ionic concentration, and the kinds of ions that are carrying the current, affect an ionic solution resistance **[46]**. Imaginary components are absent from the resistor, which is frequency independent. Both the low-frequency and high-frequency components of the analogous circuit are shown in

Figure 2.14. R_{ct} is the charge transfer resistance, R_s is the solution resistance, C is the double layer capacitor, and there is also a W is the Warburg impedance in this circuit.

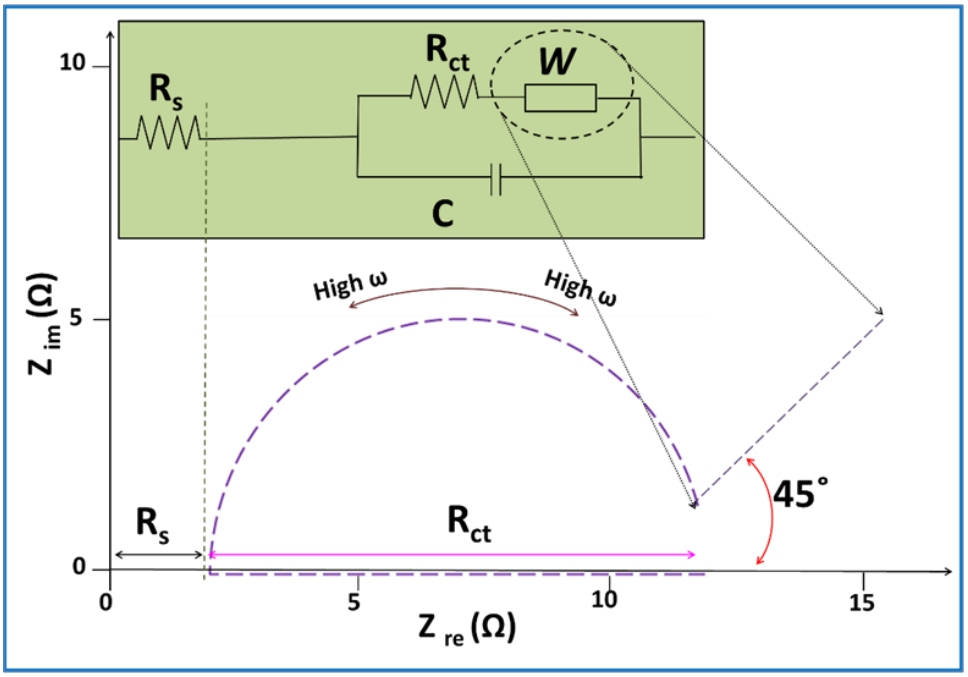

Figure 2.14: The Nyquist plot of electrode-electrolyte interface.

2. Charge transfer resistance (R_{ct}):

One distinct electrochemical reaction that is kinetically controlled creates charge transfer resistance (R_{ct}). The charge transfer resistance is shown as a half semi-circular loop in **Figure 2.14**. This resistance is connected to the current that is generated by the electrochemical reaction at an electrified interface. The following is the comparable reversible reaction:

$$Red \leftrightarrow Ox + ne^- \quad (2.15)$$

In such a scenario, O stands for the oxidant, n for the number of electrons transferred, and Red for the reduced product (reductant). Reaction type, temperature, reactant concentration, and potential all affect the way quickly a reaction proceeds in an R_{ct}.

3. Double layer capacitance (C):

There are two ways that charge can be transferred: faradic and non-faradic. The non-faradic component originates from the double layer capacitance (C), whereas the faradic component is the product of redox processes at the electrode surface. The rates of which electrons transfer at the interface determines charge transfer; this rate is

influenced by oxidant presence and reductant synthesis occurring in close proximity to the electrode surface.

4. Warburg (W):

The impedance created by diffusion is called Warburg resistance, and it changes depending on how frequently the potential fluctuation occurs. Reactants must diffuse over greater distances at lower frequencies, which increases Warburg impedance. Ion mass transit results in a diagonal line that is 45° angled to indicate Warburg impedance in a Nyquist plot. A crucial characterization technique for a variety of material systems, such as batteries, fuel cells, plating, and corrosion, is electrochemical impedance spectroscopy (EIS).

References:

[1] E. Rogers, P. Smet, P. Dorenbos, D. Poelman, E. Kolk, J. Phys.: Condens. Matter, 22, (2010), 15005-15016.

[2] D. Dubal, O. Ruiz, P. Gomez–Romero, Chem. Soc. Rev., 44, (2015), 1777-1790.

[3] Y. Jiang, and J. Liu, Energy Environ. Mater. 2, (2019), 30-37.

[4] V. Sharma, and I. Singh, A. Chandra, Sci. Rep., 8, (2018), 1307-13017.

[5] C. Lokhande, Mater. Chem. Phys., 27, (1991), 1-43.

[6] U. Patil, S. Kulkarni, V. Jamadade, C. Lokhande, J. Alloys Compd., 509, (2011), 1677-1682.

[7] J. Robins, Appl. Surf. Sci., 33, (1988), 379-394.

[8] M. Ristov, G. Sinadinovski, I. Grozdanov, Thin solid films, 123, (1985), 63-67.

[9] Y. Nicolau and J. Menard, J. Cryst. Growth, 92, (1988), 128-142.

[10] A. Bard, L. Faulkner, 2nd Edition, John Wiley & Sons, inc. Chapter 1: Introduction and overview of electrode processes, (2000).

[11] H. Pathan, C. Lokhande, Bull. Mater. Sci. 27, (2004), 85–111.

[12] https://holmarc.com/images/silar_controller_mag_stirrer_bathstand1.jpg.

[13] Y. Nicolau, Appl. Surf. Sci., 22/23, (1985), 1061-1074.

[14] V. Shinde, T. Gujar, C. Lokhande, R. Mane, S. Han, Sens. Act. B, 123, (2007), 882-887.

[15] R. Mane, C. Lokhande, Mater Chem Phys., 65, (2000), 1-31.

[16] G. Gund, D. Dubal, S. Jambure, S. Shinde, C. D. Lokhande, J. Mater. Chem. A, 1, (2013), 4793-4803.

[17] V. Petkov, Mater. Today, 11, (2008), 28-38.

[18] B. Cullity, S. Stock, Elements of X-rays Diffraction, 3rd Edition, Prentice Hall, (2014), 284-285.

[19] http://xrd.co/component-parts-x-ray-diffractometer.

[20] https://www.rigaku.com/products/xrd/miniflex.

[21] B. Cullity, “Elements of X-rays Diffraction”, Second ed., Addison-Wesley, London (1978).

[22] R. Nyquist, R. Kagel, Infrared Spectra of Inorganic Compounds, Academic Press INC, New York, (1971).

[23] J. Preudhomme, P. Tarte, Spectrochim. Acta, 27, (1971), 1817-1835.

[24] https://en.wikipedia.org/wiki/Raman_spectroscopy.

[25] I. Ebenezar, S. Ramalingam, C. Raja, P. Prabakar, J. Nano. Adv. Mat., 2, (2014), 11-25.

[26] J. Breier, S. White, C. German, Phil. Trans. R. Soc. A, 368, (2010), 3067-3086.

[27] A. Downes, A. Elfick, Sensors, 10, (2010), 1871-1889.

[28] https://www.mt.com/in/en/home/applications/L1_AutoChem_Applications/Raman-Spectroscopy.html.

[29] D. Singh, M. Pradhan, A. Materny, Modern techniques of spectroscopy. Springer Singapore, (2021), 145-184.

[30] C. Wagner, W. Riggs, L. Davis, J. Moulder, Perkin Elmer Corporation, Minnesota, (1979), 1-28.

[31] M. Vadiyar, S. Bhise, S. Patil, S. Kolekar, A. Shelke, N. Deshpande, J. Chang, K. Ghule, A. Ghule, Chem. Commun., Chem. Commun., 52, (2016), 2557-2560.

[32] http://www.ramehart.com/790.htm.

[33] https://en.wikipedia.org/wiki/Scanning_electron_microscope.

[34] https://www.nanoscience.com/wp-content/uploads/2023/09/schematic-of-scanning-electron-microscope.jpg.

[35] https://www.shutterstock.com/image-vector/diagram-transmission-electron-microscope-quantum-physics-1690518037.

[36] http://www.hk-phy.org/atomicworld/tem/tem02e.html.

[37] J. Bard, L. Faulkner, Electrochemical Methods: Fundamentals and Applications (2 ed.), Wiley, (2000-12-18), ISBN 0-471-04372-9.

[38] https://en.wikipedia.org/wiki/Cyclic_voltammetry.

[39] J. Heinze, Angew Chem. Int. Ed. Engl. 23, (1984), 831-847.

[40] R. Parsons, Chem. Rev. 90, (1990), 813–826.

[41] R. Salunkhe, Y. Kaneti, Y. Yamauchi, ACS Nano, 11, (2017), 5293-5308.

[42] P. Veerakumar, A. Sangili, S. Manavalan, P. Thanasekaran, K. Lin, Ind. Eng. Chem. Res., 59, (2020), 6347- 6374.

[43] http://www.gamry.com/application-notes/EIS/basicsofelectrochemicalimpedance-spectroscopy

[44] http://www.ecochemie.nl/download/Applicationnotes/Autolab_Application_Note_EIS06.pdf.

[45] https://www.jlab.org/conferences/tfsrf/Thursday/Th2_1EIS%20intro%20Reece.pdf.

[46] http://www.gscsg.com/Electrochemical%20Impedance%20Spectroscopy.html

CHAPTER-III

SYNTHESIS AND CHARACTERIZATION OF RUTHENIUM OXIDE (RuO_2) ELECTRODES USING SUCCESSIVE IONIC LAYER ADSORPTION AND REACTION (SILAR) METHOD

CHAPTER -III

SYNTHESIS AND CHARACTERIZATION OF RUTHENIUM OXIDE (RuO_2) ELECTRODES USING SUCCESSIVE IONIC LAYER ADSORPTION AND REACTION (SILAR) METHOD

3.1 Introduction:

Enhancing the capacity of energy storage systems has certainly been the subject of significant study worldwide because of growing need for large-capacity power storage for use in hybrid electric cars, armed forces gears, lightweight and versatile digital devices, and designate biomedical gear **[1-4].** However, the more accomplished energy that is sustainable is not suitable to meet the energy storage demands. Hence, this energy storage transformation is important for research as well as industries. Supercapacitor (SC) signifies a rising energy storage system category that has drawn interest because it offers a greater energy density than conventional capacitors. The SCs possess a higher capacity for rapid charging and discharging and longer cycle life than rechargeable batteries **[5].** The electrode material is crucial in the design of SC. It is effectively tuneable for the crucial electrochemical performances of the SC. The taxonomy of SCs is classified in three kinds, such as electric double layer capacitor (EDLC), pseudocapacitor, and hybrid capacitor, based on their charge storage techniques. In EDLCs, energy storage mechanisms arise from electronic and ionic charge processes that are separated at the interfaces between electrode and electrolyte. The EDLC-type behaviour has been shown by carbon-based materials, like activated carbon, carbon nanotubes, graphene, diamond, carbon aerogel, etc. **[6].** On the other hand, metal oxides/sulfides and conducting polymers store charge mostly by a quick, reversible redox process that results in pseudocapacitance **[7-9]**. Here, electron transport takes place chemically, producing the excess pseudocapacitance at a certain potential. Here, charge storage is carried out by bulk of material, enhancing the specific energy density and device capacitance **[10].** Both methods of charge storage reveal both beneficial and undesirable electrochemical qualities. The efficiency of a single-charge storage method is insufficient to compete with batteries. In this sense, the deployment of a performance-oriented energy storage system requires the development of a hybrid strategy. Both types of charge storage methods are included in the hybrid strategy. The capacitive method increases device stability and electronic conductivity by having a large surface area and an efficient charge transportation path **[11].**

Ruthenium oxide (RuO_2), one of the most popular metal oxide has been extensively researched due to its enormous surface area, excellent reversibility, and relatively high capacitance **[12]**. Recently, it has also been revealed that RuO_2 has

excellent electrocatalytic activity in a wide range of electrochemical processes **[13]**. The stable RuO_2 mainly adopts the "rutile structure" of RuO_2, even though it is observed in other variations with respect to liquid hydrate. Its molecular orbital theory effectively explained the thermodynamic stability and large isotropic charge transportation characteristics of RuO_2. Additionally, RuO_2 has a long cycle life with tunable metallic conductivity, multiple oxidation states, and durable stability across a broad potential range. In fact, these characteristics have greatly aided SC research. However, a few problems, as well as a strong tendency for self-aggregation, hydrophilic electrolytes exhibit weak chemical stability and improvement of a mechanism for storing charges that integrates water into the nanophase, have actually encouraged designing relatively homogenous smart hybrid structures for electrochemical devices in the future **[14, 15]**.

Supercapacitors primarily use carbon-based materials, transition-metal oxides, conducting polymers, and composites made from these materials for charge storage. Noble metals are the focus of significant research in the area of Supercapacitor electrode materials due to their excellent conductivity and electrochemical stability. Silver, gold, and the platinum group (ruthenium, rhodium, palladium, osmium, and platinum) are the most common noble metals used for SCs **[16].** Noble metals, which have a high conductivity, can efficiently transfer electrons during the oxidation or reduction of pseudocapacitors from current collectors. Noble metals are expensive and rare, thus combining them with more affordable, sustainable materials is seen as perhaps the most alluring way to enhance their benefits and reduce their use. The high cost and limited availability of noble metals prevent their extensive use as electrode materials **[17].**

Mevada and Mukhopadhyay **[18]** prepared RuO_2 thin film by spin coating method which exhibited electrochemical specific capacitance (C_s) of 676 F g^{-1} in 1 M Na_2SO_4 electrolyte. Wang et al. **[19]** reported C_s of 1099 F g^{-1} for RuO_2 thin film prepared using ion oxidising conversion method. Thangappan et al. **[20]** synthesized RuO_2 thin film via hydrothermal method and exhibited an electrochemical C_s of 226 F g^{-1} in 1 M Na_2SO_4 electrolyte. Deshmukh et al. **[21]** reported maximum C_s of 192 F g^{-1} for RuO_2-nH_2O electrode through the SILAR method. Dubal et al. **[22]** prepared RuO_2 thin film using CBD method and obtained C_s of 234 F g^{-1}. Shankar et al. **[23]** reported maximum C_s of 476 F g^{-1} RuO_2 thin films deposited by precipitation method.

3.2 Synthesis of RuO_2 thin films:

3.2.1 Introduction:

The advantages of an amorphous materials as an electroactive material significantly improve capacitive performance, cycle life, and electrochemical stability of SCs by increasing the specific surface area and increasing charge transfer **[24]**. The amorphous nature of RuO_2 is more viable than crystalline because amorphous materials are more susceptible structural disorder **[25]**. Ions can easily intercalate and deintercalate in the bulk of the amorphous electrode, enhancing the electrode's capacity to store electrochemical charges. The advantage of the proposed system focuses on the synthesis of amorphous RuO_2 thin films by SILAR method for SC application **[26]**. The SILAR method is cost effective as compared to other physical and chemical methods. It does not require high quality target and/or substrates nor vacuum at any stage, which is a great advantage if the method is used for industrial applications or large scale deposition because pure Ru material is costly as compared with other materials **[27]**. In this chapter, amorphous RuO_2 thin films of different thicknesses were synthesized by applying the SILAR method on stainless steel (SS) substrates. Structural and elemental properties were studied using different characterization techniques.

3.2.2 Experimental section:

3.2.2.1 Cleaning substrate:

To achieve high-quality thin films using chemical methods, the substrate surface should be maintained clean. On the substrate surface, defects might act as nucleation nuclei. The important conductive substrate for SCs is needed. Because of their high electrical conductivity and low cost, stainless steel (SS) substrates are perfect for SCs. These substrates need to be prepared in multiple processes, including polishing, ultrasonication, and cleaning with acetone and double distilled water (DDW). Initially, zero-grade polish paper is used to polish the SS substrates. Afterward cleaned with acetone and DDW. The substrates are then cleaned with ultrasonic technology for 10 min. The substrates are now prepared for material deposition after being air-dried.

3.2.2.2 Chemicals:

For the synthesis of RuO_2 thin films, analytical-grade chemicals such as ruthenium trichloride ($RuCl_3.xH_2O$) and sodium hydroxide (NaOH) were used without additional purification.

3.2.2.3 Synthesis of RuO_2 thin films:

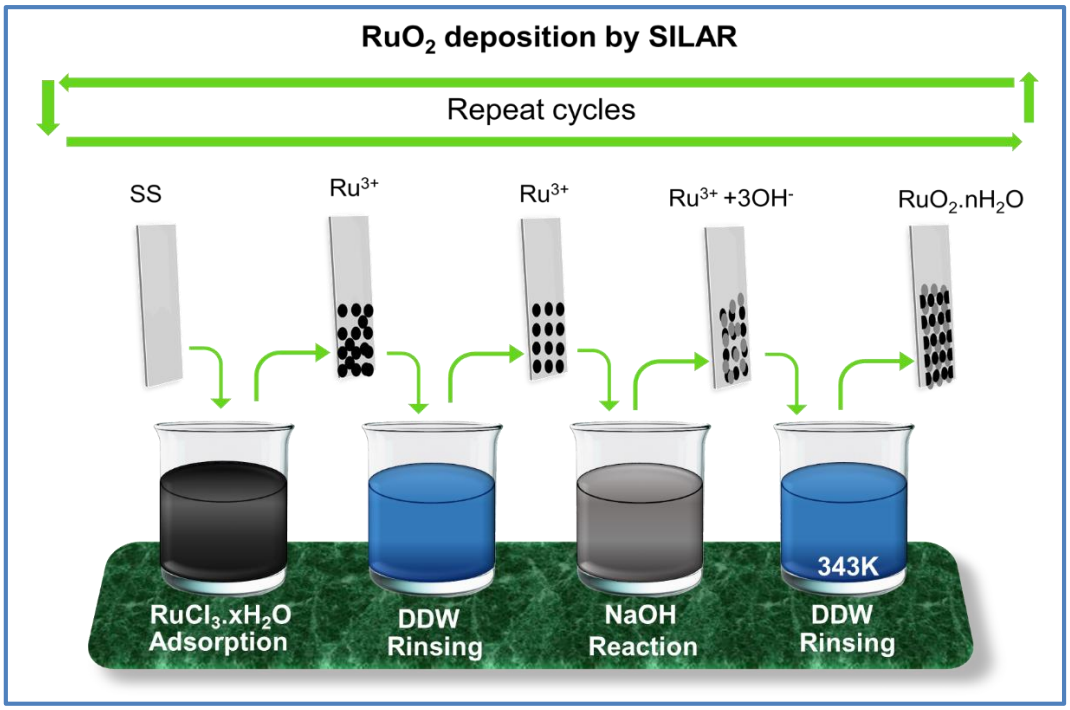

Figure: 3.1: Schematics of SILAR method for deposition of RuO_2 films.

The synthesis procedure of RuO_2 thin film by SILAR method is based upon chronological effect of successive immersion of substrate into individually kept cationic and anionic precursor resources. In the deposition procedure, cationic precursor of concentration 0.01 M $RuCl_3.xH_2O$ (25 ml) (pH = 1.98±0.10), anionic precursor of concentration 0.05 M NaOH (25 ml) (pH = 10.2±0.10) and double-distilled water (DDW) (25 ml) was utilised **[14, 28]**. **Figure 3.1** shows the schematic of four steps SILAR method used for the deposition of RuO_2 thin film. To complete one cycle of SILAR, the SS substrate was successively immersed in cationic and anionic precursors for 5 s with in between rinsing in DDW for 10 s. Such SILAR cycles were repeated for 150, 200, 250, and 300 cycles and corresponding films are denoted as R1, R2, R3, and R4, respectively. After deposition, thin films were washed by DDW and allowed to air dry at room temperature. The cations produced by the

dissociation of the cationic precursor in DDW are adsorbed on the substrate, due to the chemical or Van der Walls force of attraction between the cations and surface of SS substrate **[18].**

3.3 Material characterizations

3.3.1 Elemental and structural analysis of RuO_2:

The structural study of RuO_2 was evaluated using Rigaku miniflex-600 X-ray diffractometer operating on Cu Kα radiation at 30 kV (λ = 0.1540 nm). A precise study of functional groups and bonding presence in the obtained RuO_2 electrode material was performed using Bruker Tensor 27 FT-IR equipment. An EDAX attached to a SEM (JEOL JEM 2100) was used to investigate the morphogenesis component analysis of RuO_2 thin film. The contact angle was examined using a Rame Hart-500 advanced goniometer.

3.3.2 Electrochemical characterization:

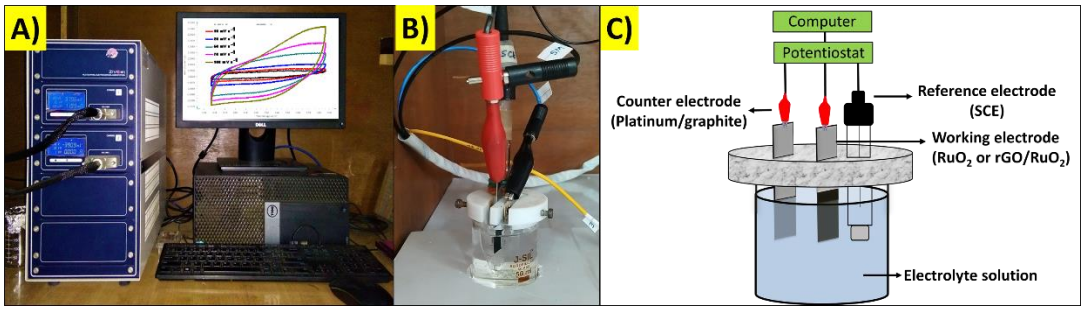

Figure 3.2: A) The electrochemical work station, B) experimental setup, and C) schematic representation of three electrode system.

The Zive MP1 electrochemical workstation was used to investigate the electrochemical supercapacitive characteristics of electrodes. A three-electrode system comprises of a RuO_2 thin film as a working electrode, saturated calomel electrode (SCE) as a reference electrode, and graphite as a counter electrode. The electrodes were evaluated using cyclic voltammetry (CV) and galvanostatic charge-discharge (GCD) in a potential window ranging from 0 to +1.0 V/SCE in 1 M H_2SO_4 electrolyte. The electrochemical impedance spectroscopy (EIS) was carried out with an AC amplitude of 10 mV **[14, 29]**. The Cs of electrodes were determined from CV

and GCD curves by utilizing the following in (eq 2.10 and 2.11), The electrochemical workstation is shown in **Figure 3.2 A**, the three electrode experimental setup is shown in **Figure 3.2 B**, and schematic of electrochemical studies are shown in **Figure 3.2 C**.

3.4 Results and discussion:

3.4.1 Growth mechanism of RuO_2 film:

The formation of RuO_2 thin film occurs through the ion-by-ion process on the submerged substrate. The surface of the SS substrate was bound with Ru^{3+} ions from the cationic precursor. To stop the precipitation, the substrate was washed in DDW to get rid of Ru^{3+} loosely bound ions. Further, the SS substrate was dipped in an anionic precursor solution where OH^- ions react with Ru^{3+} ions which form an insoluble RuO_2 film. After the reaction, SS substrates was rinsed in DDW to remove nonadherent particles on the film. It is possible to describe the reaction mechanism of RuO_2 deposition as,

$$RuCl_3 + 3NaOH \rightarrow Ru^{3+} + 3OH^- + 3NaCl \quad (3.1)$$

The substrate was immersed in DDW water bath at 343 K denoted as Δ, whereas OH^- anions react to form ruthenium hydroxide ($Ru(OH)_3$). Therefore, anions that are in excess with $Ru(OH)_3$ convert it into RuO_2, which is represented as **[21]**.

$$Ru^{3+} + 3OH^- \rightarrow Ru(OH)_3 \quad (3.2)$$

$$Ru(OH)_3 + OH^- \xrightarrow{\Delta} RuO_2 + 2H_2O \quad (3.3)$$

Such multiple SILAR cycles were repeated to get optimized mass loading RuO_2 on the substrate.

The thicknesses of thin films were determined using the weight difference method and a sensitive microbalance. Thickness (T) was determined by using the relation,

$$T = \frac{M}{A \times \rho} \quad (3.4)$$

where, '*M/A*' is the mass deposited on the SS substrate per unit area in mg cm^{-2}, and 'ρ' is the density of RuO_2 (6.97 g cm^{-3}). The thickness variation plot of R1, R2, R3, and R4 films is shown in **Figure 3.3 A**. The obtained mass deposition values of R1, R2, R3, and R4 electrodes are 0.7, 1.25, 1.56, and 1.44 mg cm^{-2}, respectively. In SILAR Method, the film thickness is influenced by the nucleation growth process and the rate of nucleus production. During the growing process, more nucleation sites

improve coagulation even more to achieve the optimum thickness **[28, 29]**. The thickness of R3 film achieves a maximum of 1.56 mg cm^{-2} at 250 cycles. Furthermore, after 250 cycles (R3 electrode), slight decrease in film thickness could be attributed to the formation of outer porous layer of film which may develop stress to cause delamination, resulting in peeling off of the film material after the film reaches its maximum thickness. **Figure 3.3 B** shows variations in film integrity and thickness after different cycling stages. Films R1 and R2 display minimal deposition. In contrast, R3 shows the greatest thickness, evidenced by its darker color, while R4 exhibits delamination and peeling.

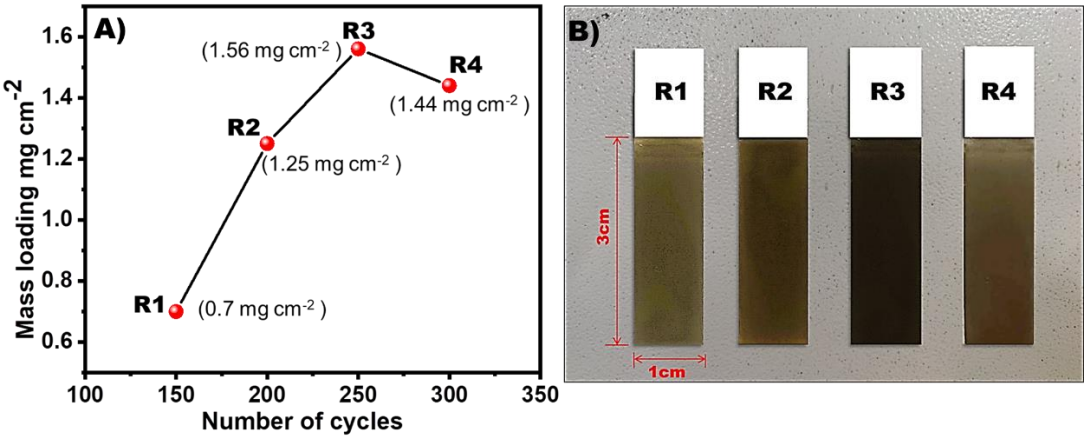

Figure 3.3: A) Mass loading variation of RuO_2 thin films with the number of deposition cycles, and B) photograph of RuO_2 films.

3.4.2 XRD analysis:

The structural analysis of RuO_2 film was performed using an X-ray diffractometer with a diffraction angle 2θ ranging from 5º - 80º. **Figure 3.4** shows the XRD patterns of R1, R2, R3, and R4 films. The peaks denoted by the symbol (#) are due to the stainless steel substrate. It reveals that deposited RuO_2 films are amorphous in nature**.** In general, after annealing at 473 K deposited RuO_2 with an amorphous structure can be usually converted to crystalline RuO_2 **[30]**. Anhydrite RuO_2 with an amorphous phase (at 343 K) has shown a relatively high porous structure than its crystalline counterpart **[31].** The amorphous material is a kind of structural irregularity; the obtained amorphous nature is more sustainable than crystalline. As a result, amorphous materials with porous structure have apparent volumetric gap fractions. Hence, the bulk of the amorphous electrode makes it simple for ions to

intercalate and deintercalate, boosting the electrode capacity to store electrochemical charge **[32]**.

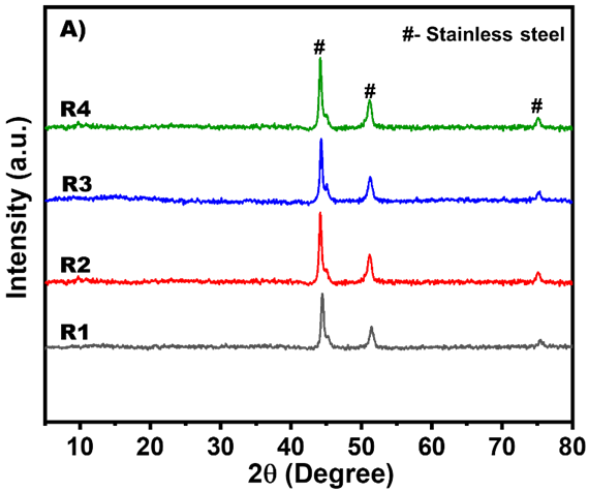

Figure 3.4: The XRD patterns of R1- R4 thin films.

3.4.3 FT-IR study:

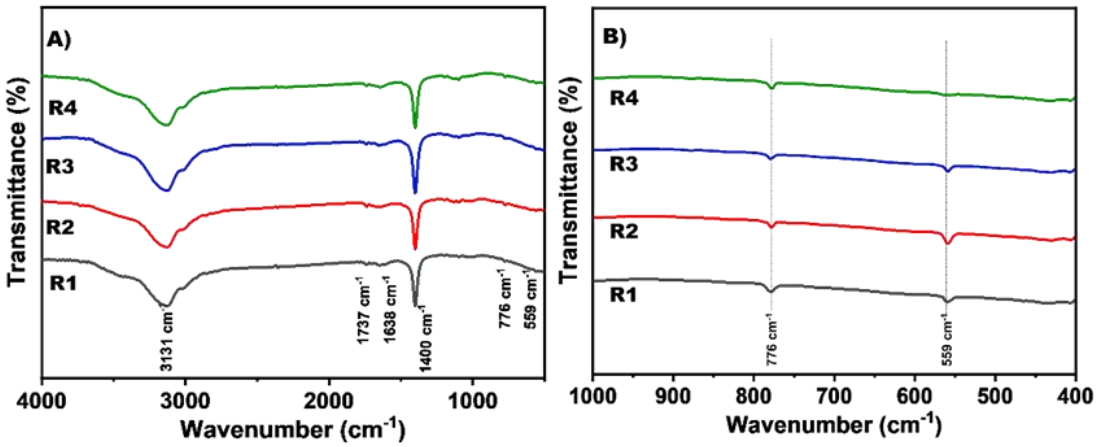

Figure 3.5: A) FT-IR studies, and B) enlarge view of FT-IR studies of R1-R4 thin films (1000-400 cm^{-1}).

FT-IR spectroscopy is an effective method for studying qualitative material functional groups and molecular bonding. **Figure 3.5 A** shows the FT-IR spectra of RuO_2 thin films (R1 to R4) in the 4000-400 cm^{-1} range. The enlarged view of FT-IR spectra (1000-400 cm^{-1}) is shown in **Figure 3.5 B.** Due to **t**he enlarged view, the small and strong bands (v_1) at around 559 cm^{-1} and (v_2) at 776 cm^{-1} corresponding to the typical asymmetric stretching mode of RuO_2 are identify clearly **[33, 34]**. The absorption band (v_3) at 1400 cm^{-1} is assigned to the characteristic stretching vibration

of bending OH groups **[30]**. The absorption bands around (v_4) 1638 cm^{-1} and (v_5) 1737 cm^{-1} are due to the vibration of hydroxyl groups from physically adsorbed water (H-O-H)**.** The broad peak (v_6) at 3110 cm^{-1} attributed to symmetric stretching of the sample confirming the existence of adsorbed water (O-H) **[35].** The presence of vibrational modes associated with RuO_2 in FT-IR spectra confirms formation of RuO_2 material on SS substrate.

3.4.4 SEM study:

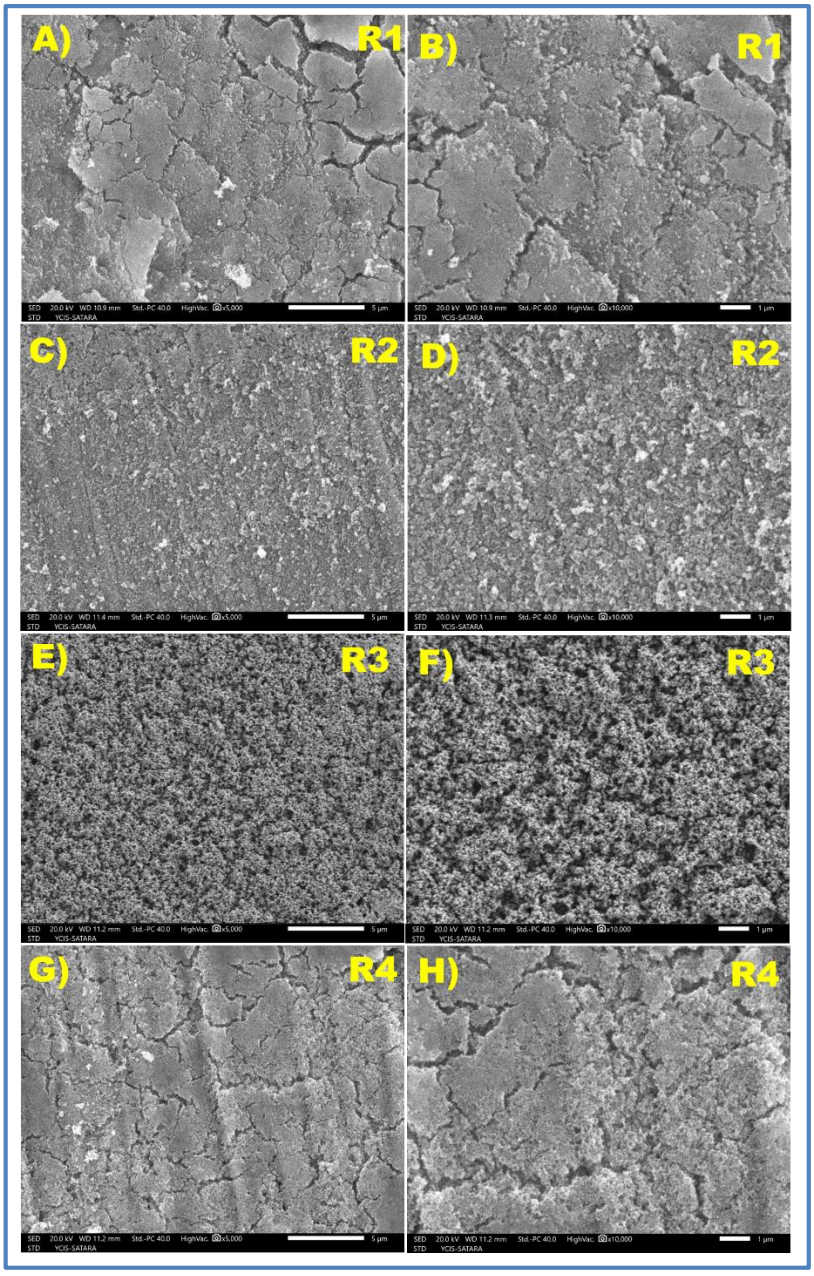

Figure 3.6: The SEM images of R1 (A, B), R2 (C, D), R3 (E, F), and R4 (G, H) electrodes at two (5 KX and 10 KX) magnifications, respectively.

The morphology of the electrode material has a significant impact on the performance of active materials. Interestingly, the formation of the microstructure is observed to be dependent on the ratio of atomic concentration during film development. The SEM images of R1 to R4 electrodes at two magnifications (5 KX and 10KX) are presented in **Figure 3.6 A-H**. From the **Figure 3.6 (A and B)** the surface of R1 electrode depicts cracks, and randomly ordered agglomerates develop a rough surface. **Figure 3.6 (C and D)**, R2 electrode shows large number of voids of average size 1 μm between the lichen-like structure and spherical structure **[36]**. For R3 electrode, compact mud-like structure with well covered granules nanoparticles is grouped together to form agglomerates making film porous and spongy **Figure 3.6 (E and F) [23]**. **Figure 3.6 (G and H)** show a dense surface of R4 electrode with cracks. The surface looks rough due to the pronounced presence of nanoparticle agglomerates. Different morphologies are produced when nanoparticles are combined to form clusters. The micrographs clearly show agglomerated particles had an undefined shape and were unable to resolve at high magnification **[35]**. Different morphologies are the consequence of the rate of nucleation formation being affected by the number of deposition cycles. Most importantly, in RuO_2 thin film nanoparticles agglomerates help efficiently to carry charges from the active material to the current collector.

3.4.5 EDAX study:

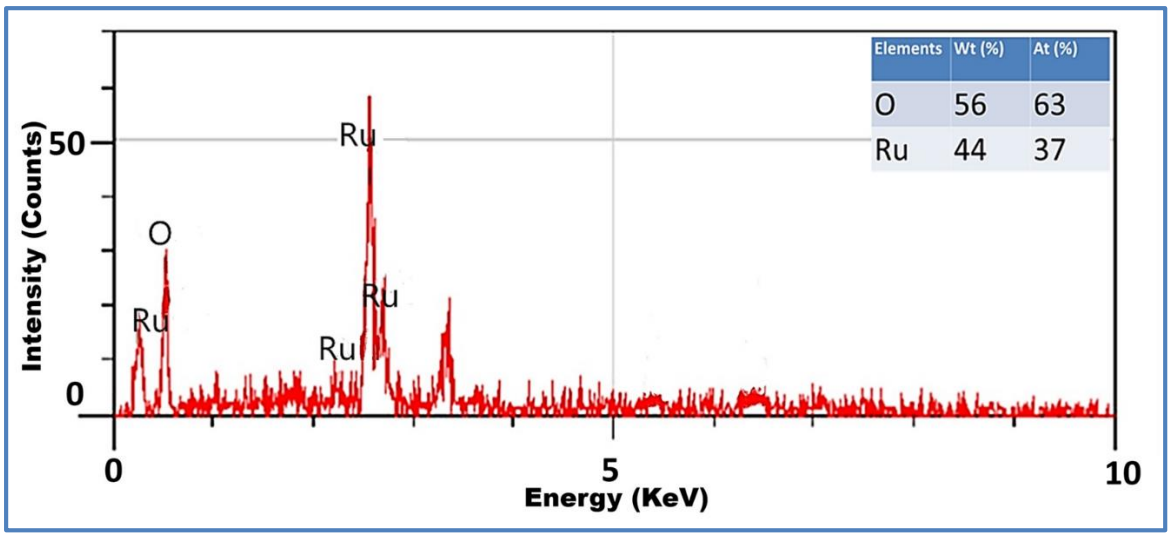

Figure 3.7: The EDAX spectrum of R3 film.

The elemental analysis of RuO_2 thin film was carried out using EDAX analysis to confirm its chemical composition. The EDAX spectrum of R3 film **(Figure 3.7)** reaffirms the presence of oxygen (O) and ruthenium (Ru). The measured atomic percentages of O and Ru elements in R3 film are 63 and 37%, respectively. From EDAX analysis, the formation of RuO_2 thin film was confirmed.

3.4.6 Contact angle analysis:

The wettability characteristic is important for thin film electrodes employed for SC applications. The contact angles for R1, R2, R3, and R4 thin films are of 74°, 53°, 28°, and 33°, respectively **(Figure 3.8 A-D),** which signify a hydrophilic character, with the lowest contact angle for R3, suggesting the highest wettability. The water contact angle decreases as deposition cycle increase up to 250 cycles (R3) film due to morphological changes **[37, 38]**.

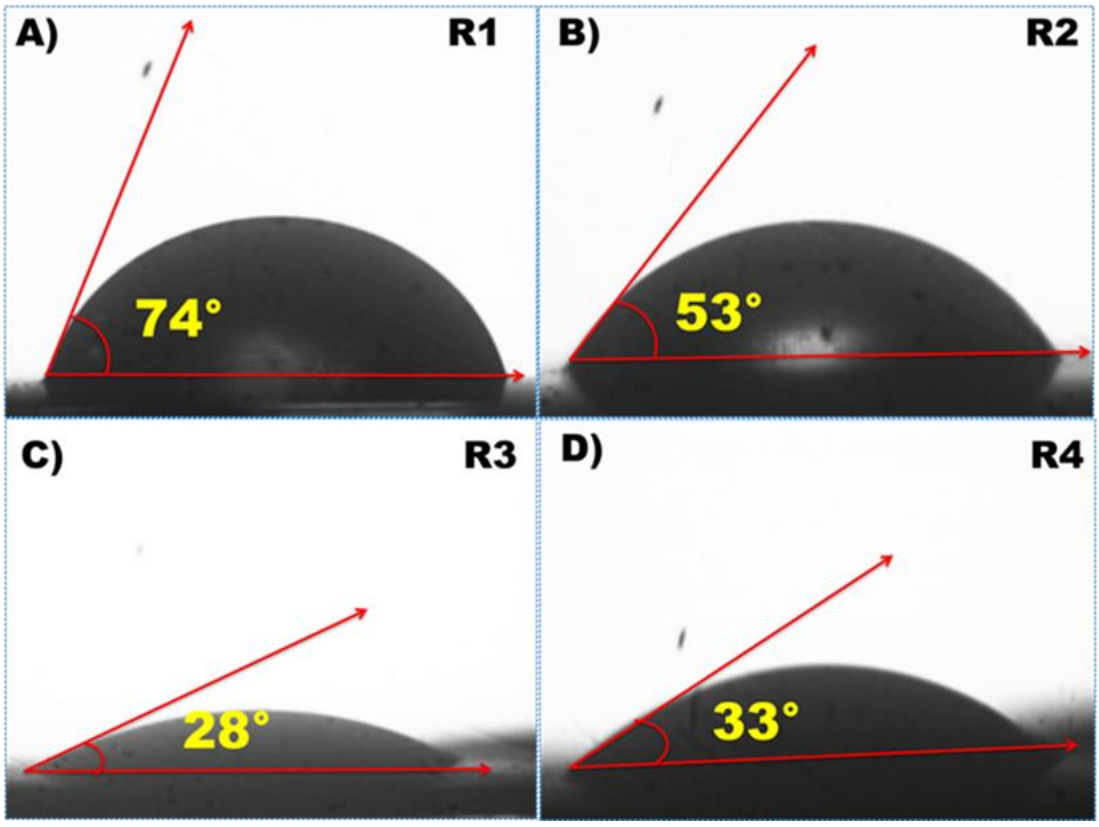

Figure 3.8: The contact angle images of A) R1, B) R2, C) R3, and D) R4.

3.5 Electrochemical study of RuO_2 thin films:

3.5.1 CV study:

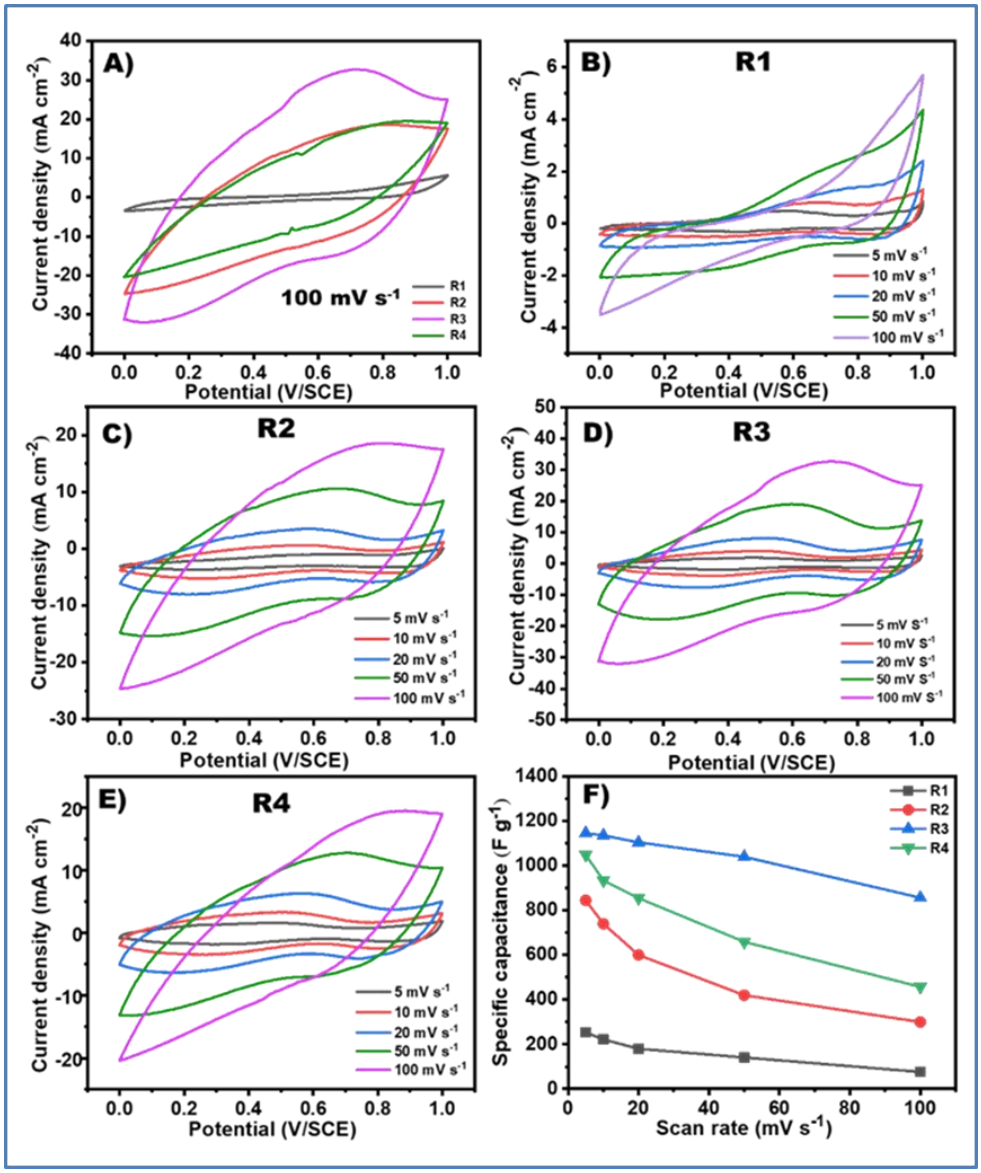

Figure 3.9: A) The comparative CV curves of R1-R4 electrodes at a scan rate of 100 mV s^{-1}, the CV curves of (B-E) R1, R2, R3, and R4 electrodes at scan rates of 5-100 mV s^{-1}, and F) the variation of C_s with various scan rates of R1- R4 electrodes.

The electrochemical properties of RuO_2 electrodes were studied using an electrochemical analyzer (Zive MP1) in 1 M H_2SO_4 electrolyte, with a potential range of 0 to +1.0 V/SCE. The comparative CV curves of R1, R2, R3, and R4 electrodes at the scan rate of 100 mV s^{-1} are shown in **Figure 3.9 A.** It is observed that R3 electrode has a larger area under CV curve with highest peak current as compared to other R1, R2, and R4 electrodes, resulting high charge storage capability. The reversible redox processes involved electron transfer between the electrode and electrolyte. Surface redox capacitance refers to the adsorption of H^+ ions from the

acidic electrolyte over the electrode surface. The redox reaction of amorphous RuO_2 in the acidic electrolyte is,

$$RuO_x\,(OH)_y \; + \; \delta_H^+ + \delta_{\bar{e}}^- \rightarrow RuO_{x-\delta}\,(OH)_{y+\delta} - \qquad (0 \leq \delta \leq 2) \qquad (3.7)$$

RuO_2 has high C_s due to the pseudocapacitive effect caused by the rapid double insertion and release of both protons and electrons during the RuO_2 redox reaction. Because protons may easily intercalate into RuO_2 amorphous structure which significantly determines the capacitive performance. The CV curves of R1, R2, R3, and R4 performed at various scan rates ranging between 5 - 100 mV s^{-1} are shown in **Figure 3.9 B-E**. At 5 mV s^{-1} scan rate, the C_s values for R1, R2, R3, and R4 electrodes are 253, 845, 1146, and 1049 F g^{-1}, respectively as shown in **Figure 3.9 F**. The R3 electrode has the maximum capacitance due to optimal mass deposition.

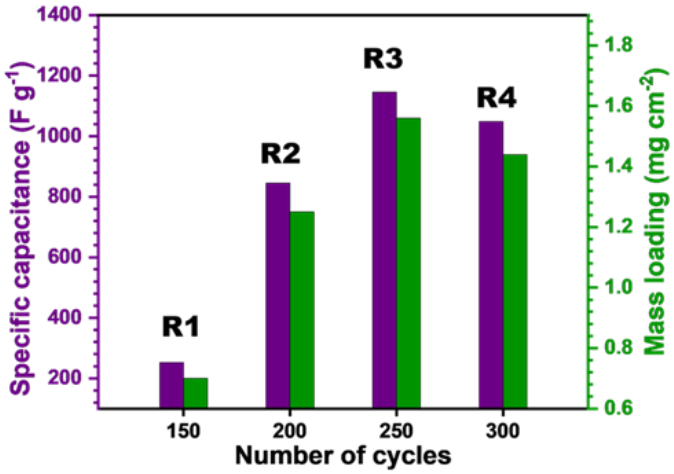

Figure 3.10: Graph of mass loading variation versus number of deposition cycles versus specific capacitance of RuO_2 thin films

The variation of specific capacitance of RuO_2 electrodes with mass loading is shown in **Figure 3.10.** Proton intercalation into the bulk material resulted in superior material efficiency at high active mass loading. As mass loading increases, the amount of material available for redox reactions increases. However, the amount of material undergoing redox reactions also depends on morphology and porosity of the material. Therefore, optimized mass loading with appropriate morphology can provide higher specific capacitance. The mass loading of R3 is highest, compared to other prepared electrodes. The C_s of R3 electrode was 1146 F g^{-1} at an active mass loading of 1.56 mg cm^{-2}. Similar report highlighting C_s rise with active mass increment was reported previously **[39]**. The asymmetrical pattern of CV curves supports to existence of a pseudocapacitive type charge storage mechanism **[40]**.

The contribution of the capacitive and diffusion processes is inversely correlated with aggregate sum charge stored by the electrode. In the course of the diffusion charge storage process, electrolyte ions are introduced into the electrode structure to undergo a redox reaction. In order to store electrical energy in capacitance, electrolyte ions must electro-adsorb to the electrode surface followed by surface redox reactions. The charge storage mechanism is explained using the power law equation,

$$i_p = a\upsilon^b \qquad (3.6)$$

where, i (mA) is the peak current and υ (mV s^{-1}) represents the scan rate, and "a" and "b" are coefficients If b ≅ 0.5, the maximum charge storage is due to diffusion-controlled processes; if b ≅ 1, the maximum charge storage is due to capacitive processes. The values of "b" as 0.75 for R3 thin film electrode indicates that the maximum amount of charge stored is through the capacitive process **Figure 3.11 A.**

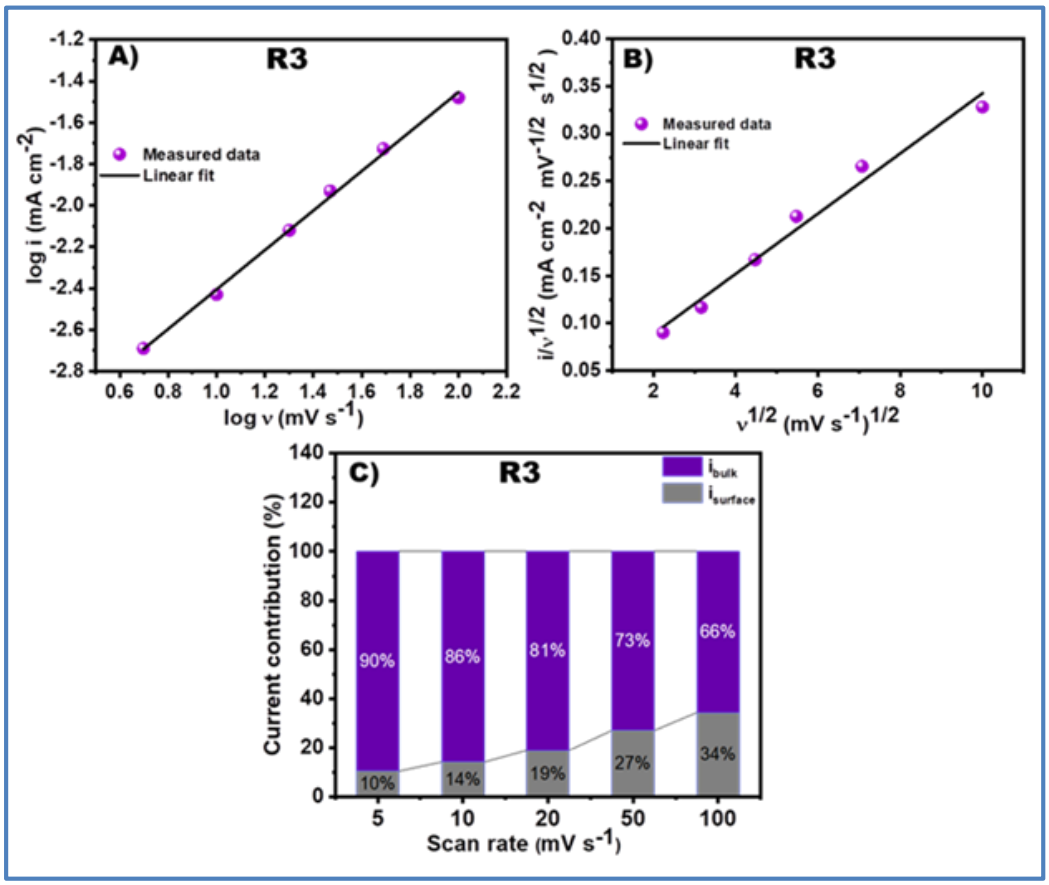

Figure 3.11: A) Plot of log i versus log υ, B) plot of $i/\upsilon^{1/2}$ versus $\upsilon^{1/}2$, and C) percentage current contribution of capacitive and diffusion mechanisms for R3 electrode.

Further analysis of the CV was done using modified eq. (3.6), as shown below, to precisely define significance of the capacitive and diffusion-controlled processes to the entire current response **[41]**.

$$i(\upsilon) = k_1\upsilon + k_2\upsilon^{1/2} = i_{\text{surface}} + i_{\text{bulk}} \qquad (3.7)$$

where, the contributions from the capacitive process and the diffusion-controlled process respectively, are denoted by $k_1\upsilon$ and $k_2\upsilon^{1/2}$. As shown in **Figure 3.11 B**, the slope and intercept of the linear fit of the graph of $i/\upsilon^{1/2}$ vs. $\upsilon^{1/2}$ yield values of k_1 and k_2, respectively. For various R series electrodes, the computed capacitive and diffusion-controlled currents from eq. (3.7). Percentage contributions in total current from capacitive and diffusion-controlled charge storage kinetics are shown in **Figure 3.11 C** for R3 electrode. It is clear that the contribution from the diffusion-controlled process rises with decreasing scan rate, leading to a higher value of C_s. Capacitive processes in the R3 electrode store about 34% of the charge at a scan rate of 100 mV s^{-1}, which drops to 10% at a scan rate of 5 mV s^{-1}. **[42, 43]**.

3.5.2 GCD study:

Further, the GCD measurement of prepared RuO_2 electrodes was performed at different current densities between 1-5 mA cm^{-2} over working potential window from 0 to +1.0 V/SCE. **Figure 3.12 A** shows the comparative GCD graphs of RuO_2 electrodes at current density of 1 mA cm^{-2}. The quasi triangular nature of the GCD curves indicated that the pseudocapacitive behaviour of RuO_2 electrode in 1 H_2SO_4 electrolyte. The exceptional charge storage capacity of the R3 electrode is demonstrated by its longer charging-discharging time period compared to other electrodes. The GCD studies for RuO_2 electrodes at various current densities of 1-5 mA cm^{-2} are shown in **Figure 3.12 B-E**. From GCD plots, the obtained capacitances of R1 to R4 electrodes are 165, 735, 930, and 800 F g^{-1} at 1 mA cm^{-2} current density, respectively. The charge/discharge time period increased during the GCD cycling test at the lower current density because the ions may completely fill the active sites between the electrode and electrolyte interface. It happens due to ions occupy a partial number of active sites between the electrode and electrolyte interface. R1 and R2 electrodes show the ohmic drop at low current densities, which is generally related to an internal resistance of the electroactive film. This internal resistance is closely attributed to the slow electron and ion transport rate due to morphologies that cause a decrease in the supercapacitive performance **[44]**. **Figure 3.12 F** displays the plots of

C_s vs applied charging current density for all RuO_2 electrodes. The capacitance decrease with the current density increment was attributed to the presence of inner active sites that are unable to undergo the redox transitions completely at higher current densities **[45, 46]**. The highest capacitance is found in the R3 electrode due to excellent mass deposition and optimized surface area, facilitating better electrolyte penetration and efficient redox reactions **[47-49]**.

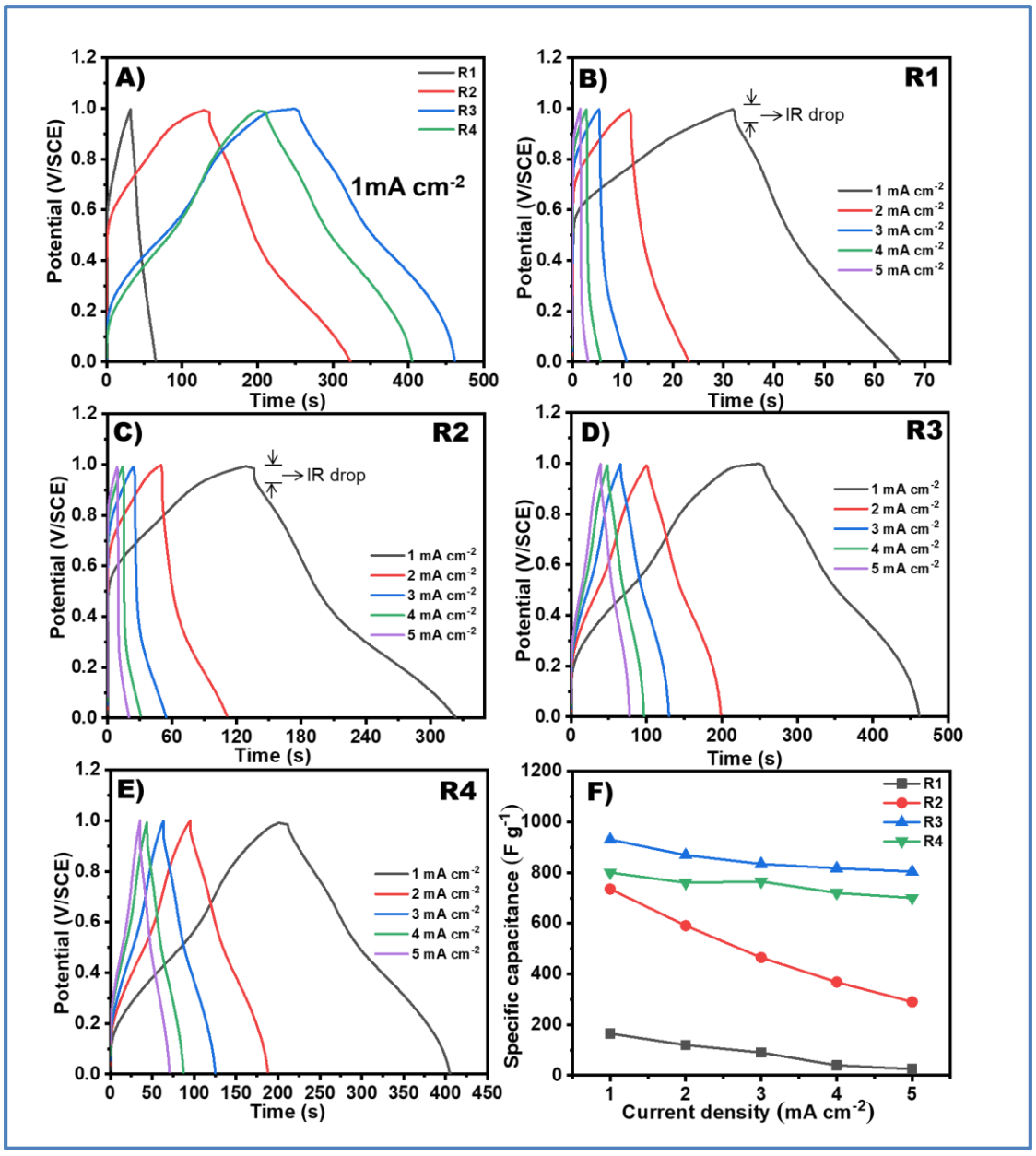

Figure 3.12: A) The comparative GCD curves of R1-R4 electrodes at a current density of 1 mA cm^{-2}, the GCD curves of (B-E) R1, R2, R3, and R4 electrodes at different current densities of 1-5 mA cm^{-2}, and F) the variation of C_s with current densities for R1- R4 electrodes.

3.5.3 EIS and stability study:

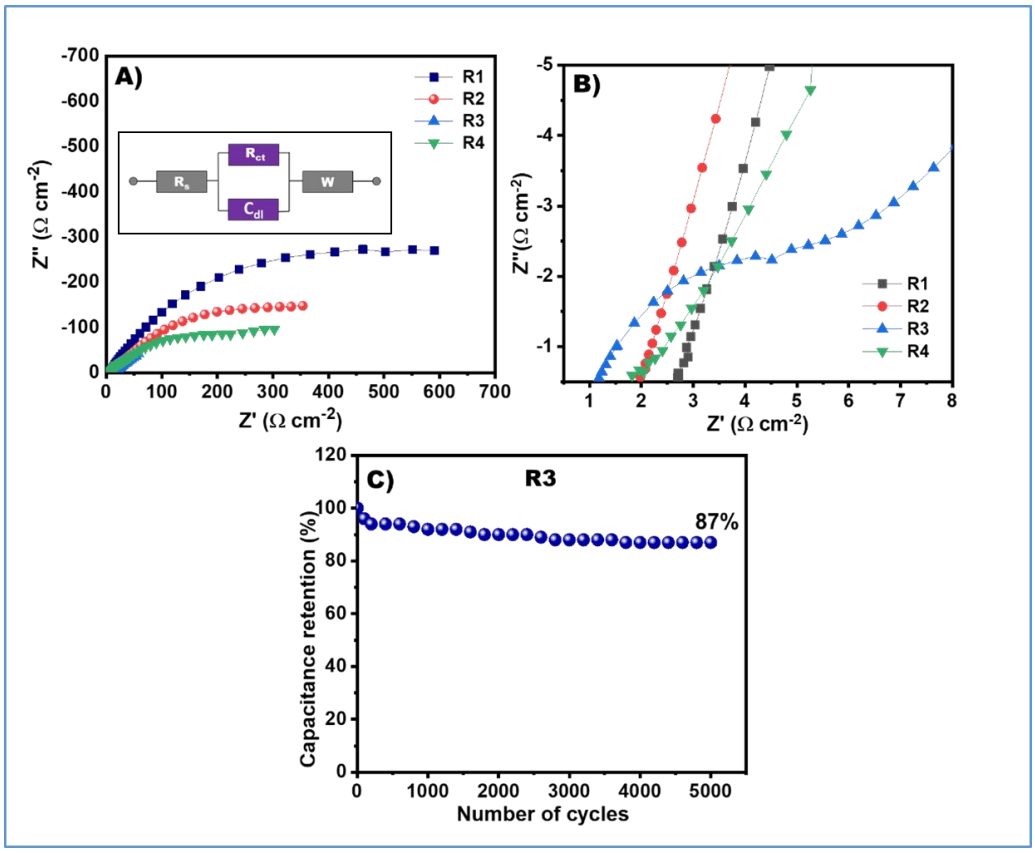

Figure. 3.13 A) The Nyquist plots of RuO_2 films (inset shows the fitted equivalent electrical circuit), B) the enlarged view of Nyquist plots of RuO_2 films, and C) the graph of specific capacitance retention with a number of cycles.

The resistance characteristics of the electrodes are crucial to the charge storage mechanism. In the Nyquist plot **(Figure 3.13 A and B),** semicircle in high-frequency region shows the charge transfer resistance (R_{ct}) due to faradaic reactions and double-layer capacitance at electrode/electrolyte interface. The straight line in the low frequency region, which corresponds to Warburg impedance (W), is caused by electrolytic ion diffusion in the active material **[50]**. The solution resistance (R_s), which combines the resistance of the electrolyte and the contact resistance at the electrode-electrolyte interface, is calculated by pointing the intersection of the Nyquist plot to the real impedance axis. The Nyquist plots of R1, R2, R3, and R4 electrodes are shown in **Figure 3.13 A** and inset depicts well fitted equivalent circuit. The enlarged view of the plots is shown in **Figure 3.13 B.** The R3 electrode shows smaller R_s (0.9 Ω cm^{-2}) and R_{ct} (6.7 Ω cm^{-2}) than R1, R2, and R4 electrodes. The

values of each fitted circuit parameters are summarized in **Table 1**. The smaller of R_s and R_{ct} values for R3 indicate feasible interaction between electrolyte and active material, responsible for higher electrochemical performance than R1, R2, and R4 **[51]**. The long-term cycling stability of R3 electrode examined at 100 mV s^{-1} for 5,000 CV cycles is shown in **Figure 3.13 C**. For R3 electrode, a capacitive retention of 87% is observed. As a result of the ionic pathway of electrolytic ions diffusing electro active sites in the bulk electrode, capacitance values decrease in correlation with an increase in CV cycles.

Table 3.1: Impedance value of RuO_2 electrodes.

Electrodes	R_s **(Ω** cm^{-2}**)**	R_{ct} **(Ω** cm^{-2}**)**	C_{dl} **(F)**	W **(cm Ω)**
R1	2.2	75	0.741	9
R2	1.5	38	0.634	5
R3	0.9	6.7	0.523	2
R4	1.2	32	0.924	4

3.6 Conclusions:

In this work, amorphous RuO_2 thin films of different thicknesses were successfully synthesized by successive ionic layer adsorption and reaction (SILAR) method. Morphology analysis proved that RuO_2 thin films are porous. The electrochemical properties of RuO_2 electrodes were studied in 1 M H_2SO_4 electrolyte. R3 electrode achieved maximum specific capacitance of 1146 F g^{-1} at a 5 mV s^{-1} due to optimum mass deposition (1.56 mg cm^{-2}) and after 5,000 CV cycles, 87% of capacitance was retained. In comparison to other electrodes, the EIS measurement demonstrated that porous R3 electrode has a low charge transfer resistance, allowing for easy access to ions for surface redox reactions.

References:

[1] D. Dubal, N. Chodankar, D. Kim, P. Gomez-Romero, Chem. Soc. Rev., 47, (2018), 2065-2129.

[2] J. Zhou, J. Yu, L. Shi, Z. Wang, H. Liu, B. Yang, C. Li, C. Zhu, J. Xu, Small, 14, (2018), 1803786-1803795.

[3] Y. Jiao, A. M. Hafez, D. Cao, A. Mukhopadhyay, Y. Ma, H. Zhu, Small, 14, (2018), 1800640-1800660.

[4] Y. Huang, F. Cui, J. Bao, Y. Zhao, J. Lian, T. Liu, H. Li, J. Mater. Chem A, 7, (2019), 20778-20789.

[5] N. Chodankar, G. Raju, B. Park, P. Shinde, S. Jun, D. Dubal, Y. Huh, Y. Han, J. Mater. Chem. A, 8, (2020), 5721-5733.

[6] X. He, W. Yang, X. Mao, L. Xu, Y. Zhou, Y. Chen, Y. Zhao, Y. Yang, J. Xu, J. Power Sources, 376, (2018), 138-146.

[7] K. Karuppasamy, D. Vikraman, S. Hussain, P. Santhoshkumar, R. Bose, P. Sivakumar, A. Alfantazi, J. Jung, H. Kim, Small, 18, (2022), 2107284-2107297.

[8] K. Karuppasamy, D. Vikraman, S. Hussain, G. Veerasubramani, P. Santhoshkumar, S. Lee, R. Bose, A. Kathalingam, H. Kim, Chem. Eng. J., 427, (2022), 131535-131549.

[9] P. Santhoshkumar, D. Vikraman, S. Hussain, K. Karuppasamy, A. Kathalingam, H. Kim, J. Alloys Compd., 928, (2022), 167215-167226.

[10] S. Suthakaran, S. Dhanapandian, N. Krishnakumar, N. Ponpandian, P. Dhamodharan, M. Anandan, Mater. Sci. Semicond., 111, (2020), 104982-104995.

[11] A. Muzaffar, M. Basheer Ahamed, K. Deshmukh, J. Thirumalai, Renewable Sustainable Energy Rev., 101, (2019), 123-145.

[12] S. Choudhury, G. Vignaud, P. Dubreuil, B. Assresahegn, D. Guay, D. Pech, Nanotechnology., 33, (2022), 495404-495413.

[13] S. Sayyed, M. Mahadik, A. Shaikh, J. Jang H. Pathan, ES Energy Environ., 3, (2019), 25–44.

[14] S. Khot, D. Malavekar, R. Nikam, S. Ubale, P. Bagwade, D. Patil, V. Lokhande, C. Lokhande, Synth. Met., 287, (2022), 117075-117088.

[15] D. Majumdar, Mater. Sci. Res., 15, (2018), 30-40.

[16] Y. Yan, T. Wang, X. Li, H. Pang, H. Xue, Inorg. Chem. Front., 4, (2017), 33-51.

[17] P. Makkar and N. Ghosh, Ind. Eng. Chem. Res., 60, (2021), 1666-1674.

[18] C. Mevada and M. Mukhopadhyay, J Energy Storage, 30, (2020), 101453-101466.

[19] P. Wang, H. Liu, Y. Xu, Y. Chen, J. Yang, Q. Tan, Electrochim. Acta**,** 194, (2016), 211-218.

[20] R. Thangappan, M. Arivanandhan, R. Kumar, R. Jayavel, J. Phys. Chem. Solids., 121, (2018), 339-349.

[21] P. Deshmukh, S. Pusawale, A. Jagadale, C. Lokhande, J. Mater. Sci., 47, (2012), 1546–1553.

[22] D. Dubal, G. Gund, R. Holze, H. Jadhav, C. Lokhande, C. Park, Electrochim. Acta, 103, (2013), 103–109.

[23] V. Shankar, P. Kumar, D. Govindarajan, P. Nethaji, G. Balji, Sustain. Energy Technol. Assess., 53, (2022), 102444-102453.

[24] Q. Li, Y. Xu, S. Zheng, X. Guo, H. Xue, H. Pang, Small, 14, (2018), 1800426-1800445.

[25] S. Yan, K. Abhilash, L. Tang, M. Yang, Y. Ma, Q. Xia, Q. Guo, H. Xia, Small, 15, (2019), 1804371-1804401.

[26] C. Lokhande, D. Dubal, O. Joo, Curr. Appl. Phys., 11, (2011), 255-270.

[27] F. Shi, L. Li, X. Wang, C. Gu, J. Tu, RSC Adv., 4, (2014), 41910-41921.

[28] R. Prataap, R. Arunachalam, R. Raj, S. Mohan, L. Peter, Curr. Appl. Phys., 18, (2018), 1143-1148.

[29] J. Theerthagiri, K. Karuppasamy, G. Durai, A. Rana, P. Arunachalam, K. Sangeetha, P. Kuppusami, H. Kim, Nanomaterials, 19, (2018), 256-284.

[30] S. Pusawale, P. Deshmukh, P. Jadhav, C. Lokhande, Mater Renew Sustain Energy, 8, (2019), 1-9.

[31] Y. Xie and C. Yao, Mater. Res. Express., 22, (2020), 125550-125562.

[32] D. Pawar, D. Malavekar, S. Khot, A. Bagde, C. Lokhande, Mater. Sci. Eng. B, 292, (2023), 116432-116448.

[33] S. Korkmaz, A. Kariper, C. Karaman, O. Karaman, Scientific reports, 27, (2022), 12-20.

[34] S. Kannan and M. Sundrarajan, Adv. Powder Technol., 26, (2015), 1505-1511.

[35] R. Ingole, B. Fugare, B. Lokhande, J. Mater. Sci.: Mater. Electron, 15, (2017), 16374-16383.

[36] A. Thakur, H. Pathan, B. Lokhande, ES energy environ., 15, (2022), 18, 75-89.

[37] V. Mane, S. Kale, S. Ubale, V. Lokhande, U. Patil, C. Lokhande, J. Solid State Electrochem., 25, (2021), 1775-1788.

[38] S. Gavande, P. Kulkarni, V. Patil, B. Karche, S. Gavande, Macromol Symp., 339, (2020), 2000169-2000175.

[39] R. Chen, M. Yu, R. Sahu, K. Puri, I. Zhitomirsky, Adv. Energy Mater., 10, (2020), 1903848-1903881.

[40] D. Patil, D. Malavekar, V. Lokhande, P. Bagwade, S. Khot, T. Ji, C. Lokhande, Energy Technol., 10, (2022), 2200295-2200310.

[41] A. Kumar, J. Mol. Struct., 1220, (2020), 128654-128680.

[42] P. Bagwade, D. Malavekar, T. Ghogare, S. Ubale, V. Mane, R. Bulakhe, I. In, C. Lokhande, J. Alloys Compd., 859, (2021), 157829-157848.

[43] Y. Huang, Y. Gao, C. Liu, Z. Cao, Y. Wang, Z. Li, Y. Yan, M. Zhang, G. Cao, J. Phys. Chem. C, 123, (2019), 30067-30076.

[44] R. Oliveira, C. Santos, J. Garcia, M. Vidotti, L. Marchesi, C. Pessoa, J. Electroanal. Chem., 878, (2020), 114662-114668.

[45] R. Kotz and M. Carlen, Electrochim. Acta, 45, (2000), 2483–2498.

[46] L. Kang, S. Sun, L. Kong, J. Lang, Y. Luo, Chin Chem Lett., 25, (2014), 957-961.

[47] K. Brousse, S. Pinaud, S. Nguyen, P. Fazzini, R. Makarem, C. Josse, Y. Thimont, B. Chaudret, P. Taberna, M. Respaud, P. Simon, Adv. Energy Mater., 10, (2020), 19033136-19033145.

[48] S. Jeon, J. Jeong, H. Yoo, H. Yu, B. Kim, M. Kim, ACS Appl. Nano Mater., 3, (2020), 3847-3858.

[49] A. Raja, N. Son, M. Swaminathan, M. Kang, J. Taiwan Inst. Chem. Eng., 138, (2022), 104471-104483.

[50] S. Marje, V. Patil, V. Parale, H. Park, P. Shinde, J. Gunjakar, C. Lokhande, U. Patil, Chem. Eng. J., 429, (2022), 132184-132199.

[51] E. Petrucci, F. Porcelli, M. Orsini, S. De Santis, G. Sotgiu, Metals, 12, (2022), 316-328.

CHAPTER-IV

SYNTHESIS AND CHARACTERIZATION OF REDUCED GRAPHENE OXIDE (rGO)/RUTHENIUM OXIDE (RuO_2) ELECTRODE USING SUCCESSIVE IONIC LAYER ADSORPTION AND REACTION (SILAR) METHOD

CHAPTER-IV

SYNTHESIS AND CHARACTERIZATION OF REDUCED GRAPHENE OXIDE (rGO)/RUTHENIUM OXIDE (RuO_2) ELECTRODES USING SUCCESSIVE IONIC LAYER ADSORPTION AND REACTION (SILAR) METHOD

4.1 Introduction:

The growing need for electrical energy storage is also fueled by advancements in electronic devices. Batteries and supercapacitors are widely used, offering complementary storage mechanisms **[1-2]**. Supercapacitive materials have been classified into two primary categories: electric double-layer capacitors (EDLCs) and pseudocapacitors **[3-5]**. In general, carbon allotropes with dimensions ranging from one to three dimensions, like carbon quantum dots (CQDs), carbon nanotubes (CNTs), and foams, exhibit characteristics of electric double-layer capacitors (EDLCs). Carbon electrodes are widely used in various electrochemical applications, including electrochemical double-layer capacitors (EDLCs), electrolysis, and certain types of batteries. These electrodes are made from carbon-based materials and are valued for their unique properties, which include high electrical conductivity, stability, and a variety of available structures **[6]**. The ability to store charge at the interface between the electrode and electrolyte. The electrochemical reactions that occur at the carbon electrode/electrolyte interface in EDLCs involve the physical adsorption and desorption of ions on the carbon surface, leading to the formation of an electric double layer **[7-9]**. On the other hand, transition metal compounds are typically categorized as pseudocapacitors. Transition metal compounds offer high energy density whereas EDLC materials provide excellent power density as well as stability.

In the past decade, graphene has been one of the most explored materials for supercapacitor application. In graphene, sp^2 hybridized carbon atoms are connected to each other hexagonally. It possesses an impressive surface area (~2600 m^2 g^{-1}), electrochemical stability, mechanical strength, and thermal stability, and showcases good electrical transport properties that make it highly suitable for utilization in supercapacitors **[10]**. Particularly, graphene exceeds CNTs, carbon fibers, and activated carbons in terms of electrochemical properties for supercapacitor applications **[11]**. However, it has a relatively low energy density. The reduced graphene oxide (rGO) exhibits a higher number of active centers for charge storage due to the presence of interconnected functional groups **[12]**. Hence, with moderate electrical properties, rGO has emerged as the preferred option. To enhance the surface area, manipulate surface texture, and ensure favorable electrochemical stability, rGO has been composited with several transition metal compounds **[13-16]**. Ruthenium

oxide (RuO_2) has been widely investigated, especially in the fields of electrochemistry and energy storage systems like supercapacitors. It is a useful candidate for a number of applications because of its remarkable electrochemical characteristics, which include high capacitance, good reversibility, and stability. The physicochemical properties behavior of $RuO_2.xH_2O$ can be modulated to improve electrochemical performance **[17-21]**.

4.2 Synthesis of rGO, rGO/RuO_2 thin films:

4.2.1 Experimental section:

4.2.1.1 Chemicals and Materials:

The analytical reagent grade Ruthenium trichloride ($RuCl_3.xH_2O$) and sodium hydroxide (NaOH) were purchased from SRL Chemicals LTD, and utilized as received. To produce GO, graphite flakes were purchased from Sigma-Aldrich. The substrate was a stainless steel (SS) sheet (304 grade).

4.2.1.2 Synthesis of rGO film:

The GO suspension was formed by exfoliating graphite, and then a chemical reduction method was used to produce rGO **[22-25]**. Schematic representation of rGO production process is depicted in **Figure 4.1**. The previously described process was used in the preparation of GO suspension. In a 500 mL conical flask, 2 g of graphite flakes with an average diameter of 100 μm and 100 mL of concentrated H_2SO_4 were added. The mixture was then held in an ice bath with constant stirring until 1 g of sodium nitrate ($NaNO_3$) was added. To keep the reaction temperature below 293 K, 8 g of potassium permanganate ($KMnO_4$) was gradually added to this mixture. Afterwards the completion of the addition, for 12 h the reaction mixture was constantly stirred at the ambient temperature. 100 mL of DDW was added after 1.5 h, and then 300 mL of DDW and 8 mL of 30% hydrogen peroxide (H_2O_2). As a result, the solution becomes yellowish. Subsequently, the mixture was repeatedly washed with 5% HCl and DDW until the pH reached 6.5. The GO slurry concentration was measured by use of the gravimetric weight difference method. For GO reduction, hydrazine hydrate (N_2H_4) (reducing agent) was employed. 500 mL of GO solution with a density of 1 mg mL^{-1} was heated for 2 h at 368 K with 2.5 mL of N_2H_4 added. The residue was repeatedly cleaned with DDW after the reaction was

finished, and it was then vacuum dried at 323 K. The rGO powder was utilized to deposit and characterize thin films **[26, 27]**.For the production of rGO films, a stainless steel (SS) substrate was chosen due to its durability and compatibility with rGO. The SS substrate was immersed in the rGO solution for 40 seconds, allowing the rGO sheets to adhere to its surface. After immersion, the substrate was dried for 60 seconds at 323 K to ensure the rGO layer was securely attached. This immersion and drying cycle was repeated 170 times to gradually build up the rGO film, layer by layer. Schematic representation of rGO production process is depicted in **Figure 4.1**.

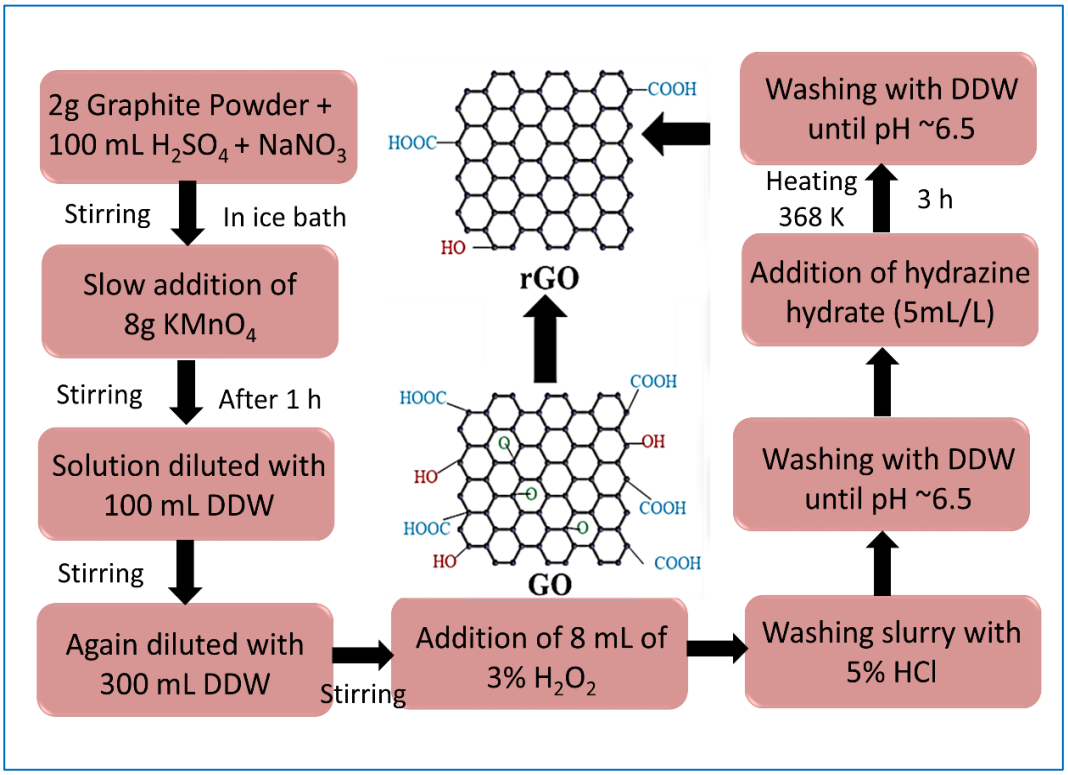

Figure 4.1: Schematic flow chart of rGO synthesis.

4.2.1.3 Synthesis of rGO/RuO_2 thin film:

The SILAR process used to deposit the rGO/RuO_2 composite thin film is depicted in **Figure 4.2**. For the formation of rGO/RuO_2 composite films, first beaker containing rGO suspension of 1 mg mL^{-1} was utilized. The SS substrate was dipped in rGO solution for 40 s and then dried for 60 s in air at ambient temperature. Afterwards, the same procedure of RuO_2 thin film deposition was repeated as previously described in chapter III section 3.2.2.3. These deposition cycles develop a homogenous layer of rGO/RuO_2 composite thin film. A schematic illustration of

rGO/RuO_2 composite structure is shown in **Figure 4.2 B**. The mass loading of synthesized films was calculated in terms of the mass deposited on the substrate using the gravimetric weight difference approach. The deposited mass increased from 130 to 170 cycles achieving a maximum of 0.58 mg cm^{-2}. After 170 cycles, the mass loading subsequently decreased due to the overgrowth of rGO/RuO_2, which caused the film to collapse. Increases in film thickness results in an increase in mass deposited on the substrate, which lowers substrate tension and causes the overgrown mass to peel off **[29]**. rGO provides a high surface area and a conductive framework, reducing the need for a thick RuO_2 layer. This leads to optimized mass loading at 170 cycles, as the rGO supports the active RuO_2 material effectively.

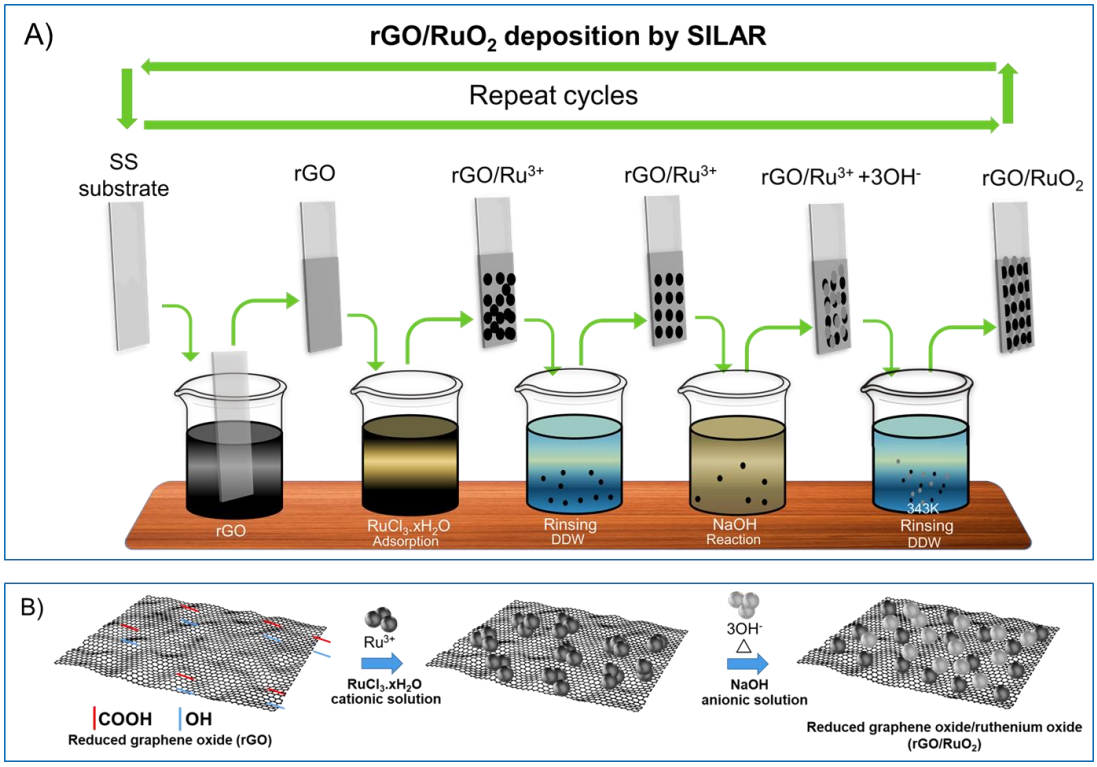

Figure 4.2: A) Schematic of SILAR method for deposition of rGO/RuO_2 thin film, and B) the schematic illustration of the formation of rGO/RuO_2 composite.

4.3 Electrochemical measurement:

The potentiostat (Zive MP1) was utilized to evaluate the supercapacitive characteristics of electrodes. The standard three-electrode system comprising reference electrode (saturated calomel electrode), counter electrode (platinum sheet), and working electrode (rGO and rGO/RuO_2 thin films) with area of active material

(1×1 cm^2) were used for electrochemical measurements. The electrochemical techniques such as voltammetry and chronopotentiometry were used to obtain CV and GCD curves in the 0 to 1 V/SCE potential window, respectively. These all electrodes were tested in 1 M H_2SO_4 electrolyte. EIS measurements have been performed with a 10 mV potential amplitude. The following relations were used to calculate C_s from CV and GCD measurements:

4.4 Results and discussion:

4.4.1 XRD study:

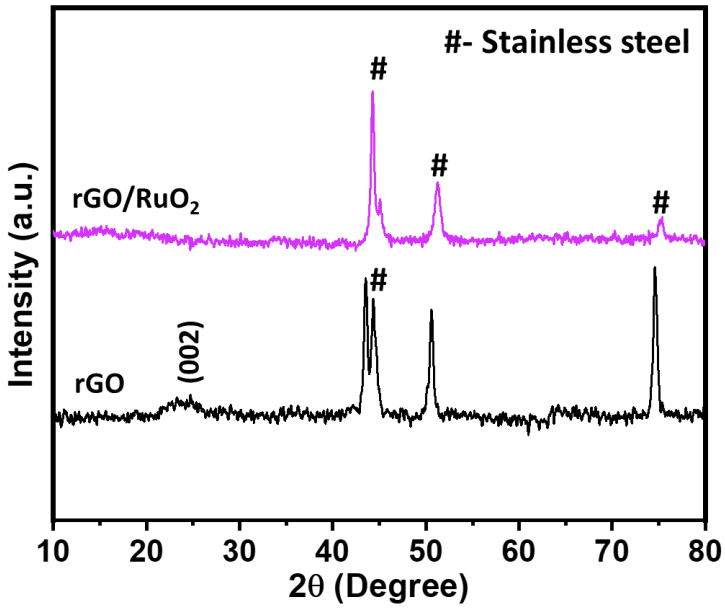

Figure 4.3: The XRD patterns of rGO and rGO/RuO_2 thin films.

The structural analysis of rGO and rGO/RuO_2 films was investigated through an X-ray diffraction technique in the range from 10° to 80°. **Figure 4.3** depicts the XRD patterns of rGO and rGO/RuO_2 composite electrodes. It does not reveal any desirable material peaks rather than using the (#) sign to denote SS peaks, confirming that rGO/RuO_2 sample is amorphous **[16, 30]**. However, the diffraction peak at 24° corresponds to (002) plane of graphite, according to PDF No. 41-1487. The absence diffraction peak in rGO/RuO_2 is due to the sandwiched growth of amorphous RuO_2 between successive layers of rGO and the low amount of rGO in rGO/RuO_2 composite **[31, 32]**. However, the presence of rGO in rGO/RuO_2 composite was confirmed by Raman and XPS analyses. Amorphous thin films are produced by the disorganized arrangement of the particles in the composite films deposited at ambient

temperature when mobility is reduced **[33]**. The resultant amorphous nature of rGO/RuO_2 composite film offers advantages like easy paths for ions to intercalate and de-intercalate due to high permeability, and excellent elasticity allowing the fabrication of flexible supercapacitor **[34]**.

4.4.2 Raman study:

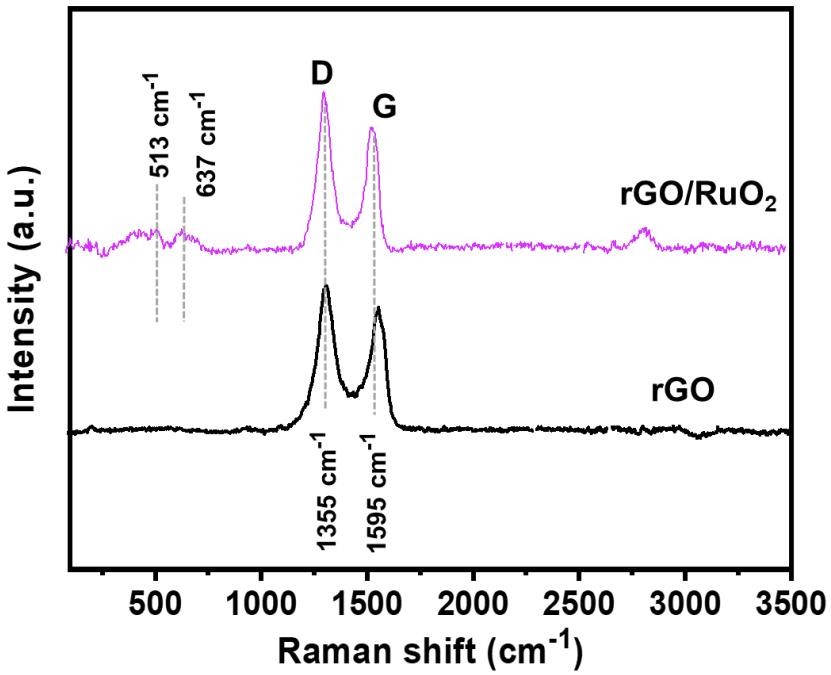

Figure 4.4: Raman spectra of rGO and rGO/RuO_2 thin films.

Raman spectroscopy reveals useful information on the structural characteristics and carbon hybridization of the materials under investigation. In Raman spectra (**Figure 4.4 C**), the wide peaks observed at 513 and 637 cms^{-1} are attributed to E_g and A_{g1} modes of rGO/RuO_2, respectively. Additionally, the Raman spectra of rGO, rGO/RuO_2 depicts a peak at 1355 cm^{-1}, which is ascribed to the D-band (disorder and defect), and the peak at 1595 cm^{-1} is ascribed to the G-band (degree of graphitization) **[35]**. In a regular honeycomb structure of graphene, sp^3 and sp^2 hybridized carbon atoms are responsible for the D and G bands in Raman spectrum, respectively. **[36]**. In rGO, the presence of sp^3 hybridized carbon implies the existence of -OH, -COOH functional groups. The peak intensity ratio I_D/I_G for rGO/RuO_2 of 0.86 shows that the disorder in graphene sheets increased with RuO_2 composition. It indicates the growth of certain layers of rGO placed between RuO_2 layers **[37]**.

4.4.3 XPS study:

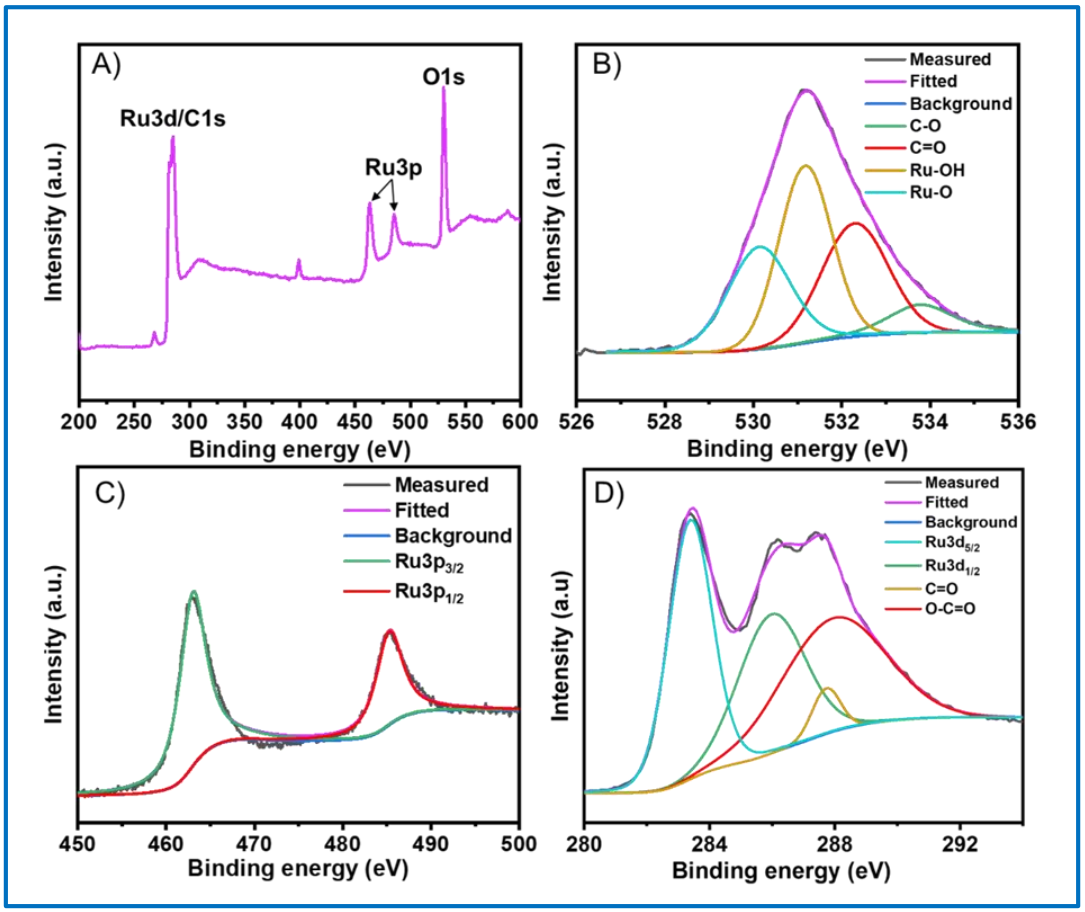

Figure 4.5: A) XPS survey and fitted spectra of B) O1s, C) Ru3p, and D) C1s/Ru3d for rGO/RuO_2 thin film.

The valence states of the elements were studied using the XPS technique. As illustrated in **Figure 4.5 A**, the survey spectrum exhibits peaks for Ru3d/C1s, Ru3p, and O1s **[38]**. The peaks at 533.8, 532.28, 531.18, and 530.18 eVs are ascribed to C-O, C=O, Ru-OH, and Ru-O bods of O1s, respectively, as shown in **Figure 4.5 B**. The observed peaks for O1s indicate that oxygen is bonded to Ru and O. Peaks of $Ru3p_{1/2}$ and $Ru3p_{3/2}$ from RuO_2 at 463.08 eV and 485.28 eV, respectively, (**Figure 4.5 C**). The XPS spectra shown in **Figure 4.5 D** depict wide spectra of C1s/Ru3d. A peak at 283.32 and 287.72 eV attributed respectively to the $Ru3d_{5/2}$ and $Ru3d_{3/2}$ spin-orbit peak of RuO_2, which correspond to Ru^{4+} oxidation state **[39, 40]**. The graphitic sp^2 carbon atoms are responsible for a peak at 286.11 eV. The weak peaks at 285.98, 287.78, and 288.28 eVs produced by the carbon atoms having C-C, C-OH, C-O-C, and O-C=O binding, respectively. This shows that rGO sheets still contain some residuals oxygenate groups attached to the hexagonal carbon ring **[41, 42]**.

4.4.4 SEM study:

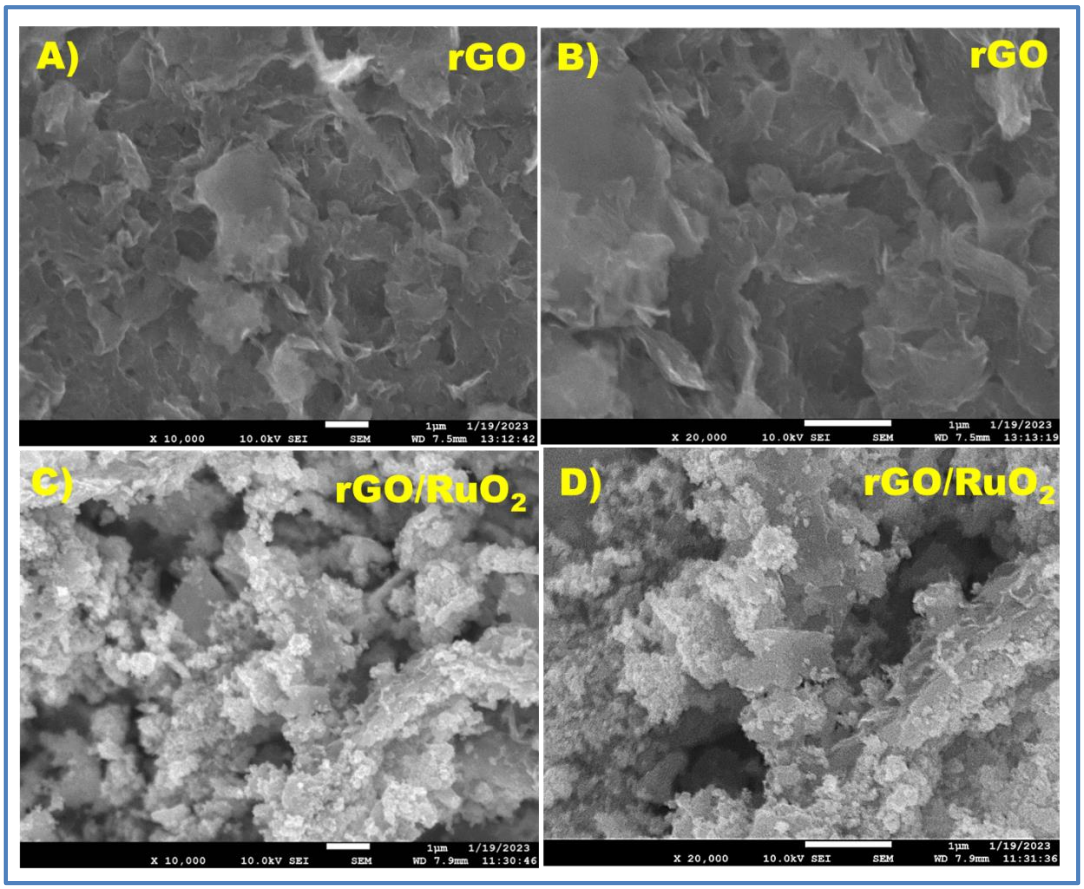

Figure 4.6: The SEM images of A, B) rGO and C, D) rGO/RuO_2 thin films at 10 KX and 20 KX magnifications, respectively

The composition and surface texture of the active material has a considerable impact on its performance. **Figure 4.6 A-F** displays the SEM images of rGO, rGO/RuO_2 electrodes at three magnifications of 10 KX and 20 KX. The surface wrinkling and ripples of rGO thin films are among their most distinctive characteristics. These characteristics result from both the reduction of graphene oxide (GO) to reduced graphene oxide (rGO) and the intrinsic features of graphene **(Figure 4.6 A-C)**. These RuO_2 microparticles are anchored over rGO sheets. The film is porous and spongy due to the compact and mud-like granule structure **[43, 44]**. The development of rGO/RuO_2 composite thin film is seen in the SEM images **(Figure 4.6 D -F)**. It is possible to develop layered structures that will make it simple for ions to transport embedded nanoparticles in rGO sheets. The rate of nucleation generation is influenced by the number of deposition cycles in the SILAR method, leading to the formation of different morphologies. **[15]**.

4.4.5 EDAX study:

The composite reduced graphene oxide/ruthenium dioxide (rGO/RuO_2) thin film was analyzed to determine its elemental composition, which includes ruthenium (Ru), oxygen (O), and carbon (C). This analysis was conducted using Energy Dispersive X-ray Spectroscopy (EDAX), and the results are illustrated in **Figure 4.7**. According to the EDAX spectrum, the atomic percentages of Ru, O, and C in the rGO/RuO_2 composite thin film are 25.61%, 42.37%, and 12.38%, respectively. These values indicate a significant deviation from the expected optimal atomic ratio of 1:2 for Ru to O. The deviation in atomic ratio suggests potential variations in the synthesis process or differences in material properties that could affect overall performance and application potential of film. Due to using of SS substrate beneath the composite layer is shown by peaks for chromium (Cr) 8.43% and iron (Fe) 11.21%.

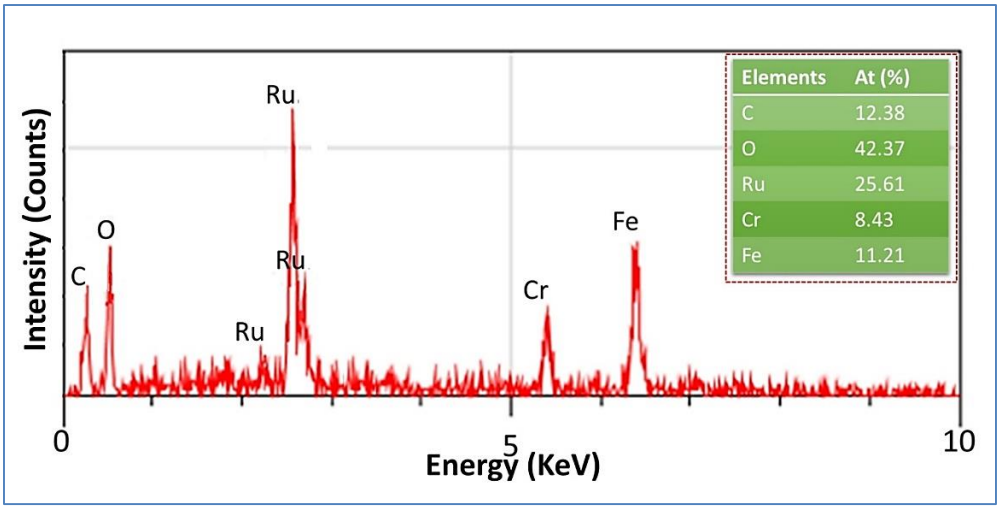

Figure 4.7: The EDAX spectrum of rGO/RuO_2 thin film.

4.4.6 TEM study:

The Transmission Electron Microscopy (TEM) image of rGO/RuO_2 composite, depicted in **Figure 4.8 A**, provides a detailed view of the material's microstructure. This image clearly shows RuO_2 nanoparticles densely packed and firmly attached to the rGO sheets, corroborating the findings from the Scanning Electron Microscopy (SEM) analysis. The high-resolution TEM (HR-TEM) images presented in **Figures 4.8 B and C** further reveal the absence of any discernible fringe patterns, which is indicative of the amorphous structure of the composite material.

This amorphous nature is further confirmed by the selected area electron diffraction (SAED) pattern shown in **Figure 4.8 D**, which displays a diffused ring pattern rather than distinct diffraction spots, a characteristic feature of amorphous materials. The observations made through TEM, HR-TEM, and SAED analyses align well with the results obtained from the X-ray diffraction (XRD) study, all of which collectively affirm the amorphous nature of rGO/RuO_2 composite **[33]**.

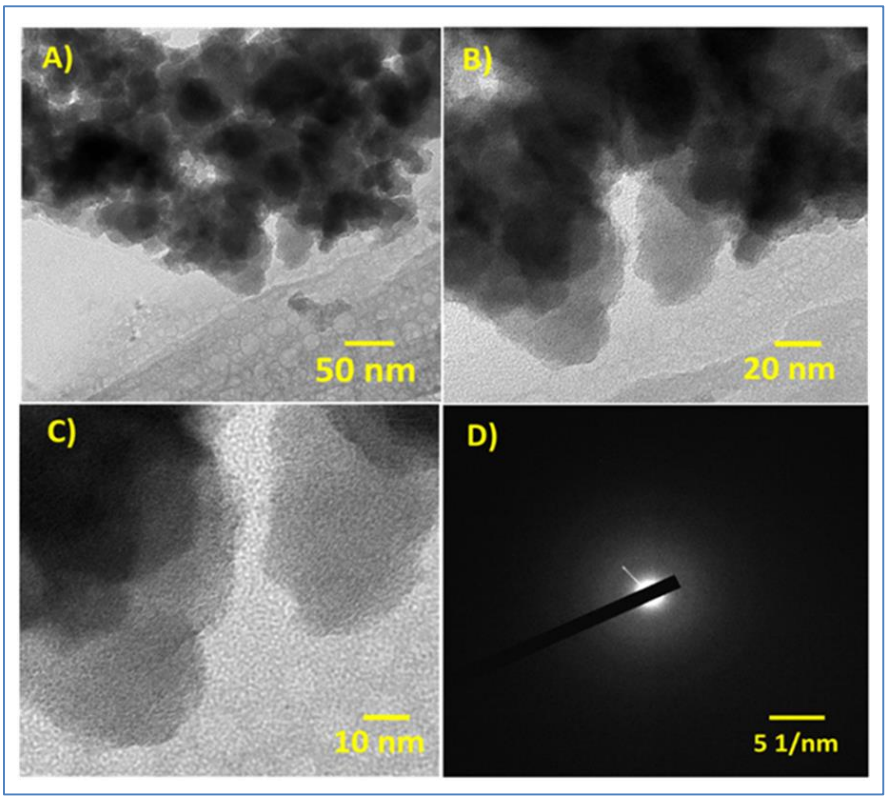

Figure 4.8: A) The TEM image, B, and C) HR-TEM images, and D) SEAD pattern of rGO/RuO_2 composite electrode.

4.4.7 Contact angle study:

The wettability is favorable for the improvement of C_s due to the large coverage of the electrode surface by an electrolyte. If the contact angle is less than 90°, the electrode surface is hydrophilic, and if it is greater than 90°, it is hydrophobic. Surface pore size and roughness have a significant association with the contact angle value. Indeed, whether the surface is thick (non-porous) or porous has a major effect on the contact angle value because water droplets can penetrate the surface due to capillary forces within the pores and spread across the surface, resulting in a contact angle reduction **[45]**. The contact angle values of 52° and 41°

are observed for rGO and rGO/RuO_2, respectively, indicating hydrophilic nature of films (**Figure 4.9 A and B)**. In addition to surface roughness and cleanliness, the factors that affect the contact angle values include heterogeneity, particle size, shape, and purity **[46]**.

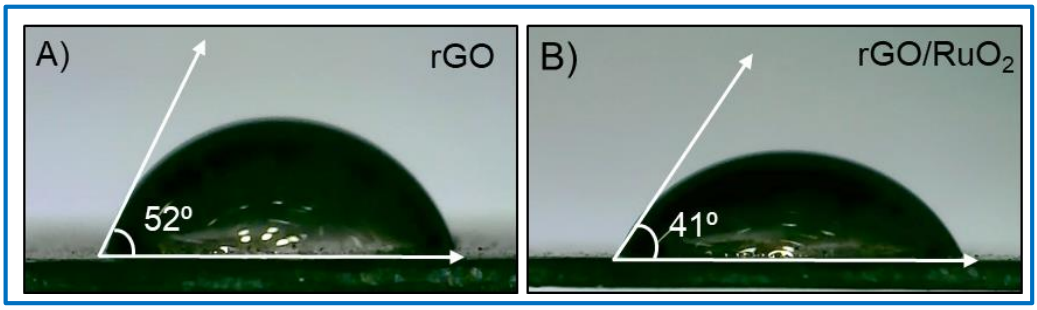

Figure 4.9: The contact angle images of A) rGO and B) rGO/RuO_2 thin films.

4.5 Electrochemical study:

4.5.1 CV study:

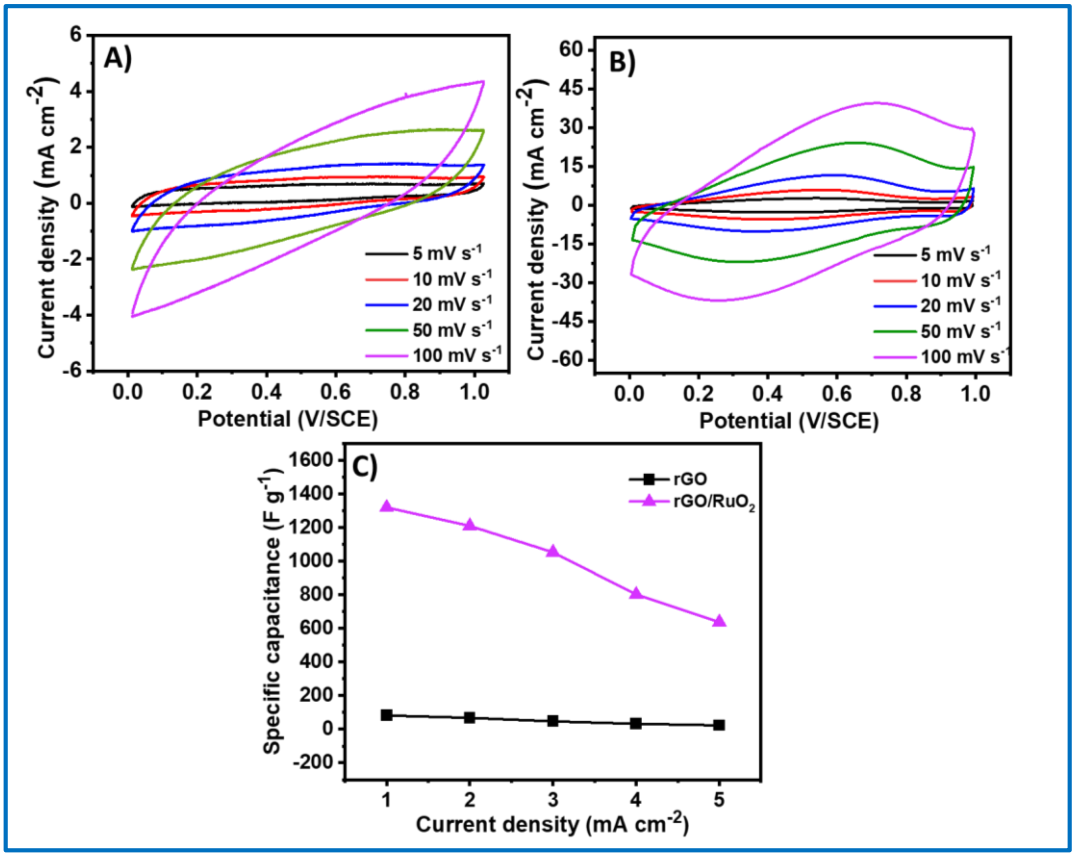

Figure 4.10: The CV curves of A) rGO, and B) rGO/RuO_2, and C) the variation of C_s with various scan rates.

The electrochemical measurements of rGO and rGO/RuO_2 were carried out in a potential window of 0 to 1 V/SCE. **Figures 4.10 A-C** depict the CV curves of rGO, RuO_2, and rGO/RuO_2 composite electrodes at various scan rates (5–100 mV s^{-1}), respectively. At a scan rate of 5 mV s^{-1}, rGO electrode exhibited C_s 98 F g^{-1} and composite rGO/RuO_2 electrode showed a C_s of 1371 F g^{-1}. The presence of a charge storage mechanism of the pseudocapacitive type is confirmed by the asymmetry of the CV curves. The CV analysis verifies the reversibility of synthesized materials **[47–50]**. The C_s variation is seen at various scan rates (5–100 mV s^{-1}) in **Figure 4.10 D.** The voltammetric measurement is a crucial technique for understanding the electrochemical properties of electrodes. Simple CV measurements at varied scan rates can help distinguish between faradaic and capacitive contributions **[51-53]**.

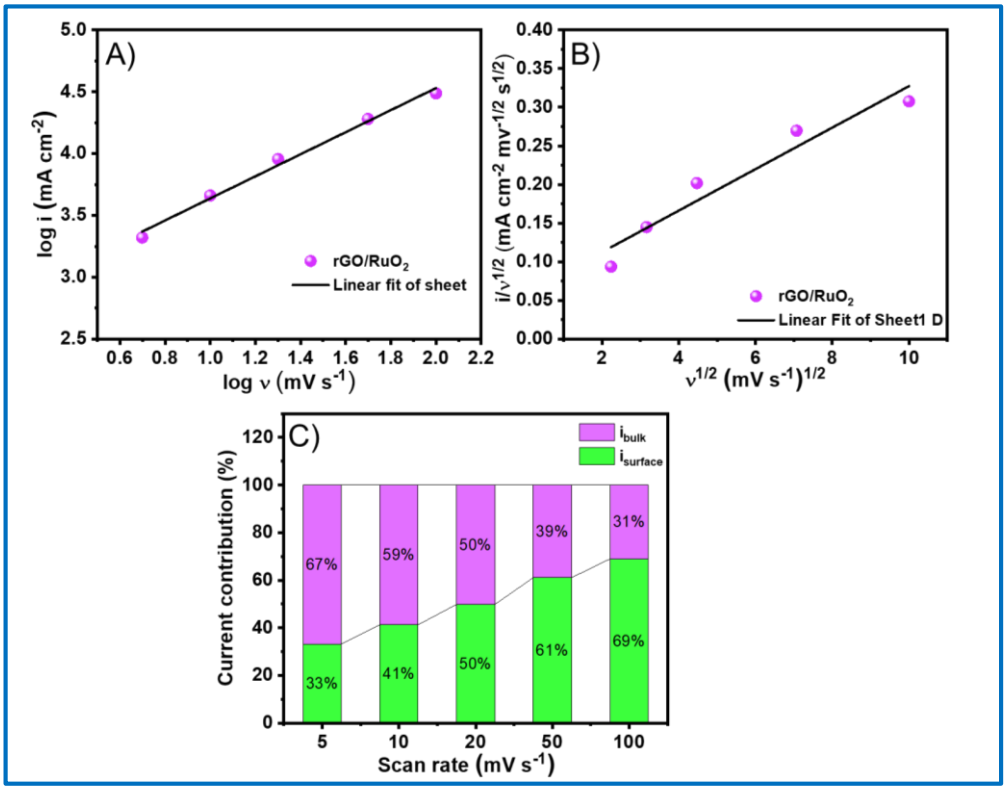

Figure 4.11: A) Plot of log *i* vs log υ, B) plot of $i/\upsilon^{1/2}$ versus $\upsilon^{1/2}$, and contribution of capacitive and diffusion-controlled currents with scan rates for C) rGO/RuO_2 electrode.

The values of b calculated using the slopes in **Figure 4.11 A** are 0.89 for rGO/RuO_2. Further analysis of the CV was done using modified eq. (3.6), as shown below, to precisely define the significance of the capacitive and diffusion-controlled processes for the entire current response **[54]**. **Figure 4.11 B** illustrates the slopes and

intercepts of the linear fit to the graph of $i/\upsilon^{1/2}$ vs. $\upsilon^{1/2}$, which provide values of k_1 and k_2, respectively **[55, 56]**. The estimated capacitive and diffusion-controlled currents from Eq. (3.7) for rGO/RuO_2 electrode, as well as their contributions, are shown in **Figure 4.11 C**, respectively. A larger diffusion-controlled current at a smaller scan increases the value of C_s. At a 100 mV s^{-1} scan rate, rGO/RuO_2 electrode store 69 % of the charge through a capacitive mechanism, respectively, and this percentage drops to 33 %, respectively at a 5 mV s^{-1} scan rate.

4.5.2 GCD study:

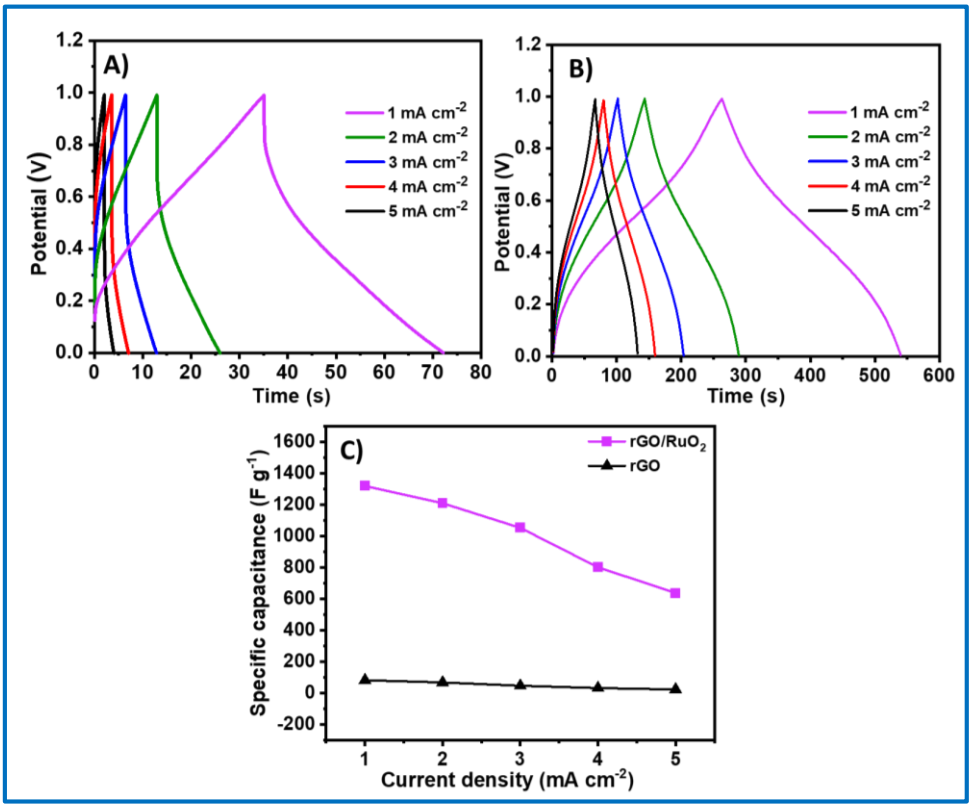

Figure 4.12: The GCD plots of A) rGO, B) rGO/RuO_2, and C) the variation of C_s with various current densities.

The GCD measurements of rGO (**Figure 4.12 A**) and rGO/RuO_2 (**Figure 4.12 B**) electrodes were carried out at different current densities between 1 to 5 mA cm^{-2}. The pseudocapacitive characteristics of the material are responsible for the quasi-triangular GCD curves for rGO and rGO/RuO_2 electrodes in 1 M H_2SO_4 electrolyte. The rGO/RuO_2 electrode shows superior charge storage capacity as observed in a longer charging-discharging time. According to GCD plots, at 1 mA cm^{-2} of current

density, the C_s of rGO and rGO/RuO_2 electrodes are 82 and 1333 F g^{-1}, respectively. The charge-discharge time increased at the reduced current densities due to the possibility of ions largely being adsorbed and undergoing redox reactions at the active sites at the interface of electrode and electrolyte and inside the electrode **[57]**. Plots of C_s against applied charging current density for rGO and rGO/RuO_2 electrodes are displayed in **Figure 4.12 C**. We observe that the C_s decreases at larger scan rates due to the electrolyte having minimum time to interact with material **[58]**.

4.5.3 EIS and stability study:

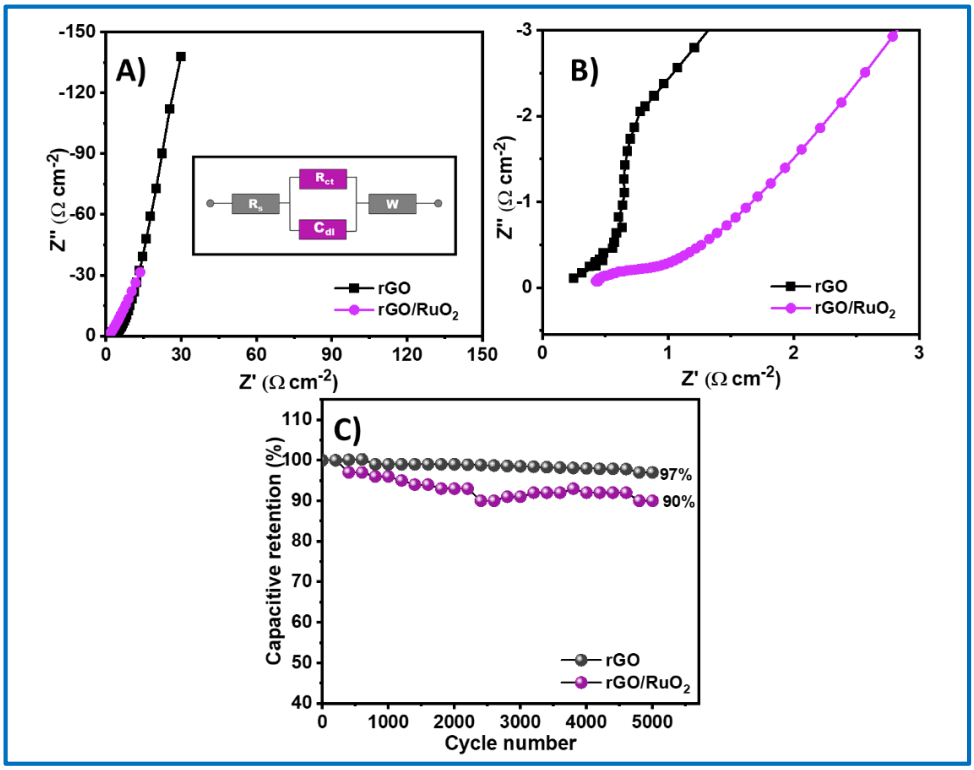

Figure 4.13: A) The Nyquist plots of rGO and rGO/RuO_2 thin films (inset shows fitted equivalent circuit), B) the enlarged view of Nyquist plots, and C) the graph of specific capacitance retention with 5,000 cycles of rGO and rGO/RuO_2 thin films.

The Nyquist plots of rGO and rGO/RuO_2 composite electrodes are displayed in the frequency range of 100 kHz and 0.01 Hz in **Figure 4.13 A** and the inset shows corresponding equivalent electrical circuit. The series resistance (R_s) denotes the ionic resistance of the applied electrolyte. A non-zero intercept from the Nyquist curve on the real axis determines it. In particular, a higher frequency region has an impact on the charge transfer resistance (R_{ct}) at an electrolyte-electrode boundary region. Ion

diffusion in the electrode leads to the development of the Warburg impedance (*W*), which may be seen in the linear tail at a lower frequency **[59]**. An enlarged view of Nyquist plots is displayed **Figure 4.13 B.** High R_{ct} value denotes more complicated charge transport through the electrode. The layered electrode of rGO/RuO_2 has better charge transfer kinetics as seen by a relatively low value for R_s and R_{ct} as it offers more electroactive sites for electrochemical reactions and a vertical path for electron transfer and ion diffusion. Due to this reason, rGO/RuO_2 electrode exhibits lower R_s (0.4 Ω cm^{-2}), R_{ct} (3.94 Ω cm^{-2}), and *W* (22 Ω cm^{-2}) values as compare to rGO and RuO_2 electrodes. Table 4.1 summarises the values of each fitted circuit parameter. The applicability of material for supercapacitors is greatly influenced by their cyclic stability. The cyclic stability of rGO and rGO/RuO_2 composite electrodes was measured at the current density of 5 mA cm^{-2} over 5,000 cycles. rGO and rGO/RuO_2 composite electrodes exhibit 97 and 90% of C_s retention, as shown in **Figure 4.13 C**. The addition of rGO facilitated rapid electron transfer in the rGO/RuO_2 composite, resulting in an improved cyclic stability compared to that of RuO_2 electrode.

Table 4.1: Electrochemical impedance spectroscopic data rGO and rGO/RuO_2 electrodes.

Electrode	**R_s (Ω cm^{-2})**	**R_{ct} (Ω cm^{-2})**	**C_{dl} (F)**	**W (mΩ cm^{-2})**
rGO	0.2	4.5	0.720	0.024
rGO/RuO_2	0.4	3.94	0.263	22

4.6. Conclusions:

In this investigation, rGO and rGO/RuO_2 composite thin films were successfully deposited on SS substrates using a simple and affordable SILAR method. The rGO/RuO_2 composite thin film is amorphous. The morphology of composite film shows the anchoring of RuO_2 nanoparticles on rGO sheets. The rGO/RuO_2 electrode achieved a maximum mass loading of 0.58 mg cm^{-2} after 170 deposition cycles. The supercapacitive performance of rGO/RuO_2 composite electrode achieved a high C_s of 1371 F g^{-1} at a scan rate of 5 mV s^{-1} in potential window of 0 to 1 V/SCE. The rGO/RuO_2 composite electrode demonstrates superior cyclic stability, with a retention of 90% after 5,000 GCD cycles.

References:

[1] C. Qin, D. Zheng, Q. Hu, X. Zhang, Z. Wang, Y. Li, J. Zhu, J. Ou, C. Yang, Y. Wang, Appl. Mater. Today, 19, (2020), 100539-100552,

[2] Z. Lin, E. Goikolea, A. Balducci, K. Naoi, P. Taberna, M. Salanne, G. Yushin, P. Simon, Mater. Today, 21, (2018), 419−436.

[3] S. Lee, G. Ali, H. Hegazy, H. Lim, K. Chong, Optimizing reduced graphene oxide aerogel for a supercapacitor, Energy Fuels, 22, (2021), 4559-4569.

[4] B. Sahoo, V. Pandey, A. Dogonchi, D. Thatoi, N. Nayak, M. Nayak, Fuel, 345, (2023), 128174-128186.

[5] D. Dubal, N. Chodankar, D. Kim, P. Gomez-Romero, Chem. Soc. Rev., 47, (2018), 2065-2129.

[6] P. Sharma, and T. Bhatti, Energy Convers. Manag., 12, (2010), 2901-2912.

[7] S. Cho, J. Kim, Y. Jo, A. Ahmed, H. Chavan, H. Woo, A. Inamdar, J. Gunjakar, S. Pawar, Y. Park, H. Kim, J. Alloys Compd., 725, (2017), 108-114.

[8] Y. Ma, H. Zhang, H. Cong, Y. Wang, S. Xin, P. Xu, Y. Qin, G. Xu, X. Kang, F. Wang, J. Alloys Compd., 968, (2023), 171985-171995.

[9] H. Tang, J. Yao, Y. Zhu, Adv. Energy Mater., 11, (2021), 2003994-2004017.

[10] X. He, W. Yang, X. Mao, L. Xu, Y. Zhou, Y. Chen, Y. Zhao, Y. Yang, J. Xu, J. Power Sources, 376, (2018), 138-146.

[11] D. Zhang, H. Zhao, F. Liang, W. Ma, Y. Lei, J. Power Sources, 493, (2021), 229722-229734.

[12] J. Song, W. Li, J. Xin, W. Wang, K. Song, X. Chen, Appl. Surf. Sci., 1, (2021), 150915-150915.

[13] M. Malik, A. Sarker, S. Rahat, S. Shuchi, Mater. Today Commun., 28, (2021), 102685-102715.

[14] T. Kim, C. Park, E. Samuel, S. An, A. Aldalbahi, F. Alotaibi, A. Yarin, S. Yoon, ACS Appl. Mater. Interfaces, 13, (2021), 10013-10025.

[15] V. Kumar, S. Polaki, R. Krishnan, R. Sarguna, T. Mathews, J. Alloys Compd., 931, (2023), 167420-167436.

[16] A. Bagde, D. Malavekar, D. Pawar, S. Khot, C. Lokhande, J. Phys. Chem. Solids, 1, (2023), 111386-111397.

[17] F. Amir, V. Pham, D. Mullinax, J. Dickerson, Carbon, 107, (2016), 338-343.

[18] F. Amir, V. Pham, J. Dickerson, RSC Adv., 5, (2015), 67638-67645.

[19] M. Ates and M. Yildirim, Polym. Bull., 77, (2020), 2285–2307.

[20] S. Korkmaz, I. Kariper, O. Karaman, C. Karaman, Ceram. Int., 15, (2021) 34514-34520.

[21] C. Zhang, H. Zhou, X. Yu, D. Shan, T. Ye, Z. Huang, Y. Kuang, RSC Adv., 22, (2014), 11197-11205.

[22] R. Wang, P. Jia, Y. Yang, N. An, Y. Zhang, H. Wu, Z. Hu, Chin. J. Chem., 34, (2016), 114-122.

[23] K. Kumar, S. Archana, R. Namitha, B. Prasanna, S. Sharma, M. Raghu, Mater. Res. Bull., 107, (2018), 347-354.

[24] Y. Chen, X. Zhang, D. Zhang, Y. Ma, J. Alloys Compd., 511 (2012), 251-256.

[25] S. Alam, N. Sharma, L. Kumar, Graphene, 6, (2017), 1-18.

[26] S. Khot, D. Malavekar, P. Bagwade, R. Nikam, C. Lokhande, J. Phys. Chem. Solids, 5, (2023),111419-111431.

[27] D. Malavekar, V. Lokhande, V. Mane, S. Kale, R. Bulakhe, U. Patil, C. Lokhande, J. Solid State Electrochem., 24, (2020), 2963-2974.

[28] P. Deshmukh, S. Pusawale, A. Jagadale, C. Lokhande, J. Mater. Sci., 47, (2012), 1546–1553.

[29] N. Maile, S. Shinde, K. Patil, A. Fulari, A. Shahzad, D. Lee, V. Fulari, SN Appl. Sci., 1, (2019), 1333-1343.

[30] R. Amin, A. Fetohi, D. Khater, J. Lin, Y. Wang, C. Wang, K. El-Khatib, RSC advances, 13, (2023), 15856-15871.

[31] N. Kwon, X. Jin, S. Kim, H. Kim, S. Hwang, Adv. Sci., 9, (2022), 2103042-2103055.

[32] S. Mehta, D. Nadargi, M. Tamboli, T. Alshahrani, V. Minnam Reddy, E. Kim, I. Mulla, C. Park, S. Suryavanshi, Sci. Rep., 11, (2021), 5023- 5040.

[33] D. Patil, D. Malavekar, J. Kim, C. Lokhande, J. Energy Storage, 72, (2023), 108729-108743.

[34] S. Bhosale, S. Kumbhar, S. Pujari, V. Patil, N. Kumar, R. Salunkhe, C. Lokhande, J. Gunjakar, U. Patil, J. Energy Storage, 72, (2023), 108417-108434.

[35] R. Thangappan, M. Arivanandhan, R. Dhinesh Kumar, R. Jayavel, J. Phys. Chem. Solids, 121, (2018), 339-349.

[36] J. Kim, K. Kim, S. Yoon, K. Kim, S. Park, K. Kim, Nanoscale, 5, (2013), 6804-6811.

[37] J. Zhao, J. Zhang, H. Yin, Y. Zhao, G. Xu, J. Yuan, X. Mo, J. Tang, F. Wang, Nanomaterials, 12, (2022), 1210-1220.

[38] S. Wang, Y. Yu, R. Li, G. Feng, Z. Wu, G. Compagnini, A. Gulino, Z. Feng, A. Hu, Electrochimica Acta., 241, (2017), 153–161.

[39] R. Al-Gaashani, A. Najjar, Y. Zakaria, S. Mansour, M. Atieh, Ceram. Int., 45, (2019), 14439–14448.

[40] M. Manuraj, J. Chacko, K. Unni, R. Rakhi, J. Alloys Compd., 836, (2020), 155420-155430.

[41] X. Gao, J. Chen, X. Sun, B. Wu, B. Li, Z. Ning, J. Li, N. Wang, ACS Appl. Nano. Mater., 3, (2020), 12269-12277.

[42] L. Wang, Y. Ding, J. Li, Y. Guan, L. Yang, H. Fang, X. Lv, J. Yuan, J. Electroanal. Chem., 919, (2022), 116501-116509.

[43] V. Shankar, P. Kumar, D. Govindarajan, P. Nethaji, G. Balji, Sustain. Energy Technol. Assess., 53, (2022), 102444-102453.

[44] Y. Guo, Z. Zhu, Y. Chen, H. He, X. Li, T. Qin, Y. Wang, J. Alloys Compd., 842, (2020), 155798-155808.

[45] S. Krainer, and U. Hirn, Colloids Surf. A: Physicochem. Eng., 619, (2021), 126503-126513.

[46] D. Pawar, D. Malavekar, A. Lokhande, C. Lokhande, J. Energy Storage, 79, (2024),110154-110170.

[47] M. Chung, and C. Lo, Electrochim. Acta, 364, (2020), 137324-137372.

[48] S. Jiaming, E. Lei, M. Chunhui, W. Zhenwei, X. Zhou, L. Yushan, L. Wei, L. Shouxin, Electrochim. Acta, 300, (2019), 225-234.

[49] D. Majumdar, Mater. Sci. Res., 15, (2018), 30-40.

[50] Y. Liu, Z. Wang, Y. Zhong, X. Xu, J. Veder, M. Rowles, M. Saunders, R. Ran, Z. Shao, Chem. Eng. J., 390, (2020), 124645-124611.

[51] S. KA, A. Shajahan, B. Chakraborty, C. Rout, RSC adv., 10, (2020), 31712-31720.

[52] N. Chodankar, H. Pham, A. Nanjundan, J. Fernando, K. Jayaramulu, D. Golberg, Y. Han, D. Dubal, Small, 16, (2020), 2002806–2002835.

[53] M. Iqbal, S. Haider, S. Siddique, M. Karim, S. Zakar, M. Tayyab, M. Faisal, M. Sulman, A. Khan, M. Baghayeri, M. Kamran, J. Energy Storage, 27, (2020), 101056-101062.

[54] A. Kumar J. Mol. Struct., 1220, (2020), 128654-128680.

[55] Y. Huang, Y. Gao, C. Liu, Z. Cao, Y. Wang, Z. Li, Y. Yan, M. Zhang, G. Cao, J. Phys. Chem. C., 123, (2019), 30067-30076.

[56] L. Ruiyi, H. Keyang, Y. Yongqiang, Z. Haiyan, L. Zaijun, Chem. Eng. J., 426, (2021), 130893-130903.

[57] Y. Wu, Y. Ding, T. Hayat, A. Alsaedi, S. Dai, Appl. Surf. Sci., 459, (2018), 430–443.

[58] M. Askari, P. Salarizadeh, M. Seifi, A. Bartolomeo, J. Alloys Compd., 860, (2021), 158497-158508.

[59] P. Sinha, and K. Kar, Electrochim. Acta., 435, (2022), 141368-141386.

CHAPTER-V

SYNTHESIS AND CHARACTERIZATION OF REDUCED GRAPHENE OXIDE (rGO)/RUTHENIUM OXIDE (RuO_2) ELECTRODE USING CHEMICAL BATH DEPOSITION (CBD) METHOD

CHAPTER-V

SYNTHESIS AND CHARACTERIZATION OF REDUCED GRAPHENE OXIDE (rGO)/RUTHENIUM OXIDE (RuO_2) ELECTRODES USING CHEMICAL BATH DEPOSITION (CBD) METHOD

5.1 Introduction:

Unique nanostructures have garnered significant attention as electrode materials for energy storage applications such as batteries, supercapacitors, and catalysis due to their advantageous properties **[1-4]**. Their high specific surface area and open architecture between 1D and 2D structures promote efficient electrolyte contact with active sites, enhancing material utilization and specific capacitance for improved energy storage efficiency **[5-8]**. Additionally, the ultrathin design of nanosheets, nanorods, and nanoneedles within nanoarrays supports rapid ion and electron transport, critical for achieving high-rate performance and fast charge-discharge cycles with minimal capacity loss **[8-10]**. Among the various materials studied, carbon-based materials, particularly graphene and its derivatives, have gained significant attention due to their exceptional electrical conductivity, large surface area, and mechanical flexibility **[11, 12]**. Reduced graphene oxide (rGO), a chemically modified form of graphene, emerges as a desirable candidate owing to its relatively low production cost and scalable synthesis while retaining many of the beneficial properties of graphene **[13, 14]**.

Despite its advantages, rGO alone typically suffers from limited capacitance due to its lower specific surface area and fewer active sites for charge storage compared to pseudocapacitive materials **[15, 16]**. To overcome these limitations, rGO is often used as a composite material in combination with metal oxides, conducting polymers, or other electroactive substances. This approach leverages the high electrical conductivity and mechanical stability of rGO, while the pseudocapacitive material contributes to enhanced charge storage through faradaic reactions. RuO_2 is one of the most promising pseudocapacitive materials due to its high C_s, fast redox kinetics, and wide operational voltage window. However, the high cost and relatively low electrical conductivity of RuO_2 necessitate the development of composites that can optimize its performance while reducing the overall material cost **[17, 18]**. In this context, the combination of RuO_2 with rGO offers a synergistic effect, where rGO provides an efficient electron transport pathway, and RuO_2 contributes to the overall capacitance, resulting in a high-performance electrode material for supercapacitors **[19]**.

This study investigates the deposition of RuO_2 thin films at various temperatures to identify the optimal conditions for producing a RuO_2/rGO composite by CBD

method. The CBD method stands out due to its simplicity, cost-effectiveness, and ability to deposit thin films with precise control over composition and thickness. This method allows for uniform coating of substrates at relatively low temperatures, making it ideal for the deposition of metal oxide films like RuO_2. The work focuses on the composite structural and electrochemical properties, intending to achieve a material that balances high capacitance and long-term stability. By optimizing the deposition process and leveraging the advantages of both rGO and RuO_2, this research aims to contribute to the development of next-generation supercapacitors with superior energy storage capabilities.

5.2 Synthesis of RuO_2 and rGO/RuO_2 thin films:

In this chapter, RuO_2 and rGO/RuO_2 composite thin films were prepared using CBD method and characterized using different physical and chemical characterization techniques like XRD, Raman, FT-IR, XPS, and SEM. The electrochemical performance of RuO_2 and rGO/RuO_2 thin film electrodes was measured in 1 M H_2SO_4 electrolyte.

5.2.1 Experimental section:

5.2.1.1 Chemicals and Materials:

The analytical reagent grade Ruthenium trichloride ($RuCl_3.xH_2O$) was purchased from SRL Chemicals LTD, Ammonium persulfate ($(NH_4)_2S_2O_8$) was purchased from Thomas Baker LTD and utilized as received. In order to produce GO, graphite flakes were purchased from Sigma-Aldrich. The substrate was a stainless steel (SS) sheet (304 grade).

5.2.1.2 Synthesis of rGO film:

The procedure of synthesis of rGO thin is already illustrated in Chapter-IV section 4.2.1.2.

5.2.1.3 Synthesis of RuO_2 thin films:

The synthesis of RuO_2 thin films were prepared via the CBD method, which involves heating an aqueous solution of $RuCl_3 \cdot xH_2O$ with SS substrates. In 25 mL

DDW bath containing 0.01 M ruthenium chloride as the ruthenium source and in another beaker, 0.05 M $(NH_4)_2S_2O_8$) as the complexing agent was prepared **[20]**. Then both solutions were mixed together and a pre-cleaned SS substrate was immersed in the resulting solution. The RuO_2 thin films were deposited at three different temperatures: 333, 343, and 353 K. At room temperature (298 K), a blackish precipitate was noted after 1 h. However, at the elevated temperatures of 333 K, 343 K, and 353 K, the precipitate formed within a few min after reaching the target temperature. During this process, a heterogeneous reaction led to the deposition of RuO_2 onto the substrates. The deposition was maintained for a consistent duration of 6 h for each temperature condition. **Figure. 5.1 s**hows the schematic of CBD method used for the deposition of RuO_2 thin film. The resulting RuO_2 thin films produced at 333, 343, and 353 K were labelled as R1, R2, and R3, respectively **[21]**. Following deposition, the thin films were rinsed with DDW and left to dry naturally at ambient temperature. The dissociated cations from the cationic precursor in the DDW are attracted and adhered to the substrate surface. This adhesion occurs due to chemical interactions or van der waals forces between the cations and SS substrate **[21]**.

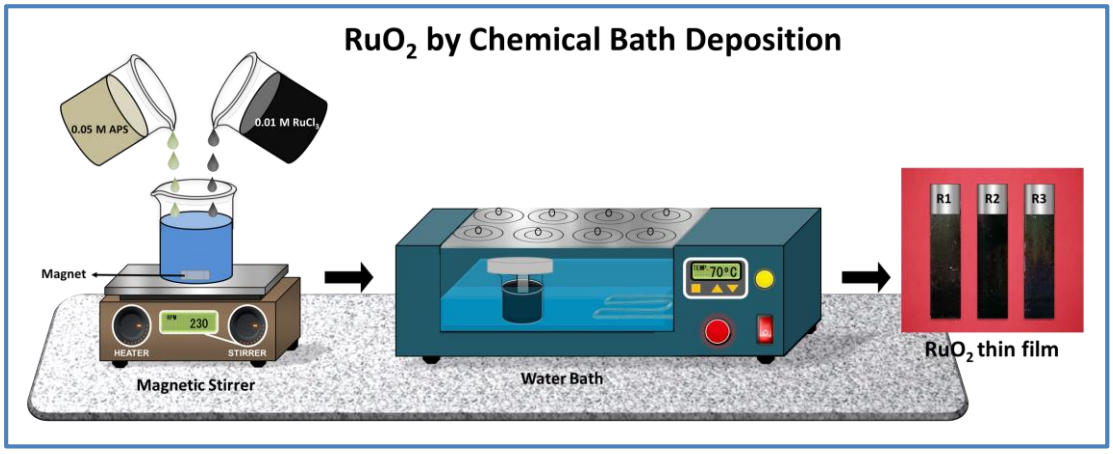

Figure. 5.1 The schematic of CBD method used for the deposition of RuO_2 thin film.

The mass loading of the thin films was determined using the weight difference technique with a precise microbalance, as calculated using Eq. 3.4. **Figure 5.2 A** displays the mass loading variation for R1, R2, and R3 films. The mass deposition values recorded for R1, R2, and R3 electrodes were 0.4, 1.41, and 1.18 mg cm^{-2}, respectively. In CBD approach, the film thickness is deposited by the rate of nucleus formation and the subsequent growth of nucleation sites. Due effect of temperature nucleation sites accelerates coagulation during the growth phase, leading to increased

film thickness. The R2 film achieved the maximum thickness of 1.41 mg cm^{-2} at a temperature of 343 K. Beyond this temperature, a slight decrease in thickness could occur due to the formation of a porous outer layer, which may induce stress and cause delamination, leading to material peeling after reaching the maximum thickness. **Figure 5.2 B** shows a photograph of the R1, R2, and R3 films.

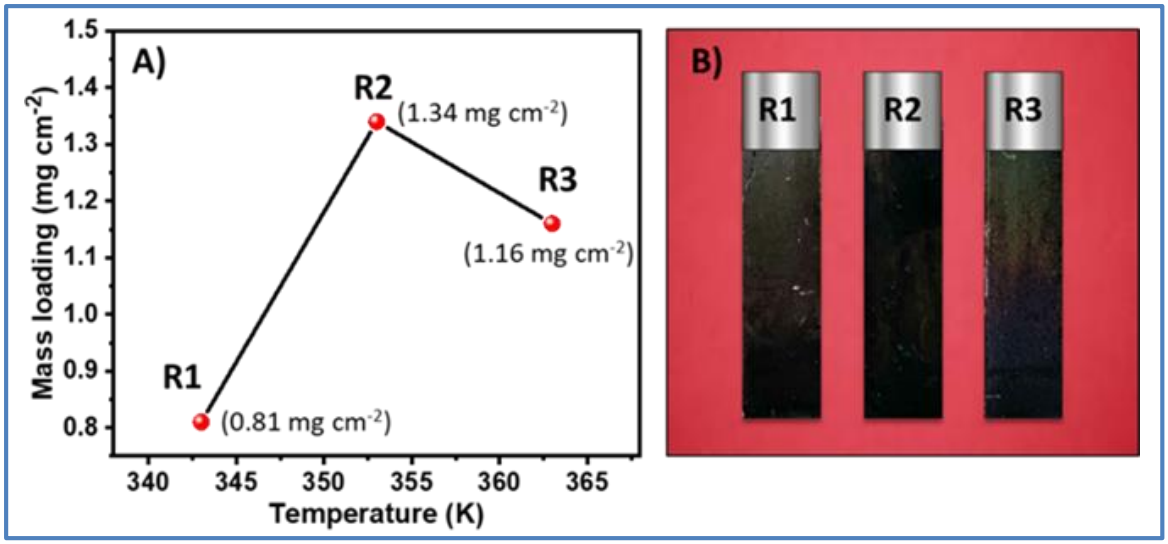

Figure 5.2: A) Mass loading variation of RuO_2 thin films with the number of deposition cycles, and B) photograph of RuO_2 films.

5.2.1.4 Synthesis of rGO/RuO_2 thin film:

To synthesize rGO/RuO_2 composite film, 1 mg/mL of rGO was dispersed in 25 mL of DDW and sonicated for 5 hrs to ensure uniform dispersion of the rGO sheets. Meanwhile, 0.01 M of $RuCl_3 \cdot xH_2O$ was dissolved in 25 mL of DDW in a separate beaker. In another beaker, 0.05 M of APS was dissolved in 25 mL of DDW, which acts as an oxidizing agent to facilitate the formation of RuO_2. Both solutions were then gradually added dropwise to rGO suspension at room temperature under continuous stirring to prevent agglomeration of the RuO_2 nanoparticles. A pre-cleaned SS substrate was immersed in the resulting solution, which was vigorously stirred and maintained at an optimized temperature of 343 K for 5 hours to enable the deposition of rGO/ RuO_2 composite thin film is denoted as rGO/R2 thin film. A schematic illustration of rGO/R2 composite structure is shown in **Figure. 5.3**. The constant stirring ensures uniform nucleation and growth of the composite on the substrate, resulting in a homogeneous thin film **[22, 23]**.

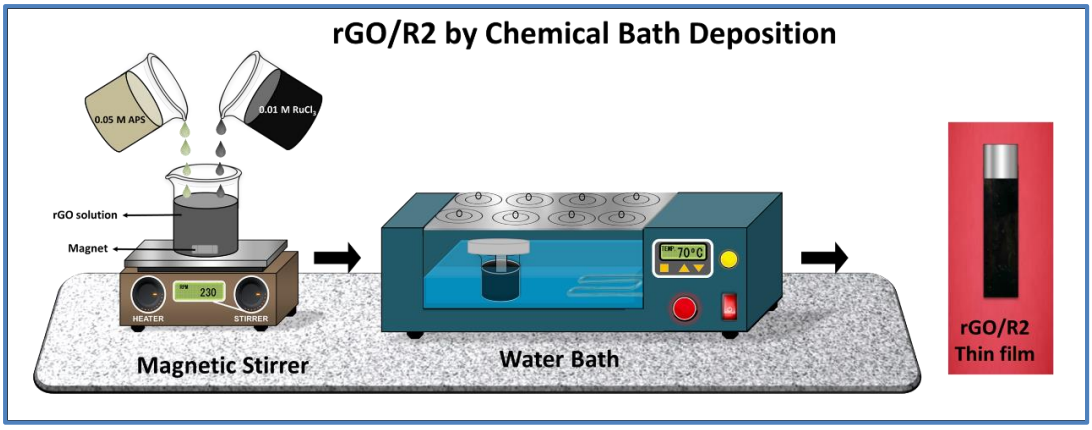

Figure. 5.3. Schematic of CBD method for deposition of rGO/R2 thin films.

5.3 Material characterizations:

5.3.1 Physico-chemical characterizations:

The Physico-chemical characterizations of RuO_2 and rGO/R2 electrodes are already illustrated in Chapter 4 section 4.3.

5.3.2 Electrochemical measurement:

The electrochemical measurements of RuO_2 and rGO/R2 electrodes are already illustrated in Chapter 4 section 4.3.

5.4 Results and discussions:

5.4.1 XRD analysis:

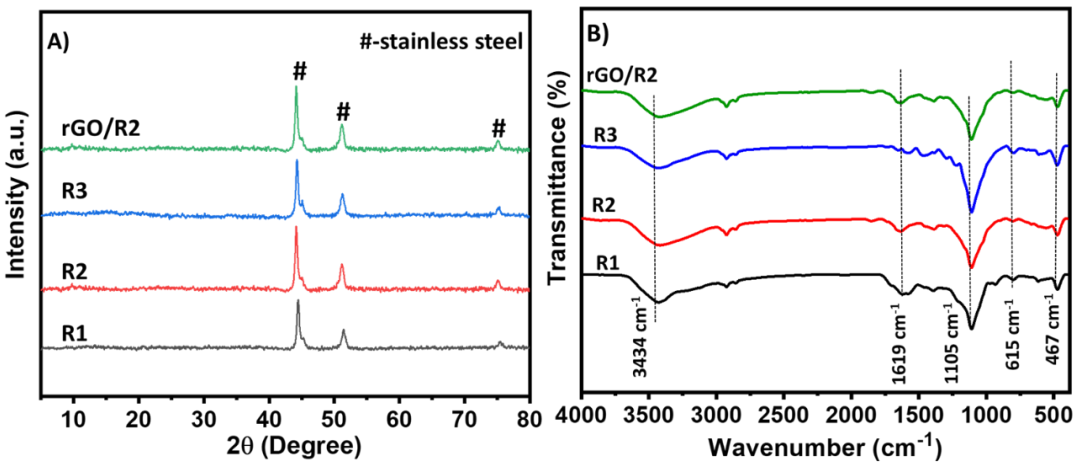

Figure. 5.4. A) The XRD patterns, and (B) FT-IR spectra of R1, R2, R3, and rGO/R2 electrodes.

The structural properties of the R1, R2, R3, and rGO/RuO_2 films were examined using XRD within the angular range of 5° to 80°. **Figure 5.4 A** illustrates the XRD patterns of the R1, R2, R3, and rGO/R2 composite electrodes. Interestingly, the diffractograms do not show any prominent peaks corresponding to crystalline phases, aside from the peaks marked by the (#) sign, which represent the stainless steel (SS) substrate. This confirms that all the samples, including the RuO_2 films, exhibit an amorphous structure, as previously reported in the literature **[24]**. However, a notable diffraction peak is observed at approximately 24°, which corresponds to the (002) plane of graphite, as referenced by PDF No. 41-1487. This peak is typically associated with stacked layers of graphene and indicates the presence of rGO in the sample. In the case of rGO/R2 composite, the absence of any distinct diffraction peak for rGO is attributed to the sandwiched growth of amorphous RuO_2 between the graphene layers, as well as the relatively low concentration of rGO in the composite **[25].**

5.4.2 FTIR analysis:

The FTIR spectroscopy analysis was carried out to investigate the functional groups present in R1, R2, R3, and rGO/R2 thin films in **Figure.5.4 B.** FTIR spectra provide valuable insights into the bonding structure and chemical composition of the thin films. For the R1, R2, and R3 thin films, the FTIR spectra revealed characteristic broad absorption bands, particularly in the region of 3400–3500 cm^{-1}, corresponding to O-H stretching vibrations. These bands indicate the presence of hydroxyl groups, which may be attributed to water molecules either adsorbed on the film surface or incorporated during the deposition process. A peak observed around 1620 cm^{-1} is associated with H-O-H bending vibrations, further confirming the presence of adsorbed water in these samples **[26]**. In the low wavenumber region, bands around 467 cm^{-1} and 615 cm^{-1} can be attributed to Ru–O stretching vibrations, indicative of the formation of RuO_2 in the films. The intensity and position of these bands may vary slightly between R1, R2, and R3 samples, reflecting differences in film thickness or growth conditions during CBD process. For rGO/R2 composite thin film, the FTIR spectrum exhibited additional peaks characteristic of reduced graphene oxide (rGO). A notable peak around 1720 cm^{-1} corresponds to the C=O stretching vibrations of carboxyl groups, which are typical of rGO. The presence of peaks near 1220 cm^{-1} and

1050 cm^{-1}, representing C-OH and C-O-C stretching vibrations, respectively, suggests the partial GO to rGO, while some oxygen-containing functional groups remain **[27]**. In the rGO/RuO_2 composite, the Ru–O stretching band is still present, indicating the coexistence of RuO_2 with rGO. The overlapping of functional groups between rGO and RuO_2 suggests a strong interaction between the two components in the composite, which may enhance its overall electrochemical performance.

5.4.3. Raman study:

The R1, R2, R3, and rGO/R2 thin films raman spectra shows in **Figure 5.5**. The prominent Raman bands observed at approximately 498 cm^{-1} and 579 cm^{-1} can be attributed to the symmetric stretching modes (A_1g) of Ru-O bonds in RuO_2. These modes are typical for RuO_2 thin films, indicating the presence of RuO_2 in all three samples **[17]**. The intensity of these peaks may vary slightly among the R1, R2, and R3 films, depending on the thickness and uniformity of the RuO_2 layer deposited during the chemical bath deposition process. The Raman spectrum rGO/R2 displayed two prominent peaks associated with the graphene structure: the D band at around 1341 cm^{-1} and the G band at approximately 1583 cm^{-1}. The D band arises from the presence of defects, disorder, or sp^3 hybridized carbon atoms in the graphene structure, while the G band corresponds to the E_2g vibrational mode of sp^2 carbon atoms in the graphitic lattice. In this case, the peak intensity ratio I_D/I_G for rGO/R2 of 0.79 shows that the disorder in graphene sheets increased with RuO_2 composition. It indicates the growth of certain layers of rGO placed between RuO_2 layers.

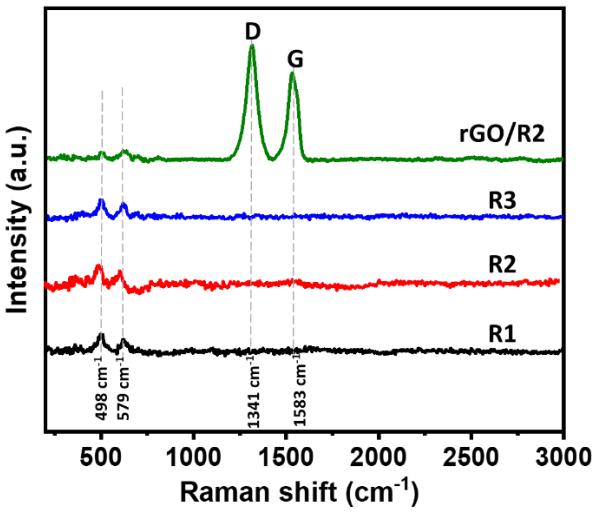

Figure 5.5: Raman spectra of R1, R2, R3, and rGO/R2 thin films.

5.4.4. SEM analysis:

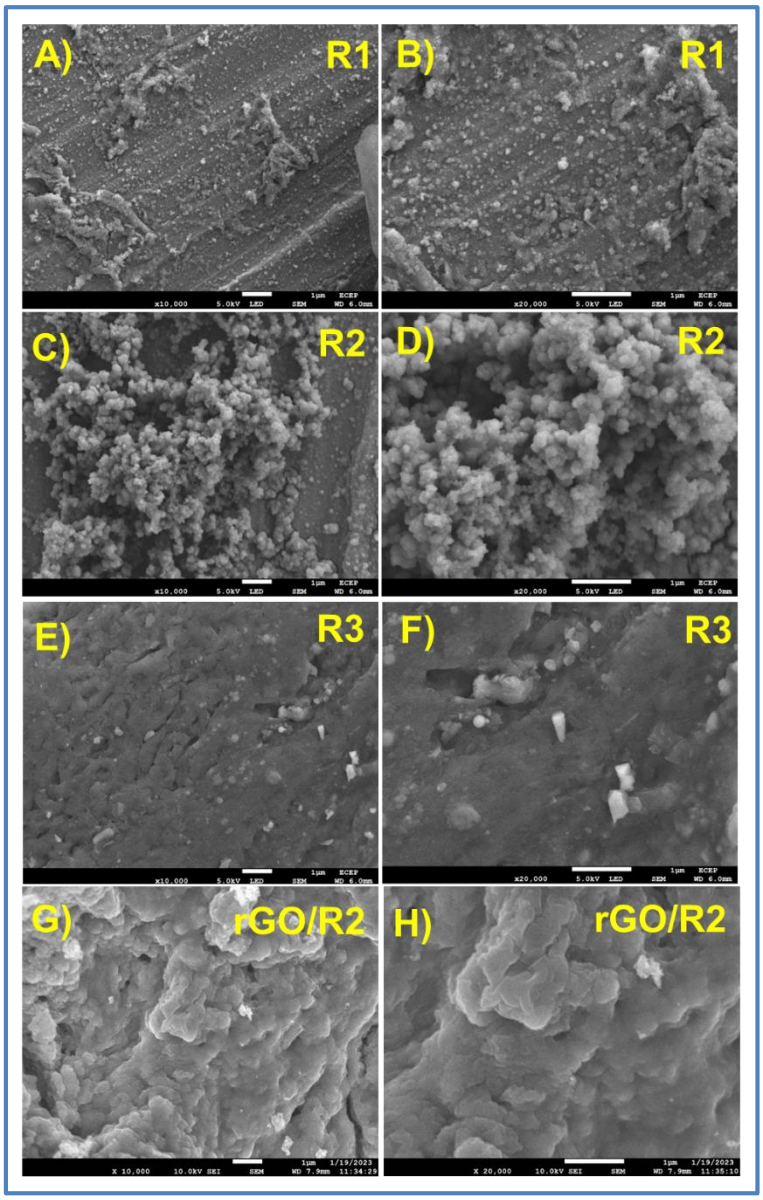

Figure 5.6. SEM images of samples A, B) R1, C, D) R2, E, F) R3, and G, H) rGO/R2 at magnifications of 10KX and 20KX.

The surface morphology of R1, R2, R3, and rGO/R2 thin films at two magnifications of 10KX, and 20KX in **Figures 5.6 A-H**. The SEM images of the R1 film **(Figure 5.6 A and B)** showed a relatively smooth surface with minimal porosity. The small, compact grains indicated limited nucleation sites and slower growth during the deposition process. This structure suggests that R1 film has a lower surface area, which may result in reduced electrochemical activity compared to other samples. In **Figure 5.6 C and D**, R2 film exhibit a more granular structure with larger, well-defined particles. The interconnected porous structure contributes to better electron

transport and increased electrochemical activity. The SEM analysis of R3 film shows in **Figure 5.6 E and F.** The morphology is similar to R2 but with slightly less porosity and more aggregated particles. This suggests that while R3 has a reasonably high surface area, it may not perform as well as R2 due to its less uniform particle distribution and reduced porosity. The denser grain structure could limit ion penetration, potentially lowering the film capacitance. The rGO/R2 film **(Figure 5.6 G and H)** displayed a distinct morphology characterized by the dispersion of RuO_2 nanoparticles over rGO sheets **[28]**. The rGO network provided a highly conductive framework, while the RuO_2 nanoparticles were uniformly distributed, creating a hierarchical structure.

5.4.5 TEM study:

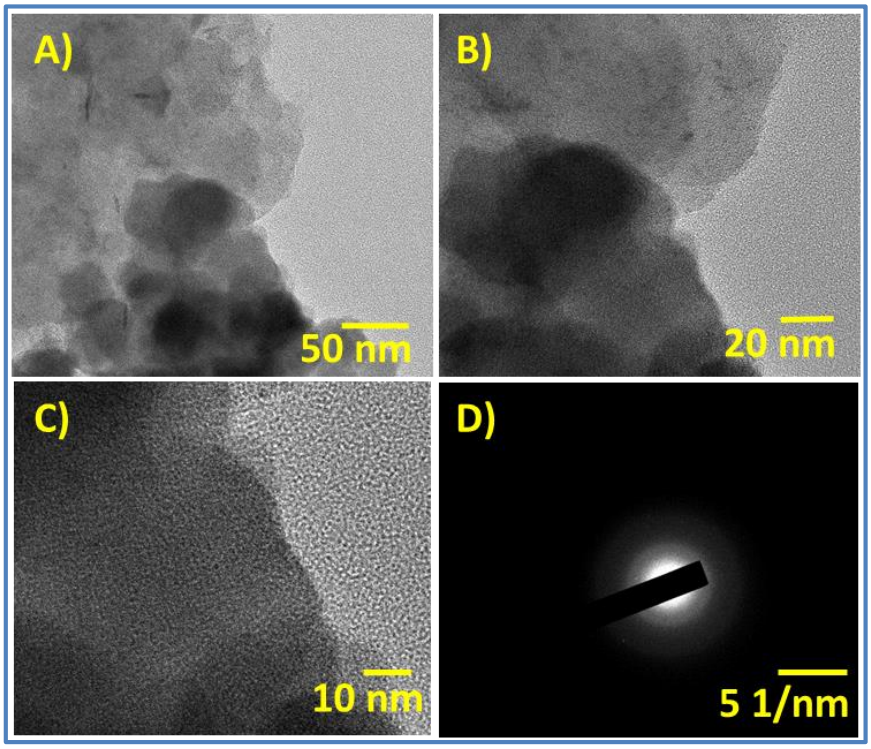

Figure 5.7: A) The TEM image, B, C) HR-TEM images, and D) SEAD pattern of rGO/R2 composite electrode.

The TEM image of the rGO/R2 composite **(Figure 5.7 A)** highlights RuO_2 nanoparticles uniformly distributed and securely anchored on rGO sheets, supporting SEM findings. HR-TEM images **(Figure 5.7 B and C)** show no visible lattice fringes, suggesting the composite's amorphous nature. This is further validated by the SAED pattern **(Figure 5.7D)**, which exhibits diffuse rings characteristic of amorphous

materials. Additionally, the uniform dispersion of RuO_2 nanoparticles across the rGO matrix ensures enhanced contact between active sites and the electrolyte, facilitating efficient electrochemical performance. These findings, in agreement with XRD results, collectively confirm the amorphous structure of the rGO/R2 composite and its potential for energy storage applications.

5.4.6 Contact angle study:

The contact angle analysis of R1, R2, R3, and rGO/R2 thin films reveals varying degrees of surface wettability. The wettability characteristic is important for thin film electrodes employed for supercapacitor applications. The contact angles for R1, R2, R3, and rGO/R2 thin films are of 67°, 42°, 58°, and 38°, respectively **(Figure 5.8 A-D).** R1 exhibits a high contact angle as compare to others, indicating a less hydrophilic surface due to its smoother, less porous structure. R2 shows a significantly lower contact angle, reflecting better wettability, likely due to its increased porosity and rough surface, which enhances electrolyte interaction. R3 has a moderate contact angle, suggesting intermediate wettability, while rGO/R2 film demonstrates the lowest contact angle, indicating a highly hydrophilic surface. This superior wettability is attributed to the porous, rough structure of rGO/R2 composite, making it ideal for enhanced ion and electron transport in electrochemical applications.

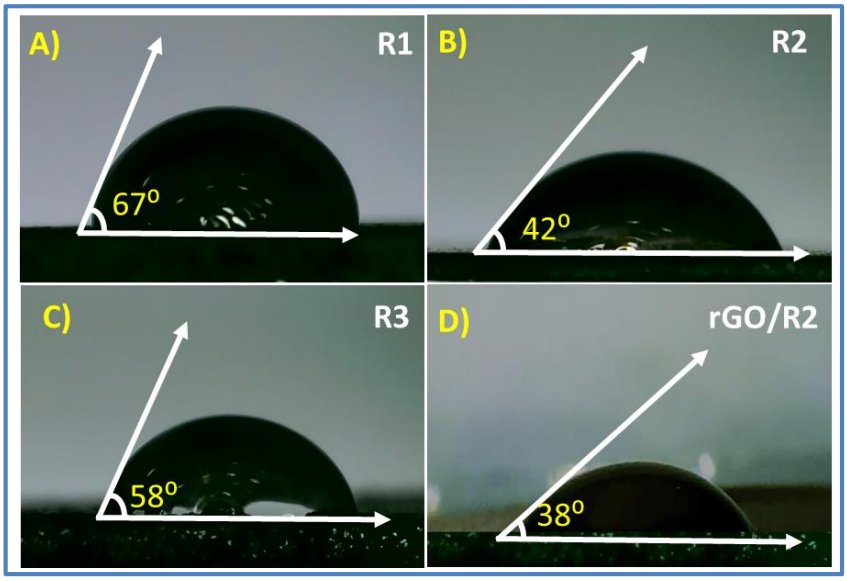

Figure. 5.8: The contact angle photographs of A) R1, B) R2, C) R3, and D) rGO/R2 electrodes.

5.5 Electrochemical analysis:

5.5.1 CV study:

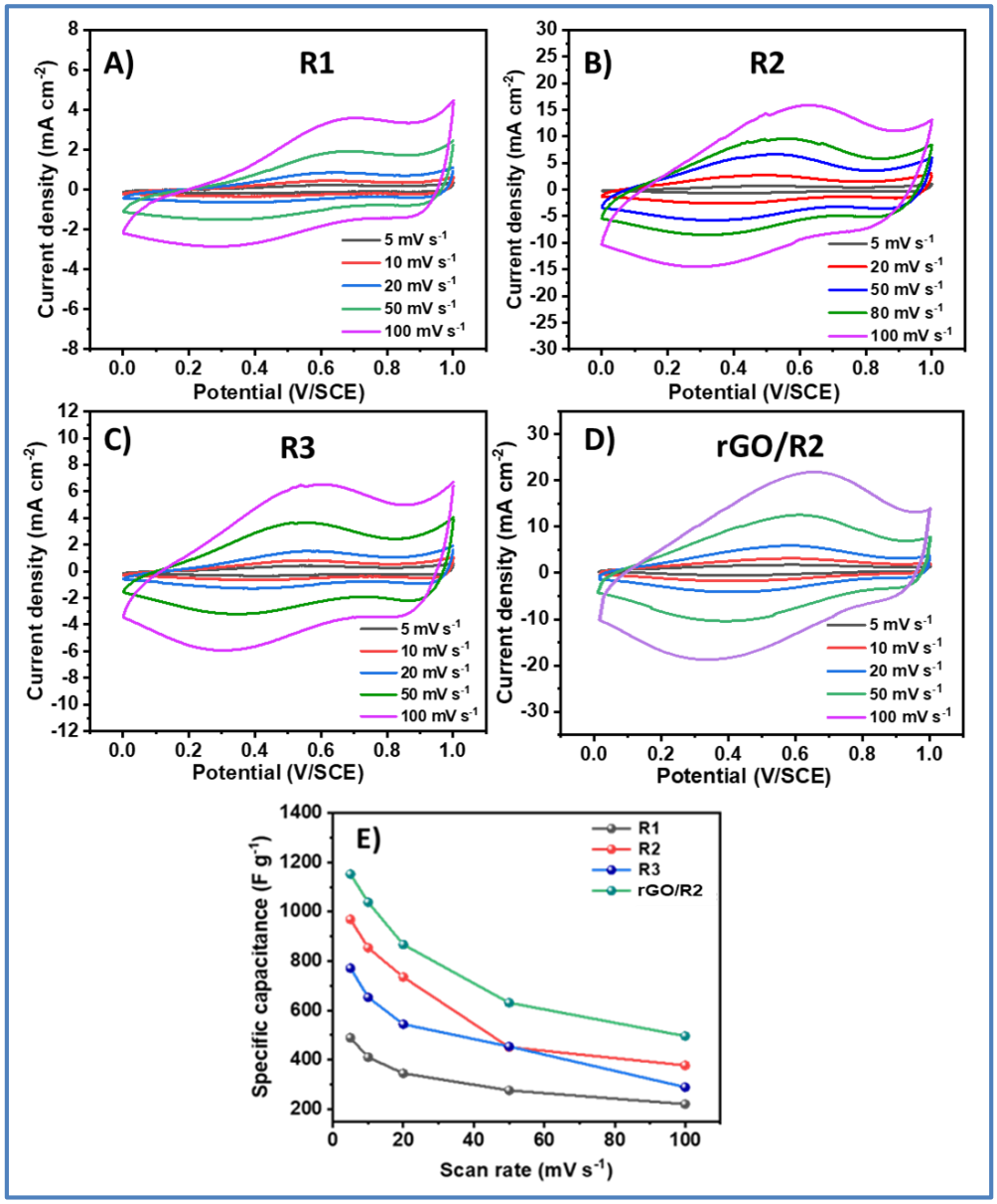

Figure. 5.9. The CV curves at different scan rates of A) R1, B) R2, C) R3, D) rGO/R2 electrodes, and E) the variation of the specific capacitance with various scan rates of all electrodes.

The electrochemical performance of R1, R2, R3, and rGO/R2 thin films was evaluated through CV within a potential window of 0 to 1 V vs. SCE in a 1M H_2SO_4 electrolyte. **Figures 5.9 A-D** present the CV curves of these electrodes at various scan rates ranging from 5 to 100 mV s^{-1}. At a scan rate of 5 mV s^{-1}, the C_s values for R1, R2, R3, and rGO/R2 electrodes were found to be 489, 996, 771 and 1152 F g^{-1}, respectively. These results highlight a clear progression in charge storage capability,

with the rGO/R2 composite exhibiting the highest C_s due to the synergistic effect between high surface area of rGO and R2 active redox sites. The asymmetry observed in the CV curves indicates the presence of a pseudocapacitive charge storage mechanism in all the films, especially in rGO/R2 composite. The redox peaks and increased current density at higher scan rates further confirm the contribution of both EDLC and pseudocapacitance **[29]**. The highly reversible nature of these reactions is also evidenced by the near-symmetric CV curves, ensuring efficient charge-discharge cycles, as supported by literature **[30, 31]**. **Figure 5.9 E** demonstrates how specific capacitance varies with scan rates for each electrode. At lower scan rates 5 mV s^{-1}, the C_s values are higher because ions in the electrolyte have sufficient time to fully penetrate the porous electrode structure, accessing more active sites for charge storage. The asymmetric shape of the CV curves indicates the presence of a pseudocapacitive charge storage mechanism, as previously reported **[32]**.

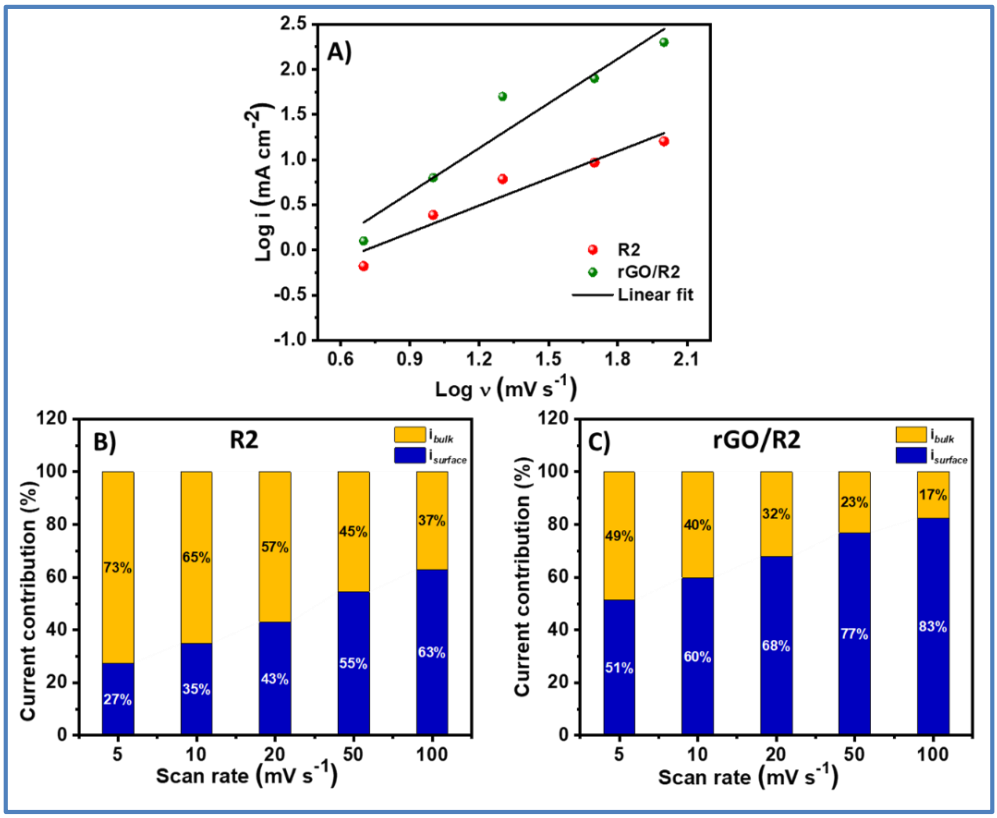

Figure. 5.10. A) Plot of log i vs log ν, contribution of capacitive and diffusion-controlled currents with scan rates for B) R2, and C) rGO/R2 electrodes.

The CV analysis also confirmed the reversibility of the electrode. **Figure 5.10** illustrates the contributions to the total current from both capacitive and diffusion-controlled charge storage mechanisms for rGO/R2 electrode. It can be observed that

as the scan rate is reduced, the contribution from diffusion-controlled charge storage becomes more significant, resulting in increased C_s. The capacitive process in the R2 electrode stores around 63% of the charge at a scan rate of 100 mV s^{-1}, which drops to 27% at a scan rate of 5 mV s^{-1}. At a scan rate of 100 mV s^{-1}, approximately 83% of the total charge is stored through capacitive processes in rGO/R2 electrode and 51% at a slower scan rate of 5 mV s^{-1}, indicating a stronger reliance on diffusion-controlled mechanisms **[33]**. This highlights the dynamic interplay between the capacitive and diffusion-controlled mechanisms depending on the scan rate.

5.5.2 GCD study:

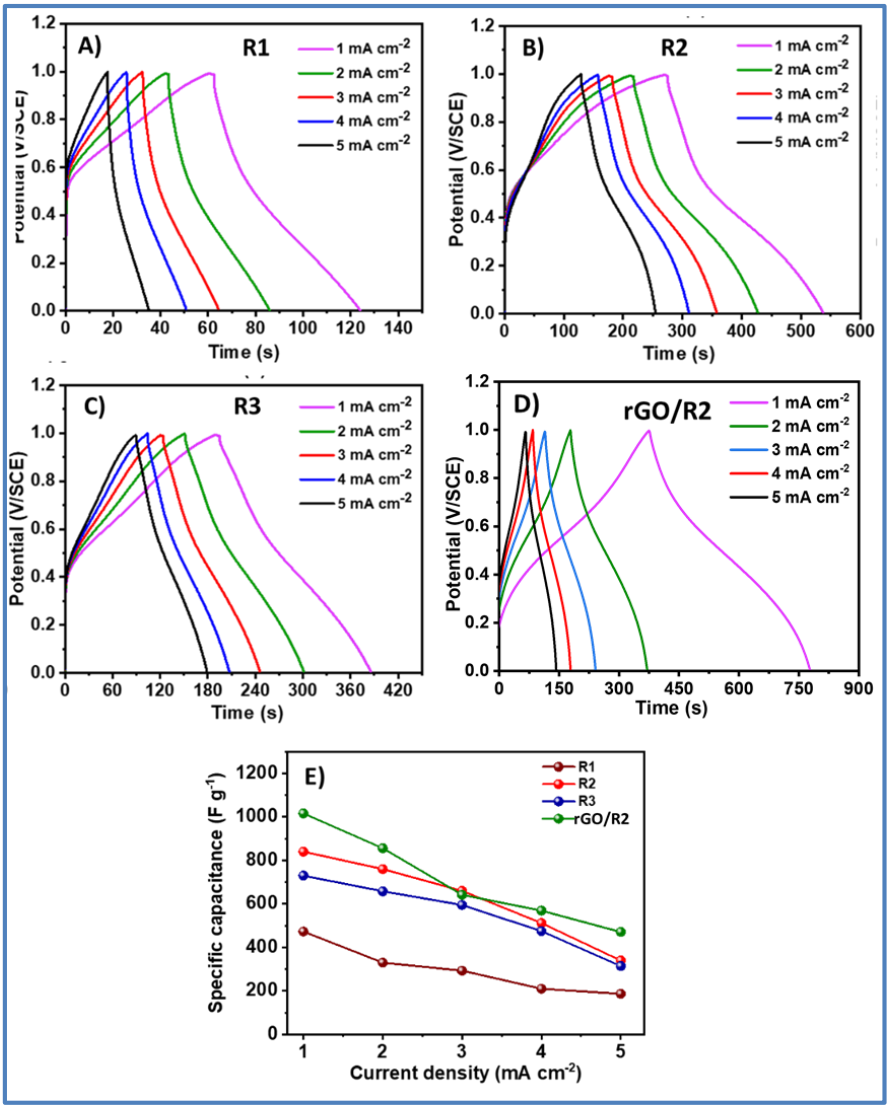

Figure. 5.11 The GCD plots at different current densities of A) R1, B) R2, C) R3, D) rGO/R2 electrodes, and E) the variation of the specific capacitance with various current densities of all electrodes.

The GCD profiles provide insights into the charge storage behavior and the reversibility of each electrode. **Figure 5.11 A-D** shows the GCD curves of R1, R2, R3, and rGO/R2 electrodes at a current density of 1 mA cm^{-2}. The non-triangular GCD profiles for all electrodes suggest that charge storage is primarily driven by surface redox reactions **[34]**. C_s values calculated using Equation 1.2 are 473, 840, 730, and 1016 F g^{-1} for R1, R2, R3, and rGO/R2, respectively, at the same current density. The surface structure of the electrode facilitates efficient ion transfer, improving the rate of intercalation and deintercalation by reducing internal resistance (IR) **[35]**. **Figure 5.11 E** depicts how C_s varies with different current density. The non-triangular shapes further indicate a pseudocapacitive charge storage mechanism. The presence of rGO significantly enhances capacitance by providing a large surface area, high conductivity, and facilitating efficient ion diffusion, thus boosting overall energy storage performance.

5.5.3 EIS and stability study:

The EIS analysis was performed on R1, R2, R3, and rGO/R2 thin film electrodes to assess their electrochemical behavior, specifically in terms of charge transfer and resistance. The Nyquist plots for these electrodes are depicted in **Figure 5.12 A**. The EIS spectra typically consist of a semicircle in the high-frequency region followed by a linear portion in the low-frequency region, representing charge transfer and diffusion processes, respectively. For the R1, R2, R3, and rGO/R2 electrodes, R_s, R_{ct}, Q, and W were determined through equivalent circuit fitting. The parameters obtained from fitting the EIS data are listed in Table 5.1. The rGO/R2 electrode, which exhibited the best performance, had fitted parameter values of R_s at 0.6 Ω cm^{-2}, R_{ct} at 72 Ω cm^{-2}, indicating low resistance and effective charge storage characteristics. The overall EIS analysis indicates that rGO/RuO_2 electrode has the lowest R_s, R_{ct}, and W values, along with the highest Q, demonstrating the advantages of combining rGO with R2 to achieve efficient charge transfer, low resistance, and enhanced ion diffusion. This synergistic effect results in superior electrochemical properties, making the rGO/R2 electrode highly suitable for energy storage applications **[36]**. The cyclic stability of R2 and rGO/R2 electrodes was studied at current density of 5 mA cm^{-2} for 5,000 GCD cycles (**Figure 5.12 B**). R2 and rGO/R2 have capacitive retentions of 83 and 89%, respectively. When compared to RuO_2, the rGO/2

composite electrode exhibits greater retention. Poor interactions with rGO sheets may be the reason of the drop in C_s with GCD cycles, which would lead to a degradation in electron transport and ion diffusion **[37]**.

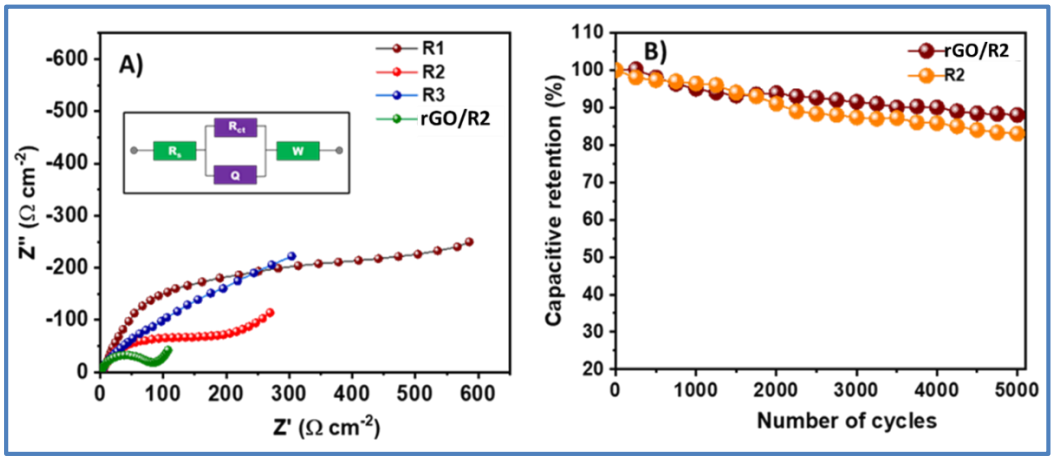

Figure. 5.12 A) Nyquist plots of R1, R2, R3, and rGO/R2 electrodes (the inset shows fitted equivalent circuit for the EIS data), and B) plots of capacitive retention versus number of cycles of R2 and rGO/2 electrodes.

Table 5.1: Impedance values of R1, R2, R3, and rGO/R2 electrodes.

Electrodes	R_s (Ω cm^{-2})	R_{ct} (Ω cm^{-2})	Q (F)	W (mΩ cm^{-2})
R1	2.6	280	540	16
R2	1.5	150	236	11
R3	2.8	310	653	22
rGO/R2	0.6	72	105	6

5.6 Conclusions:

In conclusion, CBD method was used to deposit R1, R2, R3, and rGO/R2 composite electrodes on an SS substrate at various temperatures. R2 (RuO_2 at 343 K) anchoring on rGO sheets is visible in the composite film. With a maximum C_s of 1152 F g^{-1} at a 5 mV s^{-1} scan rate in 1 M H_2SO_4 electrolyte, the rGO/R2 composite electrode superior than R2 thin film in terms of electrochemical performance. With the addition of rGO, the value of R_s decreases for rGO/R2 electrode (0.6 Ω cm^{-2}) as compared to pure R2 (1.5 Ω cm^{-2}). The rGO/R2 film electrode exhibits higher electrochemical cycling stability (89%) in comparison to R2 film electrode (83%). This illustrates the effectiveness of C_s and specific surface area can be raised via the formation of rGO/R2 composite electrodes using CBD method.

References:

[1] Y. Huang, F. Cui, J. Bao, Y. Zhao, J. Lian, T. Liu, H. Li, J. Mater. Chem A, 7, (2019), 20778-20789.

[2] K. Abbasi, M. Shahbaz, J. Zhang, M. Irfan, R. Alvarado, Renew. Energy, 187, (2022), 390–402.

[3] M. Kandasamy, S. Sahoo, S. Nayak, B. Chakraborty, C. Rout, J. Mater. Chem. A., 9, (2021), 17643–17700.

[4] G. Ren, G. Ma, N. Cong, Renew. Sust. Energ. Rev., 41, (2015), 225–236.

[5] A. Khaligh, and Z. Li, IEEE Trans. Veh. Technol., 59, (2010), 2806–2814.

[6] X. Li, and J. Wang, Info. Mat., 2, (2020), 13-22.

[7] D. Zhang, H. Zhao, F. Liang, W. Ma, Y. Lei, J. Power Sources, 493, (2021), 229722-229734.

[8] F. Naseri, S. Karimi, E. Farjah, E. Schaltz, Renew. Sust. Energ. Rev., 155, (2022), 111913-111928.

[9] Y. Wu, C. Cao, Sci. China Mater., 61, (2018), 1517–1526.

[10] R. Liang, Y. Du, P. Xiao, J. Cheng, S. Yuan, Y. Chen, Nanomaterials, 11, (2021), 1248–1275.

[11] F. Ahmad, M. Khan, U. Waqas, S. Ramayb, S. Atiq, RSC Adv., 13, (2023), 25316-25127.

[12] S. Karade, B. Sankapal, ACS Sustain. Chem. Eng., 6, (2018), 15072–15082.

[13] J. Song, W. Li, J. Xin, W. Wang, K. Song, X. Chen, Appl. Surf. Sci., 1, (2021), 150915-150924.

[14] M. Malik, A. Sarker, S. Rahat, S. Shuchi, Mater. Today Commun., 28, (2021), 102685-102715.

[15] T. Kim, C. Park, E. Samuel, S. An, A. Aldalbahi, F. Alotaibi, A. Yarin, S. Yoon, ACS Appl. Mater. Interfaces, 13, (2021), 10013-10025.

[16] V. Kumar, S. Polaki, R. Krishnan, R. Sarguna, T. Mathews, J. Alloys Compd., 931, (2023), 167420-167436.

[17] K. Kumar, S. Archana, R. Namitha, B. Prasanna, S. Sharma, M. Raghu Mater. Res. Bull., 107, (2018), 347–354.

[18] S. Korkmaz, I. Kariper, O. Karaman, C. Karaman, Ceram. Int., 15, (2021) 34514-34520.

[19] C. Zhang, H. Zhou, X. Yu, D. Shan, T. Ye, Z. Huang, Y. Kuang, RSC Adv., 22, (2014), 11197-11205.

[20] D. Dubal, G. Gund, R. Holze, H. Jadhav, C. Lokhande, C. Park, Electrochimica. Acta., 103, (2013), 103-109.

[21] S. Alam, N. Sharma, L. Kumar, Graphene, 6, (2017), 1-18.

[22] P. Deshmukh, S. Pusawale, A. Jagadale, C. Lokhande, J. Mater. Sci., 47, (2012), 1546–1553.

[23] N. Maile, S. Shinde, K. Patil, A. Fulari, A. Shahzad, D. Lee, V. Fulari, SN Appl. Sci., 1, (2019), 1333-1343.

[24] R. Amin, A. Fetohi, D. Khater, J. Lin, Y. Wang, C. Wang, K. El-Khatib, RSC advances, 13, (2023), 15856-15871.

[25] S. Mehta, D. Nadargi, M. Tamboli, T. Alshahrani, V. Reddy, E. Kim, I. Mulla, C. Park, S. Suryavanshi, Sci. Rep., 11, (2021), 5023- 5040.

[26] S. Korkmaz, A. Kariper, C. Karaman, O. Karaman, Scientific reports, 27, (2022), 12-20.

[27] R. Ingole, B. Fugare, B. Lokhande, J. Mater. Sci.: Mater. Electron, 15, (2017), 16374-16383.

[28] Y. Guo, Z. Zhu, Y. Chen, H. He, X. Li, T. Qin, Y. Wang, J. Alloys Compd., 842, (2020), 155798-155808.

[29] M. Chung, and C. Lo, Electrochim. Acta, 364, (2020), 137324-137372.

[30] Y. Liu, Z. Wang, Y. Zhong, X. Xu, J. Veder, M. Rowles, M. Saunders, R. Ran, Z. Shao, Chem. Eng. J., 390, (2020), 124645-124611.

[31] S. Jiaming, E. Lei, M. Chunhui, W. Zhenwei, X. Zhou, L. Yushan, L. Wei, L. Shouxin, Electrochim. Acta, 300, (2019), 225-234.

[32] S. KA, A. Shajahan, B. Chakraborty, C. Rout, RSC adv., 10, (2020), 31712-31720.

[33] M. Iqbal, S. Haider, S. Siddique, M. Karim, S. Zakar, M. Tayyab, M. Faisal, M. Sulman, A. Khan, M. Baghayeri, M. Kamran, J. Energy Storage, 27, (2020), 101056-101062.

[34] M. Askari, P. Salarizadeh, M. Seifi, A. Bartolomeo, J. Alloys Compd., 860, (2021), 158497-158508.

[35] Y. Wu, Y. Ding, T. Hayat, A. Alsaedi, S. Dai, Appl. Surf. Sci., 459, (2018), 430-443.

[36] P. Sinha, and K. Kar, Electrochim. Acta., 435, (2022), 141368-141386.

[37] H. Cong, X. Ren, P. Wang, S. Yu, Energy Environ. Sci., 6, (2013), 1185-1191.

CHAPTER-VI

FABRICATION AND PERFORMANCE EVALUATION OF FSS-ASC DEVICES BASED ON $rGO/RuO_2//WO_3$ THIN FILMS

CHAPTER-VI

FABRICATION AND PERFORMANCE EVALUATION OF FSS-ASC DEVICES BASED ON rGO/RuO_2//WO_3 THIN FILMS

6.1 Introduction:

The development of supercapacitors has drawn a lot of attention due to the growing demand for high-performance, sustainable energy storage devices. Supercapacitors are growing into increasingly crucial components in modern electronic systems owing to their exceptional power density, extended cycle life, and quick charge-discharge characteristics. Applications for these systems can be found in electric cars, portable gadgets, and renewable energy storage technologies **[1, 2]**. The current difficulty, consequently, is in expanding supercapacitors energy density and flexibility without sacrificing their electrochemical or mechanical durability. Wearable and flexible electronics have become increasingly popular in recent years, which has led to a significant increase in interest in the development of flexible supercapacitors **[3]**. Those devices require energy storage materials that maintain excellent electrochemical performance even during mechanical deformations as flexing, folds, and twisting. As a result, a lot of work has gone into creating electrode materials that have a high energy storage capacity and mechanical flexibility. Two such materials that have emerged as attractive possibilities for the manufacture of high-performance flexible supercapacitors are rGO and RuO_2 **[4, 5]**. Two-dimensional carbon substance graphene is well-known for its remarkable durability, excellent electrical conductivity, and enormous surface area. Nonetheless, the cost of producing flawless graphene maintains its practical use in supercapacitors **[6]**. GO is reduced to produce rGO, which is a less expensive alternative that nevertheless has many of the positive characteristics of graphene, like its high surface area and good electrical conductivity **[7]**. Additionally, rGO is a good electrode material for supercapacitors because it still has residual oxygen-containing functional groups that improve its pseudocapacitive qualities **[8]**.

Transition metal oxide RuO_2, demonstrates remarkable pseudocapacitive properties because of its quick and reversible redox processes. RuO_2 is hence well-known for having a high C_s and S_E. RuO_2 has several benefits, but its large cost and very low electrical conductivity in bulk form prevent it from being employed widely. In order to overcome these obstacles, scientists have looked at combining RuO_2 with extremely conductive substances, such as rGO, to enhance the hybrid materials electrochemical performance **[9, 10]**. The synergy between rGO has strong conductivity and flexibility and RuO_2 has outstanding pseudocapacitance makes for

composite materials that effectively utilize both components' strengths. A flexible supercapacitor device with improved mechanical flexibility, stability, and energy storage capability over extended cycling can be created thanks to this synergy. RuO_2 nanoparticles are usually scattered across rGO sheets to form a hybrid structure that has a large surface area and electrochemical reaction sites **[11-13]**.

This chapter is focused on the fabrication and electrochemical performance of a flexible solid-state asymmetric supercapacitor (FSS-ASC) device using two different synthesis methods for the electrodes: SILAR and CBD methods for the rGO/ RuO_2 positive electrode (cathode) and CBD method for WO_3 negative electrode (anode). Additionally, rGO/RuO_2 and WO_3 electrode 5×5 cm^2 were stacked with PVA-H_2SO_4 gel electrolyte for both FSS-ASC devices.

6.2 Experimental section:

6.2.1 Introduction:

The present section describes the electrode preparation (rGO/RuO_2, and WO_3), polymer gel electrolyte (PVA-H_2SO_4) preparation and fabrication of both rGO/RuO_2//WO_3 FSS-ASC devices.

6.2.2 Electrode Preparation:

The SILAR and CBD methods were used for rGO/RuO_2 thin films, and CBD method was prepared for WO_3 thin film deposited on a flexible SS substrate. Chapters IV and V, respectively, describe the optimized method parameters of rGO/RuO_2 thin film electrodes.

6.2.3 Deposition of WO_3 film:

The WO_3 is the promising electrode material utilized as an anode to fabricate flexible solid-state asymmetric supercapacitor (FSS-ASC) devices **[14, 15]**. It offers various advantages such as easy preparation, affordable, good efficiency, wide potential window, high theoretical C_s (~693 F g^{-1}), good corrosion stability, and natural abundance. As previously reported, WO_3 thin film was deposited using the CBD method **[16]**. Details of the experiment are as follows: 50 mL of DDW was used to dissolve 0.05 M sodium tungstate (Na_2WO_4), and to keep the pH of Na_2WO_4

solution at 1.5, diluted HCl was added drop by drop. The SS substrate was immersed in the solution and kept at a temperature of 353 K for 8 h. Due to temperature, controlled nucleation formation on the SS substrate surface was initiated and WO_3 particles grew by controlled heterogeneous nucleation followed by particle growth. These films were utilized for electrochemical characterizations and fabrication of an FSS-ASC device.

6.2.4 Preparation of Polymer Gel Electrolyte:

The PVA-H_2SO_4 gel electrolyte was essential in FSS-ASC device due to its flexibility and high ionic conductivity. The preparation process began by dissolving 1 g of PVA, a water-soluble synthetic polymer known for its film-forming and adhesive properties, in 10 mL of DDW. This mixture was continuously stirred at an elevated temperature of 353 K for 4 h, ensuring that PVA dissolved completely and formed a uniform, viscous solution. Once the PVA was fully dissolved, 10 mL of 1 M H_2SO_4 was carefully and gradually added to the solution to introduce proton conductivity. Sulfuric acid enhances the ionic mobility in the electrolyte. The slow addition of the acid prevented any abrupt reactions and ensured proper mixing. After the complete addition of the acid, the solution was subjected to vigorous stirring for an additional 6 h to achieve a homogeneous and stable gel electrolyte. In addition to improving ion transport between the electrodes, this gel acts as both an electrolyte and a separator, adding to mechanical flexibility and electrochemical performance of device essential components for the effective functioning of FSS-ASC devices.

6.2.5 Fabrication of rGO/RuO_2/PVA-H_2SO_4/WO_3 FSS-ASC device

To fabricate FSS-ASC device, SS substrates were cut into 5 × 5 cm^2 rectangular sheets, which served as the base for synthesizing the rGO/RuO_2 (cathode) and WO_3 (anode) electrodes. These substrates were coated with the respective electrode materials using deposition techniques, after which the surfaces of both electrodes were carefully coated with the PVA-H_2SO_4 gel electrolyte, ensuring a uniform and conductive layer between them. Once coated, the two electrodes were stacked together to form the FSS-ASC device. To secure the assembly and enhance its stability, the stacked electrodes were sealed using a plastic strip and put under to 0.5 tons of pressure for 4 h, ensuring proper contact and adhesion between the layers.

This process is illustrated in **Figure 6.1 A**. After fabrication, the thickness of the FSS-ASC device was measured at 0.455 mm, as shown in **Figure 6.1 B**. The flexibility of the device was then assessed by conducting cyclic voltammetry (CV) measurements at various bending angles, ranging from 0° to 160°, to evaluate the performance of device under mechanical stress. **Figures 6.1 C and D** depict the bending and twisting states of the fabricated rGO/RuO_2//WO_3 FSS-ASC device, demonstrating its mechanical flexibility and ability to maintain stable electrochemical performance even under significant deformation. This flexibility is crucial for its potential applications in wearable and portable electronics.

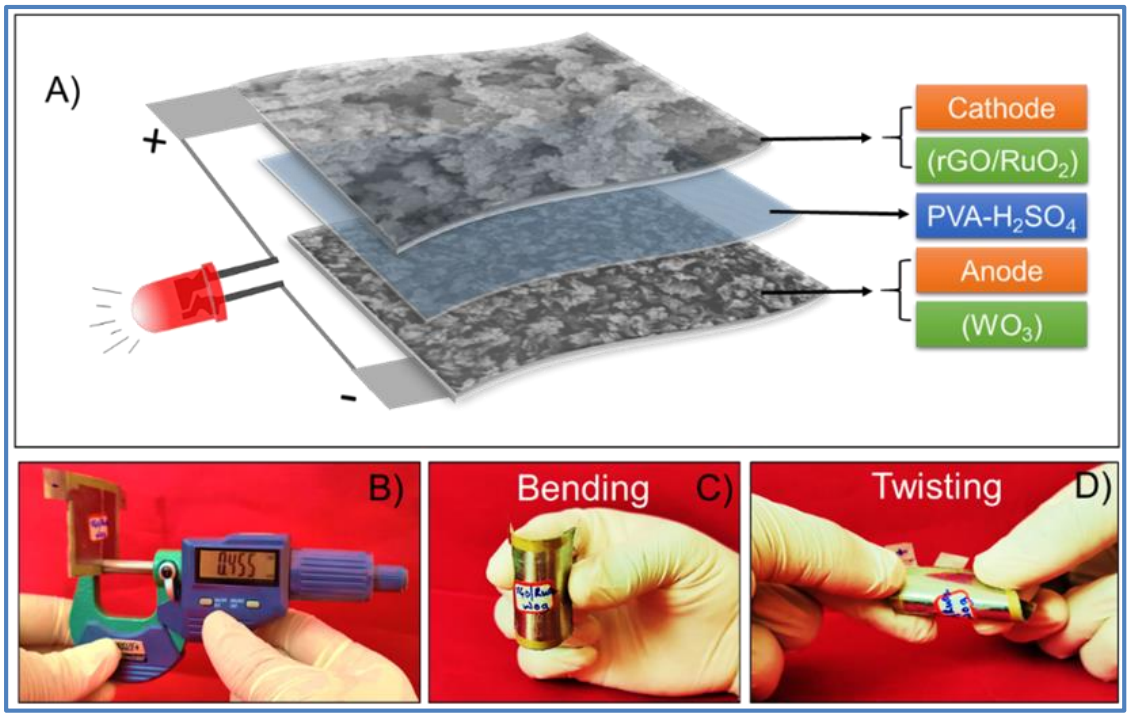

Figure 6.1: The procedure for fabrication of A) rGO/RuO_2/PVA-H_2SO_4/WO_3 FSS-ASC device, B) the thickness of the FSS-ASC device measured by the digital micrometer, and C and D) flexibility (physical bending and twisting) of FSS-ASC device.

6.2.6 Electrochemical characterization of FSS-ASC devices

Various current densities and scan rates were used in CV and GCD studies to optimize the operating voltage of FSS-ASC devices. Eq. 1.3 and 1.4 were used to determine S_E (Wh kg^{-1}) and S_P (W kg^{-1}) of the FSS-ASC device. The CV measurements were conducted at various bending angles to evaluate the mechanical

flexibility of the device and investigate the impact of deformation on its electrochemical performance. In order to guarantee long-term durability and performance retention, the FSS-ASC device cycle stability was further evaluated within 5,000 cycles using both CV and GCD techniques.

6.3 Results and Discussions:

6.3.1 Structural and Morphological Analysis of WO_3 electrode:

The XRD pattern of WO_3 thin film is presented in **Figure 6.2 A**. The observed diffraction peaks correspond to the crystallographic planes (020), (111), (002), (200), (022), (220), (202), (240), (331), (260), (402), and (440) of monoclinic WO_3, as referenced in JCPDS no.: 00-033-1387. Peaks marked with the symbol 'Δ' represent those from the stainless steel substrate. The relatively low intensity of the diffraction peaks suggests that WO_3 film is nanocrystalline in nature **[17]**.

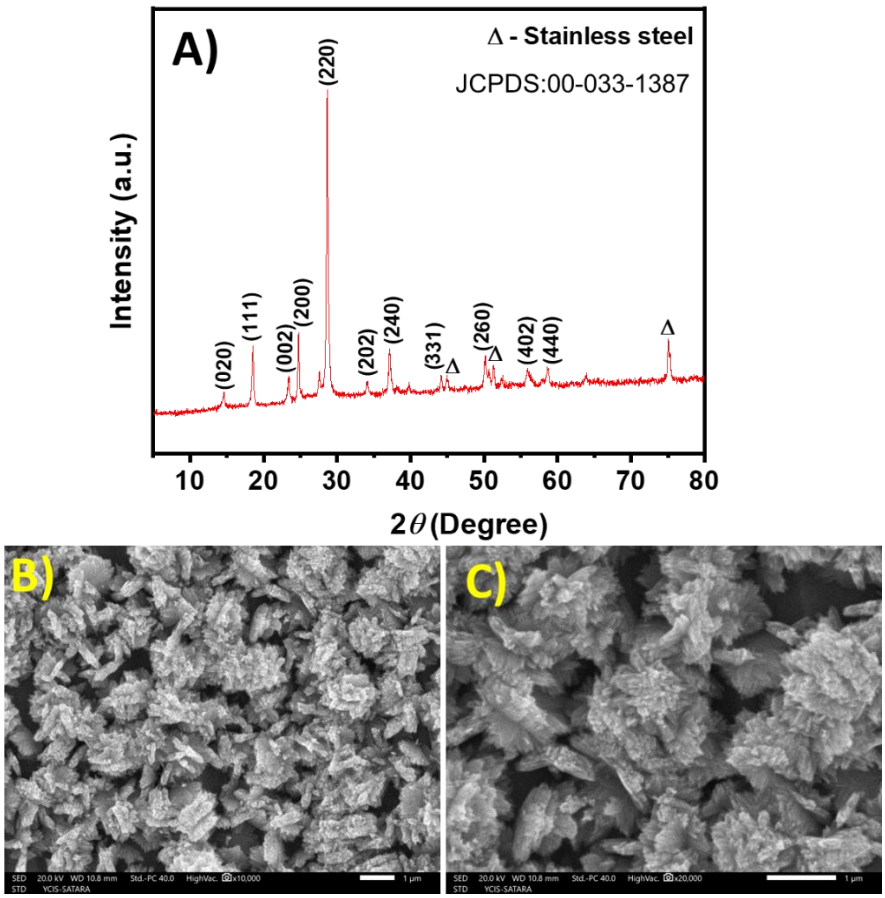

Figure 6.2: A) XRD pattern, B), and C) FE-SEM images of WO_3 film at two different magnifications (10 KX and 20 KX).

The surface morphology of the WO_3 thin film is depicted in **Figure 6.2 B and C** at magnifications of 10 KX and 20 KX, respectively. At the lower magnification, a uniform thin film formation is evident. In contrast, the higher magnification reveals a detailed surface structure characterized by interconnected nanoflakes, each approximately 1 µm in length, creating a distinctive grain-like pattern **[18]**. This morphology contributes to the overall electrochemical performance of the WO_3 film by providing an increased surface area for ion interaction. The presence of pores can be visually assessed, and increases the effective surface area for electrochemical reactions.

6.3.2 Electrochemical study of WO_3 thin film:

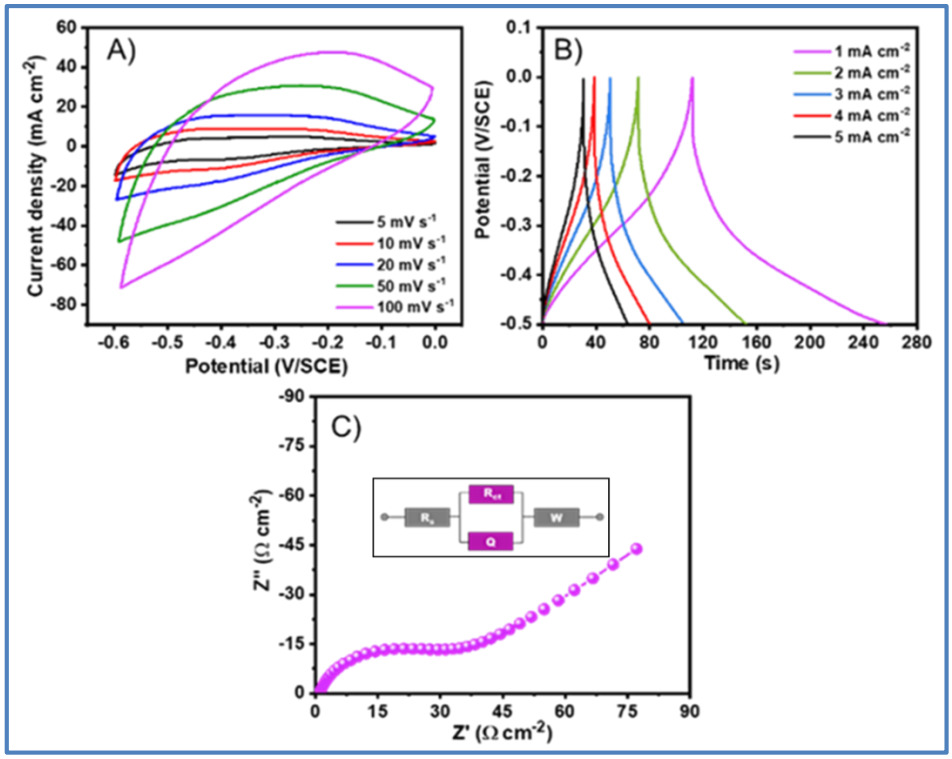

Figure 6.3: A) The CV curves at various scan rates from 5-100 mV s^{-1}, B) the GCD curves at various current densities from 1-5 mA cm^{-2}, and C) the Nyquist plot (inset shows the fitted equivalent electrical circuit) of WO_3 electrode.

Electrochemical analysis of WO_3 electrode was carried in the potential of -0.6 to 0 V/SCE in 1 M H_2SO_4 electrolyte. **Figure 6.3 A** represents the CV plots of WO_3 electrode at various scan rates (5-100 mV s^{-1}), and the area under CV curves was slowly increased with increasing scan rate and symmetric CV shape indicating the capacitive behavior **[19]**. **Figure 6.3 B** shows the GCD plots of WO_3 electrode at

various current densities (1- 5 mA cm^{-2}). A similar trend is observed in GCD plots, which shows the asymmetric nature of charging and discharging time. The C_s decreases with rising current density due to decreasing charging and discharging time. WO_3 electrode exhibited C_s of 634 F g^{-1} at 5 mV s^{-1} scan rate and 458 F g^{-1} at 1 mA cm^{-2} current density. The EIS technique was used to investigate the resistance and charge transfer characteristics of the electrode materials at frequencies ranging from 0.1 Hz to 1 MHz. Nyquist plot of WO_3 electrode is shown in **Figure 6.3 C**. The simulated equivalent electrical circuit is displayed as an inset image of **Figure 6.3 C**. The observed EIS parameters R_s, and R_{ct}, are 0.7 Ω cm^{-2}, and 53 Ω cm^{-2}, respectively. These lower values of WO_3 electrode are beneficial for electrochemical performance **[20]**.

6.3.3 Supercapacitive performance of rGO/RuO_2/PVA-H_2SO_4/WO_3 FSS-ASC device:

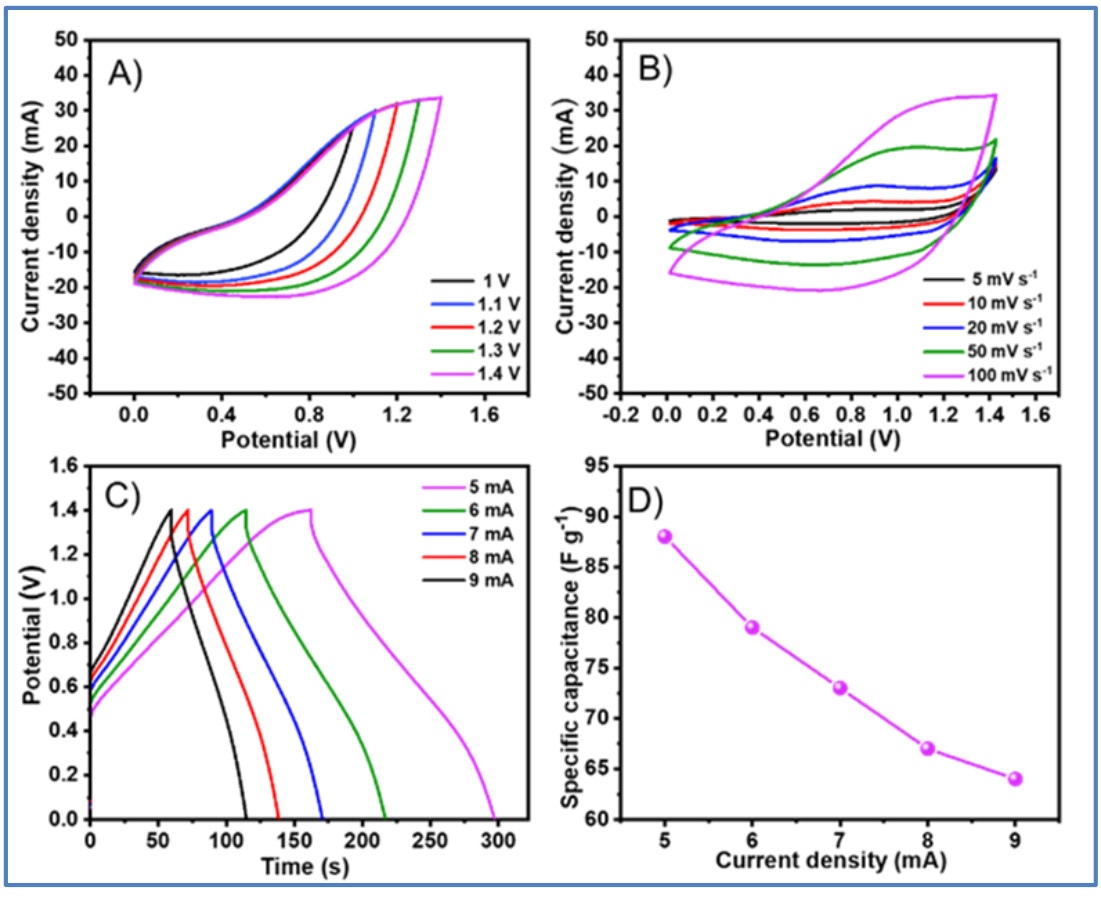

Figure 6.4: A) The CV curves measured at different potentials, B) the CV curves at measured different scan rates, C) the GCD curves measured at different current densities, and D) the variation of C_s with applied current density rGO/RuO_2/PVA-H_2SO_4/WO_3 device.

The electrochemical behavior of FSS-ASC (rGO/RuO_2/PVA-H_2SO_4/WO_3) device was assessed using the CV test. The advantages of solid-state devices are a wide potential window and safety. As shown in **Figure 6.4 A**, the CV profiles of the FSS-ASC device were evaluated at various potential windows 0 to +1.4 V at a 100 mV s^{-1} scan rate in order to optimize the operational potential window. The CV curves indicate pseudocapacitive charge storage from RuO_2, showing high current density values **[21, 22]**. It indicates that the FSS-ASC device can operate up to a potential of +1.4 V. Thus, additional CV measurements in the potential range of 0 to +1.4 V were performed at scan rates ranging from 5 to 100 mV s^{-1}, as illustrated in **Figure 6.4 B**. The C_s value of the FSS-ASC device is 114 F g^{-1} at a scan rate of 5 mV s^{-1}. The FSS-ASC device GCD graphs at various current densities ranging from 5 to 9 mA within a working potential range of 0 to +1.4 V are presented in **Figure 6.4 C**. The symmetric shape of the GCD profile indicates excellent supercapacitive behavior. It demonstrates the highest C_s of 88 F g^{-1} at 5 mA of current density. **Figure 6.4 D** displays the variation of C_s at various current densities (5–9 mA).

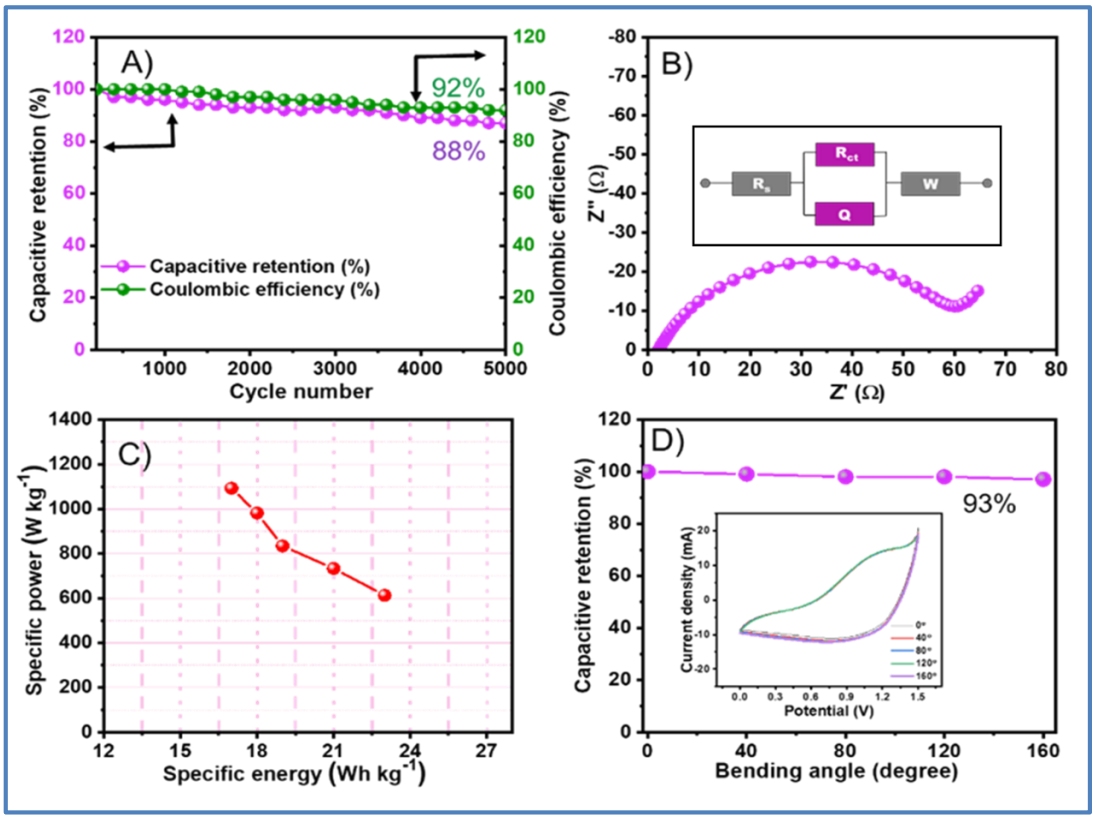

Figure 6.5 A) the specific capacitance retention and coulombic efficiency variation, B) the Nyquist plot (inset shows the fitted equivalent electrical circuit), C) Ragone plot, and D) the capacitance retention of the device at various bending angles (inset shows CV curves at different bending angles) of rGO/RuO_2/PVA-H_2SO_4/WO_3 device.

Cyclic stability is a crucial component for the use of supercapacitors. To evaluate the FSS-ASC device cyclability, GCD measurements were carried out over 5,000 cycles at a current density of 7 mA. The FSS-ASC device exhibits 92% coulombic efficiency and 88% capacitance retention, as shown in **Figure 6.5 A**. The Nyquist plot of FSS-ASC device is shown in **Figure 6.5 B,** and the inset shows a corresponding equivalent electrical circuit. The values of R_s (0.22 Ω), R_{ct} (5.2 Ω), Q (0.850 F), and W (0.053 Ω) indicate the good electrochemical behavior of FSS-ASC. The electrochemical values obtained from the Nyquist plot are listed in Table 6.2. The composition of rGO is responsible for the device improved stability over numerous GCD cycles. The Ragone plots of FSS-ASC device are presented in **Figure 6.5 C**. The FSS-ASC device shows a maximum S_E of 23 Wh kg^{-1} and S_P of 613 W kg^{-1}. These S_E and S_P values are suitable for commercial-level devices. Therefore, the flexibility of FSS-ASC was measured at different bending angles using CV technique (**Figure 6.5 D**). After bending at a 160° angle, the FSS-ASC device retained 93% of its initial C_s, suggesting that the device is flexible **(Figure 6.5 D)**. The CV profiles of the FSS-ASC device are displayed in the inset of **Figure 6.5 D** at bending angles ranging from 0° to 160° **[23]**. Additionally, the stability under bending conditions underscores its applicability in flexible and wearable energy storage systems.

To check the practical use of rGO/RuO_2/PVA-H_2SO_4/WO_3 device, two devices were connected in series and charged for 30 s at 2.6 V. Two FSS-ASC devices in series easily light up 201 light emitting diodes (LEDs) for 50 s **(Figure 6.6)**. This study demonstrated the practical use of rGO/RuO_2/PVA-H_2SO_4/WO_3 device in various portable electronic devices.

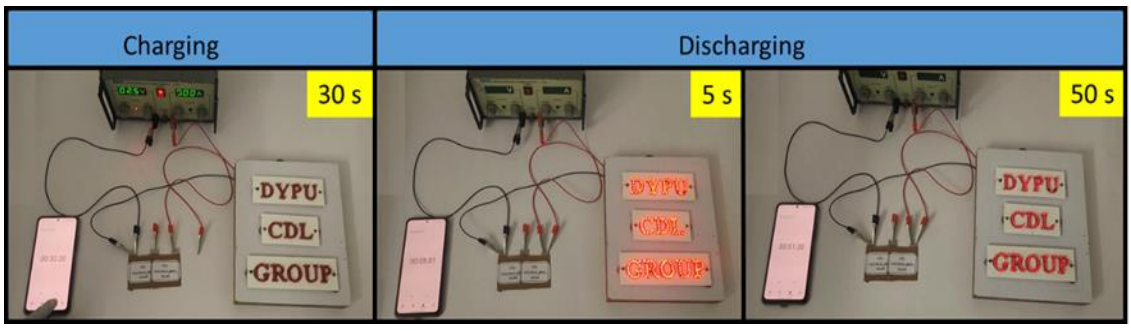

Figure 6.6: The rGO/RuO_2/PVA-H_2SO_4/WO_3 devices used to illuminate a panel of 201 red LEDs.

6.3.4 Electrochemical studies of rGO/RuO_2/PVA-H_2SO_4/WO_3 FSS-ASC device

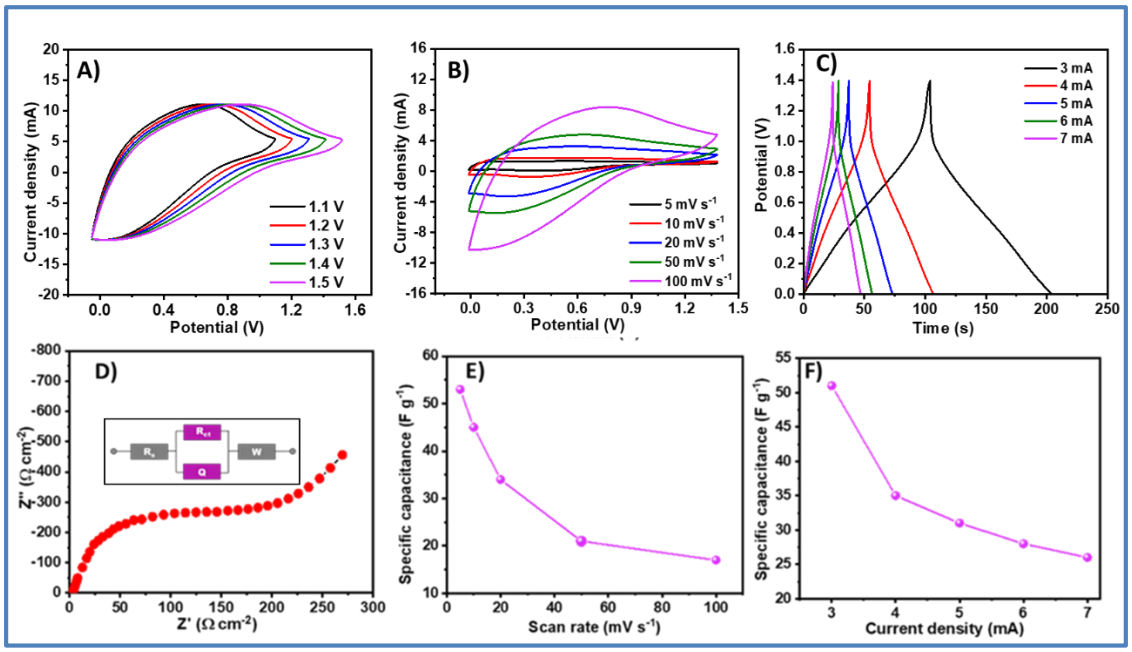

Figure 6.7: A) The CV curves measured at different potentials, B) the CV curves at measured different scan rates, C) the GCD curves measured at different current densities, D) the Nyquist plot (inset show the fitted equivalent electrical circuit), E) the variation of C_s with different scan rates, F) the variation of C_s with applied current density of rGO/RuO_2/PVA-H_2SO_4/WO_3 device.

The FSS-ASC device was developed to assess the practical viability of the prepared electrodes using a two-electrode configuration based on CBD method. In this device, rGO/RuO_2 electrode acts as the cathode, while the WO_3 electrode serves as the anode, with PVA-H_2SO_4 utilized as a gel electrolyte. The CV analysis was employed to investigate the electrochemical performance of the FSS-ASC device, which consists of rGO/RuO_2/PVA-H_2SO4/WO_3. Solid-state devices are known for having enhanced security features and large operating potential windows. To optimize the effective operational potential, the CV profiles of FSS-ASC devices were recorded at a scan rate of 100 mV s^{-1} over a range of potential windows, from 0 to +1.4 V, as shown in **Figure 6.7 A**. Due to the presence of RuO_2, the CV curves showed that the device shows pseudocapacitive charge storage abilities, which led to high current density values **[24]**. The CV measurements in the potential range of 0 to +1.4 V were performed at scan rates ranging from 5 to 100 mV s^{-1}, as illustrated in **Figure 6.7 B**. The C_s value of the FSS-ASC device is 53 F g^{-1} at a scan rate of 5 mV s^{-1}.

Longer charge-discharge times signify more capacity for storing charge at +1.4 V in the GCD plot, revealing that the FSS-ASC device exhibits superior charge storing capability. **Figure 6.7 C** illustrates the device GCD curves for currents density between 3 mA to 7mA, within the operating potential region of 0 to +1.4 V. According to calculations, the ASC maximum C_s is 49 F g^{-1} at a current density of 3 mA. Additionally, as seen in **Figure 6.7 D**, the EIS technique is utilized to compare the charge transfer mechanism of the FSS-ASC and the inset depicts the fitted equivalent circuit. The FSS-ASC displays minimum R_s (0.43 Ω) and R_{ct} (310 Ω) values. The performance of rGO/RuO_2 composite as an electrode material for supercapacitors is demonstrated by these reduced R_s and R_{ct} values, which are caused by its improved electrical conductivity and ion diffusion. More complication in the charge transport to the electrode is indicated by a higher R_{ct} value. Because the layered electrode structure offers more electro-active sites for electrochemical reactions as well as a vertical path for electron transfer and ion diffusion, it has beneficial charge transfer kinetics, demonstrated due to comparison low values of R_s and R_{ct}, which raise surface conductivity. **[25]**. The variation of C_s at different scan rates (5mV s^{-1} to 100 mV s^{-1}) shows in **Figure 6.7 E**. **Figure 6.7 F** displays the variation of C_s at various current densities (5–9 mA).

The FSS-ASC device exhibits 82% capacitance retention, as shown in **Figure 6.8 A**. The Ragone plots of FSS-ASC device are presented in **Figure 6.8 B**. The FSS-ASC device shows a maximum S_E of 15 Wh kg^{-1} and S_P of 562 W kg^{-1}. These S_E and S_P values are suitable for commercial-level devices.

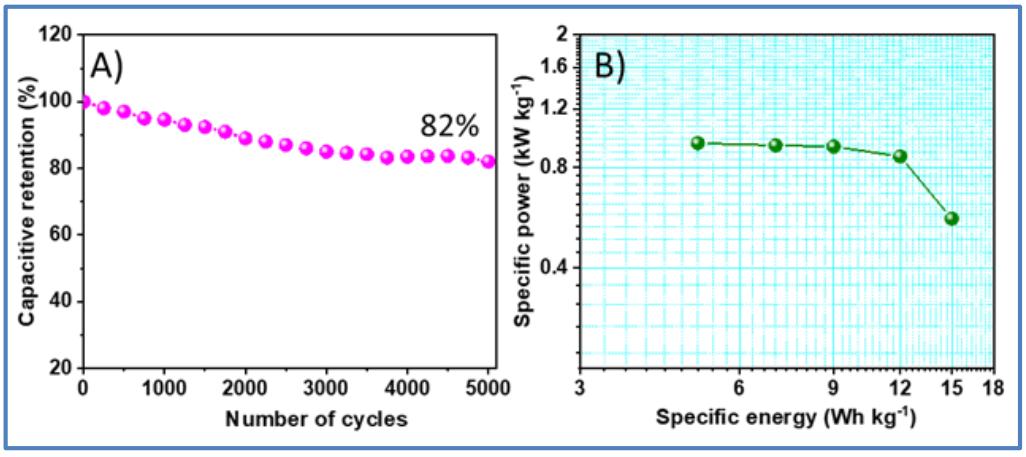

Figure 6.8 A) The specific capacitance retention and B) Ragone plot rGO/RuO_2/PVA-H_2SO_4/WO_3 device.

To check the practical use of rGO/RuO_2/PVA-H_2SO_4/WO_3 device, two devices were linked in series and charged for 30 s at 2.6 V. Two FSS-ASC devices in series easily light up 201 light emitting diodes (LEDs) for 40 s **(Figure 6.9)**. This study demonstrate the practical use of rGO/RuO_2/PVA-H_2SO_4/WO_3 device in various portable electronic devices.

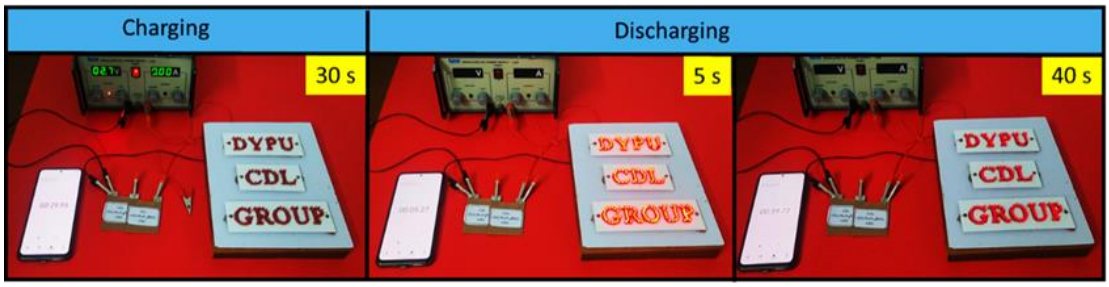

Figure 6.9: The rGO/RuO_2/PVA-H_2SO_4/WO_3 devices used to illuminate a panel of 201 red LEDs.

6.4 Conclusions:

In summary, rGO/RuO_2//WO_3 FSS-ASC device was assembled using anode and cathode electrodes such as RuO_2 and WO_3 with PVA-H_2SO_4 gel electrolyte. In the same way, rGO/RuO_2/PVA-H_2SO_4/WO_3 FSS-ASC device was also assembled. The rGO/RuO_2/PVA-H_2SO_4/WO_3 FSS-ASC (SILAR) device showed C_s of 116 and 88 F g^{-1} at a scan rate of 5 mV s^{-1} and a current density of 5 mA with excellent 88% capacity retention and columbic efficiency of 92% over 5,000 cycles with $_{SE}$ of 23 Wh kg^{-1} at S_P of 625 W kg^{-1}. The rGO/RuO_2/PVA-H_2SO_4/WO_3 (CBD) device observed C_s of 53 and 49 F g^{-1} at scan rate of 5 mV s^{-1} and a current density of 3 mA with excellent 82% capacity retention over 5,000 cycles with S_E of 15 Wh kg^{-1} at S_P of 562 W kg^{-1}. The ion transport and charge storage ability in SILAR deposited devices was improved due to their larger active surface area and enhanced interfacial contact with electrolyte. These results highlight the superior electrochemical performance of the rGO/RuO_2/PVA-H_2SO_4/WO_3 (SILAR) device, which offers higher capacitance, energy density, and overall efficiency compared to rGO/RuO_2/PVA-H_2SO_4/WO_3 (CBD) device.

References:

[1] E. Pomerantseva, and Y. Gogotsi. Nat. Energy, 7, (2017), 1-6.

[2] Y. Deng, Y. Xie, K. Zou, X. JiJ, Mater. Chem. A , 4, (2016), 1144-1173.

[3] Q. Wei, F. Xiong, S. Tan, L. Huang, E. Lan, B. Dunn, L. Mai, Adv Mater., 29, (2017), 1-39.

[4] Y.Gao and K. Huang, Chem. Asian J., 16, (2017), 1969-1984.

[5] L. Yu, H. Hu, H. Wu, X. Lou, Adv. Mater., 29, (2017), 1604563-1604576.

[6] L. Mai, X. Tian, X. Xu, L. Chang, L. Xu, Chem. Rev., 23, (2014), 11828-11862.

[7] X. Xie, K. Lee, J. Wang, K. Loh, Energy Environ. Sci., 4, (2011), 3960- 3975.

[8] K. Sankar and R. Selvan, RSC Adv., 4, (2014), 17555-17569.

[9] V. Nithya, and N. Arul, J. Mater. Chem. A, 4, (2016), 10767-10782.

[10] P. Goswami, H. Choudhury, S. Chakma, V. Moholkar, Ind. Eng. Chem., 52, (2013), 17848-17859.

[11] W. Ko, Y. Chen, K. Lu, K. Lin, Sci. Rep., 6, (2016), 18887-18899.

[12] I. Ivanishcheva, A. Ivanishchev, A. Dixit. Monatshefte Chem-Chemic, 150, (2019), 489-502.

[13] B. Zhao, D. Chen, X. Xiong, B. Song, R. Hu, Q. Zhang, B. Rainwater, G. Waller, D. Zhen, Y. Ding, Y. Chen, C. Qu, D. Dang, C. Wong, M. Liu. Energy Storage Mater., 7, (2017), 32-49.

[14] I. Kariper, F. Tezel, O. Gokkus, Phy. Lett. A, 388, (2021), 127059-127065,

[15] S. Ji, N. Chodankar, D. Kim, Electrochim. Acta., 325, (2019), 134879-134889,

[16] P. Shinde, V. Lokhande, N. Chodankar, T. Ji, J. Kim, C. Lokhande, J. Colloid Interface Sci., 483, (2016) 261-267.

[17] S. Ghosh, R. Santhosh, S. Jeniffer, V. Raghavan, G. Jacob, K. Nanaji, P. Kollu, S. Jeong, A. Grace, Sci. Rep., 9, (2019), 16315-16330.

[18] S. Gupta, H. Nishad, S. Chakane, S. Gosavi, D. Late, P. Walke, Nanoscale Adv., 2, (2020), 4689-4701.

[19] X. Liu, Q. Yang, L. Yuan, D. Qi, X. Wei, X. Zhou, S. Chen, L. Cao, Y. Zeng, J. Jia, C. Wang, J. Chem. Eng., 425, (2021), 131431-131444.

[20] F. Zheng, J. Wang, W. Liu, J. Zhou, H. Li, Y. Yu, P. Hu, W. Yan, Y. Liu, R. Li, Q. Zhen, Electrochim. Acta, 334, (2020), 135641-135682.

[21] S. Ubale, S. Kale, V. Mane, U. Patil, C. Lokhande, J. Electroanal. Chem., 897, (2021),115589-115607.

[22] S. Marje, V. Patil, V. Parale, H. Park, P. Shinde, J. Gunjakar, C. Lokhande, U. Patil, J. Chem. Eng., 429, (2022), 132184-132199.

[23] R. Bhosale, S. Kumbhar, P. Bagwade, H. Shelke, C. Lokhande, V. Jamadade. J. Mater. Sci. Mater. Electron. 35, (2024), 1-9.

[24] A. Joshi, S. Lalwani, G. Singh, R. Sharma, Electrochim. Acta, 297, (2019), 705-711.

[25] S. Ayaz, P. Mishra, R. Sharma, S. Kamal, S. Sen. ACS Appl. Nano Mater., 3, (2020), 4562-4572.

CHAPTER-VII

SUMMARY AND CONCLUSIONS

Summary and conclusions

In recent years, batteries, capacitors, and supercapacitors are among the electrical energy storage devices that are more accessible. The supercapacitor can hold charge quickly and have a better S_P than batteries. The supercapacitors are widely used in portable and wearable electronics, including medical and defence-related application. The batteries are not appropriate for use in portable electronic devices due to their short lifespan, minimal power, and safety concerns. In contrast, supercapacitors provide improved S_E, environmental storage of energy, greater S_P, and electrochemical cycle stability. As a result, supercapacitor technology is developing quickly to replace batteries and capacitors. These days, supercapacitors are utilized in many different applications, including flash cameras, hybrid electric cars, telecommunications, and power backup supplies, etc. In hybrid electric cars, more power is needed to get started.

Hybrid electric vehicles rely on supercapacitors for their high starting power and energy. The supercapacitors have limits with aqueous electrolytes, such as smaller reduction potential of metal cations and increased resistance to metal oxides. The novel energy storage supercapacitor device, the flexible solid-state ASC device, attracts attention because of its extended cycle life, high S_P, safety, and friendliness to the environment. Further research into electrode materials is needed to improve the performance of supercapacitors and address their limitations. The optimal active electrode materials combined with a supportable electrolyte effectively increases the flexible solid-state supercapacitor device power and energy capabilities quickly.

According to earlier studies, materials including CPs, metal oxides, and carbon-based materials improve the electrochemical properties of supercapacitor devices. Transition metal oxide have unique and important properties, such as high electrical conductivity like metals and the capability to transition between redox states. Thus, the fabrication of inexpensive and highly effective electrode materials of metal oxide is necessary.

The present work describes, synthesis of ruthenium oxide (RuO_2) thin films using an easy, inexpensive, and binder-free chemical method. The electrochemical properties of RuO_2 thin films were effectively increased by optimizing the number of preparative parameters to provide a highly porous structure with greater specific surface area. Compared to rGO and RuO_2 thin films, the composite thin films exhibited superior supercapacitor performance. As a result, for developing the flexible

solid-state ASC device, composite thin films with superior electrochemical properties served as positive electrode. Additionally, a broad potential window negative electrode composed of WO_3 was used.

Chapter-I provides an overview and literature review of several rGO/ RuO_2 composite electrode materials for supercapacitor application. It presents details on the methods used to extract energy from various energy sources. The significance of energy storage from renewable sources is highlighted. This article describes the basics of energy storage devices, including capacitors, batteries, and supercapacitors. There are descriptions of the advantages of supercapacitors over batteries and capacitors in terms of power and energy densities. The importance of thin films and nanostructures in materials is briefly described.

The section provides a detailed explanation of the supercapacitor mechanism. This covers the essential requirements of supercapacitors, including the active electrode material. RuO_2 play a significant role in supercapacitor application is described including contributions from non-faradaic and faradaic processes. Also, the literature review on rGO composite RuO_2 electrodes for supercapacitors and their properties are included and finally, the orientation and purpose of the thesis are described.

Chapter-II covers the introduction to thin films, a brief taxonomy of film deposition methods, the theoretical basis of SILAR and CBD methods, and their preparative parameters. Furthermore, many characterization techniques are used in the structural and surface textural analyses of thin films. Several characterisation techniques, including XRD, Raman spectroscopy, XPS, FE-SEM, EDAX, TEM, and contact angle measurement were utilized to assess the structural, morphological, and elemental compositional characteristics. Last section of this chapter focuses on supercapacitor. It covers supercapacitor device types such as symmetric, asymmetric, and hybrid capacitors. There includes a detailed explanation of the supercapacitive characteristics, such as cyclic voltammetry, galvanostatic charge-discharge and electrochemical impedance analysis.

In **Chapter-III**, amorphous RuO_2 thin films of different thicknesses were successfully synthesized using SILAR method. The variation in thickness was achieved by controlling the number of SILAR cycles (R1-150, R2-200, R3-250, R4-300) which directly influenced the morphology, mass loading, and electrochemical performance of the films. The morphology analysis confirmed that the RuO_2 thin

films exhibited a porous structure, an important factor for enhancing electrochemical properties. The thickness of the RuO_2 films played a critical role in determining their capacitive behavior. However, excessively thick films (more SILAR cycles) led to a decrease in electrochemical performance due to increased diffusion resistance, which hindered ion transport during redox reactions. Hence, an intermediate thickness, as observed in the R3 electrode, was optimal for achieving high capacitance. The electrochemical properties of RuO_2 electrodes were evaluated in a 1 M H_2SO_4 electrolyte. The R3 electrode, with an optimum thickness corresponding to a mass deposition of 1.56 mg cm^{-2}, achieved a maximum specific capacitance of 1146 F g^{-1} at a scan rate of 5 mV s^{-1}. This superior performance was attributed to the balance between sufficient active material and minimized diffusion limitations, which allowed for efficient charge storage through surface redox reactions. After 5000 cyclic voltammetry (CV) cycles, the R3 electrode retained 87% of its initial capacitance, demonstrating excellent cycling stability. This stability is crucial for practical supercapacitor applications, as it indicates sustained performance over prolonged usage. The enhanced durability can be attributed to the optimized thickness, which provided mechanical integrity and reduced stress accumulation during repeated cycling.

Furthermore, electrochemical impedance spectroscopy (EIS) measurements revealed that the porous structure of the R3 electrode, combined with its optimal thickness, resulted in a low Solution resistance (R_s), and Charge transfer resistance (R_{ct}). This low R_s and R_{ct} facilitated rapid ion diffusion and efficient electron transfer at the electrode-electrolyte interface, promoting fast surface redox reactions. In comparison to thinner or thicker electrodes, the R3 electrode's structure allowed for easier ion access, contributing to its superior electrochemical performance.

In **Chapter-IV**, RuO_2 and rGO/RuO_2 composite thin films were successfully deposited on flexible stainless steel (SS) substrates using the simple and cost-effective SILAR method. Additionally, the modified Hummer's method for rGO synthesis is discussed. The incorporation of rGO into the RuO_2 matrix significantly enhanced the electrochemical performance of the composite films. Morphological analysis revealed the successful anchoring of RuO_2 nanoparticles onto the conductive rGO sheets, which provided a synergistic effect for improved charge storage. The rGO/RuO_2 composite thin film, which was amorphous in nature, exhibited superior supercapacitive behavior compared to pure RuO_2 films. The addition of rGO

improved the overall electrical conductivity of the composite, as rGO provides a highly conductive matrix that facilitates faster electron transport. This enhanced conductivity is critical for minimizing internal resistance and ensuring efficient charge transfer during electrochemical reactions. Additionally, the 2D structure of rGO offers a large surface area, which enables better dispersion of RuO_2 nanoparticles and provides more active sites for electrochemical reactions.

As a result, the rGO/RuO_2 composite electrode achieved a high specific capacitance (C_s) of 1371 F g^{-1} at a scan rate of 5 mV s^{-1} in the potential window of 0 to +1.0 V versus the standard calomel electrode (SCE). The higher capacitance of the rGO/RuO_2 composite can be attributed to the dual contribution of pseudocapacitance from RuO_2 and the electric double-layer capacitance from the rGO sheets. The combination of these two mechanisms resulted in enhanced energy storage capabilities. The rGO/RuO_2 composite electrode demonstrates superior cyclic stability, with a retention of 90% after 5,000 GCD cycles.

In **Chapter-V**, the effect of temperature on the physico-chemical characteristics and electrochemical properties of RuO_2 thin films is studied. Chapter V covers the synthesis and characterisation of RuO_2 thin films using CBD method for evaluating electrochemical performance. The deposition RuO_2 films optimized at R1-333K, R2-343K and R3-353 K temperatures. At R2-343 K, RuO_2 film achieved a maximum thickness (1.34 mg cm^{-2}). This chapter also covers the synthesis of rGO with optimized with RuO_2 (R2-343 K) electrode using CBD method. The effect of rGO concentration on the electrochemical performance of rGO/R2 thin films was examined. The XRD, FTIR, and RAMAN study revealed formation of R1, R2, R3, and rGO/R2 thin films, respectively. The FE-SEM study shows the Millets-like surface morphology of R2 and composite film shows RuO_2 micro spherical anchoring on rGO sheets. The R2 electrode synthesized at 343 K showed a maximum C_s of 996 F g^{-1} at a scan rate of 5 mV s^{-1}, and 83% capacitive retention after 5000 cycles. The introduction of rGO nanosheet into R2 material efficiently enhances surface area of composite thin films. Due to this, rGO/R2 composite electrode showed a highest C_s of 1152 F g^{-1} at a scan rate of 5 mV s^{-1} in 1 M H_2SO_4 electrolyte and 84% capacitive retention after 5000 CV cycles. The R_s and R_{ct} values for R2 thin film were 1.3 and 150 Ω cm^{-2}, whereas rGO/R2 thin film were 0.6 and 72 Ω cm^{-2}, respectively. Therefore, by combining rGO and R2 in an appropriate ratio, it is possible to modify

the structural and morphological characteristics and enhance C_s. This chapter emphasizes the beneficial properties of rGO/RuO_2 thin film over RuO_2 and rGO thin films.

Chapter-VI, discusses the fabrication and electrochemical performance of flexible solid-state asymmetric supercapacitor (FSS-ASC) devices with the configuration rGO/RuO_2//WO_3, where reduced graphene oxide/ruthenium oxide (rGO/RuO_2) serves as the positive electrode (cathode) and tungsten trioxide (WO_3) as the negative electrode (anode). The WO_3 electrode was synthesized using the CBD method. Both devices utilize an ironically conducting PVA-H_2SO_4 gel as the electrolyte as well as a separator. For the first FSS-ASC device fabricated by SILAR method, rGO/RuO_2 and WO_3 thin films with an area of 5 × 5 cm^{-2} were used as the electrodes. The rGO/RuO_2 was employed as the positive electrode, while WO_3 was used as the negative electrode. In the second FSS-ASC device, both the rGO/RuO_2 and WO_3 electrodes were fabricated using the CBD method, with the same configuration (rGO/RuO_2//WO_3) and PVA-H_2SO_4 gel as the electrolyte. The fabrication of FSS-ASC device by SILAR method with the configuration rGO/RuO_2//WO_3. This device exhibited excellent C_s of 114 F g^{-1}. The superior performance of the FSS-ASC device can be attributed to the balanced combination of high energy and power densities. The device obtained a specific energy of 23 Wh kg^{-1} and a specific power of 613 W kg^{-1}, indicating its potential for high-performance energy storage applications. Moreover, the FSS-ASC device demonstrated excellent cycling stability, retaining 88% of its initial capacitance after 5000 GCD cycles. This retention reflects the structural stability of rGO/RuO_2 composite during repeated cycling. The incorporation of rGO not only improves the conductivity and capacitance but also enhances the mechanical robustness of the electrode material, preventing degradation during long-term operation.

In the second FSS-ASC device with the configuration of rGO/RuO_2//WO_3, the C_s achieved was 49 F g^{-1}. The impressive performance of this device is attributed to the balanced combination of high energy and power densities. Specifically, the device exhibited a specific energy of 15 Wh kg^{-1} and a specific power of 562 W kg^{-1}, demonstrating its potential for high-performance energy storage applications. Furthermore, the FSS-ASC device displayed excellent cycling stability, retaining 82% of its initial capacitance after 5000 GCD cycles, which highlights the structural integrity and durability of the rGO/RuO_2 composite during extended cycling. When

compared to devices fabricated using the CBD method, the SILAR method-based devices, such as the one described here, showed superior performance. The SILAR method enabled more controlled deposition of rGO/RuO_2, resulting in better adhesion to the substrate, improved uniformity, and enhanced porosity. These factors contributed to faster ion transport and greater utilization of active materials, leading to higher specific capacitance, improved energy and power densities, and greater cycling stability than CBD based devices. The results clearly demonstrate that the SILAR method offers a more efficient and reliable approach for fabricating high-performance supercapacitor devices.

In **Chapter-VII**, includes the conclusions from the above chapters. **Table 7.1** highlights the electrochemical properties of RuO_2, rGO/RuO_2 composite thin films. This table includes the methods of material preparation, electrolytes, C_s, R_s, R_{ct}, and cycle stability of electrodes. **Table 7.2** illustrates the electrochemical characteristics of both methods rGO/RuO_2//WO_3 FSS-ASC devices.

Table 7.1: The electrochemical parameters of RuO_2 and rGO/RuO_2 thin film electrodes deposited by SILAR and CBD methods in a three-electrode system.

Material	**Method**	**Electrolyte**	**C_s (F g^{-1})**	**R_s (Ω cm^{-2})**	**R_{ct} (Ω cm^{-2})**	**Stability (%) @ cycles**
R1	SILAR	1M H_2SO_4	253	2.2	75	-
R2			845	1.5	38	-
R3			1146	0.9	6.7	87@5,000
R4			1049	1.2	32	-
rGO	SILAR	1M H_2SO_4	98	1.2	4.5	97@5,000
rGO/RuO_2			1371	0.4	3.49	90@5,000
R1	CBD	1M H_2SO_4	489	2.6	280	-
R2			996	1.3	150	84@5,000
R3			771	2.8	310	-
rGO/R2			1152	0.6	72	89@5,000
WO_3	CBD	1M H_2SO_4	634	0.7	53	-

Table 7.2: The electrochemical parameters of flexible solid-state FSS-ASC devices evaluated using two electrode system.

Configuration of FSS-ASC device	C_s **(F g^{-1})**	S_E **(Wh kg^{-1}) at** S_P **(W kg^{-1})**	R_s	R_{ct}	**Stability (%) @ cycles**	**Flexibility (%) @160°**
rGO/RuO_2/PVA-H_2SO_4/WO_3	114	23 at 613	0.22	5.2	88@5,000	93@160°
rGO/RuO_2/PVA-H_2SO_4/WO_3	53	15 at 562	0.43	310	82@5,000	-

CHAPTER-VIII

80_RECOMMENDATIONS

80_Recommendations

8.1 Recommendations:

The present study explored the preparation of thin films of transition metal oxides using both the Successive Ionic Layer Adsorption and Reaction (SILAR) and Chemical Bath Deposition (CBD) methods. These techniques enabled the development of thin films with increased surface area and porous morphology, which are crucial for enhancing charge storage capacity in supercapacitor applications. Specifically, ruthenium oxide were combined with reduced graphene oxide (rGO) to form composite electrodes through both SILAR and CBD approaches. The goal of this composite fabrication was to improve the overall stability and electrochemical performance of the materials, resulting in higher specific capacitance compared to pristine materials. The incorporation of rGO into the composite electrodes played a key role in enhancing their electrical conductivity and providing additional active sites for electrochemical reactions. This addition not only increased the charge storage capacity but also improved the cycling stability of the electrodes, making them more suitable for long-term energy storage applications. Among the techniques used, RuO_2 thin films prepared by the SILAR method exhibited the best electrochemical performance.

The SILAR method allowed for more precise control over the film thickness and morphology, resulting in improved adhesion to the substrate, higher surface area, and enhanced porosity. These factors contributed to better ion transport and utilization of active material, leading to superior specific capacitance and cycling stability when compared to RuO_2 films prepared by the CBD method. To optimize performance, it was found that the ideal concentration of rGO in the composite electrode is 1.0 mg mL^{-1}. This optimized concentration provides the right balance between electrical conductivity and active surface area, ensuring maximum capacitance without compromising the structural integrity of the composite.

8.2 Future Directions:

In the current study, ruthenium oxide (RuO_2) thin films and their composites with highly conductive reduced graphene oxide (rGO) were successfully synthesized using both SILAR and CBD methods. These materials were systematically developed

for supercapacitor applications through controlled experimental approaches. The incorporation of rGO into the RuO_2 matrix was shown to significantly improve the electrical conductivity, specific surface area, and overall electrochemical performance of the electrodes. This, in turn, enhanced both the electrochemical energy storage capabilities and gas sensing properties of the composite materials. For future research, it is proposed to continue the development of RuO_2 and rGO/RuO_2 composite electrodes for application of gas sensors. In particular, a deeper investigation into the physical and chemical properties of these materials is needed. Advanced characterization techniques, such as X-ray diffraction (XRD), field emission scanning electron microscopy (FESEM), transmission electron microscopy (TEM), and X-ray photoelectron spectroscopy (XPS), should be employed to gain insights into the structure, morphology, and chemical composition of the electrodes. These analyses will help elucidate the mechanisms of energy storage, particularly in metal oxide based compounds, which have potential for enhanced performance in energy storage applications.

Moreover, to better understand the charge storage processes in both symmetric and asymmetric supercapacitor devices, future studies should incorporate in situ characterization techniques. Techniques such as Brunauer-Emmett-Teller (BET) surface area analysis and high-resolution transmission electron microscopy (HR-TEM) could provide real-time insights into the changes occurring within the material during energy storage and discharge cycles. This would also allow for a more thorough examination of the sensitivity, response time, and recovery time of the pristine and composite materials used in gas sensors. In addition, there is a promising avenue for further improving the electrochemical performance of RuO_2 thin films by exploring alternative carbon allotropes. While rGO has demonstrated considerable benefits, other materials such as fullerenes, carbon nanotubes (CNTs), multi-walled carbon nanotubes (MWCNTs), carbon aerogels, and carbon foams could offer even greater improvements in conductivity, surface area, and structural integrity. These materials, when combined with RuO_2, have the potential to further enhance the energy storage and sensing capabilities of the resulting composite electrodes.

The current research opens up a wide range of possibilities for the development of high-performance supercapacitors. By systematically studying the effects of different carbon-based materials and optimizing their interaction with RuO_2, it may be possible to create next-generation materials with exceptional

electrochemical properties. This could lead to more efficient energy storage devices and highly sensitive, fast-response gas sensors suitable for industrial and environmental applications.

PATENT

INTELLECTUAL PROPERTY INDIA
PATENTS | DESIGNS | TRADE MARKS
GEOGRAPHICAL INDICATIONS

सत्यमेव जयते

क्रम सं/SL No :022145459

पेटेंट कार्यालय,भारत सरकार | The Patent Office, Government Of India

पेटेंट प्रमाण पत्र | Patent Certificate

(पेटेंट नियमावली का नियम 74) | (Rule 74 of The Patents Rules)

पेटेंट सं. / Patent No.	:	542485
आवेदन सं. / Application No.	:	202321016608
फाइल करने की तारीख / Date of Filing	:	13/03/2023
पेटेंटी / Patentee	:	D.Y.PATIL EDUCATION SOCIETY (DEEMED TO BE UNIVERSITY)
आविष्कारकों का नाम /Name of Inventor(s)	:	1.PROF.CHANDRAKANT DNYANDEV LOKHANDE 2.MS.DIVYA CHANDRAKANT PAWAR 3.MR.AJINKYA GOVINDRAO BAGDE 4.MR.SURAJ RAVASAHEB SANKAPAL

प्रमाणित किया जाता है कि पेटेंटी को, उपरोक्त आवेदन में यथाप्रकटित *"METHOD OF SYNTHESIZING REDUCED GRAPHENE OXIDE/POLYANILINE COATING FOR ENERGY STORAGE APPLICATION THEREOF'* नामक आविष्कार के लिए, पेटेंट अधिनियम, 1970 के उपबंधों के अनुसार आज तारीख मार्च 2023 के तेरहवें दिन से बीस वर्ष की अवधि के लिए पेटेंट अनुदत्त किया गया है।

It is hereby certified that a patent has been granted to the patentee for an invention entitled *"METHOD OF SYNTHESIZING REDUCED GRAPHENE OXIDE/POLYANILINE COATING FOR ENERGY STORAGE APPLICATION THEREOF'* as disclosed in the above mentioned application for the term of 20 years from the 13th day of March 2023 in accordance with the provisions of the Patents Act,1970.

अनुदान की तारीख : 21/06/2024
Date of Grant :

पेटेंट नियंत्रक
Controller of Patents

टिप्पणी - इस पेटेंट के नवीकरण के लिए फीस, यदि इसे बनाए रखा जाना है, मार्च 2025 के तेरहवें दिन को और उसके पश्चात प्रत्येक वर्ष मे उसी दिन देय होगी।

Note. - The fees for renewal of this patent, if it is to be maintained, will fall / has fallen due on 13th day of March 2025 and on the same day in every year thereafter.

PUBLICATIONS

Chemical Engineering Journal 501 (2024) 157533

Contents lists available at ScienceDirect

Chemical Engineering Journal

journal homepage: www.elsevier.com/locate/cej

Review

Advancements in graphene and its derivatives based composite Materials: A comprehensive review on Synthesis, Characterization, and supercapacitive charge storage

Dhanaji Malavekar [a], Divya Pawar [b], Ajinkya Bagde [b], Sambhaji Khot [b], Suraj Sankapal [b], Shital Bachankar [c], Sharadchandra Patil [d], Chandrakant D. Lokhande [b,*], Jin Hyeok Kim [a,*]

[a] Optoelectronics Convergence Research Center and Department of Materials Science and Engineering, Chonnam National University, 300, Yongbong-Dong, Buk-Gu, Gwangju 61186, South Korea
[b] Centre for Interdisciplinary Research, D. Y. Patil Education Society, Kolhapur 416003, India
[c] Department of Intelligent Electronics and Computer Engineering, Chonnam National University, Gwangju, 61186, South Korea
[d] Department of Physics, Shivaji University, Kolhapur 416004, India

ARTICLE INFO

Keywords:
Composite materials
Graphene
Pseudocapacitor
Specific energy and power
Supercapacitor

ABSTRACT

Composite materials incorporating graphene have emerged as promising candidates for enhancing both energy and power density in supercapacitors, owing to graphene's exceptional electrical, mechanical, and chemical properties. These graphene properties enable the maintenance of cyclability without compromising performance. Over the last two decades, research on graphene and its derivatives has shifted from synthesis and applications to exploring their compositional blends with various materials for broader applications. Graphene and its derivatives like graphene oxide and reduced graphene oxide primarily consist of carbon, interconnected through σ bonds, responsible for impressive conductivity. This review presents a comprehensive overview of recent advancements in two dimensional (2D) graphene and its derivatives' composites with pseudocapacitive materials like transition metal compounds (hydroxides, oxides, chalcogenides, metalorganic frameworks, and MXenes), conducting polymers, metal nanoparticles, and other organic materials for supercapacitor applications. We highlight the evolution of synthesis and characterization methods for composite electrode materials, emphasizing their relevance to practical applications. Key compositions and the underlying charge storage mechanisms are also discussed. Finally, we explore the opportunities and challenges in using graphene and its derivatives' composites for practical energy storage in supercapacitors.

Abbreviations: **ACNRs**, Activated polyaniline-derived hollow carbon nanorods; **AgNPs**, Ag nanoparticles; **ASC**, Asymmetric supercapacitors; **ALD**, Atomic layer deposition; **BPMW**, Bi-pyrene-terminated molecular wires; **BN**, Boron nitride; **CBD**, Chemical bath deposition; **CC**, Carbon cloth; **CWCC**, Carbonized wood cell chamber; **CVD**, Chemical vapor deposition; **Co_3O_4**, Cobalt oxide; **CV**, Cyclic voltammetry; **DHAQ**, Dihydroxyanthraquinone; **EDL**, Electric double-layer; **EDLC**, Electrochemical double-layer capacitor; **EES**, Electrochemical energy storage; **EIS**, Electrochemical impedance spectroscopy; **FTIR**, Fourier transform infrared; **Au**, Gold; **G/AC**, Graphene/activated carbon; **G/SC**, Graphene/soft carbon; **GA**, Graphene aerogel; **GCD**, Galvanostatic charge discharge; **GO-CMC**, Graphene-carboxy methylcellulose; **GO**, Graphene oxide; **GQD**, Graphene quantum dots; **hrGO**, Holy reduced graphene oxide; **HSC**, Hybrid supercapacitor; **IrO_2**, Iridium oxide; **$FeCoS_2$**, Iron cobalt sulphide; **LDH**, Layered double hydroxide; **LICs**, Li-ion capacitor; **LIMCs**, Li-ion micro capacitors; **MnO_2**, Manganese oxide; **MVO**, Manganese vanadate; **MOFs**, Metal-organic frameworks; **CH_4**, Methane; **MSCs**, Micro-supercapacitors; **MoS_2**, Molybdenum disulphide; **$MoSe_2$**, Molybdenum diselenide; **MWCNT**, Multi-walled carbon nanotubes; **NiO/NLIG**, N-doped laser-induced graphene; **NiCo-P**, Nickel cobalt phosphate; **NiV-LDH**, Nickel–vanadium LDH; **NSC**, Nitrogen and sulfur in carbon mircosheets; **OCC**, Oxidized carbon cloth; **PANI**, Polyaniline; **PEDOT**, Poly 3,4-ethylenedioxythiophene; **PI**, Polyimide; **PPy**, Polypyrrole; **PTh**, Polythiophene; **PGF**, Porous graphene skeleton; **rGO**, Reduced graphene oxide; **RuO2**, Ruthenium oxide; **SEM**, Scanning electron microscopy; **SiC**, Silicon carbide; **SILAR**, Successive ionic layer adsorption and reaction; **S-rGO**, Sulfur doped graphene; **SSC**, Symmetric supercapacitors; **TGA**, Thermogravimetric analysis; **3D**, Three-dimensional; **TEM**, Transmission electron microscopy; **TMCs**, Transition metal chalcogenides; **2D**, Two-dimensional; **UCNG**, Ultrafine Co_3O_4 nanoparticles/graphene; **XRD**, X-ray diffraction; **XPS**, X-ray photoelectron spectroscopy; **ZIFs**, Zeolitic imidazolate frameworks.

* Corresponding authors at: Centre for Interdisciplinary Research, D. Y. Patil Education Society, Kolhapur 416003, India (C.D. Lokhande). Optoelectronics Convergence Research Center and Department of Materials Science and Engineering, Chonnam National University, 300, Yongbong-Dong, Buk-Gu, Gwangju 61186, South Korea (Jin Hyeok Kim).

E-mail addresses: l_chandrakant@yahoo.com (C.D. Lokhande), jinhyeok@chonnam.ac.kr (J. Hyeok Kim).

https://doi.org/10.1016/j.cej.2024.157533
Received 14 August 2024; Received in revised form 30 October 2024; Accepted 7 November 2024
Available online 9 November 2024

Journal of Physics and Chemistry of Solids 195 (2024) 112286

Contents lists available at ScienceDirect

Journal of Physics and Chemistry of Solids

journal homepage: www.elsevier.com/locate/jpcs

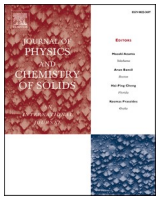

Sequential growth controlled copper vanadate nanopebbles embedded thin films: Electrode to asymmetric supercapacitive device assembly☆

Suraj R. Sankapal [a], Tushar B. Deshmukh [b], Ajinkya G. Bagde [a], Komal Patil [c], Babasaheb R. Sankapal [b], Chandrakant D. Lokhande [a,*]

[a] Centre for Interdisciplinary Research, D. Y. Patil Education Society (Deemed to Be University), Kolhapur, 416 003, India
[b] Department of Physics, NMDL (Nano Materials and Device Laboratory), Visvesvaraya National Institute of Technology, South Ambazari Road, Nagpur, Maharashtra, 440010, India
[c] Optoelectronic Convergence Research Center, Department of Materials Science and Engineering, Chonnam National University, Gwangju, 500-757, South Korea

ARTICLE INFO

Keywords:
Asymmetric supercapacitor
Chemical method
Copper vanadate oxide
Supercapacitor

ABSTRACT

Supercapacitor performance critically relies on the design of electrodes with both superior electrochemical and mechanical properties. In this study, we present a cost-effective and scalable approach for the synthesis of copper vanadate ($Cu_3V_2O_8$) nanopebbles integrated into a thin film, tailored for supercapacitor applications. The synthesis was accomplished using the successive ionic layer adsorption and reaction (SILAR) method, which enabled precise control over the deposition of $Cu_3V_2O_8$ on a stainless steel (SS) substrate. Detailed structural, morphological, and elemental characterizations confirm the successful formation and reveal critical insights into the chemical bonding and oxidation state at material. The supercapacitive performance of $Cu_3V_2O_8$ electrode has been evaluated in an aqueous $NaClO_4$ electrolyte to assess pseudocapacitive behavior. The $Cu_3V_2O_8$ electrode exhibited a specific capacitance of 443 F g^{-1} at 5 mV s^{-1} scan rate. Additionally, liquid configured an asymmetric device was designed using Multiwalled carbon nanotubes (MWCNT) combined with $Cu_3V_2O_8$, yielding a specific capacitance of 116 F g^{-1} at 5 mV s^{-1} with an energy density of 8.43 Wh kg^{-1} and a power density of 345.4 W kg^{-1}, while maintaining capacitance retention of 76 % even after 4000 cycles as stability test. This work highlights the potential of $Cu_3V_2O_8$ based materials for excellent performance of new avenues for energy storage.

1. Introduction

Worldwide energy sources are running out quite rapidly, and the ecosystem of the planet is seriously degrading. Recent survey data indicates that worldwide consumption of energy from renewable sources continues to trend upward [1,2]. The growing focus on energy from renewable sources, such as solar, wind, and tide-generated electricity, is a result of both the growing requirement for energy and the deliberate efforts to lessen the environmental damage caused by the consumption of conventional fossil fuels [3,4]. Recent years witnessed an enormous rise in interest in the issue of energy and environmental degradation, which led to the development of new, highly efficient energy conversion and storage technologies [5,6]. Supercapacitors (SCs) are one type of electrochemical energy storage device that has attracted a lot of attention due to its remarkable features, which include high power density (PD), fast charging and discharging times, and long operational life [7–10]. The utilization of SCs is on the rise, driven by advancements in nanoscale materials and technologies. The primary advantage of SCs over ordinary capacitors is their enhanced energy density (ED) [11,12]. While standard capacitors store energy through the electrostatic field between two conductive plates SCs use a different mechanism, often involving electrochemical double-layer capacitance (EDLC) and pseudocapacitor [13–15]. Energy storage mechanisms in EDLCs stem from the separation of electronic and ionic charge processes at the interfaces between the electrolyte and electrode [16]. Carbon nanotubes, activated carbon, graphene, carbon aerogel, and diamond, exhibit EDLC-type behavior whereas metal sulfides/oxides and conducting polymers primarily accumulate charge through a rapid, reversible redox course, leading to pseudocapacitance [17,18].

Transitional metal oxides (MO), including cobalt oxide (CoO), zinc oxide (ZnO), nickel oxide (Ni_2O_3), copper oxide (CuO), and manganese oxide (MnO_2), are promising candidates for SC application due to its

☆ In this article for first time, we report $Cu_3V_2O_8$ for supercapacitive study by SILAR method at various deposition cycles.

* Corresponding author.
E-mail address: l_chandrakant@yahoo.com (C.D. Lokhande).

https://doi.org/10.1016/j.jpcs.2024.112286
Received 4 June 2024; Received in revised form 17 August 2024; Accepted 22 August 2024
Available online 24 August 2024

Materials Science and Engineering B 292 (2023) 116432

Contents lists available at ScienceDirect

Materials Science & Engineering B

journal homepage: www.elsevier.com/locate/mseb

Performance of chemically synthesized polyaniline film based asymmetric supercapacitor: Effect of reaction bath temperature

D.C. Pawar [a], D.B. Malavekar [b], S.D. Khot [a], A.G. Bagde [a], C.D. Lokhande [a,*]

[a] Centre for Interdisciplinary Research, D.Y. Patil Education Society, Kolhapur 416 006, India
[b] School of Materials Science and Engineering, Chonnam National University, Gwangju 500757, South Korea

ARTICLE INFO

Keywords:
Asymmetric supercapacitor
Chemical bath deposition
Hybrid supercapacitor
Polyaniline
Tungsten oxide

ABSTRACT

Polyaniline (PANI) electrodes were prepared using chemical bath deposition method at various reaction bath temperatures ranging from 263 to 323 K. The specific surface area and wettability of films are significantly impacted by the polymerization temperature, which influences the electrochemical performance of electrodes. The electrode synthesized at 303 K showed a maximum specific surface area of 25 $m^2\ g^{-1}$, specific capacitance (C_s) of 816F g^{-1} (0.11F cm^{-2}) at a scan rate of 0.005 V s^{-1}, and 89% capacitive retention after 1,000 cyclic voltammetry (CV) cycles. An aqueous asymmetric supercapacitor device was fabricated using PANI as a cathode and tungsten oxide (WO_3) as an anode in 1 M H_2SO_4 electrolyte. The fabricated PANI/H_2SO_4/WO_3 device achieved a maximum C_s of 43 F g^{-1} with an energy density of 12 Wh kg^{-1} at a power density of 0.88 kW kg^{-1} and 72 % capacitive retention after 10,000 CV cycles.

1. Introduction:

In response to the fast growth of the global economy, the depletion of fossil fuels, and the degradation of ecosystems, there is a critical need to improve extremely effective, inexhaustible, and environment friendly methods for the conversion and storage of energy. This has animated advances in converting renewable energy through greenways and innovations related to electrochemical energy storage, i.e., supercapacitors and batteries [1,2]. Because of their inherent electrochemical properties, such as fast charge–discharge, long cycle stability, greater energy density compared to capacitors, and larger power density than ordinary batteries, supercapacitors have been explored as key enabler for the next generation energy storage device. Supercapacitor materials are split into three groups based on charge storage mechanisms: electric double-layer capacitors (EDLC), pseudocapacitors, and battery-type supercapacitors [3].

In EDLC capacitors, charge storage is caused by an electrostatic process at the electrode/electrolyte interface. EDLC materials are carbon-based, such as carbon nanotubes (CNT), activated carbon, and carbon aerogel, etc. [4-6]. The pseudocapacitor charge-storage system essentially depends on exchanging charge through the electrolyte and electrode surface redox reactions. Pseudocapacitor materials include transition metal chalcogenides and conducting polymers such as polyaniline (PANI) [7], polypyrrole (Ppy), and polythiophene (PT) [8,9]. The charge storage mechanism is based on strongly electrochemical redox reactions in battery-type materials, like Ni-based materials. Conducting polymers have unique and important properties, such as high electrical conductivity like metals and the capability to transition between redox states. PANI is an excellent material among conducting polymers and has been studied recently due to its easy synthesis process, low price, and interesting redox properties applicable in supercapacitor devices [10].

A convenient method for significant deposition on many substrates is the chemical bath deposition (CBD) method. It is quite an easy and cheap method compared to other methods. The development of nucleation is essential for the formation of precipitates. The result of nucleation in solution is that the molecular clusters produced quickly decompose, and particles combine to grow the film to a particular thickness. The controlled precipitation of the desired compound from a solution of its constituents is the fundamental principle of the CBD method [11,12].

The reaction temperature is more important in thin film preparation since it impacts the rate of reaction, morphology, thickness, surface wettability, and pore size, which determine the ions transport kinetics [13]. However, a complete understanding of its impact on electrode electrochemical activity is still lacking. The specific surface area of the

* Corresponding author.
E-mail address: l_chandrakant@yahoo.com (C.D. Lokhande).

https://doi.org/10.1016/j.mseb.2023.116432
Received 22 December 2022; Received in revised form 22 February 2023; Accepted 5 March 2023
Available online 14 March 2023

European Polymer Journal 218 (2024) 113366

Contents lists available at ScienceDirect

European Polymer Journal

journal homepage: www.elsevier.com/locate/europolj

Synthesis of reduced graphene oxide (rGO)/polyaniline (PANI) composite electrode for energy storage: Aqueous asymmetric supercapacitor

D.C. Pawar, A.G. Bagde, J.P. Thorat, C.D. Lokhande *

Centre for Interdisciplinary Research, D.Y. Patil Education Society, Kolhapur 416 003, India

ARTICLE INFO

Keywords:
Asymmetric supercapacitor
Chemical bath deposition
Composite electrodes
Polyaniline
Reduced graphene oxide

ABSTRACT

Composite materials have gained significant interest for energy storage applications due to their possible synergistic effects. This work describes the synthesis of reduced graphene oxide (rGO)/polyaniline (PANI) composite thin films using chemical bath deposition (CBD) method. A field-emission scanning electron microscope revealed that PANI spikes coated on rGO sheets in rGO/PANI composite. The electrochemical studies of a rGO/PANI composite electrode showed a specific capacitance (C_s) of 1130F/g C_s at a scan rate of 5 mV/s in 1 M H_2SO_4 electrolyte. The combined effect of rGO with PANI, a aqueous asymmetric supercapacitor device (ASC) with configuration of rGO/PANI/H_2SO_4/WO_3 produced 97F/g C_s at a 5 mV/s scan rate and retained 82 % capacitance after 5,000 galvanostatic charge–discharge cycles. The ASC achieved a high specific energy of 23 Wh kg^{-1} at a specific power of 732 W kg^{-1}. The electrochemical properties of rGO/PANI composite indicate a feasible method for creating asymmetric supercapacitors.

1. Introduction

Excessive use of non-renewable energy has raised global worries about energy consumption and ecological balance. Thus, there is a tremendous interest in the extraction and use of renewable but erratic energy sources like wind, tidal, and solar energy [1]. To accomplish this goal, significant progress needs to be achieved in the creation of energy storage and conversion technologies that are highly efficient, environmentally friendly, and affordable [2]. In term of new energy storage technologies, supercapacitors are often used in mobile phones, electric cars and laptops because of their quick charging, extended lifespans, high specific capacitance, and safety [3–5]. Supercapacitors (SCs) may be categorised into three groups based on the materials used for their electrodes: electrical double layer capacitors (EDLCs), pseudocapacitors, and hybrid supercapacitors. The value of specific capacitance for pseudocapacitor materials, resulting from the faraday charge storage process, is several times greater than that of an EDLCs [6,7]. Pseudocapacitor materials involves conductive polymers and transition metal oxides. Conducive polymers are considered as one of the best materials for flexible supercapacitor electrodes due to its remarkable benefits of excellent redox activity, electrical conductivity, and flexible mechanical properties [8]. Among the several conductive polymers, including polyaniline (PANI), polythiophene (PTh), polycarbazole and their derivatives, PANI is widely recognized as one of the most economically valuable materials due to its benefits including simple production, simple doping and dedoping, high electrical conductivity, and strong environmental stability [9]. Although PANI molecular chain undergoes repetitive contraction and expansion throughout the charging and discharging process, which damages its conjugated structure and results in the electrode materials weak cyclic stability [10].

In EDLCs, charges are accumulated at the electrode–electrolyte contact and there is no charge transfer between them. Since no chemical reactions involved in the charge storage process, it provides high reversibility with improved cycle stability of SCs. [11]. Due to this, graphene, a two-dimensional material is essential in EDLC as an electrode material. Theoretically, graphene shows a large specific surface area (2630 m^2/g), superior chemical stability, a relatively wide potential range, and rapid electron mobility [12]. The stacking of π-π bond between graphene sheets causes agglomeration in graphene, which changes its functionality and decrease the specific capacitance. Due to these inherent limitations, there is a relatively low energy density [13]. As a consequence, the drawbacks of PANI and graphene can be solved by combining them to create composite material for SCs. By adding reduced graphene oxide (rGO) sheets in PANI matrix to improve their surface area, electrochemical processes, diffusion route, and increasing energy and power density. The non-covalent bonding of rGO sheets and PANI

* Corresponding author.
E-mail address: l_chandrakant@yahoo.com (C.D. Lokhande).

https://doi.org/10.1016/j.eurpolymj.2024.113366
Received 28 March 2024; Received in revised form 30 May 2024; Accepted 31 July 2024
Available online 2 August 2024

Journal of Physics and Chemistry of Solids 179 (2023) 111386

Contents lists available at ScienceDirect

Journal of Physics and Chemistry of Solids

journal homepage: www.elsevier.com/locate/jpcs

Pseudocapacitive performance of amorphous ruthenium oxide deposited by successive ionic layer adsorption and reaction (SILAR): Effect of thickness

A.G. Bagde [a], D.B. Malavekar [b], D.C. Pawar [a], S.D. Khot [a], C.D. Lokhande [a,*]

[a] Centre for Interdisciplinary Research, D. Y. Patil Education Society, Kolhapur, 416 006, India
[b] School of Materials Science and Engineering, Chonnam National University, Gwangju, 500757, South Korea

ARTICLE INFO

Keywords:
Ruthenium oxide
Successive ionic layer adsorption and reaction (SILAR)
Supercapacitor
Thin film

ABSTRACT

Developing and fabricating effective, affordable electrode materials for supercapacitors is still a challenge. Electrical conductivity, a large surface area, dynamic faster electron transport, and other customizable qualities are present in metal oxide materials while being inexpensive to manufacture. In this work, successive ionic layer adsorption and reaction (SILAR) method was employed for deposition of amorphous ruthenium oxide (RuO_2) thin films of different thicknesses on a stainless steel substrate. At 1.56 mg cm^{-2} thickness amorphous RuO_2 achieved a maximum specific capacitance (C_s) of 1146 F g^{-1} at a scan rate of 5 mV s^{-1} with 87% capacitance retention up to 5000 cycles. These findings bolster the idea of cost effective deposition of amorphous RuO_2 material for supercapacitor applications.

1. Introduction

Enhancing the capacity of energy storage systems has certainly been the subject of significant study worldwide because of growing need for large-capacity power storage for use in hybrid electric cars, armed forces gears, lightweight and versatile digital devices, and designate biomedical gear [1–4]. However, the more accomplished energy that is sustainable is not suitable to meet the energy storage demands. Hence, this energy storage transformation is important for research as well as industries. Supercapacitor (SC) signifies a rising energy storage system category that has drawn interest because it offers a greater energy density than conventional capacitors. The SCs possess a higher capacity for rapid charging and discharging and longer cycle life than rechargeable batteries [5]. The electrode material is crucial in the design of SC. It is effectively tuneable for the crucial electrochemical performances of the SC. The taxonomy of SCs is classified in three kinds, such as electric double layer capacitor (EDLC), pseudocapacitor, and hybrid capacitor, based on their charge storage techniques. In EDLCs, energy storage mechanisms arise from electronic and ionic charge processes that are separated at the interfaces between electrode and electrolyte. The EDLC-type behaviour has been shown by carbon-based materials, like activated carbon, carbon nanotubes, graphene, diamond, carbon aerogel, etc. [6]. On the other hand, metal oxides/sulfides and conducting polymers store charge mostly by a quick, reversible redox process that results in pseudocapacitance [7–9]. Here, electron transport takes place chemically, producing the excess pseudocapacitance at a certain potential. Here, charge storage is carried out by bulk of material, enhancing the specific energy density and device capacitance [10]. Both methods of charge storage reveal both beneficial and undesirable electrochemical qualities. The efficiency of a single-charge storage method is insufficient to compete with batteries. In this sense, the deployment of a performance-oriented energy storage system requires the development of a hybrid strategy. Both types of charge storage methods are included in the hybrid strategy. The capacitive method increases device stability and electronic conductivity by having a large surface area and an efficient charge transportation path [11].

Ruthenium oxide (RuO_2), one of the most popular metal oxide has been extensively researched due to its enormous surface area, excellent reversibility, and relatively high capacitance [12]. Recently, it has also been revealed that RuO_2 has excellent electrocatalytic activity in a wide range of electrochemical processes [13]. The stable RuO_2 mainly adopts the “rutile structure” of RuO_2, even though it is observed in other variations with respect to liquid hydrate. Its molecular orbital theory effectively explained the thermodynamic stability and large isotropic charge transportation characteristics of RuO_2. Additionally, RuO_2 has a long cycle life with tunable-metallic conductivity, multiple oxidation states, and durable stability across a broad potential range. In fact, these characteristics have greatly aided SC research. However, a few

* Corresponding author.
E-mail address: l_chandrakant@yahoo.com (C.D. Lokhande).

https://doi.org/10.1016/j.jpcs.2023.111386
Received 15 February 2023; Received in revised form 6 April 2023; Accepted 17 April 2023
Available online 17 April 2023

Chemical Engineering Journal 501 (2024) 157533

Contents lists available at ScienceDirect

Chemical Engineering Journal

journal homepage: www.elsevier.com/locate/cej

Review

Advancements in graphene and its derivatives based composite Materials: A comprehensive review on Synthesis, Characterization, and supercapacitive charge storage

Dhanaji Malavekar [a], Divya Pawar [b], Ajinkya Bagde [b], Sambhaji Khot [b], Suraj Sankapal [b], Shital Bachankar [c], Sharadchandra Patil [d], Chandrakant D. Lokhande [b,*], Jin Hyeok Kim [a,*]

[a] Optoelectronics Convergence Research Center and Department of Materials Science and Engineering, Chonnam National University, 300, Yongbong-Dong, Buk-Gu, Gwangju 61186, South Korea
[b] Centre for Interdisciplinary Research, D. Y. Patil Education Society, Kolhapur 416003, India
[c] Department of Intelligent Electronics and Computer Engineering, Chonnam National University, Gwangju, 61186, South Korea
[d] Department of Physics, Shivaji University, Kolhapur 416004, India

ARTICLE INFO

Keywords:
Composite materials
Graphene
Pseudocapacitor
Specific energy and power
Supercapacitor

ABSTRACT

Composite materials incorporating graphene have emerged as promising candidates for enhancing both energy and power density in supercapacitors, owing to graphene's exceptional electrical, mechanical, and chemical properties. These graphene properties enable the maintenance of cyclability without compromising performance. Over the last two decades, research on graphene and its derivatives has shifted from synthesis and applications to exploring their compositional blends with various materials for broader applications. Graphene and its derivatives like graphene oxide and reduced graphene oxide primarily consist of carbon, interconnected through σ bonds, responsible for impressive conductivity. This review presents a comprehensive overview of recent advancements in two dimensional (2D) graphene and its derivatives' composites with pseudocapacitive materials like transition metal compounds (hydroxides, oxides, chalcogenides, metalorganic frameworks, and MXenes), conducting polymers, metal nanoparticles, and other organic materials for supercapacitor applications. We highlight the evolution of synthesis and characterization methods for composite electrode materials, emphasizing their relevance to practical applications. Key compositions and the underlying charge storage mechanisms are also discussed. Finally, we explore the opportunities and challenges in using graphene and its derivatives' composites for practical energy storage in supercapacitors.

Abbreviations: **ACNRs**, Activated polyaniline-derived hollow carbon nanorods; **AgNPs**, Ag nanoparticles; **ASC**, Asymmetric supercapacitors; **ALD**, Atomic layer deposition; **BPMW**, Bi-pyrene-terminated molecular wires; **BN**, Boron nitride; **CBD**, Chemical bath deposition; **CC**, Carbon cloth; **CWCC**, Carbonized wood cell chamber; **CVD**, Chemical vapor deposition; **Co_3O_4**, Cobalt oxide; **CV**, Cyclic voltammetry; **DHAQ**, Dihydroxyanthraquinone; **EDL**, Electric double-layer; **EDLC**, Electrochemical double-layer capacitor; **EES**, Electrochemical energy storage; **EIS**, Electrochemical impedance spectroscopy; **FTIR**, Fourier transform infrared; **Au**, Gold; **G/AC**, Graphene/activated carbon; **G/SC**, Graphene/soft carbon; **GA**, Graphene aerogel; **GCD**, Galvanostatic charge discharge; **GO-CMC**, Graphene-carboxy methylcellulose; **GO**, Graphene oxide; **GQD**, Graphene quantum dots; **hrGO**, Holy reduced graphene oxide; **HSC**, Hybrid supercapacitor; **IrO_2**, Iridium oxide; **$FeCoS_2$**, Iron cobalt sulphide; **LDH**, Layered double hydroxide; **LICs**, Li-ion capacitor; **LIMCs**, Li-ion micro capacitors; **MnO_2**, Manganese oxide; **MVO**, Manganese vanadate; **MOFs**, Metal-organic frameworks; **CH_4**, Methane; **MSCs**, Micro-supercapacitors; **MoS_2**, Molybdenum disulphide; **$MoSe_2$**, Molybdenum diselenide; **MWCNT**, Multi-walled carbon nanotubes; **NiO/NLIG**, N-doped laser-induced graphene; **NiCo-P**, Nickel cobalt phosphate; **NiV-LDH**, Nickel–vanadium LDH; **NSC**, Nitrogen and sulfur in carbon mircosheets; **OCC**, Oxidized carbon cloth; **PANI**, Polyaniline; **PEDOT**, Poly 3,4-ethylenedioxythiophene; **PI**, Polyimide; **PPy**, Polypyrrole; **PTh**, Polythiophene; **PGF**, Porous graphene skeleton; **rGO**, Reduced graphene oxide; **RuO2**, Ruthenium oxide; **SEM**, Scanning electron microscopy; **SiC**, Silicon carbide; **SILAR**, Successive ionic layer adsorption and reaction; **S-rGO**, Sulfur doped graphene; **SSC**, Symmetric supercapacitors; **TGA**, Thermogravimetric analysis; **3D**, Three-dimensional; **TEM**, Transmission electron microscopy; **TMCs**, Transition metal chalcogenides; **2D**, Two-dimensional; **UCNG**, Ultrafine Co_3O_4 nanoparticles/graphene; **XRD**, X-ray diffraction; **XPS**, X-ray photoelectron spectroscopy; **ZIFs**, Zeolitic imidazolate frameworks.

* Corresponding authors at: Centre for Interdisciplinary Research, D. Y. Patil Education Society, Kolhapur 416003, India (C.D. Lokhande). Optoelectronics Convergence Research Center and Department of Materials Science and Engineering, Chonnam National University, 300, Yongbong-Dong, Buk-Gu, Gwangju 61186, South Korea (Jin Hyeok Kim).

E-mail addresses: l_chandrakant@yahoo.com (C.D. Lokhande), jinhyeok@chonnam.ac.kr (J. Hyeok Kim).

https://doi.org/10.1016/j.cej.2024.157533
Received 14 August 2024; Received in revised form 30 October 2024; Accepted 7 November 2024
Available online 9 November 2024

CONFERENCES

DEPARTMENT OF PHYSICS
AMSCA
MAVERICK - 2022
PUNE-07
SAVITRIBAI PHULE PUNE UNIVERSITY

DEPARTMENT OF PHYSICS

Certificate of Participation

This is to certify that

Ajinkya Bagde

Centre for Interdisciplinary Research, D. Y. Patil Education Society, Kolhapur, India

Participated and presented the **Poster paper** entitled **Characterization of Amorphous ------ Ionic layer Adsorption and reaction (SILAR) method** from the **Energy Storage Materials** Theme made in the **International Conference on Advanced Materials Synthesis, Characterization and Applications (AMSCA Maverick-2022)** With Special Topic: New Education Policy held at the Department of Physics, Savitribai Phule Pune University, Pune- 07, Maharashtra, India during **18th -20th October, 2022.**

Convener
(AMSCA Maverick-2022)

Co-Convener
(AMSCA Maverick-2022)

Chairperson
(AMSCA Maverick-2022)

Three days International Conference on

Nano Composites for Aerospace Applications

Hybrid Mode

02nd to 04th February 2023

CERTIFICATE

Best Paper Award

presented to

Ajinkya Bagde

Centre for Interdisciplinary Research, D.Y. Patil Education Society, Kolhapur.

for presenting the Research Paper Entitled on

Pseudocapacitive performance of amorphous ruthenium oxide deposited by Successive ionic layer adsorption and reaction (SILAR) method.

in Three days International Conference on Nano Composites for Aerospace Applications (ICNCAS - 2023) held at the Department of Basic Sciences and Electronics & Communication Engineering, Cambridge Institute of Technology, Bengaluru, India.

Dr. Ravi Shankar	Dr. G. Indumathi	Shri. Nithin Mohan	Shri. D.K. Mohan
Assoc. Professor, Dept. of Basic Sciences	Principal	CEO	Chairman
Cambridge Institute of Technology	Cambridge Institute of Technology	Cambridge Institute of Technology	Cambridge Institute of Technology
Bangalore	Bangalore	Bangalore	Bangalore

Sponsored by AICTE

ICNCAS - 2023

CAMBRIDGE INSTITUTE OF TECHNOLOGY

Organized by
Department of Basic Sciences and Electronics & Communication Engineering

International Conference
on
"Advanced Materials Synthesis, Characterization and Applications - 2023"
(AMSCA - 2023)

DEPARTMENT OF PHYSICS

CERTIFICATE OF PARTICIPATION

This is to certify that,

Mr. Ajinkya Bagde, D. Y. Patil Education Society, Kolhapur has presented **Oral** on the topic **Chemically synthesis of reduced graphene oxide (rGO)/ruthenium oxide (RuO_2) composite electrode** in the **International Conference on AMSCA - 2023** held at the **Department of Physics, Savitribai Phule Pune University, Pune, Maharashtra, INDIA** during 21st to 24th November, 2023.

Convener
AMSCA - 2023

Co-Convener
AMSCA - 2023

Head
Department of Physics,
SPPU, Pune

"Education through self-help is our motto."- Karmaveer

Rayat Shikshan Sanstha's

RAJARSHI CHHATRAPATI SHAHU COLLEGE, KOLHAPUR

(Reaccredited 3rd Cycle by NAAC at 'A' Grade with CGPA 3.07)

DEPARTMENT OF PHYSICS and IQAC

Organizes Under G20 University Connect Program

One Day International Conference on

"Recent Trends in Fabrication of Nanomaterials and Their Applications (ICRTFNA-2023) "

Certificate

This is to certify that, Dr. /Prof./Mr./Ms./Mrs. Ajinkya Govindrao Bagade of D.Y. Patil University. has participated /~~worked as Resource Person~~/~~Chairperson~~/~~Organizing committee member~~ in **One Day International Conference on 'Recent Trends in Fabrication of Nanomaterials and Their Applications (ICRTFNA-2023)'** Organized by **Department of Physics** and **IQAC held on March 15, 2023.** He/She has presented paper entitled The Pesudocapacitive Performance of RuO_2 by SILAR : Effect of Thickness

Dr. A. R. Patil	Dr. V. V. Killedar	Dr. L. D. Kadam
Coordinator	Organizing secretary	Principal

D. Y. PATIL EDUCATION SOCIETY
(Deemed to be University), KOLHAPUR
NAAC 'A+' Grade in 3rd Cycle

Certificate

This is to certify that **Mr. /~~Ms.~~ Bagde Ajinkya Govindrao** of Centre for Interdisciplinary Research, DYPES, Kolhapur has delivered ~~invited talk~~/ chaired the ~~session~~/ presented oral/ ~~presented~~ poster/ participated in the **International Conference on Nanotechnology Addressing the Convergence of Materials Science, Biotechnology and Medical Science (IC-NACMBM-2024)** held at the Centre for Interdisciplinary Research, D. Y. Patil Education Society (Deemed to be University), Kolhapur, Maharashtra, India during 12th to 14th February 2024. His/ Her contribution to the conference is highly appreciated.

Dr. Jayavant L. Gunjakar	**Prof. Meghnad G. Joshi**	**Prof. Chandrakant D. Lokhande**
Convener	Convener	Chairman

SHIVAJI UNIVERSITY, KOLHAPUR

SOPHISTICATED ANALYTICAL INSTRUMENT FACILITY (SAIF)– COMMON FACILITY CENTRE (CFC) WORKSHOP & HANDS-ON TRAINING ON BIO-ATOMIC FORCE MICROSCOPY (BIO-AFM) ORGANISED BY SAIF-CFC UNDER MAHARASHTRA ACADEMY OF SCIENCE AND STRIDE PROGRAMME

Certificate of Participation

This is certify that Mr. *AJINKYA BAGDE* has successfully participated in the workshop & hands-on training on BIO-ATOMIC FORCE MICROSCOPY (BIO-AFM) organised by SAIF (CFC), Shivaji University, Kolhapur held during 04-05 Jan, 2022 under the Maharashtra Academy of Science and STRIDE (Scheme for Trans-disciplinary Research for India's Developing Economy) programme.

Prof. R. G. Sonkawade
Co-ordinator : SAIF, Head (i/c) : CFC
Shivaji University, Kolhapur.
Chairman

|| Tewo Sada Dnyanamay Pradeep ||

Shikshan Prasarak Mandal's

Shankarrao Mohite Mahavidyalaya, Akluj

Tal. Malshiras, Dist. Solapur, 413101 (Maharashtra State)

Affiliated to Punyashlok Ahilyadevi Holkar Solapur University, Solapur

Department of Chemistry & IQAC

organized

One Day Online National Conference on "Emerging Trends in Chemistry"

This is to certify that ***Ajinkya Bagde*** of **D Y Patil Education Society Deemed University Kolhapur** has actively participated in one Day Online National Conference on " Emerging Trends in Chemistry"(NCETC-2022) organized by Department of Chemistry & IQAC, Shankarrao Mohite Mahavidyalaya, Akluj held on 10th February 2022.

Dr. S.S.Deokar
Convener & Head of Department

Mrs. D.R.Kamble
Organizing Secretary

Prof. Dr.D.S. Bagade
I/C Principal

INTELLECTUAL PROPERTY INDIA
PATENTS | DESIGNS | TRADE MARKS
GEOGRAPHICAL INDICATIONS

सत्यमेव जयते

NIPAM
NATIONAL IP AWARENESS MISSION

Government of India
Ministry of Commerce and Industry
Department for Promotion of Industry and Internal Trade
Office of the Controller General of Patents, Designs and Trade Marks

CERTIFICATE

This is to certify that, **Mr. AJINKYA GOVINDRAO BAGDE** has successfully participated in IP Awareness/Training program under

NATIONAL INTELLECTUAL PROPERTY AWARENESS MISSION

on August 12,2022

Azadi Ka Amrit Mahotsav

Organized by

Intellectual Property Office, India

Date:August 22,2022

(Prof. (Dr) Unnat P. Pandit)
CONTROLLER GENERAL OF
PATENTS, DESIGNS & TRADE MARKS

Rayat Shikshan Sanstha's

D. P. Bhosale College, Koregaon, District- Satara

International Conference on

Emerging Trends in Material Science

e-Certificate

This is to certify that **Mr.Ajinky Bagde** of **D. Y. Patil Education Society, Kolhapur** has participated in **International Conference on "Emerging Trends in Material Science"** dated 9th & 10th November, 2022 jointly organized by Department of Physics & Chemistry in association with IQAC, D. P. Bhosale College, Koregaon, District- Satara, Maharashtra, India.

Certificate ID: ETMS-IC-119

Prof. Dr. S. D. Jadhav	Dr. V. S. Jamadade	Dr. B. S. Lokde	Dr. V. S. Sawant
Convener	Co-Convener	IQAC Coordinator	Principal

SANJAY GHODAWAT UNIVERSITY Kolhapur

Empowering Lives Globally !

(Approved by UGC & Govt.of Maharashtra)

Certificate

This is to certify that

Prof. / Dr. / Mr. / Ms. Ajinkya Govindrao Bagde, Ph.D. Scholar

of D Y Patil University Kolhapur has participated in National Seminar on

"Emerging Nano Materials for Renewable Energy"

held on Monday, 26th December, 2022 and organized by Sanjay Ghodawat University, Kolhapur.

Dr. Sambhaji M. Pawar
Convener

Dr. Pallavi D. Bhange
Convener

Dr. Sarita P. Patil
Co-ordinator

Prof. Dr. Arun S. Patil
Vice-Chancellor

Madha Taluka Shikshan Prasarak mandal's

K. N. BHISE ARTS, COMMERCE AND VINAYAKRAO PATIL SCIENCE COLLEGE,

VIDYANAGAR, Bhosare, Tal-Madha, Dist- Solapur (M.S.) (NAAC A Grade 3.10 CGPA)

Faculty of Science and I.Q. A. C.

Organized

One Day National Conference on Physical, Chemical and Biological Strategies, Tools and Ideas for Promising Future

(Sponsored by P. A. H. Solapur University, Solapur)

(10-03-2023)

Certificate

This is to certify that Prof./ Dr./Mr./Ms. AJINKYA GOVINDRAO BAGDE of K. N. Bhise Arts, Commerce and Vinayakrao Patil Science College Vidyanagar Bhosare. has participated in One Day National Conference on Physical, Chemical and Biological Strategies, Tools and Ideas for Promising Future organized by Faculty of Science and I. Q. A. C. of K. N. Bhise Arts, Commerce and Vinayakrao Patil Science College, Vidyanagar, Bhosare (Kurduwadi), Solapur, Maharashtra.

Dr. N. D. Deshmukh
Convener
Head, Dept of Microbiology

Prof. M. M. Patil
Organizing Secretary
Coordinator, Faculty of Science

Prof. Dr. P. S. Kamble
Director
I/C Principal

SWAMI RAMANAND TEERTH MARATHWADA UNIVERSITY, NANDED

Sponsored

One Day National Conference on

EMERGING TRENDS IN BASIC SCIENCES (NCETBS-2023)

Organized by

Faculty of Science

Madhavrao Patil Arts, Commerce & Science College, Palam

Dist. Parbhani (M.S.) - 431720

Certificate

This is to certify that **Mr. Ajinkya Govindrao Bagde** of **D. Y. Patil University, Kolhapur** has actively participated in One Day National Confernce on **"EMERGING TRENDS IN BASIC SCIENCES (NCETBS-2023)"** held on 20 March, 2023. He/She has presented research paper /poster presentation/delivered keynote adress / invited talk / chaired the session entitled _____

Chief Organizer
Dr. H. T. Satpute
(Principal)

Convenor
Dr. A. D. Arsule
(Vice - Principal)